A ROBUST IMMERSED BOUNDARY METHOD FOR FLOW IN COMPLEX GEOMETRIES: STUDY OF AEROSOL DEPOSITION IN THE HUMAN EXTRATHORACIC AIRWAYS

Laura Nicolaou Fernandez

Thermo-Fluids group

Department of Mechanical Engineering

Imperial College London, UK

Submitted in partial fulfilment of the requirements for the degree of Doctor of Philosophy

Department of Mechanical Engineering, Imperial College London

January 2012

Declaration of Originality

I declare that the work presented in this thesis is my own and that any work of others has been appropriately referenced.

Abstract

The flow and the transport of particles in the human respiratory system dictate the effectiveness of therapeutic aerosols used in inhaled drug delivery. The aerosol particles are generally inhaled through the mouth, passing by the throat before reaching the targeted areas in the lungs. Therefore, knowledge of the particle deposition in the mouth-throat region is critical in the design of effective inhalation devices for optimum delivery to the lungs. Numerical simulations offer a non-invasive and cost-effective alternative to *in vivo* and *in vitro* tests. However, accurate prediction remains a challenge for numerical models due to the complexity of the flow in the extrathoracic airways.

A robust immersed boundary method for flow in complex geometries is proposed. This greatly simplifies the task of grid generation and eliminates the problems associated with grid quality that exist for boundary-fitted grid techniques. The proposed method is an extension to the momentum forcing approach onto curvilinear coordinates and applies an iterative procedure to compute the forcing term implicitly, which stabilizes the scheme for higher Reynolds numbers. The use of a curvilinear grid minimizes the number of unused cells outside the geometry and increases the efficiency of the numerical scheme. The method is validated against numerical and experimental data in the literature for a number of test cases on both Cartesian and curvilinear grids. The results show good agreement with previous studies.

Direct numerical simulations were performed in a number of realistic mouth and throat geometries obtained from MRI scans. A Lagrangian particle tracking scheme was employed to advance the particles dynamically, and total and regional deposition efficiencies were determined and compared to *in vitro* data. The effect of inflow turbulence and intersubject variation on deposition was studied. Geometric variation has a large impact on total deposition whereas the effect of inflow turbulence is confined to oral deposition.

Acknowledgements

I would like to thank my advisor, Dr. Tamer Zaki, for the help and advice he has given me throughout my PhD. He has provided me with close supervision whenever it has been required, but has also allowed me to work independently whenever I have wished to do so. I am grateful to him for all the time he has dedicated to teaching me. I would also like to acknowledge the Inhaled Drug Delivery Group at GSK for their involvement in the project.

I owe my gratitude to my family and friends for their encouragement and support during these four years. In particular, Natalie and Constantina who have been my rocks. I would like to thank them for their understanding and for all the great times we have had. I could not ask for better friends.

I would like to say a massive thank you to the Wardening team in Wilson House, especially Mike, Dom, Shweta, Alex and Stuart who have made it such a great place to live in. I have had the best time as a Subwarden there. I would also like to thank my colleagues in room 503 for making my stay there an enjoyable one. Nick and Sandeep deserve a special mention for welcoming me so warmly into the group.

I owe the most gratitude to my parents for the love and support they have always given me. I wish to thank them for all their advice, their encouragement and their understanding. They have always looked after me and I cannot thank them enough. I dedicate this thesis to them.

Contents

Declaration of Originality **2**

Abstract **3**

Acknowledgements **4**

1 Introduction **18**

1.1 Background and Motivation 18

1.1.1 Flow regime 20

1.1.2 Particle deposition 21

1.2 Previous deposition research 25

1.2.1 *In vivo* studies 26

1.2.2 *In vitro* studies 28

1.2.3 *In silico* studies 31

1.3 Objectives 35

1.4 Overview 36

2 Numerical method **38**

2.1 Discretization of the governing equations 39

2.2 Immersed boundary method 45

2.2.1 Immersed boundary method in fractional step algorithm 55

2.2.2 Error analysis of explicit forcing 59

2.2.3 Stabilized momentum forcing 64

2.2.4 Treatment of mass conservation at IB cells 67

2.2.5 Geometric treatment 69

2.2.6 Implementation of immersed boundary condition 71

2.2.7 Extension of immersed boundary method to curvilinear coordinates 77
2.3 Particle tracking . . . 84
2.3.1 Governing equation and numerical integration . . . 87
2.3.2 Particle tracking algorithm . . . 94

3 Validation 103
3.1 Numerical accuracy of IB method . . . 103
3.2 Flow past a circular cylinder . . . 104
3.3 Flow past a sphere . . . 114
3.4 Flow in a wavy channel . . . 120
3.5 Flow in a square duct with strong curvature . . . 127

4 Flow and particle deposition in the extrathoracic airways 135
4.1 Geometries of the extrathoracic airways . . . 136
4.2 Computational grids . . . 140
4.3 Boundary conditions . . . 141
4.3.1 Inflow condition . . . 143
4.3.2 Outflow condition . . . 145
4.4 Flow fields . . . 145
4.4.1 Intrasubject variation (geometries S1b and S1a) . . . 147
4.4.2 Intersubject variation (geometries S2 and S4) . . . 153
4.5 Particle deposition . . . 160

5 Conclusions 176
5.1 Summary and key results . . . 176
5.1.1 Immersed boundary method . . . 177
5.1.2 Particle tracking . . . 178
5.1.3 Flow and particle deposition in the extrathoracic airways . . . 178
5.2 Future work . . . 179
5.2.1 Immersed boundary method for moving boundaries . . . 180
5.2.2 Multiblock solver . . . 185

List of Tables

2.1 Errors in the interpolation schemes for the C-space and P-space particle tracking algorithms. 102

3.1 Comparison of experimental and numerical studies for flow over a cylinder at $Re_d = 20$ and 40. 110

3.2 Comparison of experimental and numerical studies for flow over a cylinder at $Re_d = 200$. 114

3.3 Comparison of experimental and numerical studies for flow over a sphere. . 117

3.4 Comparison of experimental and numerical studies for flow over a wavy wall. 125

4.1 Major dimensions of the mouth and throat geometries. 138

4.2 Flow parameters in the mouth and throat geometries. 146

4.3 Particle Stokes numbers in the mouth and throat geometries. 161

4.4 Deposition in the different regions of the S1a geometry, given as a percentage of aerosol entering the mouth. 162

4.5 Deposition in the different regions of the S2 geometry, given as a percentage of aerosol entering the mouth. 162

4.6 Deposition in the different regions of the S4 geometry, given as a percentage of aerosol entering the mouth. 162

List of Figures

1-1 Schematic diagram of the human respiratory system. 19
1-2 Time averaged velocity field in central plane of a realistic mouth-throat geometry, obtained from PIV measurements. 22
1-3 Schematic diagram of particle deposition mechanisms in a bifurcating airway. 23
1-4 Schematic overview of total particle deposition in the human respiratory system against aerodynamic particle size. 24
1-5 Schematic of experimental setup for *in vitro* measurements. 26
1-6 Extrathoracic deposition during mouth breathing as a function of $d_{ae}^2 Q$. . . 28
1-7 Extrathoracic deposition as a function of Stokes number with Reynolds number correction. 31
1-8 Comparison of extrathoracic deposition for standard $k-\omega$ model, with and without near-wall correction. 33

2-1 Schematic of a curvilinear grid cell. 42
2-2 Schematic of the immersed boundary method. 46
2-3 Distribution functions used in the continuous forcing approach. 50
2-4 Mass conservation for a cell cut by the immersed boundary. 68
2-5 Example of a three-dimensional triangulated surface. 70
2-6 2D schematic of the ray-tracing algorithm. 72
2-7 2D schematic of the IB cells and the IB points. 73
2-8 Schematic of interpolation procedures tested by Fadlun *et al.* (2000). 74
2-9 Schematic of the various interpolation schemes applied in immersed boundary methods. 75
2-10 2D schematic showing problems encountered in determining the position of a mirror point. 77

2-11 2D schematic of the covariant and contravariant base vectors of a curvilinear grid cell. 80
2-12 2D schematic of the tetrahedrization method used for point location. 81
2-13 2D example of coupled IB points. 83
2-14 Regimes of two-phased flows as a function of particle volume fraction. . . . 85
2-15 Drag coefficient as a function of particle Reynolds number. 89
2-16 Schematic of differencing schemes for Jacobian computation. 99
2-17 2D schematic of grid transformation from physical to computational space. 101

3-1 Distribution of error in streamwise velocity: implicit versus explicit IB method. 105
3-2 Grid convergence study: L_2 and L_∞ error norms of velocities. 106
3-3 Non-uniform grid employed in the cylinder simulations. 107
3-4 Location, spacing and stretching ratio of streamwise points in the grid. . . . 108
3-5 Spanwise vorticity contours and streamlines over a cylinder at $Re_d = 20$ and $Re_d = 40$.. 109
3-6 Schematic of the recirculation zone behind a cylinder. 109
3-7 Pressure coefficient and skin friction for flow over a cylinder at different Reynolds numbers. 111
3-8 Spanwise vorticity contours and streamlines over a cylinder at $Re_d = 200$. . 111
3-9 Schematic of a triangle on the surface and the points used for computation of the body forces. 113
3-10 Temporal variation of drag coefficient and lift coefficient on a cylinder at $Re_d = 200$. 114
3-11 Variation of Strouhal number and base pressure coefficient with Reynolds number for flow over a cylinder. 115
3-12 Spanwise vorticity contours and streamlines at different Reynolds numbers in an xy plane through the centre of a sphere. 116
3-13 Schematic of the recirculation zone behind a sphere. 117
3-14 Pressure coefficient and skin friction for flow over a sphere at $Re_d = 100$. . . 118
3-15 Vortical structures behind a sphere at $Re_d = \{100, 250, 300\}$. 119
3-16 xy and xz view of the vortical structure behind a sphere at $Re_d = 300$. . . . 120
3-17 Computational domain for the flow in a wavy channel. 122
3-18 Temporal variation of the Reynolds number based on friction velocity, Re_τ. 122

3-19 Contours of instantaneous spanwise vorticity over wavy wall. 123
3-20 Vortical structures over wavy wall. 124
3-21 Contours of mean velocities over wavy wall. 125
3-22 Contours of Reynolds shear stress over wavy wall. 125
3-23 Mean streamwise velocity profiles at different streamwise locations over wavy wall. 127
3-24 Mean wall-normal velocity profiles at different streamwise locations over wavy wall. 128
3-25 Turbulence intensities over wavy wall. 128
3-26 The geometry and the grid employed for a square duct with a 90° bend. . . 130
3-27 Streamwise velocity contours and secondary velocity vectors in a square duct of strong curvature at $Re_d = 790$. 132
3-28 Streamwise velocity profiles in a square duct of strong curvature at $Re_d = 790$. 133
3-29 Pressure coefficient and skin friction for flow in a square duct of strong curvature at $Re_d = 790$. 134

4-1 Sub-regions of the extrathoracic airways. 137
4-2 STL models of the extrathoracic airway geometries. 138
4-3 Modified geometries used in the DNS. 139
4-4 Grid used for mouth and throat geometry. 142
4-5 Mean velocity and turbulence intensities in inlet pipe. 144
4-6 Contours of instantaneous velocity and fluctuations in geometry S1a. 146
4-7 Contours of mean velocity magnitude and 2D streamlines in geometry S1b. 148
4-8 Contours of mean velocity magnitude and 2D streamlines in geometry S1a. 149
4-9 Contours of mean turbulent kinetic energy in geometry S1b. 151
4-10 Contours of mean turbulent kinetic energy in geometry S1a. 151
4-11 Velocity and turbulent kinetic energy on plane of maximum velocity in geometry S1b. 152
4-12 Sagittal planes of maximum velocity and maximum turbulent kinetic energy in geometry S1a. 152
4-13 Contours of mean velocity magnitude and 2D streamlines in geometry S2. . 155
4-14 Contours of mean velocity magnitude and 2D streamlines in geometry S4. . 156
4-15 Contours of mean turbulent kinetic energy in geometry S2. 158

4-16 Contours of mean turbulent kinetic energy in geometry S4. 158
4-17 Sagittal planes of maximum velocity and maximum turbulent kinetic energy in geometry S2. 159
4-18 Sagittal planes of maximum velocity and maximum turbulent kinetic energy in geometry S4. 159
4-19 Deposition patterns on geometry S1a. 163
4-20 Deposition patterns on geometry S2. 164
4-21 Deposition patterns on geometry S4. 165
4-22 Deposition efficiency versus Stokes number. 168
4-23 Deposition efficiency versus Stokes number with Reynolds number correction. 169
4-24 Particle deposition in fully developed turbulent pipe flow. 171
4-25 Deposition efficiency versus nondimensional particle relaxation time. 174

5-1 Relationship between volume and flow rate in the breathing cycle. 183
5-2 Dynamic model of the airway geometries. 184
5-3 Schematic of the multiblock immersed boundary approach for the tracheobronchial tree. 185

Nomenclature

Acronyms

CFD	Computational fluid dynamics
CFL	Courant-Friedrichs-Lewy number
COPD	Chronic obstructive pulmonary disease
CRW	Continuous random walk
CT	Computed tomography
DNS	Direct numerical simulation
DPI	Dry powder inhaler
EIM	Eddy interaction model
IB	Immersed boundary
LES	Large eddy simulation
MDI	Metered-dose inhaler
MMAD	Mass median aerodynamic diameter
MRI	Magnetic resonance imaging

PIV	Particle image velocimetry
RANS	Reynolds-averaged Navier-Stokes

Universal Notations

$()_f$	Denotes a fluid quantity
$()_i$	Denotes the index of a vector
$()_{ij}$	Denotes the ith and jth indices of a tensor
$()_{i,j}$	Denotes the i and j location of a quantity on a 2D grid
$()_{i,j,k}$	Denotes the i,j and k location of a quantity on a 3D grid
$()^k$	Denotes a quantity at iteration step k
$()_m$	Denotes the index of a vector in generalized curvlinear coordinates
$()^m$	Denotes the index of a vector in generalized curvlinear coordinates
$()^n$	Denotes a quantity at timestep n
$()_p$	Denotes a particle quantity
$()_{rms}$	Denotes a root-mean-square quantity
$()^+$	Denotes a quantity non-dimensionalized by wall (plus) units
$\bar{()}$	Denotes a mean quantity

Roman Symbols

C_L	Lift coefficient
C_D	Drag coefficient

C_f	Skin friction coefficient
C_p	Pressure coefficient
d	Diameter
d_{ae}	Aerodynamic diameter
$d_{ae}^2 Q$	Inertial parameter
D	Discrete divergence operator
$\boldsymbol{e}_m$	Covariant base vectors
$\boldsymbol{f}$	Momentum forcing term
G	Discrete gradient operator
$\boldsymbol{J}$	Transformation matrix
J	Jacobian of transformation matrix
k	Turbulent kinetic energy per unit mass
L	Characteristic length scale
$L(\boldsymbol{u})$	Implicit diffusive terms
$N(\boldsymbol{u})$	Convective and explicit diffusive terms
p	Pressure
q	Mass source term
Q	Volumetric flow rate
Re	Reynolds number

Re_d	Reynolds number based on diameter
Re_τ	Reynolds numver based on friction velocity
Re_p	Particle Reynolds number
$\boldsymbol{r}_p$	Particle position vector
$\boldsymbol{S}^m$	Face area vector
$\boldsymbol{S}_m$	Reciprocal base of the face area vector
St	Strouhal number
Stk	Stokes number
t	Time
$\boldsymbol{u}$	Cartesian velocity vector
$\hat{\boldsymbol{u}}$	Intermediate velocity vector
$\tilde{\boldsymbol{u}}$	Explicit approximation of the intermediate velocity vector
$\boldsymbol{u}^m$	Contravariant velocity vector
$\boldsymbol{u}_\Gamma$	Boundary velocity vector
$\boldsymbol{u}_{IB}$	Velocity vector at the IB points
$\boldsymbol{u}_p$	Particle velocity vector
u_τ	Friction velocity
$\boldsymbol{U}$	Flux vector
$\hat{\boldsymbol{U}}$	Intermediate flux vector

U	Characteristic velocity scale
U_b	Bulk velocity
U_∞	Free-stream velocity
V	Volume
x	Streamwise direction
y	Wall-normal direction
z	Spanwise direction

Greek Symbols

Γ_b	Immersed boundary
δ	Dirac delta function
Δt	Time step
Δx	Grid spacing in the streamwise direction
Δy	Grid spacing in the wall-normal direction
Δz	Grid spacing in the spanwise direction
ϵ	Error
ε	Minimum tolerance
λ	Eigenvalue
λ_w	Wavelength
μ	Dynamic viscosity

ν	Kinematic viscosity
ϕ	Pseudo-pressure
ρ	Density
τ	Shear stress
τ_f	Characteristic time scale in the flow
τ_p	Particle relaxation time
(ξ, η, ζ)	Curvilinear coordinates
Ω_b	Solid domain
Ω_f	Fluid domain

Chapter 1

Introduction

1.1 Background and Motivation

Aerosolized delivery of drugs to the lungs has been used for decades to treat a number of respiratory diseases, such as asthma, chronic obstructive pulmonary disease (COPD), cystic fibrosis and pulmonary infections. Inhaled delivery provides a high concentration of the drug at the target site, a rapid onset of the drug action and low systemic exposure leading to reduced side-effects (Lipworth, 1996). More recently, the use of the inhaled route for the systemic administration of drugs has received increasing interest due to the favourable absorption characteristics of the lungs. Research has demonstrated the potential of inhaled administration for various therapeutic peptides, proteins and vaccines. Inhaled insulin for the treatment of diabetes is already in use (Patton & Byron, 2007).

A schematic of the respiratory system is shown in figure 1-1. The airways can be divided into two anatomic areas: the extrathoracic or upper airways which consist of the mouth, nose, pharynx, larynx and trachea and the intrathoracic or lower airways which begin at the level of the intrathoracic trachea and extend all the way down to the alveoli. The aerosol is generally inhaled through the mouth as it is more effective than the nasal route,

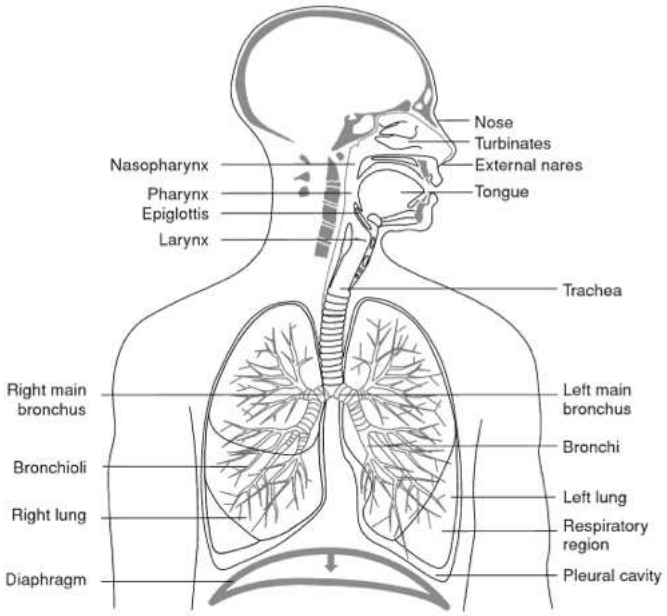


Figure 1-1: Schematic diagram of the human respiratory system (Bisgaard *et al.*, 2007).

allowing a higher dose to penetrate into the lungs. Having passed through the mouth, the inhaled particles travel through the larynx, continuing down the pharynx and trachea before entering the lungs. For effective drug delivery, the aerosol must reach the target site within the lung. Often however, significant losses are experienced in the extrathoracic airways leading to very low pulmonary deposition. Therefore, understanding the flow dynamics and deposition patterns of inhaled particles in the mouth-throat region is important in order to minimize extrathoracic losses and optimize pulmonary drug delivery. Such an understanding is not straightforward as the distribution and deposition pattern of the aerosol within the respiratory system depends on a complex relation between the morphology of the patient's airways, the particle size distribution and the inspiratory flow rate.

Studies have been conducted on subjects and in casts of the respiratory airways in order to gain an understanding on the deposition of inhaled particles and optimize drug delivery. In the last decade, numerical simulations of the flow and the particle trajectories in the extrathoracic airways have become possible with commercial computational fluid dynamics

(CFD) packages, offering a non-invasive and cost-effective alternative to *in vivo* and *in vitro* testing. However, accurate prediction of particle deposition remains a challenge due to the complexity of the flow in the extrathoracic airways. The aim of this project is to develop a numerical model that provides an accurate representation of the flow through the airways and therefore an accurate prediction of the deposition patterns and deposition efficiency in the mouth and throat region.

1.1.1 Flow regime

The average respiratory flow rate for an adult during quiet breathing is $15L/min$. Inspiratory flow rates from different inhalers typically range from $15L/min$ to $90L/min$. Due to the bifurcating nature of the lung and the effect of the breathing cycle on the flow, patterns in the respiratory airways are complex even during quiet breathing. The constriction by the vocal cords causes an increase in the velocity, and hence the Reynolds number. The flow remains turbulent in the mouth and throat and the larger airways, primarily the trachea and the main bronchi, before extensive branching increases the total cross-sectional area and therefore reduces the gas velocity through each airway, causing relaminarisation. In most of the tracheobronchial tree, flow is transitional with eddies forming at the branching points. Fully developed laminar flow only occurs in the smaller airways where the Reynolds number is very low ($Re_d \sim 1$ in the terminal bronchioles, where Re_d is the Reynolds number based on the mean diameter of the airways and the mean flow velocity).

Due to the irregular shape of the extrathoracic airways, localized regions of laminar to turbulence transition occur even at low flow rates. In fact, Dekker (1961) reported turbulent structures in the trachea at flow rates as low as $3L/min$, which correspond roughly to a Reynolds number Re_d in the larynx of only 400. Therefore, although the extrathoracic

airways approximate a bent pipe, their irregular shape and the effect of the constriction in the airways and the bifurcations downstream introduce turbulence at lower Reynolds numbers than would appear in an idealized geometry. Although the flow is more complex than that in a curved pipe, qualitatively we can expect some similarities in the main flow features. The high curvature of the ducts leads to skewed velocity profiles as centrifugal forces acting on the flow cause it to move towards the outer wall. This can lead to separation at the inner wall and strong secondary flow can also be expected due to the bend.

The highly irregular cross-sectional area of the airways also has an effect on the flow pattern. The constriction due to the epiglottis, located upstream of the larynx leads to the generation of a laryngeal jet that tends to impinge on the back wall due to the bend in the airways. Further downstream, recirculation regions in the lateral expansions of the larynx are expected, as the flow separates. Figure 1-2 shows the mean velocity field along the mid-plane of a realistic mouth and throat geometry, obtained using particle image velocimetry (PIV), in which some of the features mentioned above are visible. The geometric variation of the airways amongst subjects means that flow patterns can also differ significantly from one geometry to the other.

1.1.2 Particle deposition

Inhaled particles experience a number of forces which cause their trajectories to deviate from the streamlines and thus deposit on the airway walls. Deposition in the respiratory system occurs via four main mechanisms: sedimentation, diffusion, inertial impaction and interception (see figure 1-3). The significance of each deposition mechanism depends on the particle properties and the flow field. As discussed in the previous section, the flow in the respiratory system is complex and differs substantially from the larger to the smaller

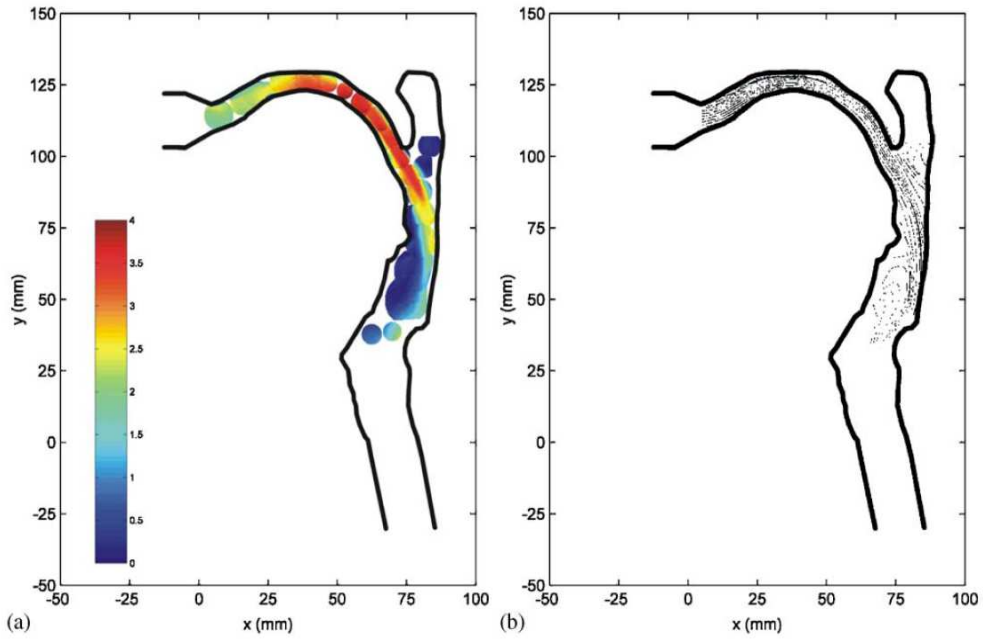


Figure 1-2: Time averaged velocity field in central plane of a realistic mouth-throat geometry, obtained from PIV measurements. (a) Velocity magnitude contours normalized by the inlet plug velocity and (b) 2D streaklines.(Heenan *et al.*, 2004).

airways, so the main mechanism of deposition also changes in the various regions of the respiratory system. Different flow rates and particle sizes affect the amount of deposition as well as the deposition pattern.

Sedimentation is the deposition of particles as a result of gravity. It is dependent on the density and diameter of the particles and requires sufficient residence time for completion. For this reason, sedimentation in the larger airways is minimal as the air velocity is high $(1 - 2m/s)$, resulting in short residence times. However, as the velocity decreases down the tracheobronchial tree, an increase in residence time allows the particles to be deposited by gravitational forces. Sedimentation is predominant in the bronchial and alveolar regions and tends to affect the smaller particles $(0.5 - 3\mu m)$.

Diffusion is a result of Brownian motion caused by the random constant collisions between the gas and the aerosol particles. Deposition by diffusion increases with time and

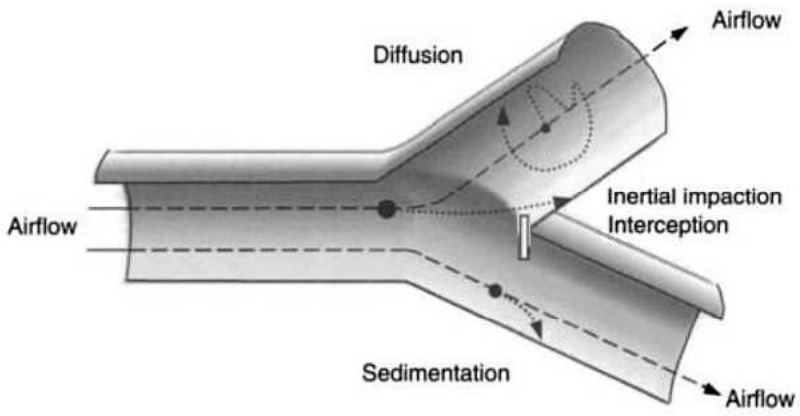


Figure 1-3: Schematic diagram of particle deposition mechanisms in a bifurcating airway (Ruzer & Harley, 2004).

decreasing particle size, as the random displacement undergone by a particle increases. It is only significant for submicrometer particles (Ounis *et al.*, 1991), and it is most likely to occur in the small airways of the lung periphery.

Inertial impaction occurs due to the momentum of particles which causes them to deviate from the fluid streamlines and collide with the airway walls. The larger the particles, the higher the probability of deposition by impaction. Particles ($> 5\mu m$) generally deposit at the back of the mouth and the upper airways by impaction as velocities are high and there are rapid changes in the flow direction.

Finally, deposition by *interception* occurs when a particle collides with the airway surface without deviating from the streamline. It is a mechanism that affects elongated particles and other particles of irregular shape. If fibres stay aligned with the direction of the flow they can penetrate as far into the lung as spherical particles of the same diameter, however if they are 'tumbling', they will have a greater likelihood of colliding with a surface and depositing by interception.

The general trend of total deposition in the respiratory tract against particle size is

shown in figure 1-4. The actual shape of this curve is harder to determine as it depends on a number of other factors as mentioned earlier. The particle size here is given by the aerodynamic diameter, d_{ae}, defined as the diameter of a sphere of unit density, ρ_0, which has the same settling velocity in air as the particle being measured:

$$d_{ae} = \sqrt{\frac{\rho_p}{\rho_0}} d_p \tag{1.1}$$

where ρ_p and d_p are the density and diameter of the particle respectively. This is the characteristic diameter normally used to describe the size of aerosol particles since particles with the same aerodynamic diameter experience the same gravitational and inertial displacements and it is the inertial behaviour of the particles that defines where and how they deposit in the airways. (This only applies to particles transported by inertia and gravitation without diffusion, therefore only for particles larger than $1\mu m$ in aerodynamic diameter.)

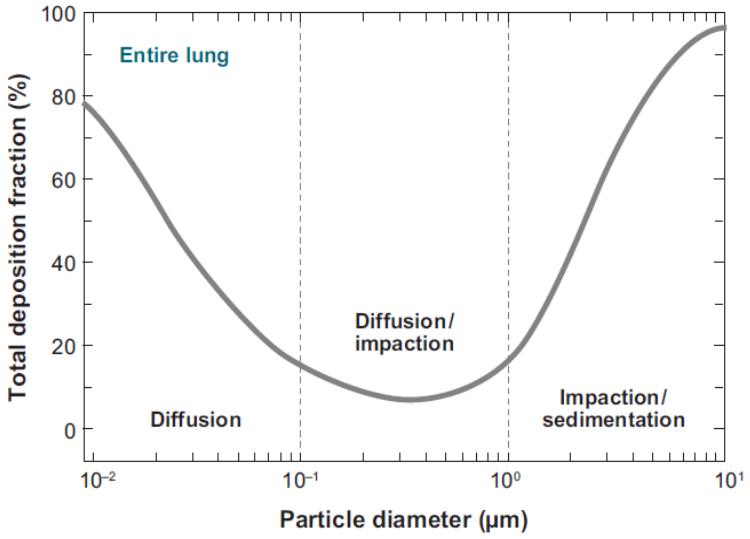


Figure 1-4: Schematic overview of total particle deposition in the human respiratory system against aerodynamic particle size (Kleinstreuer *et al.*, 2008).

Aerosols produced by inhalation devices are polydisperse so their size is usually described by the mass median aerodynamic diameter (MMAD). Sizes are usually determined

using a Cascade impactor, in which the aerosol is passed by an 'artificial throat' (a 90° bend) before measurements are made. Average size depends on the drug formulation as well as the inhalation device and MMADs range from as small as $1.1\mu m$ in some metered-dose inhalers (MDIs) (Leach, 1998) to as large as $24\mu m$ in nebulizers (Matthys & Kohler, 1985). In dry powder inhalers (DPIs) the drug particles are attached to larger carrier particles which typically range from $50 - 150\mu m$ in order to avoid agglomeration. Given the typical sizes, we can see that aerosol particles fall mainly in the sedimentation/impaction regime.

1.2 Previous deposition research

Previous research on extrathoracic deposition can be divided into three main categories: *in vivo* studies, *in vitro* experiments and numerical simulations. There are two classical ways of performing *in vivo* measurements of deposition in the respiratory system: scintigraphy and pharmacokinetics. In scintigraphy, the drug is labelled with a gamma-ray emitting isotope and deposition locations are seen by an external gamma camera. Pharmacokinetic studies measure the amount of drug appearing in the circulation or urine which represents the drug initially deposited in the lung. However, only the total amount of drug deposited in the respiratory system can be measured. No information on regional deposition can be attained, therefore pharmacokinetics cannot be used for determining extrathoracic deposition.

In vitro studies are measurements carried out in casts of the airways. The casts are either models built of regular geometric shapes for an idealized representation of the airways, or realistic geometries obtained from magnetic resonance imaging (MRI) or computed tomography (CT) scans of subjects. In the latter case, the two-dimensional slice images obtained are converted into 3D volumes from which STL models are generated and used to manufacture the casts. A pump draws the radiolabelled aerosol through the mouth and

throat cast at the desired flow rate from a mixing chamber where it has previously been diluted in air (see figure 1-5). A filter at the exit measures the amount of aerosol that has not deposited. Regional deposition measurements are performed with a gamma camera.

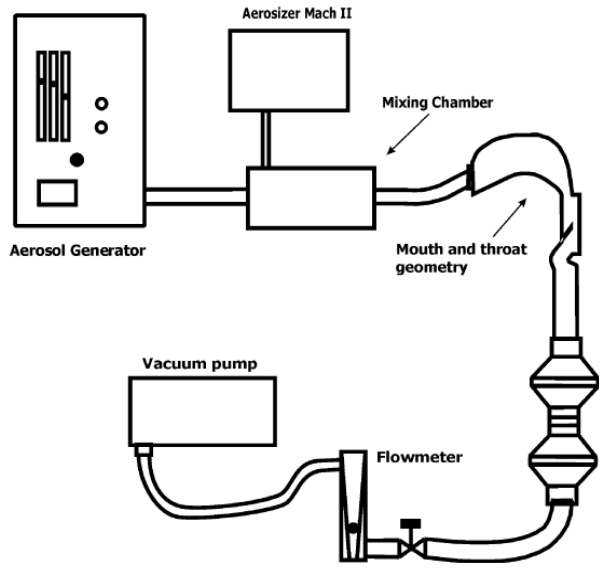


Figure 1-5: Schematic of experimental setup for *in vitro* measurements (Grgic *et al.*, 2004*b*).

Numerical models of the deposition in the extrathoracic airways require simulation of the flow and the particle trajectories. The geometries can be obtained by meshing the STL models used to manufacture casts in *in vitro* testing. For idealized geometries, structured grids can be used, whereas unstructured grids are required to model the realistic airways due to their irregular shape. Particle trajectories are computed by Lagrangian particle tracking which consists of computing the forces acting on the particles and solving the equations of motion.

1.2.1 *In vivo* studies

Various *in vivo* studies of deposition in the human respiratory tract have been conducted on a selection of healthy subjects and patients with pulmonary disease by inhalation of radioactive tracer particles (Walsh *et al.*, 1977; Foord *et al.*, 1978; Chan & Lippmann, 1980;

Stahlhofen *et al.*, 1980, 1981; Emmett & Aitken, 1982; Svartengren *et al.*, 1994). Aerosol is administered to the subjects under specified breathing conditions and the total amount deposited is determined from the difference between the inhaled and exhaled aerosol. Mouth deposition is determined from the activity measured in the mouth wash and other regional depositions are obtained using external gamma-ray detectors. Walsh *et al.* (1977) describes in detail the apparatus and methodology employed. The results obtained showed a large variation in total deposition among subjects, which was a result of the large variation in extrathoracic deposition (Stahlhofen *et al.*, 1981). Extrathoracic deposition efficiency was described as a function of $d_{ae}^2 Q$, known as the inertial parameter, where Q is the volumetric flow rate.

Agreement of the data in the literature for the deposition efficiency plotted against the inertial parameter corroborated impaction as the main mechanism of deposition in the mouth and throat and various empirical fits were suggested in an attempt to obtain a model for extrathoracic deposition (see figure 1-6). The scatter in the data was attributed to the large intersubject variation and the differences in experimental techniques.

Inspection of the inertial parameter shows that it does not take into account the characteristics of the geometry. This naturally causes the large scatter in the data observed in the literature. A non-dimensional parameter including scales related to the geometry would be a preferable measure against which to plot deposition. In addition, the impaction parameter only accounts for the mean dynamics of the flow. However, the flow in the extrathoracic airways is turbulent so particle trajectories, and hence deposition, are affected by turbulent fluctuations. The impaction parameter is therefore likely to produce discrepancies in particular at higher flow rates where the turbulence levels are higher, and smaller particles which are more affected by flow fluctuations.

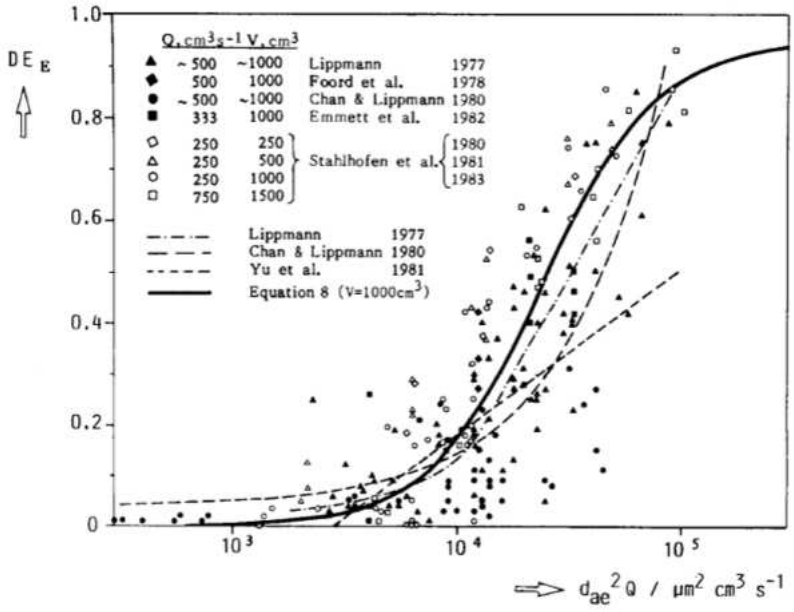


Figure 1-6: Extrathoracic deposition during mouth breathing as a function of $d_{ae}^2 Q$. Experimental data, and various approximations proposed in the literature. (Stahlhofen *et al.*, 1989).

1.2.2 *In vitro* studies

In vivo measurements are costly and complex to perform, and accurate results are difficult to obtain due to spatial resolution and tissue attenuation limit (Grgic *et al.*, 2004*a*). *In vitro* experiments offer the advantage of being easier to perform and allowing the systematic investigation of the parameters which affect deposition. The geometric characteristics of the airways are also available allowing investigation of the effect of intersubject variation. A number of *in vitro* studies of deposition in the mouth and throat are available in the literature (Cheng *et al.*, 1999, 2001; Lin *et al.*, 2001; Grgic *et al.*, 2004*b*; DeHaan & Finlay, 2004; Grgic *et al.*, 2004*a*; Heenan *et al.*, 2004), of which a couple also include flow measurements (Heenan *et al.*, 2004; Grgic *et al.*, 2004*a*).

Cheng *et al.* (1999) investigated the effects of particle size and inhalation rate on the deposition pattern in a human oral airway cast and found an increase in deposition with both particle size and flow rate. Their observations are in agreement with previous *in vivo*

data in the literature. They showed that their geometry could be described as a 180° curved tube and used the analytical solution for the trajectory of a particle in a curved pipe (Cheng & Wang, 1975, 1981) to derive a model for inertial deposition in the extrathoracic airways. Good agreement between their theoretical fit and the deposition results from the cast was observed.

Cheng *et al.* (2001) used the same geometry to study the deposition patterns from pressurized metered dose inhalers (pMDIs) and found that, surprisingly, at the higher flow rate of $90L/min$ oral deposition was in fact lower. They attributed this to the fact that the particles ejected from a pMDI travel faster than the air flow which is why heavy deposition is generally observed in the oral region due to impaction. At high air flow rates however, higher momentum transfer between the particles and the flow leads to reduced particle inertia and therefore a decrease in impaction. Another reason that was suggested was the increased evaporation rate at the higher flow rate, resulting in smaller particles which can penetrate further into the lungs.

Grgic *et al.* (2004*b*) conducted deposition measurements in an idealized geometry along with particle image velocimetry (PIV) measurements in order to visualize the flow. They suggested that the Stokes number, based on the mean diameter and the mean velocity in the geometry, was a better parameter to describe deposition efficiency rather than the inertial parameter traditionally used in the literature, as the inertial parameter does not take into account the geometric characteristics of the mouth and throat (hence the large scatter in *in vivo* data due to intersubject variation). However, deposition data plotted versus Stokes number showed that results at different flow rates appeared to lie on different curves, indicating a possible dependence on the Reynolds number. This dependence was attributed to the difference in the velocity profile at different flow rates, which was observed

in the PIV measurements. An empirical Reynolds number correction, $Re^{0.37}$, was applied to the Stokes number for which their data collapsed onto one curve.

As well as different flow rates, DeHaan & Finlay (2004) used a turbulence generator to study the effect of the inlet turbulence intensity in an idealized geometry of the oral cavity and found an increase in deposition with increasing turbulence. They chose to compute a Stokes number based on the velocity and dimensions of the jet at the inlet (rather than the mean length and velocity of the entire geometry) arguing that the jet impinging at the back of the mouth is the main mechanism of deposition in the oral cavity. In order to account for the higher depositions due to turbulence, they suggested an empirical function for a 'turbulent velocity scale', based on the mean bulk velocity and the turbulent kinetic energy per unit mass, k. They concluded that the inlet turbulence levels which they considered had a smaller effect on oral deposition than inlet diameter and mean velocity.

Grgic *et al.* (2004*a*) and Heenan *et al.* (2004) studied the effects of geometric variation in realistic mouth and throat geometries. Comparison of the deposition patterns and the flow field showed a strong correlation between the deposition levels and the local velocity magnitude and flow curvature (Heenan *et al.*, 2004). Grgic *et al.* (2004*a*) related the regional depositions to the geometric characteristics of the different mouth and throat casts and observed that intrasubject variability was considerably smaller than intersubject variability. Their results showed good correlation with Stokes number, but even better collapse of the data onto a single curve, with the empirical Reynolds number correction of Grgic *et al.* (2004*b*). A least squares curve fit for the deposition efficiency was proposed (see figure 1-7).

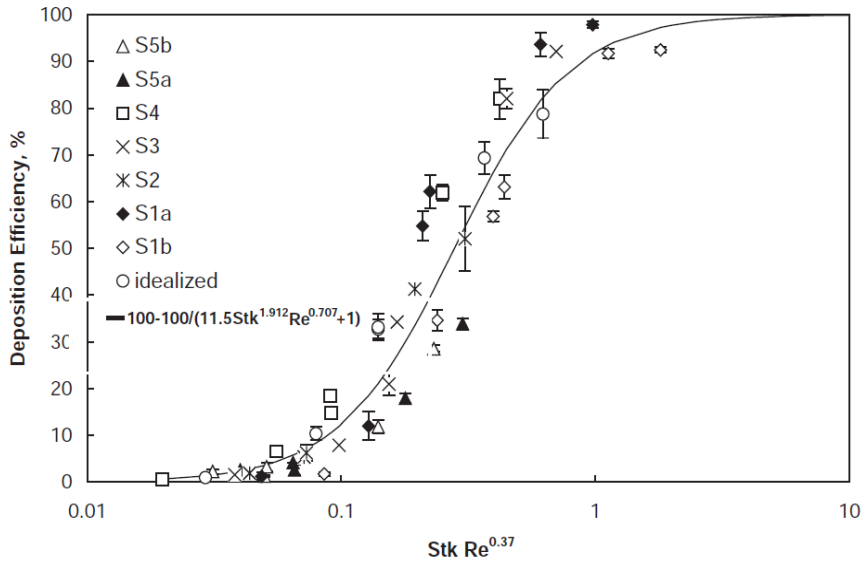


Figure 1-7: Extrathoracic deposition as a function of Stokes number with Reynolds number correction. Experimental data for all mouth-throat geometries tested along with least square curve fit function. (Grgic *et al.*, 2004*a*).

1.2.3 *In silico* studies

In more recent years, deposition in the respiratory system has been studied using CFD. Accurate prediction poses a particular challenge in the extrathoracic airways due to the complexity of the flow. A number of Reynolds-averaged Navier-Stokes (RANS) and a couple of large eddy simulation (LES) models have been proposed in the literature. Finlay *et al.* (1996) discussed the adequacy of standard $k-\epsilon$ models for the simulation of flow in the mouth and throat. Most models are designed for high-Reynolds-number flows in simple geometries and may therefore be unsuitable for low-Reynolds-number turbulence in complex geometries like the extrathoracic airways. They are known to perform poorly in flows with recirculating regions, free-shear layers and mean streamline curvature, all of which are present in the mouth and throat. Stapleton *et al.* (2000) investigated the suitability of such a model on an idealized mouth and throat geometry, running a laminar and a turbulent case and comparing it to *in vitro* measurements. Whereas the laminar case showed excellent agreement with the experimental data, a large overprediction in deposition was observed in

the turbulent case, due to the inadequacy of the turbulence model.

Comparison of $k-\epsilon$ and $k-\omega$ models showed that the $k-\omega$ models performed better (Matida *et al.*, 2004). Two different tracking models were used, 'mean flow tracking' where the particles were made to follow or deviate from the mean flow field according to their inertia only, and 'turbulent tracking' where the effects of the velocity fluctuations on the particles were included. This was done using an eddy interaction model (EIM) (Gosman & Ioannides, 1983), that assumes isotropic turbulence and uses a Gaussian distribution to obtain the fluctuating velocity, $(u^{'}, v^{'}, w^{'})$, acting on a particle from the turbulent kinetic energy:

$$\begin{aligned} u^{'} &= N_u \left(\frac{2k}{3}\right)^{0.5} \\ v^{'} &= N_v \left(\frac{2k}{3}\right)^{0.5} \\ w^{'} &= N_w \left(\frac{2k}{3}\right)^{0.5} \end{aligned} \tag{1.2}$$

where N_u, N_v, N_w are random numbers generated from a Gaussian distribution and $k = \frac{1}{2}\left(u^{'2} + v^{'2} + w^{'2}\right)$ is the turbulent kinetic energy per unit mass. In this model, particles interact with an eddy until either the lifetime of the eddy is over or the particle crosses the eddy, after which interaction with a new eddy begins. A much better correlation with experimental data was observed for the 'mean-flow tracking' rather than the 'turbulent tracking' simulations. This was ascribed to the artificially high turbulent diffusivity near the wall in the turbulence model, caused by the isotropic decomposition of the turbulence kinetic energy. Therefore, a near-wall correction which takes into account the turbulence anisotropy was proposed, using a function for the wall-normal fluctuating velocity in channel flow. This correction significantly improved the results, as can been seen in figure 1-8,

although there was still some discrepancy with experimental data.

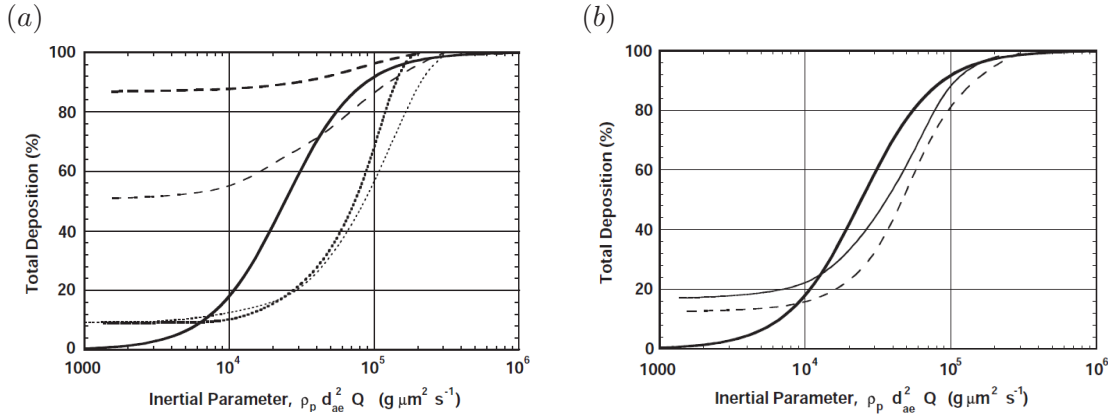


Figure 1-8: Total deposition compared to Stahlhofen *et al.* (1989)'s experimental fitting curve for different inhalation flow rates in an idealized mouth-throat geometry. (a) Standard $k-\omega$ model, (b) Near-wall correction on 'turbulent tracking', - - -$Q = 30L/min$, —$Q = 90L/min$ (Matida *et al.*, 2004).

Using different $k-\omega$ models, Jayaraju *et al.* (2007) and Zhang *et al.* (2002) on the other hand, showed much better agreement with experimental data in comparison to the 'turbulent tracking' model of Matida *et al.* (2004) without any near-wall correction. Based on these results, Jayaraju *et al.* (2007) concluded that the deposition efficiency is probably more sensitive to the turbulence model rather than the near-wall anisotropy affecting the particles. The turbulence model affects the computation of the flow field everywhere in the domain, whereas the near-wall anisotropy is confined to a small region of the flow. If the turbulence model does not describe the flow field accurately then errors are introduced in the advection of the particles at every time step. These errors accumulate in time as the particles travel through the flow and could lead to a substantial inaccuracy in their trajectories, and hence the deposition. The near-wall anisotropy only affects particles once they are close to the wall, therefore one would expect the turbulence model to have a bigger effect on the prediction of particle deposition.

Recently, Debhi (2011) examined the use of a continuous random walk (CRW) model rather than EIM for particle tracking in an idealized mouth and throat geometry arguing

that it provides a more realistic prediction of turbulent particle dispersion. In this model, the fluctuations acting on a particle are defined by the Langevin equation, which takes two forms: one in the boundary layer region and the other in the bulk region of the flow. LES simulations were also performed for direct comparison with the RANS model. Predicted deposition compared to experimental data showed comparable accuracy between RANS and LES leading the author to state, contrary to Jayaraju *et al.* (2007), that previous failures to achieve accurate predictions with RANS models were due to inadequate modelling of the fluctuations rather than the RANS model limitations.

To date, there has not been a complete study including both a realistic geometry and a realistic representation of the turbulent field. Due to computational limitations, studies have focused either on accurately modelling the geometry, and have employed a RANS turbulence model for the flow, or have performed the more accurate LES but have used a simplified representation of the airways. Although LES solves for the large scales in the flow which are responsible for turbulent dispersion, experiments have already shown the large effect that the geometric complexity has on the flow, and hence deposition. RANS models, on the other hand, do not resolve any of the scales in the flow, but rather model the fluctuations, usually based on empirical data obtained from canonical and often equilibrium flows. The flow in the complex extrathoracic airways is certain to differ significantly from a canonical duct flow however, and the inaccurate modelling of the fluctuations, which cause dispersion, will affect the prediction of deposition. The effect will be more significant for the smaller particles whose trajectories are influenced more by the fluctuations in the flow.

1.3 Objectives

As discussed above, there has not yet been a complete model of deposition in the extrathoracic airways. The aim of this work is to develop an accurate and efficient numerical model to simulate the flow and the particle deposition in the mouth and throat, in order to gain an understanding of the deposition mechanism and optimize drug delivery to the lungs. Particle tracking in turbulent flows is very susceptible to numerical inaccuracies and errors in particle positions can grow rapidly in time (Yeung & Pope, 1988). Using direct numerical simulation (DNS) to resolve all the scales in the flow and yield an accurate representation of the velocity field removes one source of error in the computation of the particle trajectories, and should lead to improved deposition predictions. Realistic geometries allow us to study the effect of geometric variation on deposition and observe features in the flow that would not be present in an idealized geometry.

DNS requires very high grid resolutions which can be prohibitively expensive so it is desirable that an efficient solver can be used. In order to do so, a robust immersed boundary method for turbulent flows in complex geometries is developed, so that structured grids can be used to model the realistic airways. The method, traditionally applied to Cartesian grids, is extended to curvilinear coordinates which minimizes the number of unused cells outside the geometry and increases the efficiency of the numerical scheme. An implicit approach is proposed, which stabilizes the scheme for higher Reynolds numbers. The main objectives are enumerated below:

1. Develop an immersed boundary method to allow the use of a structured grid solver as opposed to the more inefficient unstructured solvers used to date.

2. Obtain an accurate representation of the turbulent field by use of direct numerical

simulation in order to solve for all the scales in the flow, thus avoiding any turbulence modelling.

3. Implement an accurate particle tracking algorithm in curvilinear coordinates.

4. Investigate the effect of geometric variation on deposition efficiency.

5. Validate the flow and particle deposition patterns against experimental results in the literature.

In this work, a new immersed boundary method is proposed, which is robust and can be applied in generalized curvilinear systems. This method allows efficient simulations of aerosol deposition in different mouth and throat geometries, and has more general applicability to a wider class of turbulent flows in complex geometries. The simulations presented herein are the first DNS of the flow in the extrathoracic airways, and the first numerical study of the effect of geometric variation on particle deposition using realistic geometries. Finally, this work establishes the essential building blocks towards efficient subject-specific assessment of drug delivery in the lungs.

1.4 Overview

This thesis is organized into five chapters. This first chapter motivated the work and discussed the various previous approaches used to determine extrathoracic deposition of inhaled aerosols. It highlighted the shortcomings of the numerical models used to date and laid out the objectives of this work; mainly to develop accurate predictive capabilities for particle deposition in extrathoracic airways.

Chapter 2 describes the numerical methods, namely: (a) the discretization of the governing equations, (b) the immersed boundary approach and (c) the particle tracking scheme.

An error analysis is presented to demonstrate the stability of the proposed method. The implementation of the immersed boundary condition is explained, including the algorithm to determine the location of the boundary in relation to the grid and the interpolation scheme, in any arbitrary geometry. Finally, Chapter 2 describes the extension of the immersed boundary method to curvilinear coordinates.

Chapter 3 consists of a number of validation cases which demonstrate the accuracy of the immersed boundary method developed herein. The algorithm is tested in both laminar and turbulent flows, and on Cartesian and curvilinear grids. The simulations of flow and particle deposition in realistic mouth and throat geometries are presented in chapter 4. The results are compared against experimental data and the effects of inflow turbulence and geometric variation on deposition are investigated. Some insight is gained on the physical significance of the empirical fits for particle efficiency. Finally, the last chapter comprises of a summary of the main findings and a discussion of future work.

Chapter 2

Numerical method

This chapter begins with the discretization of the governing equations in generalized curvilinear systems. A review of immersed boundary methods is given next. Their use in conjunction with the fractional step algorithm is discussed and an error analysis is performed in order to assess the stability of explicit forcing methods. The implicit iterative approach proposed in this work is then presented, and proof of its convergence is given. The treatment of mass conservation, the geometric representation of the boundary and the implementation of the immersed boundary condition are explained. Finally, extension of the IB method to curvilinear coordinates is described. The equations of motion for the aerosol particles are then introduced, along with a discussion of the relevant forces acting on the particles. The particle tracking algorithms in physical and in computational space are presented, as well as the interpolation schemes suitable for use on curvilinear grids.

2.1 Discretization of the governing equations

The governing equations for unsteady incompressible flow are the momentum and continuity equations given below in non-dimensional form,

$$\frac{\partial \boldsymbol{u}}{\partial t} + (\boldsymbol{u} \cdot \nabla)\,\boldsymbol{u} = -\nabla p + \frac{1}{Re}\nabla^2 \boldsymbol{u} \tag{2.1}$$

$$\nabla \cdot \boldsymbol{u} = 0. \tag{2.2}$$

where $\boldsymbol{u} = (u, v, w)$ is the velocity vector, p is the pressure and $Re = LU/\nu$ is the Reynolds number based on the characteristic length L and the characteristic velocity U of the flow being considered. Applying the divergence theorem and defining S as the surface bounding an arbitrary time-constant control volume V, equations 2.1 and 2.2 can be rewritten in integral form:

$$\frac{\partial}{\partial t}\int_V \boldsymbol{u} dV = \int_S (-\boldsymbol{u}\boldsymbol{u}) \cdot d\boldsymbol{S} + \int_S (-p\boldsymbol{I}) \cdot d\boldsymbol{S} + \frac{1}{Re}\int_S (\nabla \boldsymbol{u}) \cdot d\boldsymbol{S} \tag{2.3}$$

$$\int_S \boldsymbol{u} \cdot d\boldsymbol{S} = 0 \tag{2.4}$$

The equations are discretized in a generalized coordinate system using a finite volume scheme, following the method described in Rosenfeld *et al.* (1991). Transformation of the governing equations to generalized coordinates first requires transformation of the Cartesian system, $\boldsymbol{r}(x, y, z)$, to a curvilinear nonorthogonal system, $\boldsymbol{r}(\xi, \eta, \zeta)$. The transformation matrix, $\boldsymbol{J}$, mapping the two coordinate systems is given by

$$\boldsymbol{J} = \begin{pmatrix} \frac{\partial x}{\partial \xi} & \frac{\partial x}{\partial \eta} & \frac{\partial x}{\partial \zeta} \\ \frac{\partial y}{\partial \xi} & \frac{\partial y}{\partial \eta} & \frac{\partial y}{\partial \zeta} \\ \frac{\partial z}{\partial \xi} & \frac{\partial z}{\partial \eta} & \frac{\partial z}{\partial \zeta} \end{pmatrix}, \tag{2.5}$$

and the covariant base vectors of the curvilinear system are denoted

$$\boldsymbol{e}_m = \frac{\partial \boldsymbol{x}}{\partial m} \tag{2.6}$$

where $m = \{\xi, \eta, \zeta\}$ in cyclic order. A new base vector, $\boldsymbol{S}^m$, is created by the vector product of the covariant bases,

$$\begin{aligned} \boldsymbol{S}^\xi &= \boldsymbol{e}_\eta \times \boldsymbol{e}_\zeta \\ \boldsymbol{S}^\eta &= \boldsymbol{e}_\zeta \times \boldsymbol{e}_\xi \\ \boldsymbol{S}^\zeta &= \boldsymbol{e}_\xi \times \boldsymbol{e}_\eta. \end{aligned} \tag{2.7}$$

The vector $\boldsymbol{S}^m$ has a magnitude equal to the area spanned by the covariant vectors $(\boldsymbol{e}_{m+1}, \boldsymbol{e}_{m+2})$, and a direction normal to it. A schematic of a general control volume along with the base vectors is shown in figure 2.1*a*. In computational space, the domain is divided into uniform cells with mesh size $\Delta\xi = \Delta\eta = \Delta\zeta = 1$. The base vector $\boldsymbol{S}^m$ therefore has the magnitude of the cell face area, and the Jacobian of the transformation matrix $J = \det(\boldsymbol{J})$ is the volume of the computational cell.

The volume fluxes across the cell faces of the computational cells are chosen as the dependent variables, rather than the Cartesian components of the velocity, allowing easier and more accurate conservation of mass on a staggered curvilinear grid (see figure 2.1*b*). The fluxes, $\boldsymbol{U}^m = (U^\xi, U^\zeta, U^\eta)$ correspond to the contravariant velocity components, $\boldsymbol{u}^m$, multiplied by the volume of the cell:

$$\boldsymbol{U}^m = J\boldsymbol{u}^m. \tag{2.8}$$

In terms of the Cartesian components of the velocity $\boldsymbol{u}$, the fluxes $\boldsymbol{U}^m$ can be obtained from,

$$\boldsymbol{U}^m = \boldsymbol{S}^m \cdot \boldsymbol{u}. \tag{2.9}$$

The Cartesian velocity field can be recovered from the volume fluxes by the identity

$$\boldsymbol{u} = \boldsymbol{S}_m \boldsymbol{U}^m, \tag{2.10}$$

where $\boldsymbol{S}_m$ is the reciprocal base of the face area vector $\boldsymbol{S}^m$, computed from the relation

$$\boldsymbol{S}_m = \frac{\boldsymbol{S}^{m+1} \times \boldsymbol{S}^{m+2}}{\boldsymbol{S}^m \cdot \left(\boldsymbol{S}^{m+1} \times \boldsymbol{S}^{m+2}\right)}. \tag{2.11}$$

Discretization of the continuity equation (2.4) for a cell yields

$$\sum_{faces} \boldsymbol{S}^m \cdot \boldsymbol{u} = 0. \tag{2.12}$$

Recasting it in terms of volume fluxes, the mass conservation equation now takes the simple form

$$U^{\xi}_{i+1,j,k} - U^{\xi}_{i,j,k} + U^{\eta}_{i,j+1,k} - U^{\eta}_{i,j,k} + U^{\zeta}_{i,j,k+1} - U^{\zeta}_{i,j,k} = 0 \tag{2.13}$$

which is easily satisfied in any generalized coordinate system. Reformulation of the momentum equations in terms of volume fluxes is done by scalar multiplication of equation 2.3 with the corresponding face area vector $\boldsymbol{S}^m$. Details of the discretization are given in Rosenfeld *et al.* (1991).

The equations are discretized in space using a second-order, central difference scheme

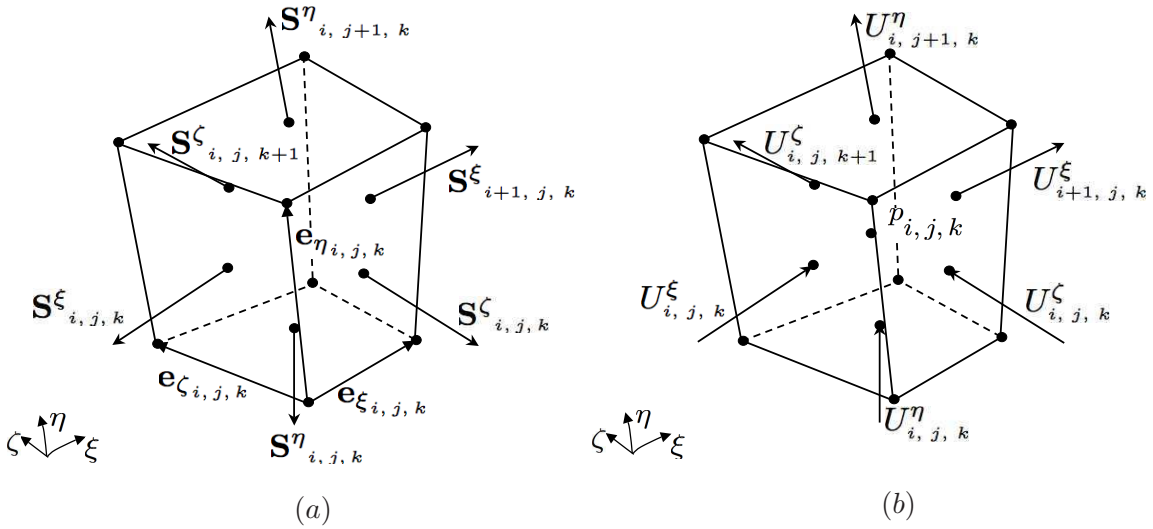


Figure 2-1: Schematic of a cell in a curvilinear grid showing (a) base vectors and (b) primary variables.

and advanced in time with a second-order fractional step method. The diagonal diffusive terms are treated implicitly, using the Crank-Nicholson scheme, in order to avoid the restrictive viscous stability condition, $\Delta t \leq \frac{\Delta x^2}{\nu}$. The off-diagonal diffusive terms are cross-derivative terms which arise from the non-orthogonality of the curvilinear grid. Unless the grid is severely skewed, these terms are small so they are treated explicitly along with the non-linear convective terms, using an Adams-Bashforth scheme.

For generality, the fractional step method will be described in terms of velocities. Extension to a curvilinear system with volume fluxes as the dependent variables will be shown later. Consider the discretized equations

$$\frac{\boldsymbol{u}^n - \boldsymbol{u}^{n-1}}{\Delta t} = \frac{3}{2}N(\boldsymbol{u})^{n-1} - \frac{1}{2}N(\boldsymbol{u})^{n-2} - \nabla p^n + \frac{1}{2Re}\left(L(\boldsymbol{u})^n + L(\boldsymbol{u})^{n-1}\right) \quad (2.14)$$

$$\nabla \cdot \boldsymbol{u}^n = 0 \quad (2.15)$$

where $N(\boldsymbol{u})$ are the convective and explicit diffusive terms and $L(\boldsymbol{u})/Re$ are the implicit diffusive terms. The fractional step method decouples the solution of the momentum equations

from that of the continuity equation so that the velocities and the pressure can be solved separately in two steps. This is done by splitting equation 2.14 into two new equations:

$$\frac{\hat{\boldsymbol{u}} - \boldsymbol{u}^{n-1}}{\Delta t} = \frac{3}{2}N(\boldsymbol{u})^{n-1} - \frac{1}{2}N(\boldsymbol{u})^{n-2} + \frac{1}{2Re}\left(L(\hat{\boldsymbol{u}}) + L(\boldsymbol{u})^{n-1}\right) \tag{2.16}$$

$$\frac{\boldsymbol{u}^{n} - \hat{\boldsymbol{u}}}{\Delta t} = -\nabla\phi^{n} \tag{2.17}$$

where ϕ, called the pseudo-pressure, will be defined below. In the first step, known as the predictor step, an intermediate velocity, $\hat{\boldsymbol{u}}$, which does not satisfy continuity is obtained. Then, the pseudo-pressure is used to project the approximate velocity to a divergence-free velocity $\boldsymbol{u}^n$, in the corrector step. Substituting equation 2.17 into equation 2.16 using $p^n = \phi^n$ does not recover the original momentum equation (equation 2.14). For a Cartesian case, Kim & Moin (1985) were able to derive the exact expression for pressure, $p = \phi + \frac{\Delta t}{2Re}\nabla^2\phi$. In a curvilinear system however, no such simple relation can be found due to the splitting of the diffusive terms. The error in the pressure from applying $p^n = \phi^n$ is $\mathcal{O}\left(\frac{\Delta t}{Re}\right)$. Therefore, at high Reynolds numbers this error is small. Rosenfeld *et al.* (1991) showed that although this simplification reduces the temporal accuracy of the pressure to first-order, the velocity remains second-order accurate in time.

The pseudo-pressure is found by taking the divergence of equation 2.17 and applying the incompressibility condition (equation 2.15). This results in a Poisson equation which is independent of $\boldsymbol{u}^n$ and is easier to solve than the fully-coupled set of original equations:

$$\nabla^2\phi^n = \frac{1}{\Delta t}\left(\nabla \cdot \hat{\boldsymbol{u}}\right). \tag{2.18}$$

With some rearranging, the equations solved at each time step are given by:

$$\left[1 - \left(\frac{\Delta t}{2Re}\right) L\right] \hat{\boldsymbol{u}} = \boldsymbol{u}^n + \Delta t \left[\frac{3}{2} N(\boldsymbol{u})^{n-1} + \frac{1}{2} N(\boldsymbol{u})^{n-2} + \frac{1}{2Re} L(\boldsymbol{u})^n\right] \tag{2.19a}$$

$$\nabla^2 \phi^n = \frac{1}{\Delta t} (\nabla \cdot \hat{\boldsymbol{u}}) \tag{2.19b}$$

$$\boldsymbol{u}^n = \hat{\boldsymbol{u}} - \Delta t \nabla \phi^n \tag{2.19c}$$

$$p^n = \phi^n \tag{2.19d}$$

Written in compact form, the fractional step method can be expressed as

$$A\hat{\boldsymbol{u}} = \boldsymbol{rhs} \tag{2.20a}$$

$$\Delta t DG\phi^n = D\hat{\boldsymbol{u}} \tag{2.20b}$$

$$\boldsymbol{u}^n = \hat{\boldsymbol{u}} - \Delta t G\phi^n \tag{2.20c}$$

$$p^n = \phi^n \tag{2.20d}$$

where D and G are the discrete divergence and gradient operators respectively. The exact expressions for A and $\boldsymbol{rhs}$ depend on the discretization scheme. In generalized curvilinear coordinates, the series of operations are given by

$$A\hat{\boldsymbol{U}} = (\boldsymbol{S}^\xi, \boldsymbol{S}^\eta, \boldsymbol{S}^\zeta)^T \cdot \boldsymbol{rhs} \tag{2.21a}$$

$$(\boldsymbol{S}^\xi, \boldsymbol{S}^\eta, \boldsymbol{S}^\zeta)^T \cdot \Delta t DG\phi^n = D\hat{\boldsymbol{U}} \tag{2.21b}$$

$$\boldsymbol{U}^n = \hat{\boldsymbol{U}} - (\boldsymbol{S}^\xi, \boldsymbol{S}^\eta, \boldsymbol{S}^\zeta)^T \cdot \Delta t G\phi^n \tag{2.21c}$$

$$p^n = \phi^n \tag{2.21d}$$

2.2 Immersed boundary method

Numerical simulations of fluid flows have become increasingly popular in industrial applications, offering a cost-effective alternative to experiments. Due to the increase in computational power, the simulation time has decreased drastically. However, grid generation is still a time-consuming process. Structured grids have the advantage of lending themselves to much more efficient solvers which have better convergence and stability properties than unstructured grid methods (Mavriplis, 1997). However, one main disadvantage is that they can only be applied to relatively simple geometries without loss in grid quality which affects the accuracy of the solution.

Most flows of engineering interest are encountered in complex geometries so there is value in schemes that can retain the efficiency of structured solvers whilst being suitable for any geometry. One such set of schemes is the immersed boundary method which was first developed by Peskin (1972) to model the flow around a heart valve. The immersed boundary method offers two main advantages over body-fitted grids: it greatly simplifies the task of grid generation and simplifies the modelling of moving boundaries as it circumvents the need for re-meshing at every time step. Since Peskin (1972), many variations of the immersed boundary method have been proposed. An overview of the different approaches will be given in this section.

Consider the simulation of flow over a cylinder as shown in figure 2.2*a*. In an immersed boundary method, the domain is discretized by a non-conforming Cartesian grid, in which the body is embedded (see figure 2.2*b*).

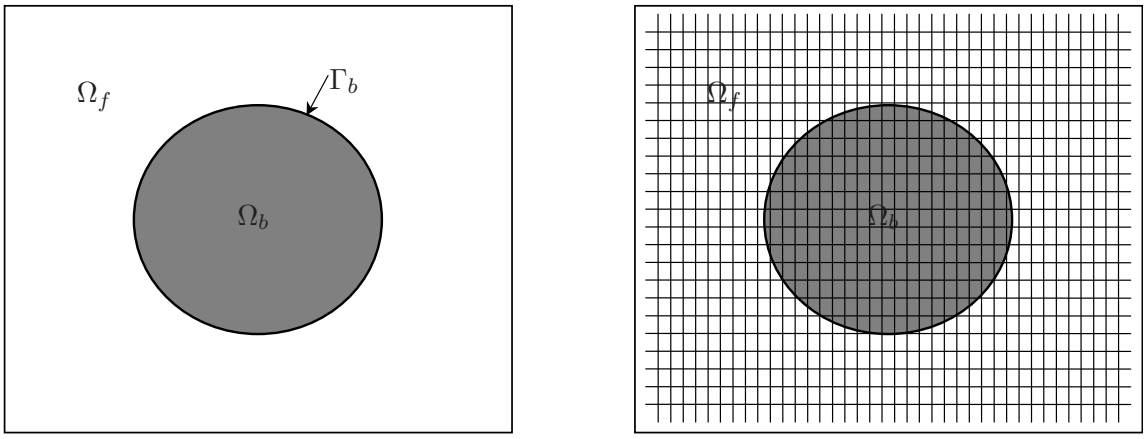


Figure 2-2: (a) Schematic showing simulation domain for flow over a cylinder. The fluid occupies the volume Ω_f, and the cylinder occupies the solid domain, Ω_b, with boundary, Γ_b. (b) Schematic of the cylinder immersed in a Cartesian grid on which the governing equations are discretized.

The equations for the fluid and the immersed boundary are

$$\begin{aligned} \frac{\partial \boldsymbol{u}}{\partial t} + \boldsymbol{u}\cdot\nabla\boldsymbol{u} + \nabla p - \frac{1}{Re}\nabla^2\boldsymbol{u} &= 0 \qquad \text{in } \Omega_f, \\ \nabla\cdot\boldsymbol{u} &= 0 \qquad \text{in } \Omega_f, \\ \boldsymbol{u} &= \boldsymbol{u}_\Gamma \qquad \text{on } \Gamma_b. \end{aligned} \tag{2.22}$$

Because the boundary and the grid do not match, special treatment of the equations near the surface of the body is required in order to incorporate the boundary conditions. The way in which the boundary conditions are imposed on the immersed boundary (IB) differentiates the various IB methods from one another. Generally, the effect of the boundary is included by introducing a force, $\boldsymbol{f}$, into the Navier-Stokes equations which can now be

solved everywhere in the domain:

$$\frac{\partial \boldsymbol{u}}{\partial t} + \boldsymbol{u} \cdot \nabla \boldsymbol{u} + \nabla p - \frac{1}{Re} \nabla^2 \boldsymbol{u} = \boldsymbol{f} \qquad \text{and} \tag{2.23}$$

$$\nabla \cdot \boldsymbol{u} = 0 \qquad \text{in } (\Omega_f + \Omega_b) \tag{2.24}$$

Following the classification given in the review by Mittal & Iaccarino (2005), IB methods can be grouped into continuous forcing and discrete forcing approaches depending on whether the forcing is applied to the governing equations before or after discretization. In the former approach, the force is applied to the continuous governing equations whilst in the latter, the equations are discretized first and then cells near the IB are modified in order to account for its presence. We now discuss each of these approaches in turn.

Continuous forcing approach

The first immersed boundary method developed by Peskin (1972) applies to elastic boundaries moved by the fluid. As the boundary moves, it exerts a force on the fluid. The boundary motion is determined by the fluid velocity and the elastic properties of the boundary determine the forces at each instant as the boundary moves. The equations that need to be solved are the Navier-Stokes equations for the fluid, the elastic boundary conditions for the body and the connecting equations for the interaction between the boundary and the fluid.

The immersed boundary is described by a collection of points connected by elastic fibres. The location of the boundary is given by $\boldsymbol{X}(s,t)$, where s represents a given point for all times t. In order to determine the forcing term in equation 2.23, the tension, $T(s,t)$, at each Lagrangian point in the boundary is obtained from a stress-strain constitutive relation such as Hooke's law, from which the local force density, $\boldsymbol{f}(s,t)$, acting on the fluid is then computed ($\boldsymbol{f}(s,t)ds$ is the force exerted on the fluid by the fibre lying in the interval

$(s, s + ds)$):

$$T = \sigma \left(\frac{\partial \boldsymbol{X}}{\partial s} \right) \tag{2.25}$$

$$\boldsymbol{f} = \frac{\partial}{\partial s} \left(T \boldsymbol{\tau} \right) \tag{2.26}$$

where $\boldsymbol{\tau}$ is the unit tangent to the boundary.

This force is then transmitted to the fluid by means of a Dirac δ function, since the fluid points and the Lagrangian points describing the boundary do not match,

$$\boldsymbol{F}(x, t) = \int_{\Gamma_b} \boldsymbol{f}(s, t) \delta(\boldsymbol{x} - \boldsymbol{X}(s, t)) ds. \tag{2.27}$$

The equation of motion for the boundary is given by

$$\frac{\partial \boldsymbol{X}}{\partial t}(s, t) = \boldsymbol{u}(\boldsymbol{X}(s, t), t) \tag{2.28}$$

where $\boldsymbol{u}$ is the local fluid velocity, and is solved for the position of the boundary at each time step. Again, since the velocity is unknown at the Lagrangian points describing the boundary, the velocity is obtained using the Dirac δ function:

$$\boldsymbol{u}(\boldsymbol{X}(s, t), t) = \int_{\Omega_f} \boldsymbol{u}(\boldsymbol{x}, t) \delta(\boldsymbol{x} - \boldsymbol{X}(s, t)) d\boldsymbol{x}. \tag{2.29}$$

In this method neither the boundary motion nor the boundary forces are known in advance, and one must know the elastic properties of the boundary in order to determine the forces exerted on the fluid.

A modification to this approach for use with rigid boundaries was proposed by Beyer & Leveque (1992), which consists in modelling the boundary as a set of points, each attached

to a very stiff spring bringing it back to its equilibrium position, $\boldsymbol{X^e}(s)$, if it deviates from the correct location of the fixed boundary. The force exerted on the fluid is given by

$$\boldsymbol{f}(s,t) = \kappa(\boldsymbol{X^e}(s) - \boldsymbol{X}(s,t)) \tag{2.30}$$

where κ is a negative spring constant. In order to avoid elastic motion of the boundary, this method requires very large stiffness constants which can lead to severe stability constraints.

Another approach for rigid boundaries, introduced by Goldstein *et al.* (1993) consists of a feedback forcing function given by

$$\boldsymbol{f}(s,t) = \alpha \int_0^t \boldsymbol{U}(s,t')dt' + \beta \boldsymbol{U}(s,t) \tag{2.31}$$

where α and β are negative constants which must be chosen. The first term generates the force field that drives the velocity field at the boundary to rest. It introduces oscillations in the flow so the second term is applied in order to dampen them out. The force increases in time to oppose the flow and, provided α and β are sufficiently large, the fluid comes to rest on the surface points. Comparison of equations 2.30 and 2.31 shows that the forcing term of Beyer & Leveque (1992) is essentially a feedback force without the damping.

The natural frequency of the feedback response needs to be higher than the highest frequency present in the flow in order for the force to respond fast enough to changes in the flow so that no-slip conditions can be accurately enforced at the boundary. This makes it particularly difficult to apply in the case of unsteady flows since the method is unstable for large values of α and β.

Apart from the temporal oscillations generated by the feedback force, Goldstein *et al.* (1993) also observed unrealistic spatial oscillations caused by the introduction of point

forces in a spectral method. These fluctuations did not seem to grow in an unstable manner and use of a finite difference method was shown to significantly attenuate these oscillations (Saiki & Biringen, 1996). The temporal oscillations, however, are unavoidable as they arise from the actual solution of equation 2.31.

Another drawback to the continuous forcing approach, both for elastic and rigid boundaries, is the fact that a sharp representation of the boundary cannot be obtained since the exact location of the surface is blurred when the forcing is transmitted from the boundary to the fluid points. Different distribution functions were proposed in the literature: various discrete delta functions (Peskin, 1972; Beyer & Leveque, 1992; Lai & Peskin, 2000), the narrow Gaussian distribution (Goldstein *et al.*, 1993), the area-weighted averaging (Saiki & Biringen, 1996). These approaches spread the point force $\boldsymbol{f}(s,t)$ to several neighbouring grid points resulting in an effective boundary thickness of at least one grid cell. Figure 2-3 shows the extent of this spreading for various smoothing functions.

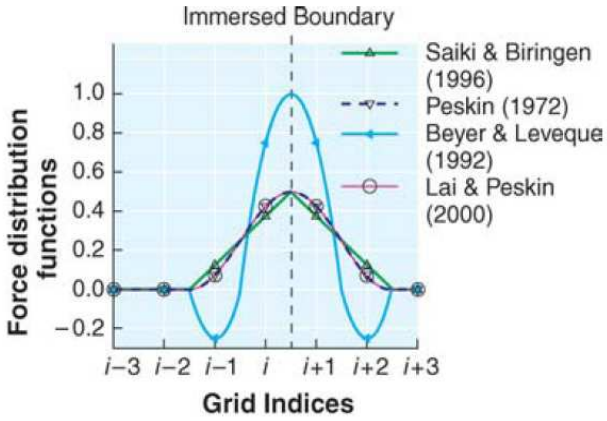


Figure 2-3: Distribution functions used to transmit the force to the fluid (Mittal & Iaccarino, 2005).

The use of continuous forcing methods is better suited to cases with elastic boundaries. For such flows, the forcing applied has a physical significance and, in cases where the elastic properties of the boundary are known, the method is easy to implement. However,

in the case of rigid boundaries this set of methods is subject to accuracy and stability constraints, and suffers severe limitations when applied to unsteady flows in particular. The smoothing of the forcing function which essentially spreads the location of the boundary is also undesirable, especially when modelling high-Reynolds-number flows in which thin boundary layers need to be resolved accurately.

Discrete forcing approach

Mohd-Yusof (1997) was the first to implement a discrete derivation of the forcing term, in what is now commonly referred to as *direct forcing*. The forcing was applied at the surface of the body in order to drive the velocity to zero, as well as on internal points adjacent to the boundary. On these, the tangential velocity was forced to be the reverse of the velocity across the surface in order to generate a smooth gradient across the boundary. Since then, many direct forcing methods have appeared in the literature (Verzicco *et al.*, 1998; Fadlun *et al.*, 2000; Kim *et al.*, 2001; Balaras, 2004; Taira & Colonius, 2007; Ikeno & Kajishima, 2007; Domenichini, 2008; Guy & Hartenstine, 2010). *Implicit forcing* is a sub-set of these methods, in which the forcing term is not actually computed, but instead its effect is imposed *implicitly* through direct imposition of the boundary conditions on the variables. The ghost-cell method falls into this category (Majumdar *et al.*, 2001; Tseng & Ferziger, 2003; Ghias *et al.*, 2007; Berthelsen & Faltinsen, 2008; Mittal *et al.*, 2008). In this approach, a specified boundary condition is imposed by extrapolating the variable to a ghost point inside the body.

Other discrete forcing approaches exist, such as immersed interface methods (IIM) and Cartesian grid methods. IIM was first developed by Leveque & Li (1994) in order to improve the accuracy of the original immersed boundary method (Peskin, 1972), as the discrete delta

function provided too much smoothing to obtain second order accuracy. IIM retains a sharp interface by incorporating the jump in pressure and velocity across the boundary into the discretization scheme, thus maintaining second order accuracy. However, it suffers from the same stability issues as its continuous forcing counterpart. Cartesian grid methods, also known as cut-cell methods (Ye *et al.*, 1999; Udaykumar *et al.*, 2001; Kirkpatrick *et al.*, 2003) consist in truncating the cells cut by the boundary to create new cells which conform to the shape of the surface. Cells whose centres lie in the fluid, are reshaped by discarding the portion that lies in the solid, whilst those whose centres lie in the solid are usually absorbed by neighbouring cells in order to prevent stability problems. The difficulty in these methods is accurately computing the fluxes and gradients in the new trapezoidal cells. Although they have been applied in two dimensions, extension to three dimensions is non-trivial as it involves complex polyhedral cells which complicate the discretization of the Navier-Stokes equations.

Here we shall focus on the direct forcing approach due to its simplicity and enhanced stability compared to other discrete forcing methods. Although a force is not explicitly computed in the implicit forcing technique, a mathematical formulation including a forcing term can still be derived so that a general equation can be written for all direct forcing methods. Consider the discretized Navier-Stokes equations in general form:

$$\boldsymbol{u}^{n+1} = \boldsymbol{u}^n + \Delta t \left(-N(\boldsymbol{u}) - \nabla p + \frac{1}{Re} L(\boldsymbol{u}) + \boldsymbol{f} \right) \tag{2.32}$$

By rearranging equation 2.32, Mohd-Yusof (1997) formulated an expression for the forcing:

$$\boldsymbol{f} = \begin{cases} N(\boldsymbol{u}) + \nabla p - \frac{1}{Re} L(\boldsymbol{u}) + \frac{1}{\Delta t} \left(\boldsymbol{u}_\Gamma - \boldsymbol{u}^n \right) & \text{on } \Gamma_b \\ 0 & \text{elsewhere} \end{cases} \tag{2.33}$$

where $\boldsymbol{u}_\Gamma$ is the boundary velocity. Equation 2.33 gives the forcing term for points on the immersed boundary. In general however, the grid points do not coincide with the boundary so the forcing must be interpolated to the points closest to the boundary in some way. We will call these grid points, on which the forcing is applied, IB points. A more suitable form of equation 2.33 would therefore be,

$$\boldsymbol{f} = \begin{cases} N(\boldsymbol{u}) + \nabla p - \frac{1}{Re} L(\boldsymbol{u}) + \frac{1}{\Delta t} \left(\boldsymbol{u}_{IB} - \boldsymbol{u}^n \right) & \text{at IB points} \\ 0 & \text{elsewhere} \end{cases} \tag{2.34}$$

where $\boldsymbol{u}_{IB}$ is the desired value of the velocity at the IB points such that the velocity at the boundary satisfies the no-slip condition.

The main aspects in which the various direct forcing methods in the literature differ are:

1. The computation of the momentum forcing term.
2. The treatment of mass conservation in cells cut by the boundary.
3. The geometric representation of the boundary.
4. The location of the IB points and the interpolation scheme for the IB velocities.

Each aspect will be discussed in turn in sections 2.2.3 to 2.2.6. Section 2.2.1 deals with the use of immersed boundary methods in conjunction with the fractional step algorithm. The

fractional step method is a popular means of solving the Navier-Stokes equations, therefore extensive literature exists on IB methods used with this particular algorithm (Fadlun *et al.*, 2000; Kim *et al.*, 2001; Balaras, 2004; Roman *et al.*, 2009). Certain issues arising in IB methods in fractional step algorithms have been highlighted, such as the accuracy of the no-slip condition or of mass conservation (Taira & Colonius, 2007; Ikeno & Kajishima, 2007; Domenichini, 2008). A recent paper by Guy & Hartenstine (2010) explored the performance of projection methods when used with direct forcing, focusing on the effect of the solid domain on the fluid when projection is performed over the entire domain. These issues are discussed in more detail in the following section. In addition, it is shown that the accuracy of the IB method depends on the form of the fractional step algorithm chosen; a point which has not been addressed in the literature. The two variants of the fractional step method which we refer to here as the p and the Δp-forms are both used extensively, however immersed boundary conditions applied on the p-form are only first-order accurate in time.

Most immersed boundary methods have been developed for use on Cartesian grids but certain simulations are better suited to curvilinear grids. For example, with some geometries a Cartesian grid would be inefficient, as many grid points would be wasted outside the fluid domain. A curvilinear grid might also have a more natural alignment with the streamlines, which is desirable for the accuracy of the solution, and might provide a better wall-normal resolution than a Cartesian grid. This last advantage is particularly important in turbulent flows. So far, extension of the immersed boundary method to a curvilinear coordinate system has only been carried out by Ge & Sotiropoulos (2007) and Roman *et al.* (2009). Ge & Sotiropoulos (2007) used the immersed boundary method originally developed by Gilmanov & Sotiropoulos (2005) for use on a Cartesian grid and implemented it into a

curvilinear grid solver in order to model the flow in a mechanical heart valve. The focus of the paper was on the development of the curvilinear grid solver. Roman *et al.* (2009) showed the extension of a direct forcing method onto curvilinear coordinates for use along with the fractional step method. The procedure proposed introduces an error in the velocities near the boundary, but they showed this did not appreciably affect the solution for large enough Reynolds numbers. The method does not satisfy continuity however, and was used in conjunction with the less accurate variant of the fractional step method. Section 2.2.7 shows the extension of the current direct forcing method to the curvilinear form of the governing equations and discusses certain issues specific to curvilinear grids.

2.2.1 Immersed boundary method in fractional step algorithm

In the immersed boundary method presented in this work, a momentum forcing, $\boldsymbol{f}$ is applied in order to satisfy the no-slip condition at the immersed boundary. The forcing drives the velocity at points surrounding the boundary, referred to as IB points, to a particular value such that the velocity at the surface of the immersed body satisfies the boundary conditions. Kim *et al.* (2001) showed how cells containing the immersed boundary do not directly satisfy mass conservation. A mass source/sink term, q, is applied to those cells in order to ensure mass is conserved (Kim *et al.*, 2001). The governing equations for flow with an immersed boundary are given below

$$\frac{\partial \boldsymbol{u}}{\partial t} + (\boldsymbol{u} \cdot \nabla)\, \boldsymbol{u} = -\nabla p + \frac{1}{Re}\nabla^2 \boldsymbol{u} + \boldsymbol{f} \tag{2.35}$$

$$\nabla \cdot \boldsymbol{u} - q = 0 \tag{2.36}$$

As discussed in section 2.1, the equations are solved using a fractional step method. Before showing the discretized equations, it should be noted that there are two slightly different

forms of the fractional step method. The most common, which we shall refer to as the p-form (Kim & Moin, 1985), neglects the pressure term in the equation for the intermediate velocity and then solves the Poisson equation for pressure. The second, the Δp-form, includes the pressure term from the previous time step when computing the intermediate velocity field and then determines the pressure *difference* from the Poisson equation. Although the distinction may seem subtle, the accuracy of the immersed boundary method when applied in conjunction with the two variants of the fractional step method is different. Note that when the immersed boundary approach is used in a fractional step solver, the forcing term, $\boldsymbol{f}$, is determined such that the intermediate velocity $\hat{\boldsymbol{u}}$ (see equation 2.16) satisfies the immersed boundary conditions rather than $\boldsymbol{u}^n$. We shall show that this does not affect the overall second-order accuracy of the scheme when using the Δp-form. This is not however the case when the p-form is used.

Following the analysis and notation in Kim & Moin (1985), we regard the intermediate velocity $\hat{\boldsymbol{u}}$ as an approximation of the continuous function $\boldsymbol{u}^*$, that satisfies

$$\begin{aligned} \frac{\partial u_i^*}{\partial t} &= -\frac{\partial u_i^* u_j^*}{\partial x_j} - \frac{\partial p^*}{\partial x_i} + \frac{1}{Re}\frac{\partial^2 u_i^*}{\partial x_j x_j} + f_i^* \\ u_i^*(x, t_{n-1}) &= u_i(x, t_{n-1}) \end{aligned} \tag{2.37}$$

We can then write

$$\begin{aligned} \hat{u}_i &\approx u_i^*(x, t_{n-1} + \Delta t) \\ &\approx u_i^*(x, t_{n-1}) + \Delta t \frac{\partial u_i^*}{\partial t} + \frac{1}{2}\Delta t^2 \frac{\partial^2 u_i^*}{\partial t^2} \\ &= u_i^*(x, t_{n-1}) + \Delta t \left(-\frac{\partial u_i^* u_j^*}{\partial x_j} - \frac{\partial p^*}{\partial x_i} + \frac{1}{Re}\frac{\partial^2 u_i^*}{\partial x_j x_j} + f_i^* \right) \\ &\quad + \frac{1}{2}\Delta t^2 \frac{\partial}{\partial t}\left(-\frac{\partial u_i^* u_j^*}{\partial x_j} - \frac{\partial p^*}{\partial x_i} + \frac{1}{Re}\frac{\partial^2 u_i^*}{\partial x_j x_j} + f_i^* \right) \end{aligned} \tag{2.38}$$

Since $u_i^*(x, t_{n-1}) = u_i(x, t_{n-1})$,

$$\begin{aligned}
\hat{u}_i &= u_i(x, t_{n-1}) + \Delta t \left(-\frac{\partial u_i u_j}{\partial x_j} - \frac{\partial p}{\partial x_i} + \frac{1}{Re} \frac{\partial^2 u_i}{\partial x_j x_j} + f_i \right) + \mathcal{O}(\Delta t^2) \\
&= u_i(x, t_{n-1}) + \Delta t \left(\frac{\partial u_i}{\partial t} \right) + \mathcal{O}(\Delta t^2) \\
&= u_i(x, t_n) + \mathcal{O}\left(\Delta t^2\right)
\end{aligned} \tag{2.39}$$

We can see from equation 2.39 that the immersed boundary conditions, applied on $\boldsymbol{u^*}$ rather than $\boldsymbol{u}(x, t_n)$, are second-order accurate.

The same analysis applied to the p-form shows that the immersed boundary conditions in this variation of the fractional step method are only first-order accurate in time. The continuous function $\boldsymbol{u}^*$ in this case satisfies the intermediate velocity equation:

$$\begin{aligned}
\frac{\partial u_i^*}{\partial t} &= -\frac{\partial u_i^* u_j^*}{\partial x_j} + \frac{1}{Re} \frac{\partial^2 u_i^*}{\partial x_j x_j} + f_i^* \\
u_i^*(x, t_{n-1}) &= u_i(x, t_{n-1})
\end{aligned} \tag{2.40}$$

We can then write

$$\begin{aligned}
\hat{u}_i &\approx u_i^*(x, t_{n-1} + \Delta t) \\
&\approx u_i^*(x, t_{n-1}) + \Delta t \frac{\partial u_i^*}{\partial t} + \frac{1}{2} \Delta t^2 \frac{\partial^2 u_i^*}{\partial t^2} \\
&= u_i^*(x, t_{n-1}) + \Delta t \left(-\frac{\partial u_i^* u_j^*}{\partial x_j} + \frac{1}{Re} \frac{\partial^2 u_i^*}{\partial x_j x_j} + f_i^* \right) \\
&\quad + \frac{1}{2} \Delta t^2 \frac{\partial}{\partial t} \left(-\frac{\partial u_i^* u_j^*}{\partial x_j} + \frac{1}{Re} \frac{\partial^2 u_i^*}{\partial x_j x_j} + f_i^* \right)
\end{aligned} \tag{2.41}$$

Since $u_i^*(x, t_{n-1}) = u_i(x, t_{n-1})$,

$$\begin{aligned}
\hat{u}_i &= u_i(x, t_{n-1}) + \Delta t \left(-\frac{\partial u_i u_j}{\partial x_j} + \frac{1}{Re}\frac{\partial^2 u_i}{\partial x_j x_j} + f_i \right) + \mathcal{O}(\Delta t^2) \\
&= u_i(x, t_{n-1}) + \Delta t \left(\frac{\partial u_i}{\partial t} + \frac{\partial p}{\partial x_i} \right) + \mathcal{O}(\Delta t^2) \\
&= u_i(x, t_n) + \Delta t \frac{\partial p}{\partial x_i} + \mathcal{O}\left(\Delta t^2\right)
\end{aligned} \tag{2.42}$$

We can see that the error at the immersed boundary with this variation of the fractional step method is larger. Kim & Moin (1985) showed that, if the boundary conditions are inconsistent with the governing equations, the solution can incur considerable numerical errors. For global boundaries, they proposed the appropriate treatment of the boundary conditions for the intermediate velocity field, $\hat{u}_i = u_i^n + \Delta t \frac{\partial \phi}{\partial x_i}$, in order to maintain second order accuracy. In immersed boundary methods however, no such special treatment of the immersed boundary conditions is applied, thereby introducing an error at the boundary. For this reason, the original solver described in section 2.1 was modified to the Δp-form of the fractional step method for use with the immersed boundary algorithm, giving boundary conditions accurate to $\mathcal{O}(\Delta t^2)$.

A few schemes which enforce boundary conditions exactly on $\boldsymbol{u}^n$ rather than $\hat{\boldsymbol{u}}$ have been proposed in the literature. Taira & Colonius (2007) and Ikeno & Kajishima (2007) suggested modified pressure equations whilst Domenichini (2008) enforced boundary conditions on $\boldsymbol{u}^n$ after projection and iterated between the Poisson solve and the projection step in order to reduce the error in the velocity. The first two approaches complicate the implementation of the immersed boundary method as they require considerable changes to the solver. The latter is computationally inefficient because it requires multiple solutions of the Poisson equation at every time step. Additionally, the flow solver itself is second-order

accurate, therefore applying boundary conditions with higher than second-order accuracy would be superfluous.

For the sake of simplicity, and in keeping with the notation given in the literature the discretized equations will be shown in terms of velocities, for a Cartesian case. The extension to curvilinear coordinates will be discussed later, in section 2.2.7. The discretized equations are given by

$$\frac{\hat{\boldsymbol{u}} - \boldsymbol{u}^{n-1}}{\Delta t} = \frac{1}{Re}\left(\alpha L(\hat{\boldsymbol{u}}) + \beta L(\boldsymbol{u}^{n-1})\right) - Gp^{n-1} - \gamma N(\boldsymbol{u}^{n-1}) - \vartheta N(\boldsymbol{u}^{n-2}) + \boldsymbol{f}^n \tag{2.43}$$

$$DG\phi^n = \frac{1}{\Delta t}\left(D\hat{\boldsymbol{u}} - q^n\right) \tag{2.44}$$

$$\boldsymbol{u}^n = \hat{\boldsymbol{u}} - \Delta t G\phi^n \tag{2.45}$$

$$p^n = p^{n-1} + \phi^n \tag{2.46}$$

where the weighting coefficients $(\alpha, \beta, \gamma, \vartheta)$ depend on the numerical scheme adopted. In our case, $\alpha = \beta = 1/2$ with the Crank-Nicholson scheme and $\gamma = 3/2$, $\vartheta = -1/2$ with the Adams-Bashforth scheme. The next section will show how the forcing term, $\boldsymbol{f}$, is calculated.

2.2.2 Error analysis of explicit forcing

In order to demonstrate the errors introduced when an inconsistent scheme is used for the computation of the forcing term, explicit discretization of the intermediate velocity equations will be analyzed first:

$$\frac{\hat{\boldsymbol{u}} - \boldsymbol{u}^{n-1}}{\Delta t} = \frac{1}{Re}\left(\gamma L(\boldsymbol{u}^{n-1}) + \vartheta L(\boldsymbol{u}^{n-2})\right) - Gp^{n-1} - \gamma N(\boldsymbol{u}^{n-1}) - \vartheta N(\boldsymbol{u}^{n-2}) + \boldsymbol{f}^n \tag{2.47}$$

Both $\boldsymbol{f}^n$ and $\hat{\boldsymbol{u}}$ are unknowns, but the velocity $\hat{\boldsymbol{u}}$ at non-IB points can be computed since, at these points, $\boldsymbol{f}^n = 0$. From this velocity field, the desired velocity $\boldsymbol{u}_{IB}^n$ at the IB points so as to satisfy the boundary conditions can be obtained by interpolation. Having computed $\boldsymbol{u}_{IB}^n$, the forcing term can be obtained from:

$$\begin{aligned} \boldsymbol{f}^n &= \frac{\boldsymbol{u}_{IB}^n - \boldsymbol{u}^{n-1}}{\Delta t} - \frac{1}{Re}\left(\gamma L(\boldsymbol{u}^{n-1}) + \vartheta L(\boldsymbol{u}^{n-2})\right) + Gp^{n-1} + \gamma N(\boldsymbol{u}^{n-1}) + \vartheta N(\boldsymbol{u}^{n-2}) \quad \text{at IB points} \\ \boldsymbol{f}^n &= 0 \quad \text{elsewhere} \end{aligned} \tag{2.48}$$

and added to equation 2.47 to solve for the intermediate velocity field. Substituting equation 2.48 into equation 2.47 shows that the scheme is consistent, and no error is introduced at the boundary:

$$\begin{aligned} \hat{\boldsymbol{u}} &= \boldsymbol{u}_{IB}^n \quad \text{at IB points} \\ \hat{\boldsymbol{u}} &= \boldsymbol{u}^{n-1} - \left(\frac{1}{Re}\left(\gamma L(\boldsymbol{u}^{n-1}) - \vartheta L(\boldsymbol{u}^{n-2})\right) + Gp^{n-1} + \gamma N(\boldsymbol{u}^{n-1}) + \vartheta N(\boldsymbol{u}^{n-2})\right)\Delta t \quad \text{elsewhere} \end{aligned} \tag{2.49}$$

Since explicit schemes are limited by the viscous stability constraint, fractional step methods often apply a semi-implicit approach, in which the diffusive terms are treated implicitly:

$$\frac{\hat{\boldsymbol{u}} - \boldsymbol{u}^{n-1}}{\Delta t} = \frac{1}{Re}\left(\alpha L(\hat{\boldsymbol{u}}) + \beta L(\boldsymbol{u}^{n-1})\right) - Gp^{n-1} - \gamma N(\boldsymbol{u}^{n-1}) - \vartheta N(\boldsymbol{u}^{n-2}) + \boldsymbol{f}^n \tag{2.50}$$

Evaluating the forcing term becomes more complicated because the velocities at non-IB points required for the computation of $\boldsymbol{u}_{IB}^n$ now depend on velocities at IB points, which are still unknown, through the second-order derivatives in the implicit diffusive terms.

The solution employed in the literature (Kim *et al.*, 2001; Balaras, 2004; Yang & Balaras, 2006), originally proposed by Kim *et al.* (2001) has been to obtain the forcing by provisionally discretizing equation 2.32 explicitly in order to find an approximation of $\boldsymbol{u}^n$, denoted $\tilde{\boldsymbol{u}}$. This yields:

$$\frac{\tilde{\boldsymbol{u}} - \boldsymbol{u}^{n-1}}{\Delta t} = \frac{1}{Re}\left(\gamma L(\boldsymbol{u}^{n-1}) + \vartheta L(\boldsymbol{u}^{n-2})\right) - Gp^{n-1} - \gamma N(\boldsymbol{u}^{n-1}) - \vartheta N(\boldsymbol{u}^{n-2}) + \boldsymbol{f}^n \quad (2.51)$$

where $\boldsymbol{f}^n$ only exists at IB points. $\tilde{\boldsymbol{u}}$ can be computed at non-IB points as it does not depend on $\tilde{\boldsymbol{u}}$ at IB points, so the velocity at IB points can be determined and used to evaluate the forcing term:

$$\begin{aligned} \boldsymbol{f}^n &= \frac{\boldsymbol{u}^n_{IB} - \boldsymbol{u}^{n-1}}{\Delta t} - \frac{1}{Re}\left(\gamma L(\boldsymbol{u}^{n-1}) + \vartheta L(\boldsymbol{u}^{n-2})\right) + Gp^{n-1} + \gamma N(\boldsymbol{u}^{n-1}) + \vartheta N(\boldsymbol{u}^{n-2}) \quad \text{at IB points} \\ \boldsymbol{f}^n &= 0 \quad \text{elsewhere} \end{aligned} \quad (2.52)$$

However, introducing this forcing term into equation 2.50 does not recover the correct velocities at the IB points:

$$\hat{\boldsymbol{u}} = \boldsymbol{u}^n_{IB} + \frac{\Delta t}{Re}\left(\alpha L(\hat{\boldsymbol{u}}) + \beta L(\boldsymbol{u}^{n-1}) - \gamma L(\boldsymbol{u}^{n-1}) - \vartheta L(\boldsymbol{u}^{n-2})\right) \quad (2.53)$$

Due to the implicit treatment of the diffusive term, this error also affects neighbouring non-IB points. The inconsistency caused by the explicit treatment of the diffusive terms in the calculation of the forcing term can cause the scheme to become unstable as the Reynolds numbers is increased. At high Reynolds numbers, the viscous stability constraint, $\Delta t/Re\Delta x^2 < 0.5$ for central differencing, becomes much more restrictive than the convective CFL condition, $u\Delta t/\Delta x < 1$. In particular, because of the very fine grids required to

resolve high-Reynolds-number flows, the time step required to satisfy the viscous stability condition becomes prohibitively expensive. For example, in a test case of flow inside an IC piston at $Re = 2000$, Fadlun *et al.* (2000) showed that the time step needed to satisfy the stability condition was 10 times smaller than that required by the convective CFL limit when the viscous terms were treated explicitly. Even with a very small time step, the error introduced at the immersed boundary can become destabilizing at high Reynolds numbers as the viscous effects which are dominant at low Reynolds numbers and can dampen out errors are no longer present.

If we consider fully-developed turbulent flow in a pipe, grid spacings in the streamwise direction are typically $\Delta x^+ \sim 10$ and in the wall-normal direction $\Delta y^+ \sim 0.2$ at the wall where

$$\Delta x^+ = \frac{\Delta x u_\tau}{\nu}, \quad \Delta y^+ = \frac{\Delta y u_\tau}{\nu} \quad \text{and} \quad u_\tau = \frac{0.3164 U^2}{8 Re^{1/4}}. \tag{2.54}$$

The viscous stability constraint for explicit diffusive terms is given by

$$\begin{aligned} \Delta t_{visc} &< 0.5 \Delta y^2 Re \\ &< 0.5 \frac{(8/0.3164) \Delta y^{+^2}}{Re^{6/8} U^2}, \end{aligned} \tag{2.55}$$

and the CFL constraint is given by

$$\begin{aligned} \Delta t_{CFL} &< \frac{\Delta x}{U} \\ &< \frac{(8/0.3164)^{0.5} \Delta x^+}{Re^{7/8} U^2}. \end{aligned} \tag{2.56}$$

Therefore,

$$\frac{\Delta t_{visc}}{\Delta t_{CFL}} = \frac{0.5(8/0.3164)}{(8/0.3164)^2}\frac{\Delta y^{+^2}}{\Delta x^+}Re^{1/8} \approx \frac{12.5}{5}\frac{\Delta y^{+^2}}{\Delta x^+}Re^{1/8} \approx 0.01Re^{1/8}. \tag{2.57}$$

The viscous stability constraint is therefore much more restrictive than the CFL condition when the diffusive terms are treated explicitly.

In the explicit method $\boldsymbol{f}$ affects the provisional field $\tilde{\boldsymbol{u}}$ at IB points only. Therefore solving for $\tilde{\boldsymbol{u}}$ with $\boldsymbol{f} = 0$, computing $\boldsymbol{f}$ from this $\tilde{\boldsymbol{u}}$ and adding it to the IB points is essentially the same as solving for $\tilde{\boldsymbol{u}}$ with the forcing term. Calculating the forcing term implicitly using the same method would introduce errors in the field near the immersed boundary as the velocities $\tilde{\boldsymbol{u}}$ at non-IB points depend on the velocities $\tilde{\boldsymbol{u}}$ of neighbouring IB points through the implicit diffusive term.

Roman *et al.* (2009) proposed an alternative approach to enforce the immersed boundary conditions based on directly prescribing the velocities at the IB points rather than introducing a forcing term in the momentum equation. They solved equation 2.32 implicitly, setting $\boldsymbol{f} = 0$, to obtain a provisional field, $\tilde{\boldsymbol{u}}$:

$$\frac{\tilde{\boldsymbol{u}} - \boldsymbol{u}^{n-1}}{\Delta t} = \frac{1}{Re}\left(\alpha L(\tilde{\boldsymbol{u}}) + \beta L(\boldsymbol{u}^{n-1})\right) - Gp^{n-1} - \gamma N(\boldsymbol{u}^{n-1}) - \vartheta N(\boldsymbol{u}^{n-2}) \tag{2.58}$$

and then use the provisional field to enforce the immersed boundary conditions directly:

$$\begin{aligned} \hat{\boldsymbol{u}} &= \boldsymbol{u}_{IB}^n && \text{at IB points} \\ \hat{\boldsymbol{u}} &= \tilde{\boldsymbol{u}} && \text{elsewhere} \end{aligned} \tag{2.59}$$

Although this approach removes the viscous stability constraint, it introduces errors in the

vicinity of the immersed boundary as it neglects the dependence of the velocities at non-IB points on the forcing at neighbouring IB points. The error can be determined by subtracting equation 2.58 from equation 2.43:

$$[1 - \frac{\alpha \Delta t}{Re} L](\hat{\boldsymbol{u}} - \tilde{\boldsymbol{u}}) = \Delta t \boldsymbol{f} \tag{2.60}$$

An expression for the error at the IB points is difficult to obtain since $\boldsymbol{f}$ is not known. However at non-IB points, where $\boldsymbol{f} = 0$, the error is given by:

$$\hat{\boldsymbol{u}} = \tilde{\boldsymbol{u}} + \frac{\alpha \Delta t}{Re} \left(L(\hat{\boldsymbol{u}}) - L(\tilde{\boldsymbol{u}}) \right) \tag{2.61}$$

The error is proportional to Δt, therefore this method does not retain the second-order accuracy of the numerical scheme.

In order to remove any errors from the semi-implicit fractional step method, implicit computation of $\boldsymbol{f}^n$ and $\hat{\boldsymbol{u}}$ would be necessary. This involves the inversion of a large sparse matrix, unless a simplified interpolation scheme is applied (Fadlun *et al.*, 2000), which would require considerable changes to the solution method and would significantly increase the computational cost of the scheme.

2.2.3 Stabilized momentum forcing

The method proposed here consists in an iterative scheme to compute $\boldsymbol{f}$ implicitly such that the immersed boundary conditions are enforced on $\hat{\boldsymbol{u}}$ rather than $\tilde{\boldsymbol{u}}$. This removes the errors at the immersed boundary and enhances the stability of the scheme. Rapid convergence is observed, with only three to four iterations required.

The scheme can be summarized as follows:

1. Start with an initial guess $\boldsymbol{f}^n = 0$, and solve the equations for the intermediate velocities, $\hat{\boldsymbol{u}}$.

2. Use $\hat{\boldsymbol{u}}$ to compute a better estimate for the forcing term, $\boldsymbol{f}^n$

$$\boldsymbol{f}^n = \frac{\boldsymbol{u}_{IB}^n - \boldsymbol{u}^{n-1}}{\Delta t} - \frac{1}{Re}\left(\alpha L(\hat{\boldsymbol{u}}) + \beta L(\boldsymbol{u}^{n-1})\right) + Gp^{n-1} + \gamma N(\boldsymbol{u}^{n-1}) + \vartheta N(\boldsymbol{u}^{n-2}) \quad (2.62)$$

3. Add the forcing term to the intermediate velocity equation and update $\hat{u}$.

$$\hat{\boldsymbol{u}} = \boldsymbol{u}^{n-1} + \Delta t\left(\frac{1}{Re}\left(\alpha L(\hat{\boldsymbol{u}}) + \beta L(\boldsymbol{u}^{n-1})\right) - Gp^{n-1} - \gamma N(\boldsymbol{u}^{n-1}) - \vartheta N(\boldsymbol{u}^{n-2}) + \boldsymbol{f}^n\right) \quad (2.63)$$

4. Go back to step 2 until $\hat{\boldsymbol{u}}$ has converged.

The pseudocode for the method is given below:

Algorithm 1 Iterative IB scheme

$\boldsymbol{f}^{n,1} = 0$
for $k = 1$ to nk **do**
  $\hat{\boldsymbol{u}}^k = \boldsymbol{u}^{n-1} + \Delta t\left(\frac{1}{Re}\left(\alpha L(\hat{\boldsymbol{u}}^k) + \beta L(\boldsymbol{u}^{n-1})\right) - Gp^{n-1} - \gamma N(\boldsymbol{u}^{n-1}) - \vartheta N(\boldsymbol{u}^{n-2}) + \boldsymbol{f}^{n,k}\right)$
  $\boldsymbol{f}^{n,k+1} = \frac{\boldsymbol{u_{IB}}^n - \boldsymbol{u}^{n-1}}{\Delta t} - \frac{1}{Re}\left(\alpha L(\hat{\boldsymbol{u}}^k) + \beta L(\boldsymbol{u}^{n-1})\right) + Gp^{n-1} + \gamma N(\boldsymbol{u}^{n-1}) + \vartheta N(\boldsymbol{u}^{n-2})$
end for
$\frac{\hat{\boldsymbol{u}}^{nk+1} - \boldsymbol{u}^{n-1}}{\Delta t} = \frac{1}{Re}\left(\alpha L(\hat{\boldsymbol{u}}) + \beta L(\boldsymbol{u}^{n-1})\right) - Gp^{n-1} - \gamma N(\boldsymbol{u}^{n-1}) - \vartheta N(\boldsymbol{u}^{n-2}) + \boldsymbol{f}^{n,nk+1}$

The error between two consecutive iterations is

$$\hat{\boldsymbol{u}}^{k+1} - \hat{\boldsymbol{u}}^k = \frac{\alpha \Delta t}{Re}\left(L(\hat{\boldsymbol{u}}^{k+1}) - L(\hat{\boldsymbol{u}}^k)\right) + \Delta t(\boldsymbol{f}^{n,k+1} - \boldsymbol{f}^{n,k}). \quad (2.64)$$

We shall now show that this error quickly vanishes, ensuring that the immersed boundary conditions are being enforced accurately.

The error introduced, originates from the IB points and is spread to surrounding non-IB points through the implicit diffusive term. If the error at the IB points vanishes, so does

the error everywhere else in the domain. Therefore, in order to analyze the convergence of the scheme let us consider the error at an IB point. At iteration $k+1$, the equation for the intermediate velocity after adding the forcing term is given by:

$$\hat{\boldsymbol{u}}^{k+1} = \boldsymbol{u}_{IB}^{n} + \frac{\alpha\Delta t}{Re}\left(L(\hat{\boldsymbol{u}}^{k+1}) - L(\hat{\boldsymbol{u}}^{k})\right). \tag{2.65}$$

We can rearrange this as

$$\left[1 - \frac{\alpha\Delta t}{Re}L\right]\hat{\boldsymbol{u}}^{k+1} = \boldsymbol{u}_{IB}^{n} - \frac{\alpha\Delta t}{Re}L(\hat{\boldsymbol{u}}^{k}), \tag{2.66}$$

and we can write a similar expression for the velocity at iteration k:

$$\left[1 - \frac{\alpha\Delta t}{Re}L\right]\hat{\boldsymbol{u}}^{k} = \boldsymbol{u}_{IB}^{n} - \frac{\alpha\Delta t}{Re}L(\hat{\boldsymbol{u}}^{k-1}). \tag{2.67}$$

Hence the error between two consecutive iterations is

$$\begin{aligned}
\left[1 - \frac{\alpha\Delta t}{Re}L\right]\left(\hat{\boldsymbol{u}}^{k+1} - \hat{\boldsymbol{u}}^{k}\right) &= -\frac{\alpha\Delta t}{Re}L\left(\hat{\boldsymbol{u}}^{k} - \hat{\boldsymbol{u}}^{k-1}\right) \qquad \text{or} \\
\left[1 - \frac{\alpha\Delta t}{Re}L\right]\left(\epsilon^{k+1}\right) &= -\frac{\alpha\Delta t}{Re}L\left(\epsilon^{k}\right)
\end{aligned} \tag{2.68}$$

where $\epsilon^{k+1} = \hat{\boldsymbol{u}}^{k+1} - \hat{\boldsymbol{u}}^{k}$. This can be rewritten in the form $\epsilon^{k+1} = M\epsilon^{k}$:

$$\epsilon^{k+1} = \left[\left(-\frac{\alpha\Delta t}{Re}L\right)^{-1} + 1\right]^{-1}(\epsilon^{k}). \tag{2.69}$$

Since $\epsilon^{k+1} = M\epsilon^{k} = M^{k}\epsilon^{0}$, the solution converges if the eigenvalues of M satisfy the

condition $|\lambda_M| < 1$. λ_M is given by:

$$\lambda_M = \frac{\frac{\alpha\Delta t}{Re}\lambda_L}{\frac{\alpha\Delta t}{Re}\lambda_L - 1} \tag{2.70}$$

where λ_L are the eigenvalues of the discrete Laplacian operator, L. Therefore the solution converges if

$$\frac{\alpha\Delta t}{Re}\lambda_L < \frac{1}{2}. \tag{2.71}$$

The spectrum of the Laplacian operator lies within $\lambda_L \in [0, 2]$ and $\alpha = \frac{1}{2}$ in the Crank-Nicolson method, therefore convergence requires

$$\frac{\Delta t}{Re} < \frac{1}{2} \tag{2.72}$$

which is always satisfied (except for $Re \to 0$) since the CFL constraint on the time step is much more restrictive.

2.2.4 Treatment of mass conservation at IB cells

In order to satisfy the no-slip condition at the immersed boundary, the velocities at the IB points are forced to particular values. These velocities are not solutions to the Navier-Stokes equations and hence are unphysical. Therefore, in cells with an IB velocity, mass is not necessarily conserved. Different approaches have been proposed in the literature to ensure conservation of mass at the cells cut by the immersed boundary. In ghost-cell approaches, Neumann boundary conditions are applied on the pressure such that $\frac{\partial p}{\partial n} = 0$ across the boundary. The argument behind this is that if the pressure is the same on either side of the boundary then there will be no flow across it. Mark & van Wachem (2008) stated that, although this approach results in a zero pressure force over the immersed boundary, a mass

flux still exists due to the flow and other forces. Additionally, it can lead to unphysical solutions as unnecessary information is being inserted into the pressure equation. They proposed excluding the fictitious field from the continuity equation in order to remove the mass flux over the immersed boundary. This method is essentially the same as introducing a mass source/sink in the IB cells which counteracts the fictitious velocities (Kim *et al.*, 2001). This approach is adopted herein and is described below.

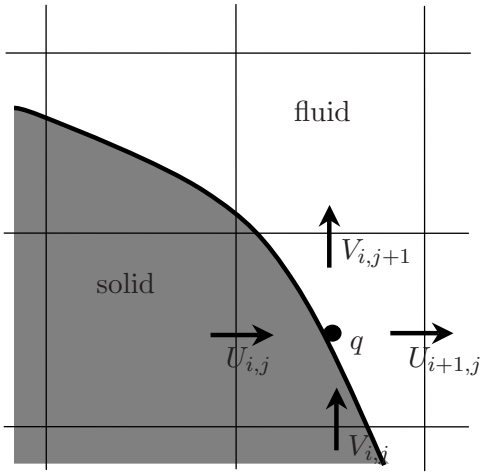


Figure 2-4: Addition of mass source in a cell cut by the immersed boundary for conservation of mass.

Consider a cell cut by the immersed boundary as shown in figure 2-4. For mass to be conserved, the continuity equation, as solved in terms of fluxes, should satisfy:

$$U_{i+1,j} + V_{i,j+1} = 0 \tag{2.73}$$

However, the equation being solved for the entire cell is:

$$U_{i+1,j} - U_{i,j} + V_{i,j+1} - V_{i,j} = 0 \tag{2.74}$$

Since it includes fictitious velocities from inside the boundary, this equation is incorrect. By

adding a mass source to equation 2.74, we can recover the correct equation (equation 2.73) so that no mass flux exists across the boundary:

$$U_{i+1,j} - U_{i,j} + V_{i,j+1} - V_{i,j} - q = 0 \tag{2.75}$$

where $q = -U_{i,j} - V_{i,j}$.

The general expression for the mass source in a cell is given by

$$q = \sum_{i=1}^{6} \omega_i \mathbf{U} \cdot \mathbf{n} \tag{2.76}$$

where $\mathbf{n}$ is the unit outward normal of the cell face and ω_i is 1 for IB points and 0 otherwise. Note that each IB point provides equal and opposite mass fluxes to the two cells sharing that face, therefore the total sum of all the mass sources added in the domain is zero, and both local and global mass conservation are satisfied.

2.2.5 Geometric treatment

One of the main requirements of our method is the capability of modelling complex geometries. In addition, minimizing the computational overhead for geometric operations associated with the immersed boundary surface is also desirable for an efficient solver. Different geometric representations in the literature include level-set formulations (Marella *et al.*, 2005; Yang & Balaras, 2006), splines or piecewise linear elements (Tseng & Ferziger, 2003; Ghias *et al.*, 2007; Berthelsen & Faltinsen, 2008) and unstructured triangulated meshes (Kalitzin & Iaccarino, 2003; Balaras, 2004; Gilmanov & Sotiropoulos, 2005; Mark & van Wachem, 2008; Mittal *et al.*, 2008; Roman *et al.*, 2009). In the method presented here, the

immersed boundary consists of a three-dimensional triangulated surface as this representation offers a number of advantages. An example of a surface is shown in figure 2-5.

Non-uniform meshes can easily be created with different-sized triangular elements allowing complex geometries to be modelled accurately. Triangular meshes are also very popular in computer graphics and CFD so there are many algorithms available to manipulate these surfaces. The GNU triangulated surface library (GTS) provides a wide range of useful functions and data structures to efficiently deal with 3D triangulated surfaces. Operations such as surface smoothing or refinement can easily be performed, surface normals at any point can readily be computed and the use of bounding-box trees allows for efficient point location based on nearest neighbour searches.

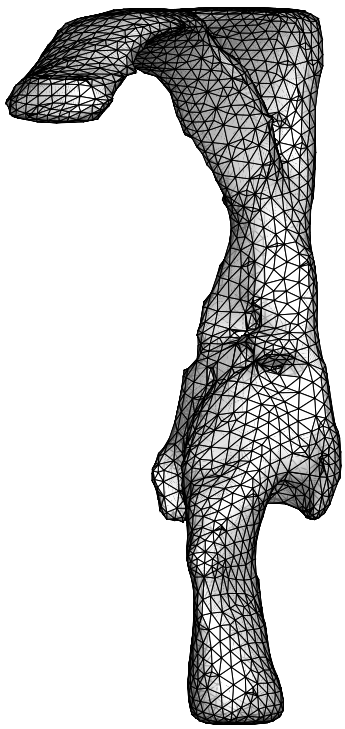


Figure 2-5: Example of a three-dimensional triangulated surface: the extrathoracic airways of a subject.

Another advantage of triangulated surfaces is the compatibility with a wide range of

software, making them easy to generate, modify and visualize. CAD packages which are popularly used in engineering and biomedical applications generate triangulated surface models in a number of different file formats, STL being the most common. For many biological flow problems, these surfaces are constructed from 2D MRI or CT scans. Scans can often have a lot of noise leading to the generation of surfaces with holes, intersections or incorrect orientation. However there are many programs available for pre-processing of triangulated geometries that can resolve these issues. Finally, these surfaces can also be imported into post-processing programs for visualization alongside the flow field.

The models of the extrathoracic airways are provided in STL format. The surface geometries used in the validation section are generated using the CAD program SolidWorks, and subsequently meshed with triangular elements in Abaqus. The STL files are converted to GTS format to be read by the IB preprocessor, which uses a number of functions from the GTS library to determine the relation between the structured grid and the geometry. The IB preprocessor determines the IB points, the location of the mirror points and the interpolation points and weights. This information is then read into the flow solver at the beginning of the simulation. The details relating to the preprocessor are discussed in the following section.

2.2.6 Implementation of immersed boundary condition

In order to enforce the immersed boundary conditions the position of the immersed boundary in relation to the grid needs to be determined. The first step in the procedure is to establish whether the velocity points lie inside or outside the geometry. This is done with a ray tracing algorithm from the GTS library which uses a binary tree of the bounding boxes of the surface. This allows for a faster search of the triangles intersected by the ray.

The search time is on average $\mathcal{O}(\log n)$ as opposed to $\mathcal{O}(n)$ if we were to loop through the entire list of triangles (Cormen, 2001). A ray is traced starting from the velocity point at (x_p, y_p, z_p) to a point outside the parent bounding box of the surface at $(x_2 + |x_2/10|, y_p, z_p)$ where x_2 is the x coordinate of the upper-right-back corner of the box (see figure 2-6). The algorithm checks which bounding boxes have been intersected by the ray and then loops through these bounding boxes to determine the triangles that have been intersected. If the surface has been intersected an odd number of times, the point lies inside the geometry; if it has been intersected an even number of times the point is outside. For external flows, the points located inside the geometry are classified as solid points and those outside as fluid points, and vice versa for internal flows.

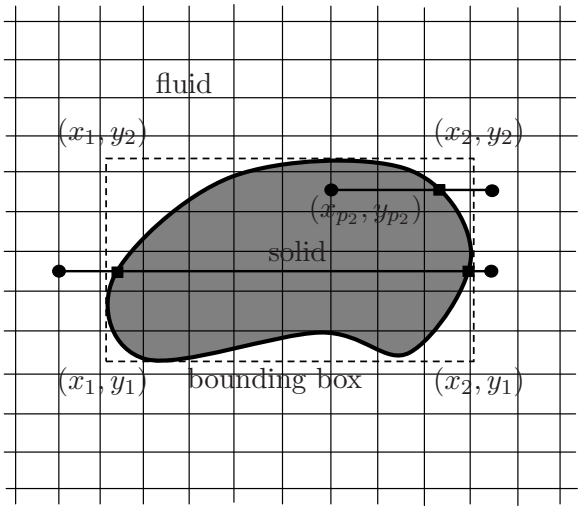


Figure 2-6: 2D schematic of the ray-tracing algorithm. The ray from point (x_{p_1}, y_{p_1}) in the fluid intersects the surface an even number of times; the ray from point (x_{p_2}, y_{p_2}) in the solid intersects the surface an odd number of times.

Once the points have been identified as fluid or solid, the following step is to determine the IB points where the forcing is to be applied. Some immersed boundary approaches (Fadlun *et al.*, 2000; Balaras, 2004; Roman *et al.*, 2009) apply the forcing on fluid points whilst others, such as the ghost-cell method, apply the boundary conditions inside the solid. Iaccarino & Verzicco (2003) compared the two approaches and found minor differences. In

the current method, the IB points are chosen to be solid points with at least one neighbour in the fluid. By imposing the boundary conditions inside the solid and not on fluid points, all velocities in the flow domain are solutions to the Navier-Stokes equations. Any cell containing an IB point is classified as an IB cell, in which a mass source/sink, q, is applied to ensure mass conservation. A schematic of the IB points and IB cells in an arbitrary geometry is shown in figure 2-7.

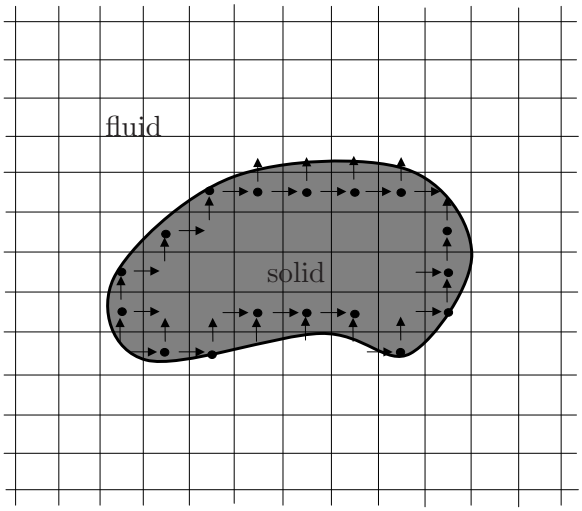


Figure 2-7: 2D schematic describing IB cells and IB points. •, IB cells; →, IB u velocities; ↑, IB v velocities.

In order to calculate the forcing term to be applied at an IB point, the velocity $\boldsymbol{u}_{IB}$ required so that the immersed boundary conditions are satisfied must first be determined. In the case where the IB point coincides exactly with the boundary, it is clear that $\boldsymbol{u}_{IB} = \boldsymbol{u}_{\Gamma}$. However, this is not generally the case as the grid does not conform to the geometry, so $\boldsymbol{u}_{IB}$ must be determined by an appropriate interpolation scheme.

A variety of interpolation procedures for the velocity at the IB points has been suggested in the literature. Fadlun *et al.* (2000) tested three different interpolation procedures, shown in figure 2-8. The first simply sets the velocity at the IB points to that at the boundary, $\boldsymbol{u}_{IB} = \boldsymbol{u}_{\Gamma}$, (i.e: there is no interpolation and the geometry is described in a stepwise

manner). In the second procedure, the forcing for all cells cut by the boundary was scaled by the volume fraction of the cell occupied by the body, Ψ_b/Ψ. The third case consisted of a linear interpolation for the velocity at the IB points, $\boldsymbol{u}_{IB} = \alpha\boldsymbol{u}_\Gamma + \beta\boldsymbol{u}_{i+1}$ where α and β are the weighting coefficients and $\boldsymbol{u}_{i+1}$ is the velocity at the fluid point adjacent to the IB point. A grid convergence study showed that best accuracy was achieved with linear interpolation of the velocity. This yielded second order accurate results, whereas the stepwise geometry and volume fraction weighting were less than first-order and first-order accurate, respectively.

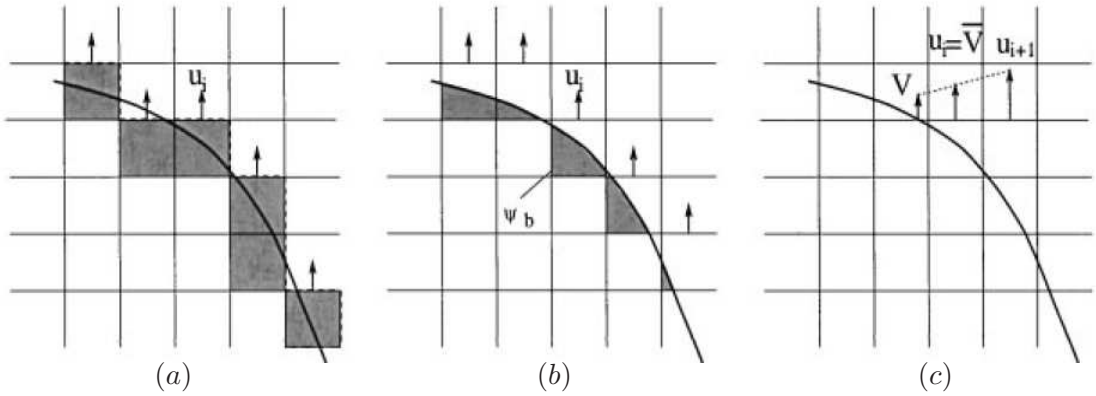


Figure 2-8: Schematic of interpolation procedures tested by Fadlun *et al.* (2000). (*a*) No interpolation. (*b*) Volume weighting. (*c*) Linear interpolation of velocity.

Another approach is to apply interpolation of the four velocity components surrounding a surface point (see figure 2-9*b*). When all surrounding points apart from the IB point exist outside the body, bilinear interpolation is applied to compute the velocity at the IB point:

$$\boldsymbol{u}_{IB} = \frac{1}{\alpha\beta}\left[\boldsymbol{u}_\Gamma - \alpha\left(1-\beta\right)\boldsymbol{u}_{i+1,j} + \left(1-\alpha\right)\left(1-\beta\right)\boldsymbol{u}_{i+1,j+1} + \left(1-\alpha\right)\beta\boldsymbol{u}_{i,j+1}\right] \qquad (2.77)$$

where $\alpha = (x_{i+1} - x_\Gamma)/(x_{i+1} - x_i)$ and $\beta = (y_{j+1} - y_\Gamma)/(y_{j+1} - y_j)$.

However, special treatment is required if any of the interpolation points is also an IB point in order to decouple the two unknowns. Often, in this case, linear interpolation is

applied instead (Kim *et al.*, 2001). In the case where the interpolation point is much closer to the surface than the IB point, this scheme produces large non-physical values of $\boldsymbol{u}_{IB}$, which can cause numerical instability.

The need for a more robust interpolation procedure, applicable to all IB points and for use on any complex geometry has led many to interpolation along the normal to the boundary (Balaras, 2004; Mark & van Wachem, 2008; Mittal *et al.*, 2008; Roman *et al.*, 2009). This provides a more general approach as opposed to interpolating along a Cartesian direction which can yield ambiguities in complex geometries as there can often be more than one direction over which the interpolation could be performed (Balaras, 2004). The use of trilinear interpolation around the surface would involve a number of coupled IB points, which would either require an iterative method or special treatment as applied by Kim *et al.* (2001), reducing the scheme to linear interpolation along the grid-lines.

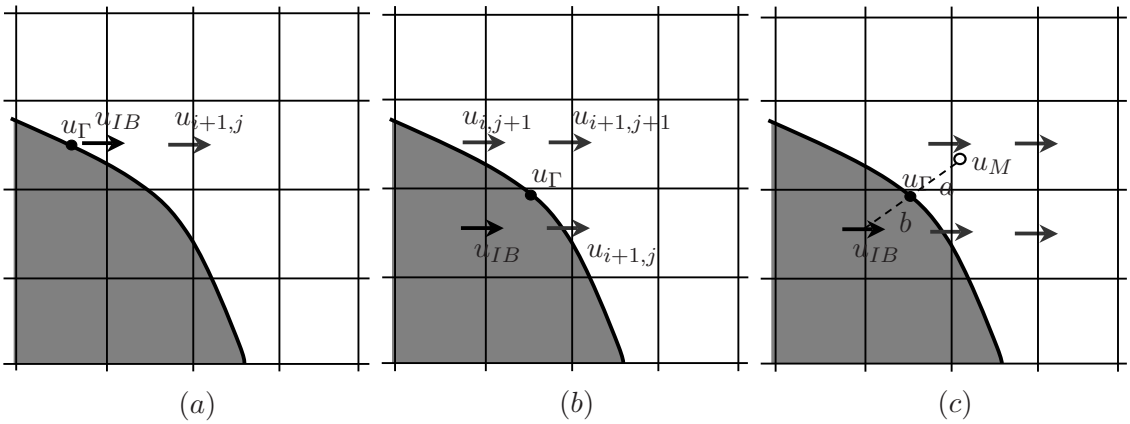


Figure 2-9: Schematic of the various interpolation schemes. (a) Linear interpolation along grid-lines. (b) Bilinear interpolation. (c) Linear interpolation along normal to the boundary.

In the method used herein, the velocity is interpolated along the normal to the boundary, with help of a mirror point which lies in the fluid as shown in figure 2-9c. $\boldsymbol{u}_{IB}$ is computed such that linear interpolation between the velocity at the mirror point, $\boldsymbol{u}_M$, and

that at the IB point yields the correct velocity at the surface:

$$\boldsymbol{u}_{IB} = \frac{(a+b)}{a}\boldsymbol{u}_{\Gamma} - \frac{b}{a}\boldsymbol{u}_{M} \tag{2.78}$$

where $\boldsymbol{u}_M$ is computed from surrounding velocities.

Determining the location of the mirror point along the normal of the boundary is not always straightforward with an irregular 3D surface. A simple procedure to use would be to mirror the IB point along the normal of the closest triangle. However, while this works well for simple geometries, it can present complications when dealing with more complex surfaces and non-uniform grids. Figure 2-10 shows two cases where this approach would not place the mirror point at the correct location. The first case is at sharp corners. The surface point computed along the normal of the closest triangle does not lie on the surface and the mirror point is on the wrong side of the immersed boundary. Using these points would yield incorrect boundary conditions. The second case arises in high-aspect-ratio cells, which are common particularly in simulations of turbulent flows, where a very high grid resolution in the wall-normal direction is required. Consider the IB point in figure 2-10*b*. It is an IB point to segment A of the boundary. However the closest point on the surface lies on segment B. By mirroring this IB point along the closest point on the surface, the boundary conditions are being enforced at an incorrect location on the immersed boundary. This leads to part of the surface on which no boundary conditions are being enforced and another where they are over-determined.

A robust algorithm that works for any geometry and any grid is desirable. Therefore, a different approach is used to determine the location of the mirror points. A ray is traced from the IB point to its neighbouring fluid point in order to find the triangle intersected by the ray along with its neighbours. The closest point on these triangles is chosen as the

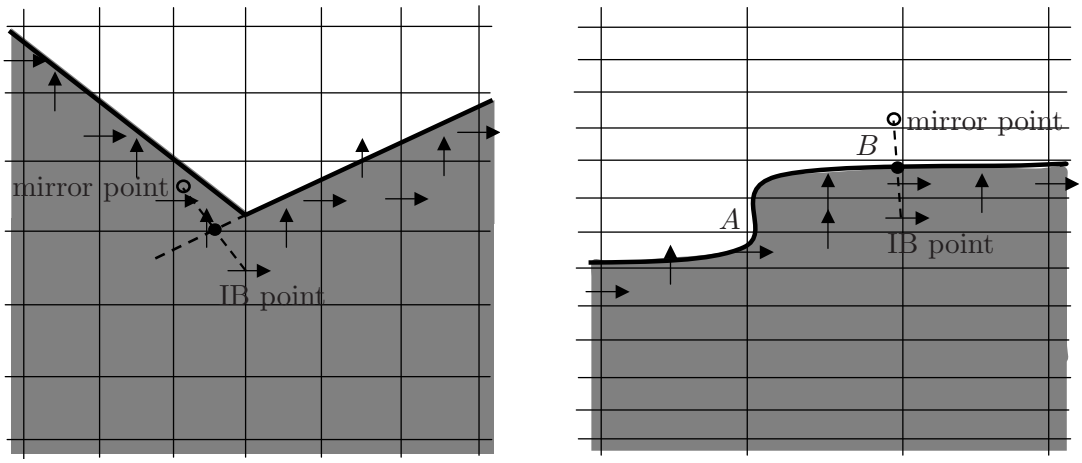


Figure 2-10: 2D schematic showing problems encountered in determining the position of the mirror point. (a) Sharp corner. (b) High aspect-ratio cells.

surface point. The mirror point is then placed on the other side of the boundary, at an equal distance from the surface as the IB point. The eight surrounding velocity points are used to interpolate the velocity at the mirror point. Setting the mirror point equidistant to the boundary ensures that the interpolation scheme remains well behaved in the limit of the mirror point approaching the immersed boundary, thereby circumventing the need for special treatment to avoid numerical instabilities. At the same time, it is sufficiently close to the boundary in order to minimize the error in the interpolation, since a linear velocity profile is only valid in close proximity to the wall.

2.2.7 Extension of immersed boundary method to curvilinear coordinates

So far, we have considered the immersed boundary method in Cartesian coordinates, conforming with the literature. Recall however that the flow equations are solved on a curvilinear coordinate system, and have been reformulated in terms of volume fluxes. The discretized momentum equation for the intermediate flux field can be written as

$$\frac{\hat{\boldsymbol{U}} - (\boldsymbol{U})^{n-1}}{\Delta t} = \boldsymbol{Rhs} + \boldsymbol{F} \tag{2.79}$$

where Rhs includes the transformed convective, $C(\boldsymbol{U})$, diffusive, $D(\boldsymbol{U})$, and pressure terms, $R(p)$, and $\boldsymbol{F}$ are the forcing components in curvilinear coordinates. Rearranging equation 2.79 for $\boldsymbol{F}$, shows that a forcing *flux*, $\boldsymbol{U}_{IB}$, is required in order to enforce the immersed boundary conditions:

$$\boldsymbol{F} = \frac{\boldsymbol{U}_{IB} - (\boldsymbol{U})^{n-1}}{\Delta t} - \boldsymbol{Rhs} \tag{2.80}$$

However, it is only meaningful to apply the boundary conditions in terms of Cartesian velocities. (Enforcing $\boldsymbol{U}_{IB} = \frac{(a+b)}{a}\boldsymbol{U}_{\Gamma} - \frac{b}{a}\boldsymbol{U}_{M}$, as done with velocities, would be incorrect). Therefore, the velocities, $\boldsymbol{u}_{IB}$, that satisfy the boundary conditions at the surface need to be determined first and then used to compute the forcing flux, $\boldsymbol{U}_{IB}^{m} = \boldsymbol{S}^{m} \cdot \boldsymbol{u}_{IB}$.

In the case of a Cartesian grid, the flux $\boldsymbol{U}_{IB}^{m}$ only depends on the Cartesian velocity at that point since $\boldsymbol{S}_{i}^{m} = 0$ for $m \neq i$. However on a curvilinear grid, the forcing flux depends on all three components of the velocity which are located at different positions of the staggered grid. In order to enforce the immersed boundary conditions exactly, and avoid interpolating from surrounding velocities which could introduce errors at the boundary, all three Cartesian forcing velocities (u_{IB}, v_{IB}, w_{IB}) are computed at each IB point. For this, the intermediate velocity at the mirror points is required. However, in the curvilinear system, the equations solve for an intermediate flux field instead so the intermediate Cartesian velocity field must be computed from the fluxes:

$$\hat{\boldsymbol{u}} = \boldsymbol{S}_{m}\hat{\boldsymbol{U}}^{m} \tag{2.81}$$

The overall algorithm for immersed boundaries can be summarized as follows:

1. Read in the immersed boundary surface and identify the solid, fluid and IB points.

Determine the surface points using ray tracing and mirror the IB points. Compute the interpolation weights for the mirror points. For stationary boundaries, this step needs to be performed only once as a pre-processing step.

2. Solve the momentum equations provisionally to obtain an approximation of the intermediate flux field.

3. Compute the intermediate Cartesian velocities from the fluxes.

4. Interpolate from surrounding velocity points to obtain the velocity at the mirror point.

5. Interpolate along the normal of the boundary to determine $\boldsymbol{u}_{IB}$.

6. Transform $\boldsymbol{u}_{IB}$ to $\boldsymbol{U}_{IB}$ and compute the forcing term using the stabilized implicit scheme.

7. Solve the equations for the intermediate flux field with the forcing term.

8. Solve the Poisson equation.

9. Update the fluxes and the pressure.

10. Go back to step 2 at the next time step.

Up to now, we have discussed the modifications required in the flow solver in order to enforce the immersed boundary conditions on a curvilinear grid. Next, features related to the IB preprocessor will be discussed. The first issue is determining the cell which contains the mirror point. This is a trivial procedure on a Cartesian grid, but on a curvilinear grid there is no explicit relation between a physical spatial position and the grid cell that contains it. Consider the grid cell shown in figure 2-11. The position vector of the mirror point in relation to one of the vertices is given by $\boldsymbol{r}$ and $\boldsymbol{e_i}$ and $\boldsymbol{e^i}$ are the covariant and

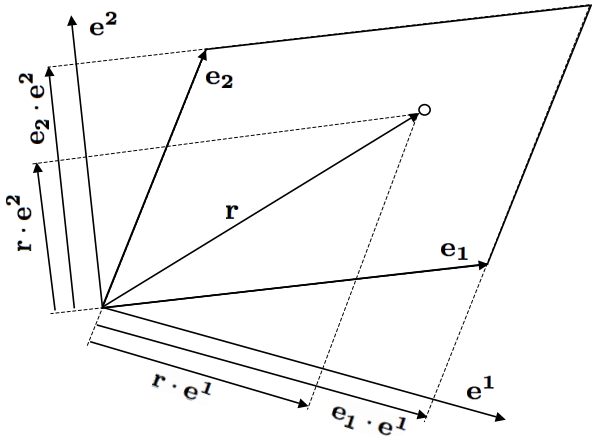


Figure 2-11: 2D schematic of a curvilinear grid cell showing the position vector, $\boldsymbol{r}$, and the covariant, $\boldsymbol{e_i}$, and contravariant, $\boldsymbol{e^i}$, base vectors.

contravariant base vectors respectively, at that vertex. Recalling the transformation matrix, $\boldsymbol{J}$, between the Cartesian and the curvilinear coordinate systems given by:

$$J_{ij} = \frac{\partial x_i}{\partial \xi^j} \tag{2.82}$$

The contravariant and covariant vectors are given by:

$$(e_i)_j = J_{ji} \tag{2.83}$$

$$\left(e^i\right)_j = J^{-1}_{ij}. \tag{2.84}$$

Therefore

$$\boldsymbol{e_i} \cdot \boldsymbol{e^j} = \delta_{ij}, \tag{2.85}$$

and the mirror point is located in a particular cell if the following relations are satisfied:

$$\begin{aligned} 0 \leq \boldsymbol{r} \cdot \boldsymbol{e^1} \leq 1 \\ 0 \leq \boldsymbol{r} \cdot \boldsymbol{e^2} \leq 1 \\ 0 \leq \boldsymbol{r} \cdot \boldsymbol{e^3} \leq 1 \end{aligned} \tag{2.86}$$

However, this algorithm assumes that the cell is a parallelogram, and could fail to find the correct cell location if this is not the case. In order to determine the location of the mirror points, the cells are split into tetrahedrons (triangles in 2D). Figure 2-12 illustrates the case of a 2D grid cell.

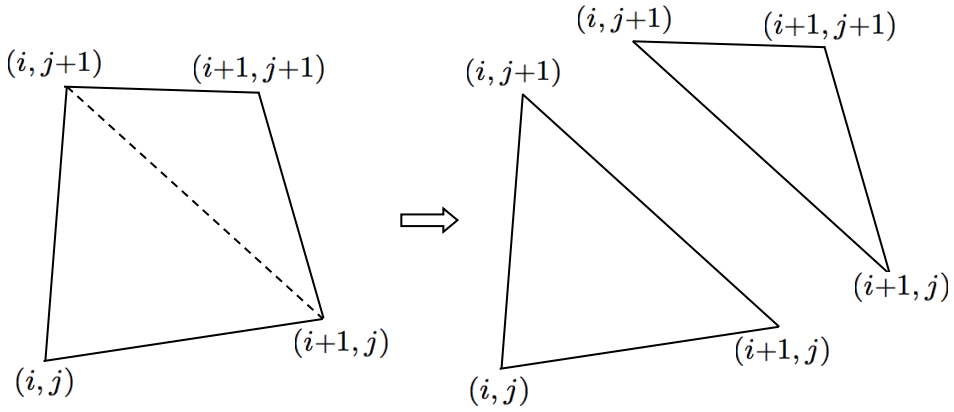


Figure 2-12: 2D schematic of the tetrahedrization method used for point location.

The four planar surfaces of the tetrahedron are given by $\boldsymbol{r} \cdot \boldsymbol{e^1} = 0$, $\boldsymbol{r} \cdot \boldsymbol{e^2} = 0$, $\boldsymbol{r} \cdot \boldsymbol{e^3} = 0$ and $\boldsymbol{r} \cdot \boldsymbol{e^1} + \boldsymbol{r} \cdot \boldsymbol{e^2} + \boldsymbol{r} \cdot \boldsymbol{e^3} = 1$. A point lies inside a particular tetrahedron if all three

relations in equation 2.87 are satisfied:

$$\begin{aligned} \boldsymbol{r} \cdot \boldsymbol{e^1} &\geq 0 \\ \boldsymbol{r} \cdot \boldsymbol{e^2} &\geq 0 \\ \boldsymbol{r} \cdot \boldsymbol{e^3} &\geq 0 \\ \boldsymbol{r} \cdot \boldsymbol{e^1} + \boldsymbol{r} \cdot \boldsymbol{e^2} + \boldsymbol{r} \cdot \boldsymbol{e^3} &\leq 1 \end{aligned} \tag{2.87}$$

Since the mirror point lies only a few cells away from the IB point, and the location of the IB point is known, the search is confined to a small group of cells around the IB point, thus avoiding the computational overhead that a global search over the entire grid would incur.

Another modification that must be made is in the interpolation scheme used to calculate the velocity at the mirror point. Whereas a standard trilinear interpolation can be used if the grid is Cartesian, only if the cell is a parallelepiped can it be applied to a curvilinear grid. Therefore, an inverse distance weighting scheme is applied instead, in which the weights of the eight surrounding velocity points are calculated as a function of the Euclidean distance to the mirror point, s_n. The velocity at the mirror point is given by equation 2.88, where u_n is the velocity at an interpolation point and ε is the minimum tolerance for s_n. When the distance between the mirror point and an interpolation point is very small, computational error becomes significant as $s_n \approx 0$. Therefore if a distance is less than ε, the velocity is set to that of the interpolation point and all other interpolation points are given zero weighting.

The minimum tolerance is computed from the cell size, $\varepsilon = 10^{-3} \times \sqrt{(\Delta\xi^2 + \Delta\eta^2 + \Delta\zeta^2)}$.

$$\boldsymbol{u}_M = \begin{cases} \sum_{i=1}^{N} \dfrac{s_n^{-2}\boldsymbol{u}_n}{\sum_{n=1}^{N} s_n^{-2}} & \text{if } s_n > \varepsilon \text{ for all interpolation points} \\ \boldsymbol{u}_n & \text{if } s_n < \varepsilon \text{ for one interpolation point} \end{cases} \tag{2.88}$$

Using this interpolation stencil on a Cartesian or a curvilinear grid, situations might arise in which one of the interpolation points is the IB point itself or some other IB point, as shown in figure 2-13. The first case poses a problem as one of the interpolation velocities is unknown and the second case requires the coupled solution of the two IB point velocities.

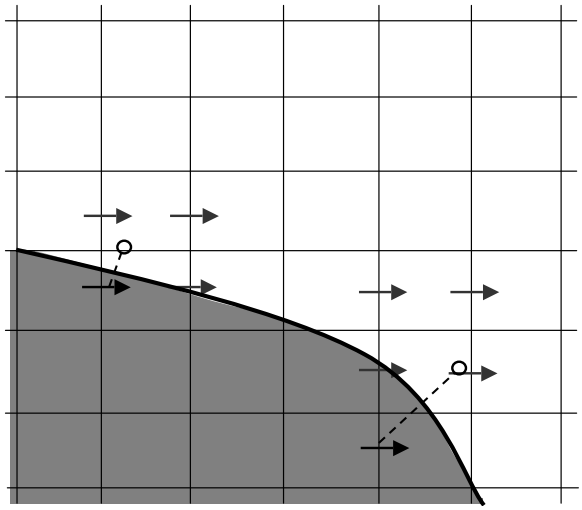


Figure 2-13: 2D example of coupled IB points.

The inverse distance weighting scheme allows simple solutions to these cases which would not be possible with a standard trilinear interpolation. Two options can be adopted. The first is to remove the unknown interpolation point from the stencil, and compute the velocity at the mirror point from the inverse distance average of the other seven points. This is a very simple procedure, but could overpredict the velocity at the mirror point, as the contribution from a point close to the wall is being removed. In the second option, rather than removing the interpolation point from the stencil, it is projected along the surface

normal onto the boundary, where the velocity is known. Although this requires a slight increase in computational effort, it ensures accuracy is maintained.

2.3 Particle tracking

Dispersed two-phase flows can be categorized into two flow regimes, dilute and dense dispersed flows. In dilute dispersed flows, the separation between particles is large relative to their size so interaction between particles is rare and their transport is governed by the fluid forces acting on them. In dense dispersed flows, on the other hand, inter-particle spacing is small and particle motion is dominated by the collisions between them.

The characterization of such flows is made based on the volume fraction of the dispersed phase, α_p, which is the volume occupied by the particles in a unit volume:

$$\alpha_p = \frac{\sum N V_p}{V} \tag{2.89}$$

where N is the number of particles, V_p is the volume of a particle and V is the total volume. Based on the classification given by Elghobashi (1994), a dispersed flow can be regarded as dilute for volume fractions up to $\alpha_p = 10^{-3}$. In this regime, for $\alpha_p < 10^{-6}$, the particles have no effect on the fluid. This is referred to as one-way coupling. At higher volume fractions, the effect of the particles on the flow must be taken into account as well; this is known as two-way coupling. In dense dispersed flows, in addition to the fluid-particle coupling, inter-particle interactions become important in what is called four-way coupling. The different regimes are shown in figure 2-14. The typical drug content in a single dose from a metered-dosed inhaler is $100\mu g \sim 10^{-7}L$ and the average tidal volume at rest, i.e. the volume of air inhaled in one breath is roughly $0.5L$. Therefore the volume fraction, $\alpha_p \sim \mathcal{O}(10^{-7})$, so aerosols lie in the one-way coupling regime.

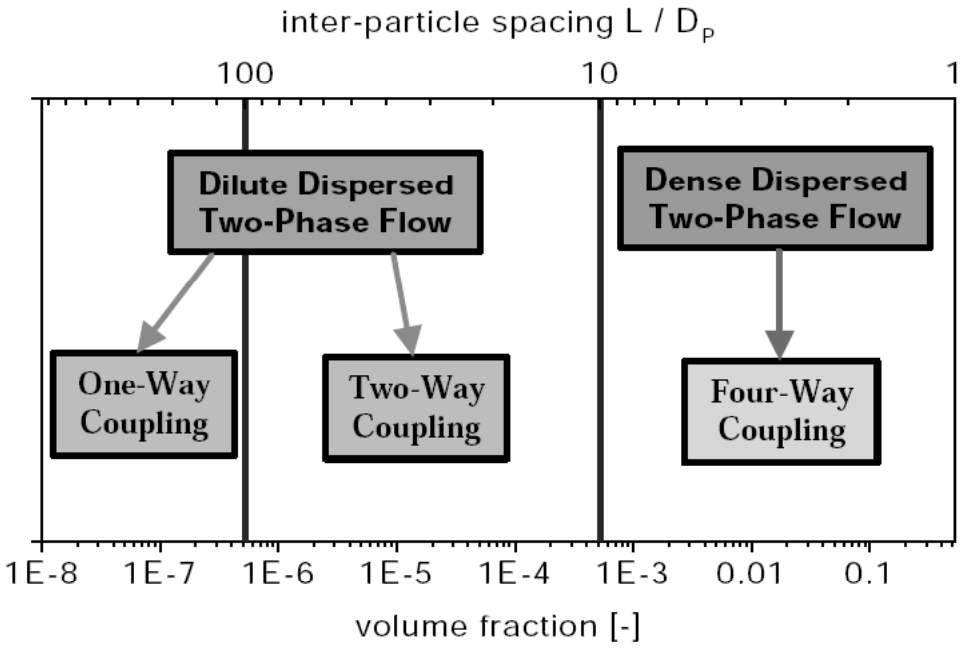


Figure 2-14: Regimes of two-phased flows as a function of particle volume fraction (Sommerfeld, 2000).

Simulation of particles in a flow can be performed with two different methods: the Eulerian or the Eulerian-Lagrangian approach. The Eulerian or two-fluid approach treats the dispersed phase as a continuum, solving the conservation equations of particle mass and momentum. It provides an average description of the particle phase thereby avoiding the cost of tracking individual particles. However, this also leads to loss of accuracy and closure problems, analogous to RANS modelling of turbulence. It is best suited to discontinuous and dense two-phase flows.

For dispersed two-phase flows, such as aerosols, the Eulerian-Lagrangian approach which treats the dispersed phase as a set of individual particles in a continuous carrier phase is more suitable. The particles are tracked through the flow field by solving the equations of motion for each particle with the relevant forces acting on it. Description of turbulent diffusion and collision of particles with a wall is more natural with this approach.

In both Eulerian and Lagrangian tracking methods, the particles are treated as point particles since resolution of the flow around each particle would be computationally unfeasible. This requires the particles to be much smaller than the grid cells so that interpolation of the fluid velocity from surrounding grid points to the centre of the particle is accurate. For DNS of turbulent flows, this condition requires the particle to be much smaller than the Kolmogorov length scale.

When simulating aerosol distribution, two major simplifying assumptions are generally invoked: The particles are assumed to be spherical, and the particle density is assumed to be much larger than the surrounding fluid density. The first assumption is valid for liquid aerosols, since such small liquid droplets are spherical. For dry powder aerosols and evaporated metered dose inhaler aerosols the assumption is not exact, but since the particles are compact, the drag acting on them is similar to that on a sphere. The second assumption is also justified for inhaled aerosols since the densities of the drugs are close to that of water, which is 1000 times denser than air, $\rho_p/\rho_f \sim 10^3$. The motion of spheres in fluids has been studied extensively, so the first assumption also facilitates comparison to a wealth of existing literature. The second assumption simplifies the analysis because it results in the drag force on the particle being much larger than all the other fluid forces which can act on the particle, and which are described in the following section.

2.3.1 Governing equation and numerical integration

The motion of particles in a fluid can be described in a Lagrangian way by the particle equations of motion that describe the change in position and in velocity along their trajectory:

$$\frac{d\boldsymbol{x_p}}{dt} = \boldsymbol{u_p} \tag{2.90}$$

$$m_p \frac{d\boldsymbol{u_p}}{dt} = \sum \boldsymbol{F} \tag{2.91}$$

where $\sum \boldsymbol{F}$ represents all the forces acting on the particles.

The balance of forces acting on the particles as they move along the fluid was derived from first principles by Maxey & Riley (1983), and is given by:

$$\begin{aligned} m_p \frac{d\boldsymbol{u}_p}{dt} = & \frac{18\mu_f}{\rho_p d_p^2} m_p \left(\boldsymbol{u}_f - \boldsymbol{u}_p\right) \\ & + m_f \left(\frac{D\boldsymbol{u}_f}{Dt}\right) \\ & + \frac{1}{2} m_f \left(\frac{D\boldsymbol{u}_f}{Dt} - \frac{d\boldsymbol{u}_p}{dt}\right) \\ & + \frac{3}{2} d_p^2 \left(\pi \rho_f \mu_f\right)^{\frac{1}{2}} \int_{t_0}^{t} \frac{\frac{D\boldsymbol{u}_f}{D\tau} - \frac{d\boldsymbol{u}_p}{d\tau}}{(t-\tau)} d\tau \\ & + \boldsymbol{g}\left(m_p - m_f\right) \end{aligned} \tag{2.92}$$

where the terms on the right-hand side are the drag force, the force due to the fluid pressure gradient and viscous stresses, the inertia force of the added mass, the viscous force due to unsteady relative acceleration (Basset force) and the gravity force respectively (Elghobashi & Truesdell, 1992).

This equation is limited to small particle-Reynolds-numbers, $Re_p < 1$. Extension to higher Reynolds numbers can be achieved using empirical correlations, obtained from

experiments or direct numerical simulations. The particle and flow properties determine which forces are significant. In most cases, the drag force is the dominating force acting on the particles. Extension to higher particle-Reynolds-numbers is obtained via the drag coefficient, C_D, defined as:

$$C_D = \frac{|\boldsymbol{F_D}|}{\frac{1}{2}\rho_f |\boldsymbol{u}_f - \boldsymbol{u}_p|^2 A_p} \tag{2.93}$$

where $A_p = \frac{\pi d_p^2}{4} \left(= \frac{3V_p}{2d_p} = \frac{3m_p}{2d_p\rho_p} \right)$ is the cross-sectional area of a spherical particle, $|\boldsymbol{F_D}|$ is the magnitude of the drag force and $|\boldsymbol{u}_f - \boldsymbol{u}_p|$ is the speed of the fluid relative to the particle. Rearranging gives the expression for the drag force:

$$\boldsymbol{F_D} = \frac{3}{4}\frac{\rho_f}{\rho_p}\frac{m_p}{d_p} C_D (\boldsymbol{u}_f - \boldsymbol{u}_p)|\boldsymbol{u}_f - \boldsymbol{u}_p| \tag{2.94}$$

The drag coefficient is a function of the particle Reynolds number, Re_p, defined as the ratio of inertial to viscous forces acting on the particle:

$$Re_p = \frac{\rho_f d_p |\boldsymbol{u}_f - \boldsymbol{u}_p|}{\mu_f} \tag{2.95}$$

The dependence of C_D on particle Reynolds number is shown by the standard drag curve in figure 2-15.

For small Reynolds numbers, $Re_p < 1$, viscous effects dominate so the analytical solution for the drag coefficient given by "Stokes law" for steady creeping flow is valid:

$$C_D = \frac{24}{Re_p}. \tag{2.96}$$

At higher Reynolds numbers, inertial forces become significant, and for $Re_p > 20$ separation occurs behind the sphere. The wake widens and lengthens with Reynolds number, and

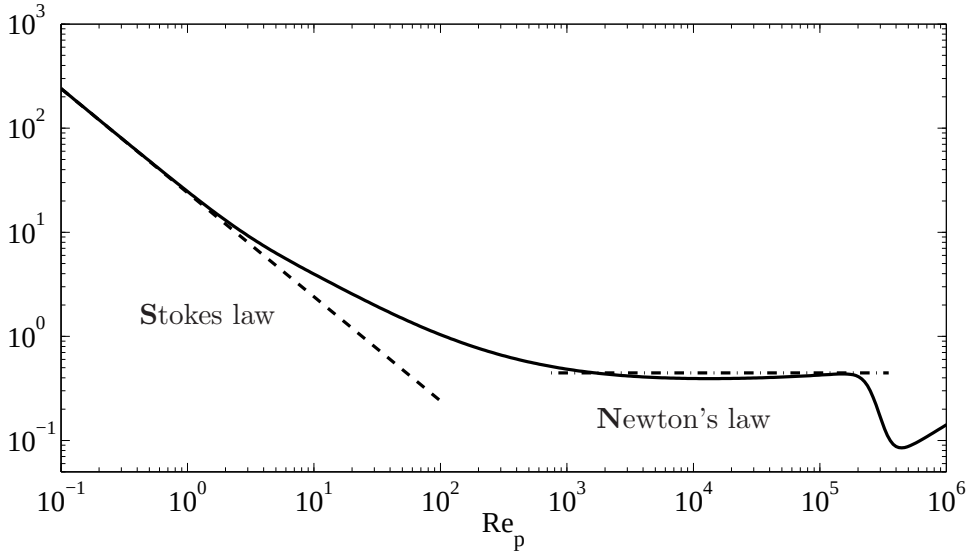


Figure 2-15: Drag coefficient as a function of particle Reynolds number. Standard drag curve along with the Stokes law and Newton law correlations for the different regimes.

above $Re_p \sim 130$ the flow becomes unsteady. In this range, the form drag increases relative to the skin friction. In the range $750 < Re_p < 3 \times 10^5$, the form drag which now predominates remains fairly constant since the wake size and structure do not change appreciably. Therefore C_D is also insensitive to Re_p. This range is often referred to as the "Newton's law" regime with:

$$C_D \approx 0.445. \tag{2.97}$$

Many empirical and semi-empirical equations have been proposed to approximate this curve over different Reynolds number ranges. The correlation proposed by Clift & Gauvin (1970), which fits the curve up to $Re_p < 3 \times 10^5$, is adopted here:

$$C_D = \frac{24}{Re_p}\left(1 + 0.15 Re_p^{0.687}\right) + \frac{0.42}{1 + 4.25 \times 10^4 Re_p^{-1.16}}. \tag{2.98}$$

The drag coefficient is affected by other physical effects such as the turbulence in the flow, rarefaction and wall effects. Lumley (1978) showed that the particle equation is only

valid for use in turbulent flows if two requirements are satisfied:

1. The particle Reynolds number based on the fluctuating relative velocity is less than 0.5.

2. The flow in the vicinity of the particle is at most homogeneous shear, which requires the particle diameters to be much smaller than the turbulence length scale, $\frac{d_p}{\eta} << 1$.

For an in-depth review of particle tracking in turbulent flows, the reader is referred to McLaughlin (1994).

Rarefaction is only significant for particles of comparable size to the mean-free-path of the fluid molecules. At this point, the fluid can no longer be treated as a continuum and so Stokes' law for the drag on the particle, which was derived from the Navier-Stokes equations, is no longer valid. A correction factor needs to be applied to the drag in order to take into account the slip at the particle surface due to non-continuum effects. For typical inhalation conditions the reduction in drag is only larger than 10% for particles smaller than $\sim 1.7\mu m$.

The motion of particles in the vicinity of a wall also affects the drag, causing an increase in the drag coefficient due to the shear at the wall. However, wall effects decay very rapidly as the distance between the particle and the wall increases and they are generally only important in high viscosity fluids. Young & Leeming (1997) who studied deposition of particles in a turbulent pipe flow, claimed that although the wall could influence particle concentration profiles very near the wall, it was unlikely to affect the overall deposition rate.

A transverse lift force, known as the Saffman lift, is generated when particles move through a shear layer. This lift force is generated by the non-uniform relative velocity over the particle, resulting in a non-uniform pressure distribution. The lift force is generally only important if the shear rate is high. For flow through the airways, this is only the case inside

the boundary layer, close to the wall. Kallio & Reeks (1989) showed that the lift force was most prominent for large particles and small particle-to-fluid density ratios, ρ_p/ρ_f, which agrees with the theoretical predictions of particle deposition made by Young & Leeming (1997). Considering that aerosol particles are small and much denser than air, and that the lift force is only significant within the viscous sublayer the lift force is neglected herein.

The second term in equation 2.92 is the force generated by the local pressure gradient and shear stress,

$$\boldsymbol{F_p} = \frac{m_p}{\rho_p} \left(-\nabla p + \nabla \tau\right). \tag{2.99}$$

From the Navier-Stokes equation the fluid pressure gradient and shear stress can be related to the fluid acceleration via

$$-\nabla p + \nabla \tau = \rho_f \left(\frac{D\boldsymbol{u}_f}{Dt} - \boldsymbol{g}\right). \tag{2.100}$$

Hence the force can be expressed as

$$\boldsymbol{F_p} = m_p \frac{\rho_f}{\rho_p} \left(\frac{D\boldsymbol{u}_f}{Dt} - \boldsymbol{g}\right). \tag{2.101}$$

For gas-aerosol flows in which $\rho_f/\rho_p \sim 10^{-3}$, the pressure force may be neglected.

The third and fourth force terms in the particle equation exist in unsteady flows. The inertia force of added mass is due to the acceleration/deceleration of the particles causing the acceleration/deceleration of a certain fraction of the surrounding fluid. The Basset force is caused by the lagging of the boundary layer development on the particle with change in relative velocity, as the drag not only depends on the instantaneous velocities and accelerations but also on the conditions during the development of the flow. For this reason, it is sometimes referred to as the 'history force'. Again, extension of these forces

to higher Reynolds numbers is only possible with empirical coefficients. Computation of the Basset force is particularly time consuming as it has to be integrated along the entire particle trajectory at each time step. For particles moving through gases, as is the case of inhaled pharmaceutical aerosols, because of the large density ratio (ρ_p/ρ_f), the motion of particles is characterized by slow changes in their Reynolds numbers, and therefore the effect of these forces is negligible.

Finally, the last term in the equation of motion is the gravity force, given by

$$\boldsymbol{F_g} = m_p \boldsymbol{g} \tag{2.102}$$

In equation 2.92, this term has been grouped with the gravity term from the pressure gradient force (equation 2.101).

At high Knudsen numbers, the particles are also subjected to a Brownian force, caused by the random collisions with the gas molecules. However Brownian motion in air is only significant for submicrometer particles, $d_p < 0.03\mu m$ (Ounis *et al.*, 1991).

For aerosol particles in the range $3 - 10\mu m$, several terms in the particle equation of motion can be neglected and the forcing terms reduce to the drag and gravitational forces:

$$m_p \frac{d\boldsymbol{u}_p}{dt} = \frac{3}{4}\frac{\rho_f}{\rho_p}\frac{m_p}{d_p} C_D |\boldsymbol{u}_f - \boldsymbol{u}_p| (\boldsymbol{u}_f - \boldsymbol{u}_p) + m_p \boldsymbol{g} \frac{\rho_p - \rho_f}{\rho_p} \tag{2.103}$$

Two important parameters which characterize the motion of particles are the particle response time, τ_p, and the non-dimensional Stokes number, Stk. The particle response time is a measure of the time required for a particle to respond to changes in the local fluid velocity and can be derived from the equations of motion. Dividing equation 2.103 by the

mass of the particle and introducing the particle Reynolds number gives:

$$\frac{d\boldsymbol{u}_p}{dt} = \frac{18\mu_f}{\rho_p d_p^2}\frac{C_D Re_p}{24}\left(\boldsymbol{u}_f - \boldsymbol{u}_p\right) + \boldsymbol{g}\frac{\rho_p - \rho_f}{\rho_p}, \tag{2.104}$$

which can be rewritten as

$$\frac{d\boldsymbol{u}_p}{dt} = \frac{1}{\tau_p}\left(\boldsymbol{u}_f - \boldsymbol{u}_p\right) + \boldsymbol{g}\frac{\rho_p - \rho_f}{\rho_p}, \tag{2.105}$$

where

$$\tau_p = \frac{\rho_p d_p^2}{18\mu_f}\frac{24}{C_D Re_p}. \tag{2.106}$$

For $Re_p < 1$, $\frac{24}{C_D Re_p} = 1$ so the particle response time is given by

$$\tau_p = \frac{\rho_p d_p^2}{18\mu_f} \tag{2.107}$$

Introducing the characteristic length scale, L, and velocity, U, of the fluid in equation 2.105 gives

$$\frac{U}{L/U}\frac{d(\boldsymbol{u}_p/U)}{d(tU/L)} = \frac{U}{\tau_p}\left(\boldsymbol{u}_f/U - \boldsymbol{u}_p/U\right) + \frac{U^2}{L}\frac{\boldsymbol{g}L}{U^2}\frac{\rho_p - \rho_f}{\rho_p} \tag{2.108}$$

Rearranging and introducing the non-dimensional variables $\boldsymbol{u}^* = \boldsymbol{u}/U$, $t^* = tU/L$, $\boldsymbol{g}^* = \boldsymbol{g}L/U^2$, equation 2.108 becomes

$$\frac{\tau_p U}{L}\frac{d\boldsymbol{u}^*{}_p}{dt^*} = \left(\boldsymbol{u}^*{}_f - \boldsymbol{u}^*{}_p\right) + \frac{\tau_p U}{L}\boldsymbol{g}^*\frac{\rho_p - \rho_f}{\rho_p} \tag{2.109}$$

where the parameter in front of the acceleration and gravitational terms is the Stokes number, defined as the ratio of the particle response time to the characteristic time scale

in the flow:

$$Stk = \frac{\tau_p}{\tau_f}. \tag{2.110}$$

In the absence of gravity, if the Stokes number tends to zero, the left hand side of equation 2.109 vanishes and so the relative velocity must also be zero for the equation to be satisfied. This shows that for small Stokes numbers, $Stk << 1$, the particle velocity is roughly that of the fluid and the particles follow the streamlines. For $Stk \sim 1$ or larger, the particle motion becomes increasingly insensitive to the fluid motion, and particles deviate from the streamlines. This suggests that the larger the Stokes number the more likely a particle will undergo inertial impaction.

Finally, the non-dimensional equations of motion solved for the particle velocities and accelerations are given by:

$$\frac{d\boldsymbol{r}_p}{dt} = \boldsymbol{u}_p \tag{2.111}$$

$$\frac{d\boldsymbol{u}_p}{dt} = \frac{1}{Stk}\left(\boldsymbol{u}_f - \boldsymbol{u}_p\right) + \boldsymbol{g}\frac{\rho_p - \rho_f}{\rho_p} \tag{2.112}$$

Integration of these equations is performed via a fourth-order Runge-Kutta (RK4) scheme.

2.3.2 Particle tracking algorithm

The governing equations and the numerical integration have been considered in physical space (P-space). For curvilinear grids, transformation to a simple Cartesian grid in computational space (C-space) renders many calculations, such as point location and interpolation, much more efficient to perform. The disadvantage of C-space algorithms however, is that

they tend to be less accurate as they suffer from additional sources of error compared to P-space schemes. Both P-space and C-space particle tracking algorithms have been developed here for use with the DNS solver. The details, along with the performance and relative merits of each method, will be discussed below.

P-space scheme

In P-space, point location is not straightforward as there is no explicit relation between a physical position and the grid cell that contains it. Additionally, the cells in a curvilinear grid are not parallelepipeds, making it difficult to perform trilinear interpolation of the velocity as the position of a particle in relation to the surrounding nodes cannot be easily determined.

In order to determine the cell position of a particle on a curvilinear grid, various point location methods exist. Global and local search algorithms need to be distinguished. Since particles are only advanced a small distance each time step, a local search using the particle's previous location as a starting point can be conducted, thus avoiding the expense of a global search through all the grid cells. At the first time step, where a previous location does not exist, a global search is also unnecessary since the particles are released at the inlet of the geometry which limits the search to the inflow plane.

Popular local search methods include tetrahedrization, stencil walk, and Newton-Raphson iteration. The stencil walk method uses an initial guess for the location of the particle in C-space, $\boldsymbol{\xi}_k$, which is transformed to P-space so that the difference between the position of the particle and the guess can be computed, $\boldsymbol{\Delta x}_k = \boldsymbol{x}_k - \boldsymbol{x}_p$. The difference vector is then transformed back to computational space, $\boldsymbol{\Delta \xi}_k = \boldsymbol{J}^{-1}\boldsymbol{\Delta x}_k$, and added to the previous position resulting in a new guess for the particle location. The iterative method in 2.113 is

performed until the value of $\boldsymbol{\Delta\xi}$ is sufficiently small.

$$\boldsymbol{\xi}_{k+1} = \boldsymbol{\xi}_k + \boldsymbol{J}^{-1}(\boldsymbol{x}_k - \boldsymbol{x}_p) \tag{2.113}$$

The Newton-Raphson method seeks the root of the equation $\mathcal{F}(\boldsymbol{\xi}) = 0$ by the following iteration:

$$\boldsymbol{\xi}_{k+1} = \boldsymbol{\xi}_k - \frac{\mathcal{F}(\boldsymbol{\xi})}{\mathcal{F}'(\boldsymbol{\xi})}. \tag{2.114}$$

Here $\mathcal{F}(\boldsymbol{\xi}) = \boldsymbol{x}_p - \mathcal{T}(\boldsymbol{\xi})$, where $\mathcal{T}$ is the function that transforms a point from C-space to P-space, and $\boldsymbol{\xi}_k$ is the distance in physical space between the particle location and the guess. Tetrahedrization was used to determine the position of the mirror points on a curvilinear grid and was described in section 2.2.7. It is adopted for point location of the particles also as it is easy to implement and has been shown to be more efficient than the Newton-Raphson iterative method (Schafer & Breuer, 2002).

Since the Navier-Stokes equations are solved in terms of contravariant fluxes in our computational algorithm, the velocity field must be computed via a transformation, as mentioned in section 2.2.7:

$$\boldsymbol{u} = \boldsymbol{S}_q U^q. \tag{2.115}$$

Due to the staggered grid arrangement, the transformation 2.115 requires interpolation of the fluxes that do not share the same cell face as the velocity. In addition, $\boldsymbol{S}_q$ is not computed at every location in the domain as it would be prohibitively expensive. Instead, the quantities $\boldsymbol{S}^{\xi}_{i,j,k}$, $\boldsymbol{S}^{\xi}_{i+1,j,k}$, $\boldsymbol{S}^{\eta}_{i,j,k}$, $\boldsymbol{S}^{\eta}_{i,j+1,k}$, $\boldsymbol{S}^{\zeta}_{i,j,k}$, $\boldsymbol{S}^{\zeta}_{i,j,k+1}$, are stored for each cell due to storage requirements. The geometric parameters at other positions are computed by simple averaging (Rosenfeld *et al.*, 1991). Although the approximation of the $\boldsymbol{S}_q$ terms by simple averaging does not lead to serious degradation of results, the small errors introduced in

combination with the errors from the interpolation of the fluxes could accumulate in time when advancing the particles, leading to significant inaccuracies in the particle trajectories. Therefore, although C-space schemes are considered to be less accurate than P-space schemes, the former could be more attractive in the case where the flow equations are solved in terms of contravariant, rather than Cartesian, components.

The general structure of the P-space algorithm is shown in the pseudo-code below

Algorithm 2 P-space particle tracking

```
release particle into flow
find cell containing initial position (tetrahedrization)
for n = 1 to ntimesteps do
  compute Cartesian velocities from volume fluxes (transformation
  requiring interpolation)
  determine fluid velocities at current position
  calculate force per unit mass acting on particle
  compute new velocity and position of particle
  find cell containing new position (tetrahedrization)
  if particle has exited domain or deposited on wall then
    exit
  end if
end for
```

C-space scheme

The equations of motion for the particles when transformed to computational space are expressed in terms of the contravariant components of the velocity and the acceleration:

$$\frac{d\boldsymbol{u}_p^m}{dt} = \boldsymbol{a}_p^m, \tag{2.116}$$

$$\frac{d\boldsymbol{\xi}_p^m}{dt} = \boldsymbol{u}_p^m. \tag{2.117}$$

The contravariant velocities are computed from the fluxes available from the Navier-Stokes solver, by dividing by the volume of the cell:

$$\boldsymbol{u}^m = J^{-1}\boldsymbol{U}^m \tag{2.118}$$

In this case, no interpolation from surrounding points is required, and so the error introduced in the P-space algorithm in the computation of the velocities is avoided.

The gravitational acceleration term is transformed from Cartesian to contravariant components by :

$$\boldsymbol{a_G}^q = \boldsymbol{J}^{-1} \cdot \boldsymbol{a_G} = \boldsymbol{J}^{-1} \cdot \left(\boldsymbol{g} \frac{\rho_p - \rho_f}{\rho_p} \right). \tag{2.119}$$

The Jacobian is discontinuous at the cell faces, resulting in a discontinuous field in computational space. The accuracy of the computed velocity field, and hence of the tracking algorithm, depends largely on how the Jacobian is evaluated. Given the coordinates of a grid point, $x_{i,j,k}$, the first term in the Jacobian, for example, can be computed by

1. forward differencing, $\frac{\partial x}{\partial \xi} = x_{i+1,j,k} - x_{i,j,k}$,
2. backward differencing, $\frac{\partial x}{\partial \xi} = x_{i,j,k} - x_{i-1,j,k}$, or
3. central differencing, $\frac{\partial x}{\partial \xi} = \frac{1}{2}\left(x_{i+1,j,k} - x_{i-1,j,k}\right)$.

Although central differencing is the most accurate of the three (it is second-order accurate whereas forward and backward differencing are only first-order accurate), the most accurate discretization scheme for the Jacobian at a given grid point, is a mixed forward/backward difference scheme depending on the cell that the particle belongs to. The various cases are shown in figure 2-16. The C-space algorithm circumvents the overhead of point location, since the computational grid is Cartesian so there is an explicit relation between the position

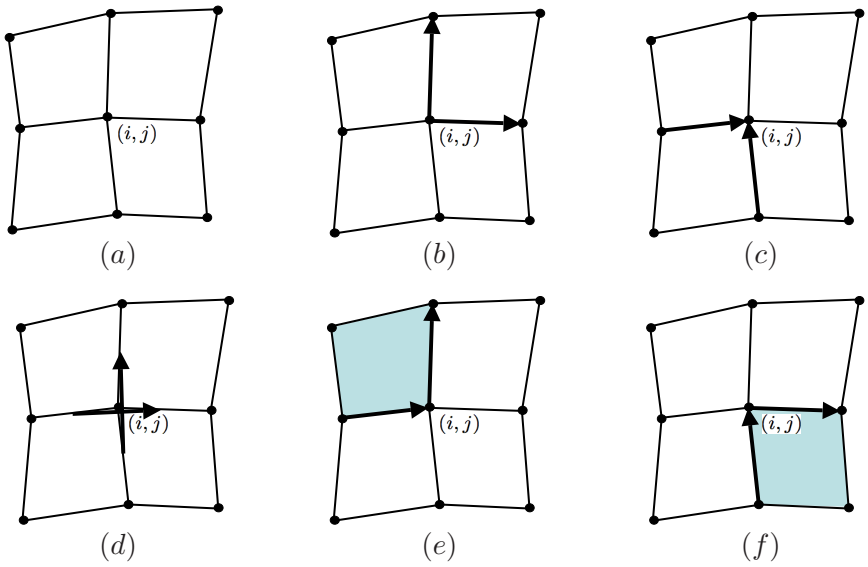


Figure 2-16: Schematic of differencing schemes for Jacobian computation. (a) grid node, (b) forward-differencing, (c) backward-differencing, (d) central differencing, (e) and (f) mixed forward/backward differencing.

of the particle and the cell in which it resides. The grid in computational space is uniform and orthogonal, with cell size $\Delta\xi = \Delta\eta = \Delta\zeta = 1$, therefore the cell in which the particle lies is simply given by

$$\begin{aligned} i &= int(\xi_p) \\ j &= int(\eta_p) \\ k &= int(\zeta_p) \end{aligned} \tag{2.120}$$

The position of the particle within the cell (it's fractional offset) is

$$\begin{aligned} \delta\xi_p &= \xi_p - i \\ \delta\eta_p &= \eta_p - j \\ \delta\zeta_p &= \zeta_p - k \end{aligned} \tag{2.121}$$

After the solution of the particle equations of motion in computational space, transformation of the particle positions to physical coordinates is performed to determined deposition. This transformation is straightforward, and can be defined by a trilinear interpolation of the cell corner physical positions:

$$
\begin{aligned}
\boldsymbol{x}_p &= \mathcal{T}(\boldsymbol{\xi}_p) \\
&= (1-\delta\xi_p)(1-\delta\eta_p)(1-\delta\zeta_p)\boldsymbol{x}_{i,j,k} \quad +(\quad \delta\xi_p)(1-\delta\eta_p)(1-\delta\zeta_p)\boldsymbol{x}_{i+1,j,k} \\
&+(\quad \delta\xi_p)(\quad \delta\eta_p)(1-\delta\zeta_p)\boldsymbol{x}_{i+1,j+1,k} \quad +(1-\delta\xi_p)(\quad \delta\eta_p)(1-\delta\zeta_p)\boldsymbol{x}_{i,j+1,k} \\
&+(1-\delta\xi_p)(1-\delta\eta_p)(\quad \delta\zeta_p)\boldsymbol{x}_{i,j,k+1} \quad +(\quad \delta\xi_p)(1-\delta\eta_p)(\quad \delta\zeta_p)\boldsymbol{x}_{i+1,j,k+1} \\
&+(\quad \delta\xi_p)(\quad \delta\eta_p)(\quad \delta\zeta_p)\boldsymbol{x}_{i+1,j+1,k+1} \quad +(1-\delta\xi_p)(\quad \delta\eta_p)(\quad \delta\zeta_p)\boldsymbol{x}_{i,j+1,k+1}
\end{aligned}
$$

The general structure of the C-space algorithm is shown in the pseudo-code below

Algorithm 3 C-space particle tracking

```
release particle into flow (set particle P-position at inflow)
find cell containing initial position and determine C-position
(tetrahedrization)
for n = 1 to ntimesteps do
  compute contravariant velocities from volume fluxes
  determine fluid C-velocities at current C-position
  calculate C-force per unit mass acting on particle
  compute new C-velocity and C-position of particle
  transform C-position to P (transformation)
  if particle has exited domain or deposited on wall then
    exit
  end if
end for
```

Interpolation

Interpolation of the fluid velocity at the particle location is required for the computation of the drag force acting on the particle. Various interpolation schemes for use on Cartesian grids (linear interpolation, cubic splines, partial Hermite, Lagrange polynomials, etc) have

been investigated in the literature (Yeung & Pope, 1988; Kontomaris & Hanratty, 1992) but relatively less is available for curvilinear grids. Standard trilinear interpolation cannot be applied in P-space as the grid is not orthogonal. Transformation onto computational space leads to an orthogonal grid for the grid points but not for the staggered velocities (see figure 2-17). Therefore trilinear interpolation requires the additional transformation of all three 'velocity grids', increasing the cost of the scheme. Additionally, errors are introduced in C-space since the contravariant velocity field is discontinuous.

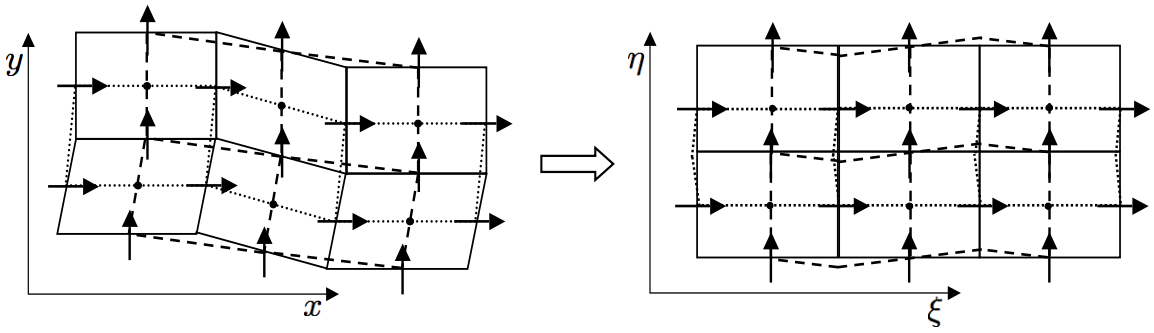


Figure 2-17: 2D schematic of grid transformation from physical to computational space. While the grid is orthonormal in C-space, the velocity grids are not.

Marchioli *et al.* (2007) proposed an interpolation scheme for use in computational space based on a Taylor series expansion about the nearest velocity point. Considering the nearest point with indices (i, j, k), the velocity at the particle location in P-space is given by:

$$\boldsymbol{u}_p = \boldsymbol{u}_{i,j,k} + \frac{\partial \boldsymbol{u}_{i,j,k}}{\partial x}\left(x_p - x_{i,j,k}\right) + \frac{\partial \boldsymbol{u}_{i,j,k}}{\partial y}\left(y_p - y_{i,j,k}\right) + \frac{\partial \boldsymbol{u}_{i,j,k}}{\partial z}\left(z_p - z_{i,j,k}\right) \qquad (2.122)$$

Taylor series are only valid for continuous, differentiable functions, and so cannot be applied to the contravariant velocities. Marchioli *et al.* (2007) applied the interpolation in computational space, using the Cartesian components of the velocity, by transforming the

derivatives in equation 2.122 as follows:

$$\begin{aligned}
\frac{\partial \boldsymbol{u}_{i,j,k}}{\partial x} &= \frac{\partial \boldsymbol{u}_{i,j,k}}{\partial \xi}\frac{\partial \xi}{\partial x} + \frac{\partial \boldsymbol{u}_{i,j,k}}{\partial \eta}\frac{\partial \eta}{\partial x} + \frac{\partial \boldsymbol{u}_{i,j,k}}{\partial \zeta}\frac{\partial \zeta}{\partial x} \\
\frac{\partial \boldsymbol{u}_{i,j,k}}{\partial y} &= \frac{\partial \boldsymbol{u}_{i,j,k}}{\partial \xi}\frac{\partial \xi}{\partial y} + \frac{\partial \boldsymbol{u}_{i,j,k}}{\partial \eta}\frac{\partial \eta}{\partial y} + \frac{\partial \boldsymbol{u}_{i,j,k}}{\partial \zeta}\frac{\partial \zeta}{\partial y} \\
\frac{\partial \boldsymbol{u}_{i,j,k}}{\partial z} &= \frac{\partial \boldsymbol{u}_{i,j,k}}{\partial \xi}\frac{\partial \xi}{\partial z} + \frac{\partial \boldsymbol{u}_{i,j,k}}{\partial \eta}\frac{\partial \eta}{\partial z} + \frac{\partial \boldsymbol{u}_{i,j,k}}{\partial \zeta}\frac{\partial \zeta}{\partial z}
\end{aligned} \tag{2.123}$$

However, the original motivation behind the C-space algorithm was to avoid the computation of the Cartesian velocities from the contravariant fluxes which would be necessary for this interpolation.

A simple alternative is the inverse distance weighting procedure, which was used to determine the velocity at the mirror points in the immersed boundary method (see section 2.2.7) and can easily be applied in both C-space and P-space algorithms. Both algorithms along with the Taylor expansion and inverse-distance weighting interpolation schemes were tested on a Cartesian and a curvilinear grid in order to determine the most accurate implementation. Massless particles were released in a laminar flow in a curved pipe approximating the shape of the mouth and throat, and the percentage of particles deposited was determined. The results are summarized in table 2.1.

Table 2.1: Errors in the interpolation schemes in C-space and P-space.

		Taylor expansion	Inverse distance weighting
Cartesian grid	P-space	0.20	0.04
	C-space	1.53	0.04
curvilinear grid	P-space	0.77	6.90
	C-space	0.86	0.25

Chapter 3

Validation

In order to demonstrate the accuracy of the immersed boundary method and its ability to handle complex boundaries, a number of validation cases will be presented and compared to both numerical and experimental results from the literature. First, two-dimensional flow over a circular cylinder and flow over a sphere as an example of three-dimensional flow are considered. These are standard test cases for non-conforming grid methods in the literature. Next, the ability of the method to accurately model turbulent flows is investigated in a channel with a wavy wall. Finally, flow in a duct with strong curvature is studied as a test case for the method on curvilinear grids. These results show the capability of the method to accurately model complex flows.

3.1 Numerical accuracy of IB method

In order to determine the spatial accuracy of the method, a grid refinement study is carried out. The flow solver is second-order accurate in space for the velocities, and it should be verified that introducing the immersed boundary method still maintains this accuracy. The grid convergence study is executed for flow around a circular cylinder for both the explicit IB method of Kim *et al.* (2001) and the current implicit iterative method. Four different

uniform Cartesian grids 96^2, 192^2, 384^2 and 768^2 are used on a $4d \times 4d$ domain, where d is the cylinder's diameter, with the cylinder located at the centre. Free-slip is applied at the top and bottom boundaries and the simulations are run at a Reynolds number $Re_d = 40$, based on the diameter of the cylinder d, and the far-field velocity U_∞. Since there is no exact solution for this flow, the solution obtained from the highly resolved 768×768 grid is used as the benchmark. The same time step, $\Delta t = 0.0001$, is applied with all grids in order to avoid the effect of any temporal errors on the analysis. The L_2 and L_∞ norms, that measure the difference between the computed and the exact solution, are given by,

$$L_2^N = \left[\frac{1}{N^2} \sum_{i=1}^{N} \sum_{j=1}^{N} \left(\phi_{i,j}^{num} - \phi_{i,j}^{ref} \right)^2 \right]^{\frac{1}{2}}, \qquad L_\infty^N = max|\phi_{i,j}^{num} - \phi_{i,j}^{ref}|.$$

As can been seen from figure 3-1, the largest errors are located around the cylinder, making the L_∞ norm a good measure of local error around the immersed boundary. The L_2 norm is a good measure of the global error. Figure 3-2 shows both error norms for the u and v velocities. Reference lines showing first and second-order rates of convergence have been plotted alongside. The error norms for the implicit IB method are lower but both methods exhibit similar convergence. Comparison of the error norms with the reference lines shows that the methods are close to second-order accurate. The slight deviation from second-order convergence observed in the L_∞ norm has also been reported in the literature and attributed to the lack of a true exact solution of the governing equations (Udaykumar *et al.*, 2001; Gilmanov & Sotiropoulos, 2005).

3.2 Flow past a circular cylinder

The flow around a cylinder has become one of the standard cases for testing IB methods. Even in the laminar regime, the dynamics are complex and unsteady, and therefore accurate

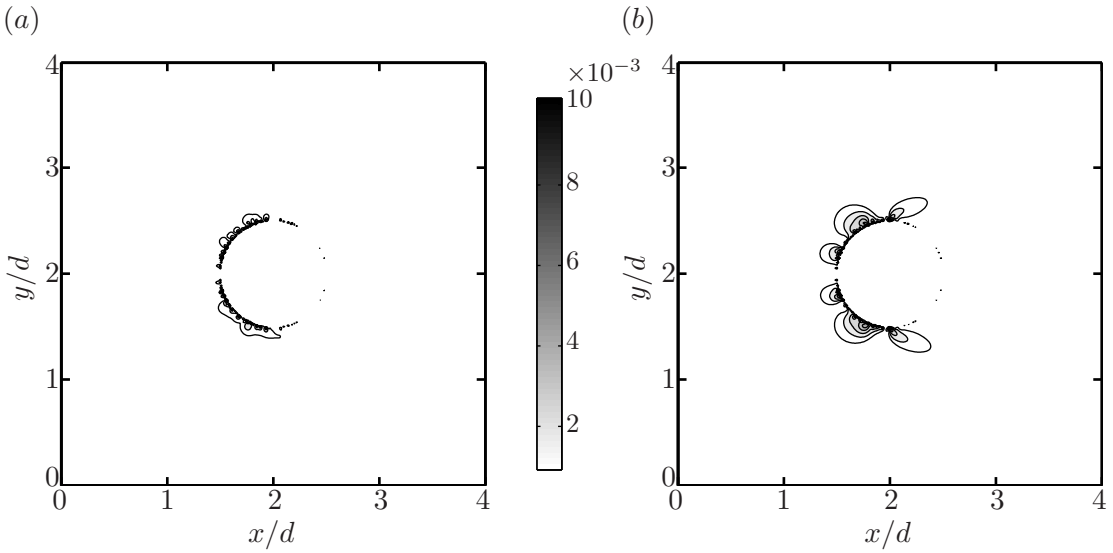


Figure 3-1: Distribution of u velocity error on the 384×384 grid. (a) Implicit iterative IB method and (b) explicit IB method (Kim *et al.*, 2001).

prediction of the flow is a challenging task for any numerical method. It has been studied widely, over a range of Reynolds numbers, so a large number of numerical and experimental results are available for comparison (Braza *et al.*, 1986; Coutanceau & Bouard, 1977; Fornberg, 1980; Taneda, 1956).

Simulations are performed at $Re_d = \{20, 40, 100, 200, 300, 1000\}$ and compared with established experimental and numerical results. In order to minimize the effect of the boundaries on the flow, the size of the computational domain is $40d \times 40d$, where d is the cylinder diameter. Free-slip conditions are imposed at the top and bottom computational boundaries. Sen *et al.* (2009) showed that compared to no-slip, the free-slip boundary condition gives results closer to the ones for unbounded flow. A 768×768 non-uniform Cartesian grid is employed to provide high resolution around the cylinder. The grid in the vicinity of the cylinder is shown in figure 3-3. Cosine stretching is applied in both the streamwise and transverse directions, with a maximum stretching ratio, defined as the ratio of grid spacing on two adjacent cells, of 1.01. The ratio between the largest and smallest cells is $\Delta x_{max}/\Delta x_{min} = 8.0$; the largest cells being those on the edge of the domain and

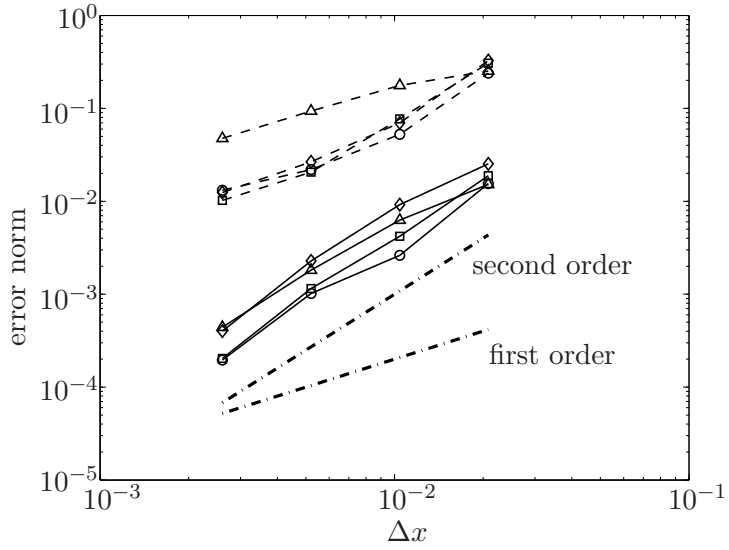


Figure 3-2: L_2 (—) and L_∞ (- - -) error norms versus grid spacing for the streamwise u velocity (□, implicit IB; ◊, explicit IB) and transverse v velocity (◯, implicit IB; △, explicit IB).

the smallest are those at the centre. The grid spacing near the cylinder is $\Delta x \approx 0.013$. The grid, grid spacing and stretching ratio are shown in figures 3-4 *a*,*b* and *c* respectively.

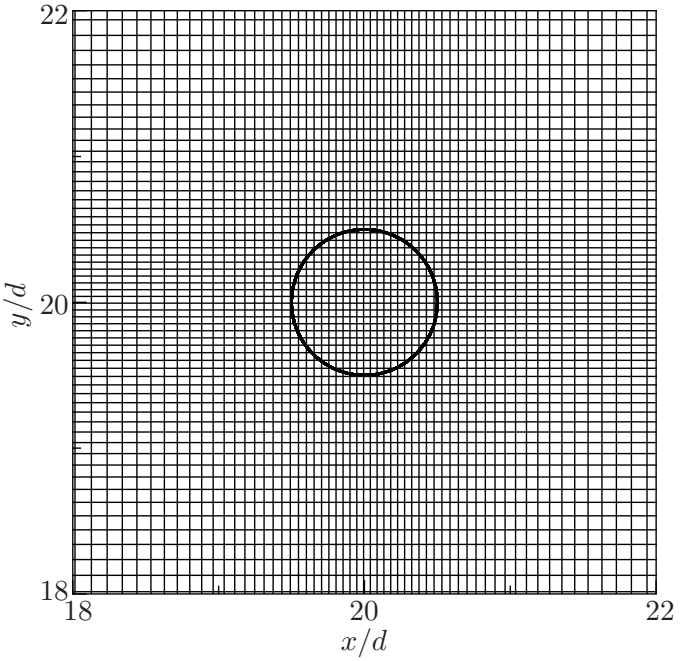


Figure 3-3: Non-uniform grid employed in the vicinity of the cylinder. Every fourth grid line has been plotted.

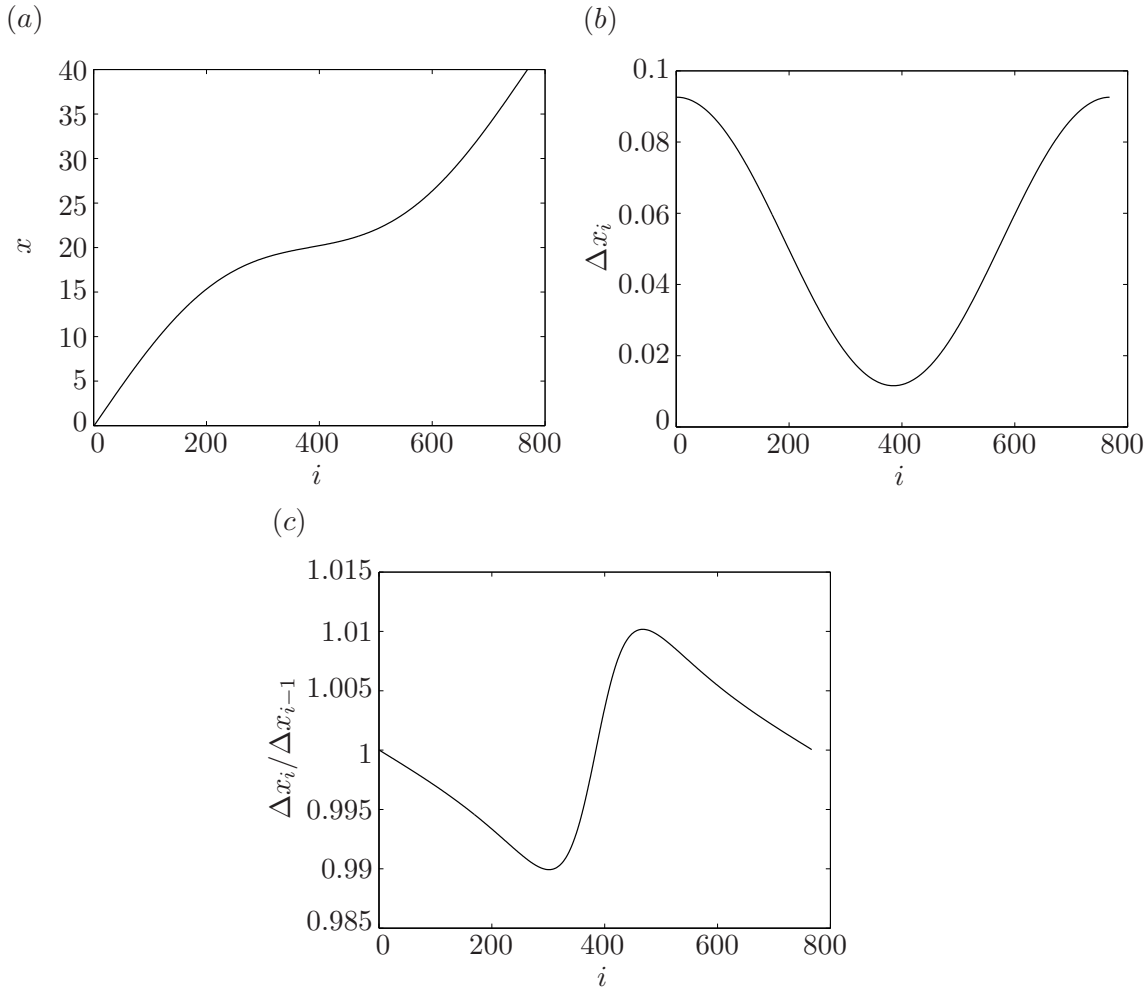


Figure 3-4: (a) Location of streamwise points, (b) spacing of streamwise points and (c) stretching ratio between streamwise points.

The dynamics of the flow over a cylinder are strongly dependant on the Reynolds number. At low Reynolds numbers, the flow around a cylinder remains axisymmetric and steady, with two standing eddies in its wake. These eddies elongate as the Reynolds number increases. Figure 3-5 shows the spanwise vorticity contours and the streamlines at $Re_d = 20$ and $Re_d = 40$. As expected, the flow is steady and symmetric about the streamwise axis, and the separation bubble behind the cylinder is longer at the higher Reynolds number.

Table 3.1 shows the wake dimensions and drag coefficients compared to values reported in the literature. The parameters L_w, a, and b represent the length of the recirculation zone, the distance from the centre of the vortex to the edge of the cylinder, and the distance

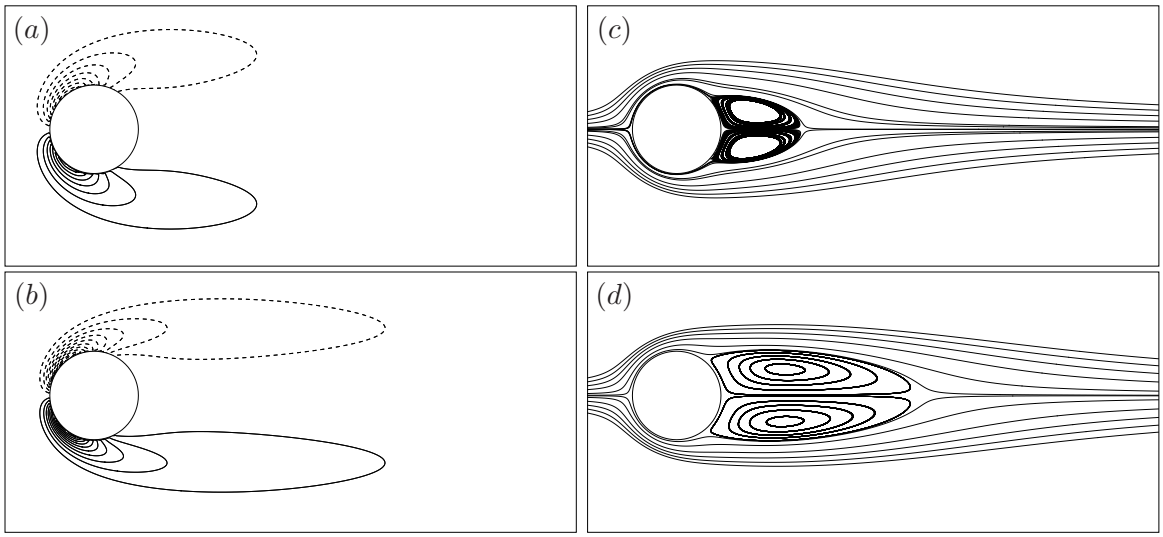


Figure 3-5: At left, spanwise vorticity contours from -10.0 to 10.0 with increments of 1.0, —, positive; - - -negative. At right, streamlines over a cylinder. (a), (c) $Re_d = 20$; (b), (d) $Re_d = 40$.

between the centres of the two vortices respectively (Coutanceau & Bouard, 1977), as shown in figure 3-6. The results show very good agreement with previous studies.

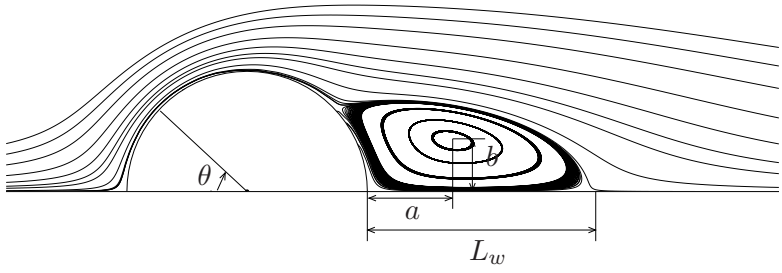


Figure 3-6: Nomenclature used in table 3.1.

The vorticity contours and streamline plots show that the immersed boundary method predicts the general dynamics of the flow accurately. However, the flow close to the body is of particular interest, as it should be verified that the forcing introduced at the immersed boundary is preserving the correct velocities and pressure near the wall. In order to examine the flow close to the boundary and determine its accuracy, the pressure coefficient and skin friction at the wall of the cylinder are computed at various Reynolds numbers and compared

Table 3.1: Comparison of experimental and numerical studies for flow over a cylinder at $Re_d = 20$ and 40.

		L_w/d	a/d	b/d	C_D
$Re_d = 20$	Coutanceau & Bouard (1977)[e]	0.93	0.33	0.46	-
	Dennis & Chang (1970)	0.94	-	-	2.05
	Fornberg (1980)	0.91	-	-	2.00
	Linnik & Fasel (2005)	0.93	0.36	0.43	2.06
	Taira & Colonius (2007)	0.94	0.37	0.43	2.06
	Tritton (1959)[e]	-	-	-	2.09
	Ye *et al.* (1999)	0.92	-	-	2.03
	Present method	**0.93**	**0.37**	**0.43**	**2.07**
$Re_d = 40$	Coutanceau & Bouard (1977)[e]	2.13	0.76	0.59	-
	Berthelsen & Faltinsen (2008)	2.29	0.72	0.60	1.59
	Dennis & Chang (1970)	2.35	-	-	1.52
	Fornberg (1980)	2.24	-	-	1.50
	Linnik & Fasel (2005)	2.28	0.72	0.60	1.54
	Marella *et al.* (2005)	2.30	-	-	1.52
	Taira & Colonius (2007)	2.30	0.73	0.60	1.54
	Tritton (1959)[e]	-	-	-	1.59
	Tseng & Ferziger (2003)	2.21	-	-	1.53
	Ye *et al.* (1999).	2.27	-	-	1.52
	Present method	**2.26**	**0.71**	**0.60**	**1.52**

[e] experimental results.

to solutions using boundary-fitted grids. The pressure coefficient and skin friction are defined as,

$$C_p = \frac{p - p_\infty}{\frac{1}{2}\rho U_\infty^2}, \qquad C_f = \frac{\tau_w}{\frac{1}{2}\rho U_\infty^2}$$

where p_∞ is the far-field pressure and τ_w is the wall shear stress. As can be seen from figure 3-7, results are in very close agreement to the boundary-fitted grid results, showing the ability of the method to accurately model the flow near the boundary over a range of Reynolds numbers.

At a Reynolds number of approximately 47, the wake behind the cylinder starts to become unstable to perturbations and develops a slow oscillation which increases downstream. As Re_d is increased beyond 80, the oscillations in the wake grow in amplitude and finally roll up into vortices which break off alternately from the cylinder, resulting in unsteady flow. This trail of vortices is known as the von Kármán vortex street. In order

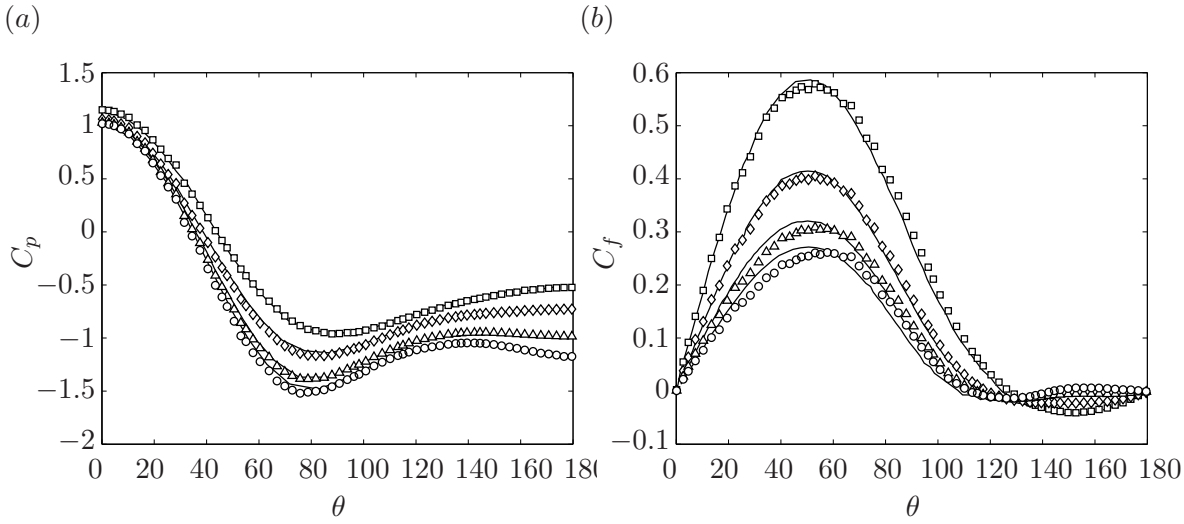


Figure 3-7: (a) Pressure coefficient and (b) skin friction for flow over a cylinder at different Reynolds numbers. □, ◊, △, ◯, current method; —, boundary-fitted grid: $Re_d = 40$ (Tseng & Ferziger, 2003), $Re_d = 100$, $Re_d = 200$, $Re_d = 300$ (Rajani *et al.*, 2009).

to generate unsteady flow, random perturbations are introduced in the initial flow field. At the lower Reynolds numbers these perturbations eventually die out, and the flow becomes steady whilst at the higher Reynolds numbers these perturbations lead to unsteady flow and trigger vortex shedding behind the cylinder. Figure 3-8 shows the spanwise vorticity contours and streamlines around the cylinder at $Re_d = 200$. The presence of vortex shedding is clearly visible.

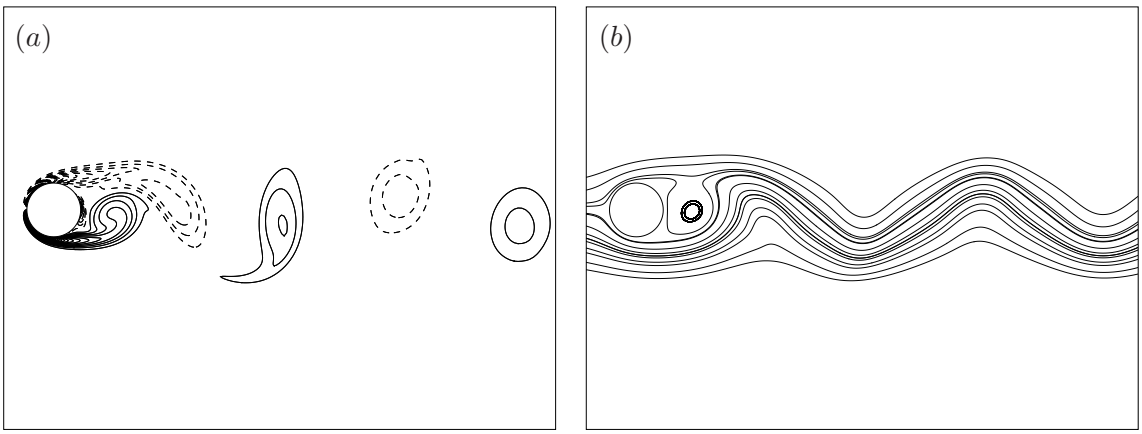


Figure 3-8: Flow over a cylinder at $Re_d = 200$. (a) Spanwise vorticity contours from -30.0 to 30.0 with increments of 1.0, —, positive; - - -negative. (b) Streamlines.

Once the flow reaches a steady or periodic state, the drag and lift coefficients are computed according to,

$$C_D(t) = \frac{F_D(t)}{\frac{1}{2}\rho U_\infty^2 l d}, \qquad C_L(t) = \frac{F_L(t)}{\frac{1}{2}\rho U_\infty^2 l d}$$

where l is the spanwise length of the cylinder. The force acting on the cylinder $\boldsymbol{F} = (F_D, F_L)$ is calculated by integration of the pressure and the shear stresses acting on the surface:

$$\boldsymbol{F} = \int_{IB} \left(-\boldsymbol{n}p + \boldsymbol{n} \cdot \boldsymbol{\tau}\right) dS \tag{3.1}$$

where $\boldsymbol{\tau}$ is the viscous shear tensor, p the pressure and $\boldsymbol{n}$ the normal vector pointing towards the fluid. The pressure and viscous components of the force are computed by discretization of the integral over all the triangles on the surface of the cylinder given by,

$$\begin{aligned} F_i^{press} = \int_{IB} -p\delta_{ij} n_j dS &= \sum_k^{k\in IB} -p^k n_i^k dS^k \\ F_i^{visc} = \int_{IB} \tau_{ij} n_j dS &= \sum_k^{k\in IB} -\mu \left(\frac{\partial u_i}{\partial x_j} + \frac{\partial u_j}{\partial x_i}\right)^k n_j^k dS^k \end{aligned} \tag{3.2}$$

In order to obtain the pressure and shear stresses at each triangle, three points in the fluid, $\boldsymbol{r_1}$, $\boldsymbol{r_2}$ and $\boldsymbol{r_3}$, lying on the normal to the triangle are used to extrapolate the pressure and velocity gradients to the centre, $\boldsymbol{r_c}$. The pressure and velocity gradients at these points are evaluated from the surrounding cells using trilinear interpolation, in the same way the velocity at the mirror points is computed. This is similar to the method used by Mark & van Wachem (2008). Point $\boldsymbol{r_1}$ is at a distance $d_1 = \sqrt{\left((n_x\Delta x)^2 + (n_y\Delta y)^2 + (n_z\Delta z)^2\right)}$ from the centre of the triangle, where Δx, Δy, Δz are the local grid spacings and n_x, n_y, n_z are the x, y, and z components of the triangle normal vector. Point $\boldsymbol{r_2}$ is at a distance

$d_2 = 1.5d_1$ from the centre and $\boldsymbol{r_3}$ at a distance $d_3 = 2d_2$. A schematic is shown in figure 3-9.

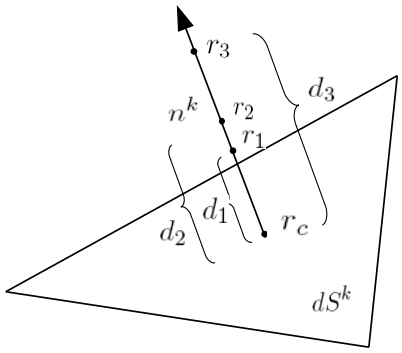


Figure 3-9: Schematic of triangle k on the surface of the body, showing the extrapolation points, $\boldsymbol{r_1}$, $\boldsymbol{r_2}$, $\boldsymbol{r_3}$, and the centre $\boldsymbol{r_c}$, normal vector $\boldsymbol{n}^k$ and area dS^k of the triangle.

For the pressure, $\boldsymbol{r_2}$ and $\boldsymbol{r_3}$ are used to extrapolate to the centre of the triangle. These points are sufficiently close to the surface so that the extrapolation is accurate, but far away such that no pressure points used in the interpolation procedure lie inside the body. For the velocity gradients, $\boldsymbol{r_1}$ and $\boldsymbol{r_2}$ are used. The velocity gradients are more sensitive to distance from the surface, so the extrapolation points must be close to the boundary. Some $\boldsymbol{r_1}$ interpolation points lie inside the body but are retained because the IB velocities are mirror velocities to the flow outside, therefore, the velocity gradients in the IB cells are correct.

As vortices of opposite circulations are shed, oscillatory drag and lift forces are created. The temporal variations of the drag and lift coefficients at $Re_d = 200$ are shown in figure 3-10 and a comparison with experimental and numerical studies in the literature is given in table 3.2. The vortex shedding process is dependent on the Reynolds number and is characterized by the Strouhal number, given by $St \equiv fd/U_\infty$, where f is the shedding frequency. The higher the Reynolds number, the higher the frequency of shedding. The variation of Strouhal number with Re_d is shown in figure 3-11. The base coefficient of

pressure as a function of Re_d has also been plotted to demonstrate the agreement with other results in the literature.

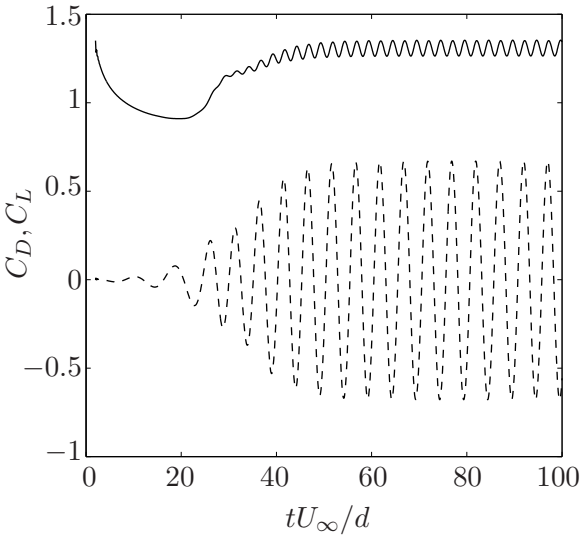


Figure 3-10: Temporal variation of drag coffined C_D (—) and lift coefficient C_L (- - -) on cylinder at $Re_d = 200$.

Table 3.2: Comparison of experimental and numerical studies for flow over a cylinder at $Re_d = 200$.

		St	$C_{D,m}$	$C_{D,a}$	$C_{L,a}$
$Re_d = 200$	Berthelsen & Faltinsen (2008)	0.200	1.37	0.046	0.70
	Calhoun (2002)	0.202	1.17	0.058	0.668
	Linnik & Fasel (2005)	0.197	1.34	0.040	0.69
	Liu *et al.* (1998)	0.192	1.31	0.049	0.69
	Russel & Wang (2003)	0.195	1.29	0.044	0.50
	Taira & Colonius (2007)	0.197	1.36	0.043	0.69
	Williamson (1989)[e]	0.197	-	-	-
	Present method	**0.199**	**1.31**	**0.045**	**0.67**

[e] experimental results.

3.3 Flow past a sphere

The simulation of flow past a stationary sphere is commonly used as the test case to validate the accuracy of a numerical method in solving three-dimensional flows (Fadlun *et al.*, 2000; Kim *et al.*, 2001; Mark & van Wachem, 2008). Simulations have been carried out at $Re_d = \{20, 100, 250, 300\}$, based on the sphere diameter d, and the far-field velocity U_∞, in order

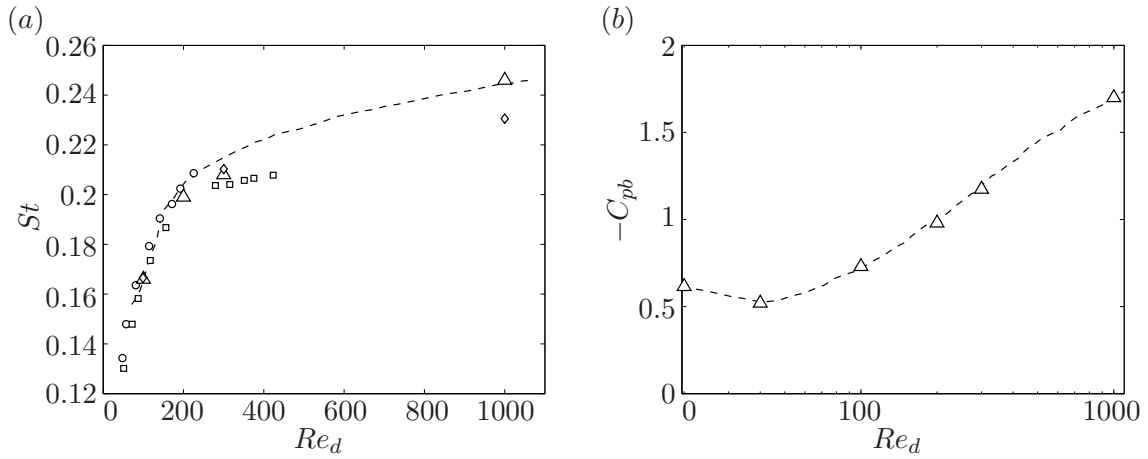


Figure 3-11: (a) Strouhal number and (b) base pressure coefficient at different Reynolds numbers. △, current method; - - -Ghias *et al.* (2007); ◊, Mittal *et al.* (2008); □, Williamson & Roshko (1990); ◯, Zhang *et al.* (1995).

to span the range of possible dynamics in the laminar regime. These consist of steady attached flow, steady axisymmetric flow, steady non-axisymmetric flow and unsteady flow. The objective is to verify that the method can accurately predict all of these flows and the transition from one regime to the other. The size of the domain used is $15d \times 15d \times 15d$, consistent with other studies in the literature (Marella *et al.*, 2005; Mittal *et al.*, 2008). A Cartesian grid is used, with cosine stretching in x and y, and uniform in z. The maximum stretching ratio is 1.008, and the grid spacing around the sphere is $\Delta x \approx 0.035$. Free-slip is imposed on the top and bottom boundaries and periodic boundary conditions are applied in the spanwise direction. Again, random perturbations are introduced in the initial field in order to trigger flow unsteadiness at the higher Re values.

The flow over a sphere is qualitatively similar to that over a cylinder. Figure 3-12 shows the vorticity contours and streamlines on an xy plane through the centre of the sphere for different Reynolds numbers. At low Reynolds numbers the fluid remains attached to the surface and there is no separation behind the sphere (see figures 3-12a and e). At $Re_d \approx 24$ a wake containing a standing ring-eddy, forms behind the sphere, which grows with Re_d.

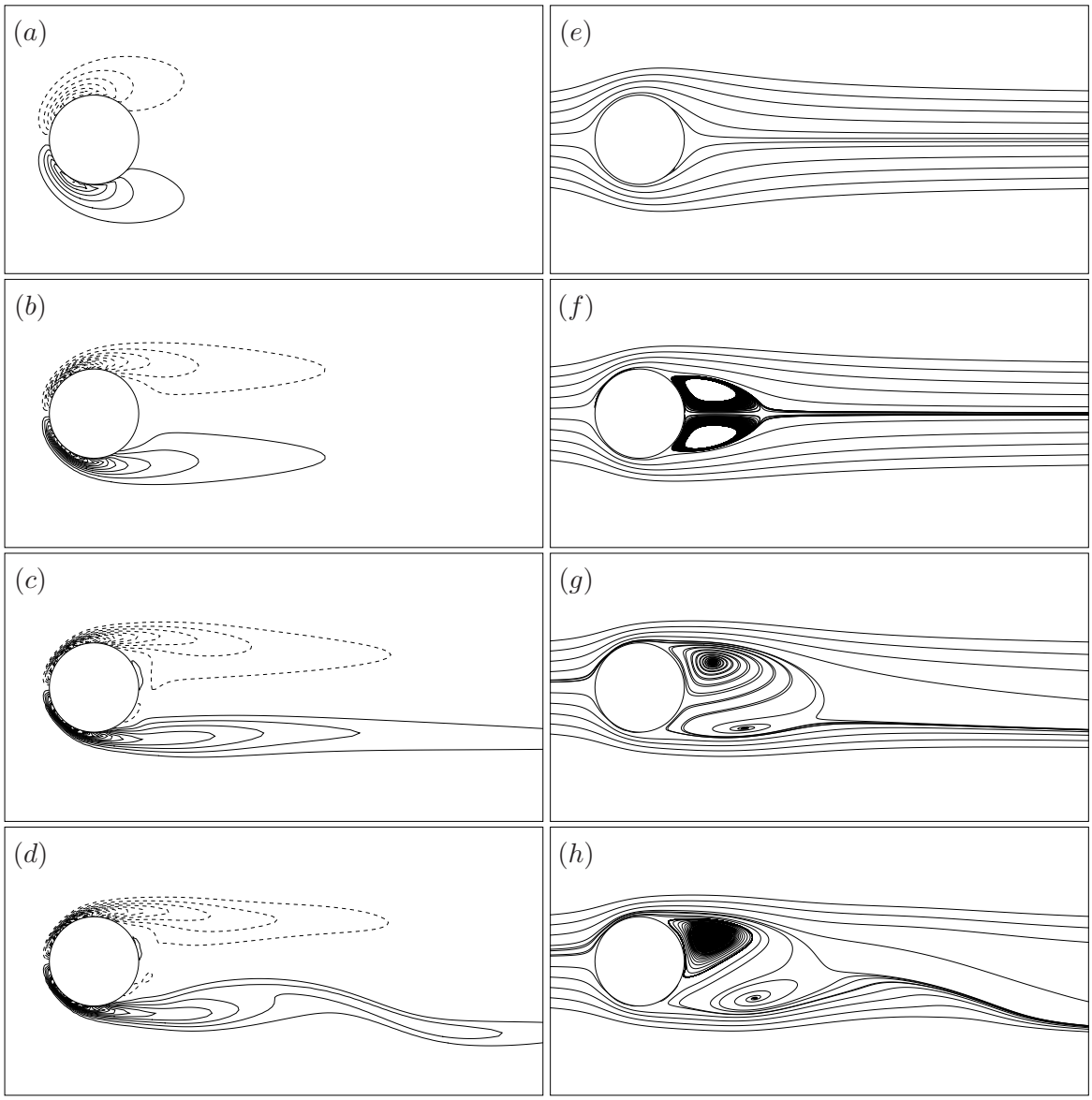


Figure 3-12: Flow at different Reynolds numbers in an xy plane through the centre of the sphere. At left, spanwise vorticity contours from -12.0 to 12.0 with intervals of 1.0, —, positive; - - -, negative. At right, streamlines.

Taneda (1956) observed a very faint periodic motion at the rear of the vortex ring beginning at $Re_d = 130$. The flow up until $Re_d = 210$ remains stable and axisymmetric with respect to the free-steam direction (figures 3-12b and f), after which it looses its axisymmetry as the vortices shift off-axis and a double-threaded wake develops at the rear of the sphere. The flow however does remain steady and it still contains one plane of symmetry.

Figures 3-12*c* and *g* show the asymmetric flow in the xy plane. The flow in the xz plane retains its symmetry. In order to quantitatively validate the results, the length of the separation bubble and the distance of the centres of the vortices from the centre of the sphere, cf. figure 3-13, are computed for the steady flow cases. These parameters are compared to results in previous studies in table 3.3, together with the drag coefficient, $C_D(t) = F_D(t)/\left(\frac{1}{2}\rho U_\infty^2 \pi d^2/4\right)$, at each Reynolds number. The Strouhal number and lift coefficient, $C_L(t) = F_L(t)/\left(\frac{1}{2}\rho U_\infty^2 \pi d^2/4\right)$, are also shown for the unsteady case.

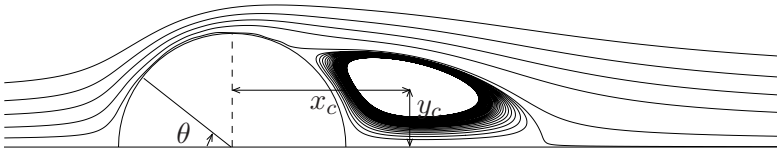


Figure 3-13: Nomenclature used in table 3.3.

Table 3.3: Comparison of experimental and numerical studies for flow over a sphere.

	Re	C_D	l/d	a/d	b/d	C_L	St
Johnson & Patel (1999)	100	1.08	0.88	0.75	0.29		
Kim *et al.* (2001)	100	1.087	-	-	-		
Marella *et al.* (2005)	100	1.06	0.88	-	-		
Mittal *et al.* (2008)	100	-	0.84	0.742	0.278		
Present method	**100**	**1.05**	**0.86**	**0.755**	**0.285**		
Johnson & Patel (1999)	250	0.701				-0.062	
Kim *et al.* (2001)	250	0.701				0.059	
Pan & Shen (2009)	250	0.696				0.0611	
Present method	**250**	**0.684**				**-0.062**	
Johnson & Patel (1999)	300	$0.656 \pm 3.5\times10^{-3}$				$-0.069 \pm 1.6\times10^{-2}$	0.137
Kim *et al.* (2001)	300	0.657				0.067	0.134
Marella *et al.* (2005)	300	0.621				-	0.133
Pan & Shen (2009)	300	$0.638 \pm 2\times10^{-3}$				$0.069 \pm 1.3\times10^{-2}$	
Present method	**300**	$\mathbf{0.641 \pm 3.45\times10^{-3}}$				$\mathbf{-0.065 \pm 1.3\times10^{-2}}$	**0.135**

Figure 3-14 shows the pressure coefficient and skin friction at $Re_d = 100$. The pressure coefficient has been plotted against boundary-fitted grid results; the close agreement between the two shows that the current method accurately represents the geometry and the

near-wall flow.

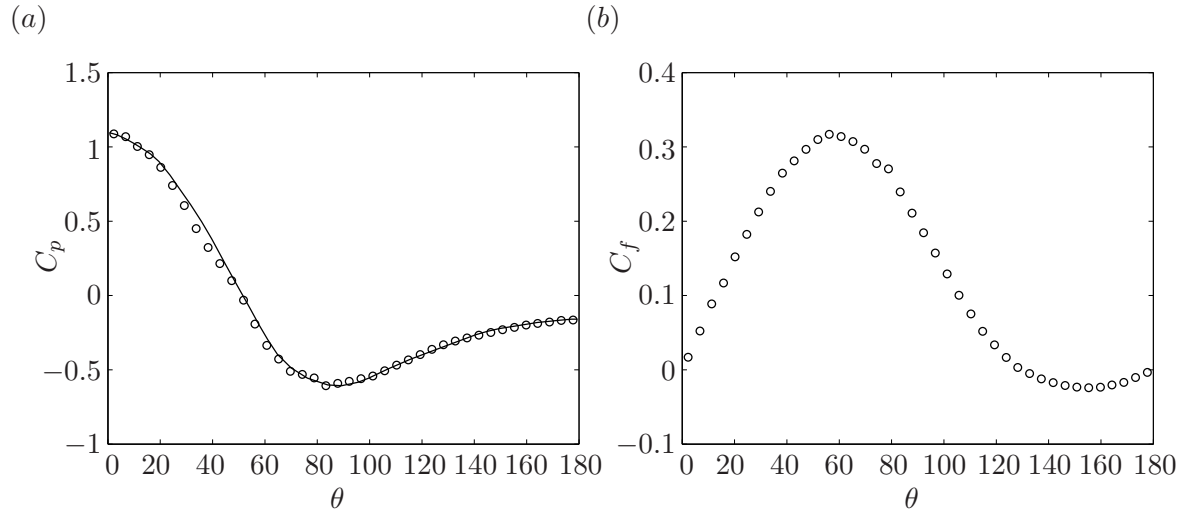


Figure 3-14: (a) Pressure coefficient and (b) skin friction for flow over a sphere at $Re_d = 100$. ○, current method; —, Johnson (1996).

Above $Re_d = 270$ the flow becomes unsteady and the wake begins to oscillate (figures 3-12d and h), eventually leading to vortex loops shedding from the sphere as 'hair-pin' vortices. Achenbach (1974) showed that these vortices are all shed in the same orientation, forming a 'ladder-like chain of overlapping loops'. A surprising observation made by Johnson & Patel (1999) is the fact that the planar symmetry is still present in the unsteady flow and that this symmetry plane remains fixed in time. Isosurfaces of the vortical structures behind the sphere will demonstrate this behaviour.

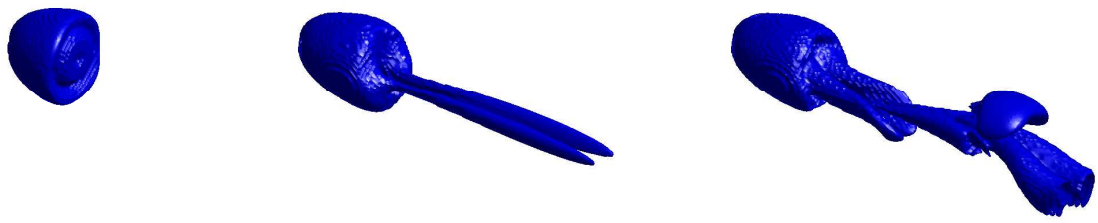
In order to visualize these vortical structures, the method proposed by Jeong & Hussain (1995) is employed. They define a vortex core as the region where a local pressure minimum occurs. For a local pressure minimum, the Hessian of pressure, $\nabla(\nabla p)$, should have two positive eigenvalues. Taking the gradient of the Navier-Stokes equations and expressing $\nabla \boldsymbol{u}$ in terms of its symmetric and antisymmetric components ($\nabla \boldsymbol{u} = S + \Omega$), where

$$S = \frac{1}{2}\left[\nabla \boldsymbol{u} + \nabla \boldsymbol{u}^T\right], \qquad \Omega = \frac{1}{2}\left[\nabla \boldsymbol{u} - \nabla \boldsymbol{u}^T\right]$$

yields the following equation for the Hessian of the pressure

$$-\nabla\left(\nabla p\right) = \frac{\partial S}{\partial t} + \frac{\partial \Omega}{\partial t} - \left(S+\Omega\right)\left(S+\Omega\right) - \nu\nabla^2\left(S+\Omega\right). \tag{3.3}$$

Jeong & Hussain (1995) state that unsteady straining can lead to a pressure minimum without the existence of vorticity and that viscous effects can eliminate pressure minima in a flow with vortical motion. Therefore, excluding the unsteady straining and the viscous terms and eliminating the vorticity transport equation from equation 3.3, leaves only $S^2+\Omega^2$. Thus, the vortical structure is defined by any point in the domain where the matrix $S^2+\Omega^2$ has two negative eigenvalues.



(a) (b) (c)

Figure 3-15: Vortical structures at (a) $Re_d = 100$, (b) $Re_d = 250$ and (c) $Re_d = 300$. Isosurface of $\lambda_2 = -0.002$. An instantaneous field is shown.

Figure 3-15 shows the three-dimensional vortical structures at $Re_d = \{100, 250, 300\}$. At $Re_d = 100$ it can be seen that the flow is axisymmetric and there are no vortical structures behind the sphere. At $Re_d = 250$ and 300, planar symmetry is present and the double-threaded wake behind the sphere and the chain of overlapping vortices are visible for the steady and unsteady cases respectively. Figure 3-16 shows the side and top views of the vortical structure at $Re_d = 300$, alongside those of Johnson & Patel (1999). These structures match those recorded in experimental studies and other numerical simulations,

indicating that the present method accurately determines the three-dimensional vorticity field.

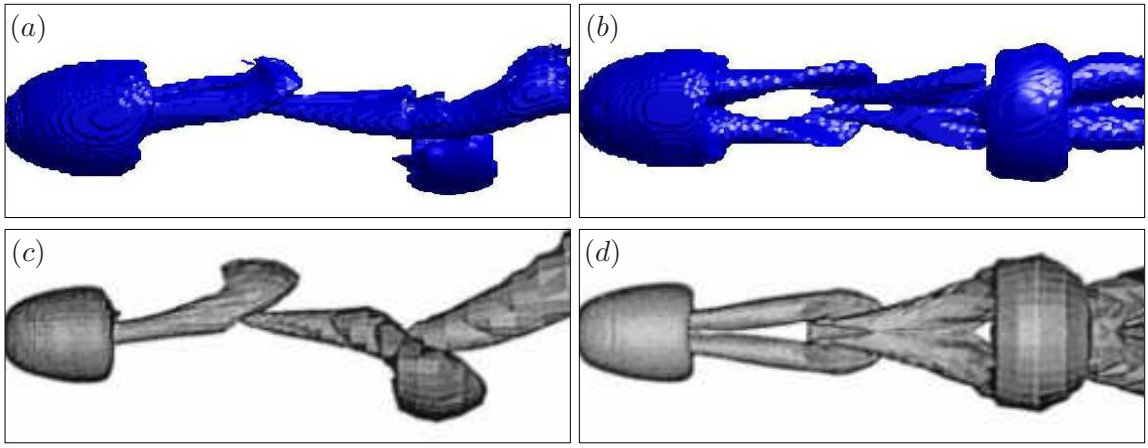


Figure 3-16: Vortical structure at $Re_d = 300$. xy view: (a) present method, (c) Johnson & Patel (1999). xz view: (b) present method, (d) Johnson & Patel (1999).

3.4 Flow in a wavy channel

Although the above test cases exhibit complex flow dynamics which are challenging to accurately reproduce in a numerical simulation, the range of Reynolds numbers considered lies within the laminar regime. Turbulent flows are more challenging to simulate accurately as the range of flow scales increases with Reynolds number (Pope, 2000), and fine grids are required in order to resolve the flow. In addition, the thin shear layers and high velocity gradients at the walls pose a greater challenge for non-conforming grid methods.

In order to evaluate the accuracy of the current method in the context of turbulent flows, the flow in a channel with a wavy wall is studied. The motivation for this test case, as opposed to turbulent flow in a flat channel, is two-fold: Firstly, the boundary is not aligned with the grid-lines and therefore is a more challenging test of the immersed boundary method; Secondly, the mean flow exhibits spatial variations which are not present

over a flat wall.

The computational domain and the grid used in the simulation are shown in figure 3-17. The simulation setup matches the experimental work of Hudson *et al.* (1996), the DNS of Maas & Schumann (1996) and Cherukat *et al.* (1998) and the LES of Balaras (2004). The height of the wavy wall, y_w, is given by

$$y_w = \alpha \cos\left(\frac{2\pi x}{\lambda_w}\right) + \alpha, \tag{3.4}$$

where α is the amplitude of the wave and λ_w is the wavelength. The wave slope is set to $2\alpha/\lambda_w = 0.1$ and the Reynolds number $Re_b = \frac{(H-\alpha)U_b}{\nu} = 6760$ is based on the mean channel height, $H - \alpha$, and the bulk mean velocity, U_b. At this Reynolds number, the mean flow separates from the bottom wall. The bulk velocity which is independent of the streamwise coordinates is given by

$$U_b = \frac{1}{H-\alpha}\int_{y_w}^{H} \bar{u} dy, \tag{3.5}$$

where $\bar{u}$ is the streamwise velocity averaged in time and in the spanwise direction.

The domain size in the streamwise and spanwise directions is twice the wavelength of the wavy wall. No-slip conditions are enforced at the top and bottom walls and periodic boundary conditions are applied in the streamwise and spanwise directions. A Cartesian grid with $512 \times 384 \times 192$ points in the three coordinate dimensions is employed. The grid points are clustered near the top and bottom boundaries by applying a hyperbolic tangent stretching in the wall-normal direction, in order to resolve the near-wall shear. Also note that the grid resolves the separated shear layer near the bottom wall.

In order to generate a fully-developed turbulent field, the flow is initially simulated at a constant mass flow rate from an initial field consisting of the Poiseuille flow profile along

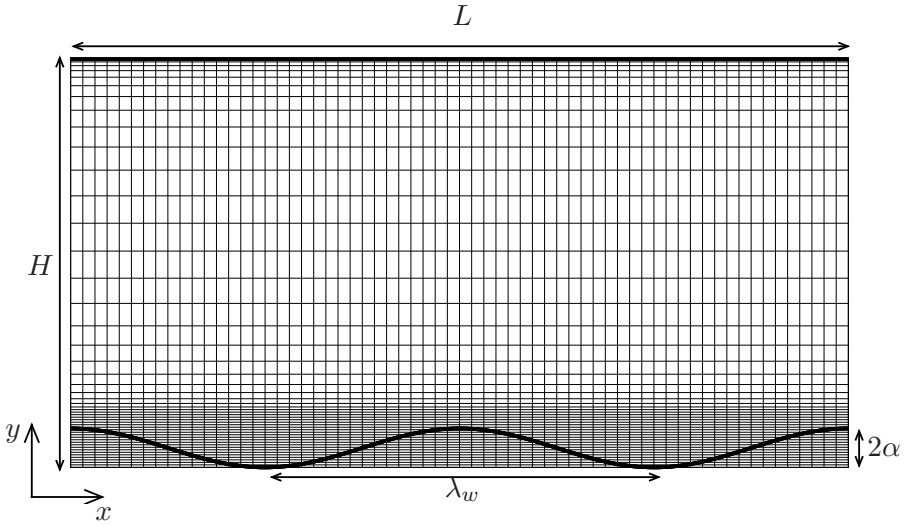


Figure 3-17: Computational domain and grid used for the flow in a wavy channel: Every eighth grid line is shown.

with random velocity perturbations. Transition to turbulence is determined by monitoring the time evolution of $Re_\tau = \frac{u_\tau h}{\nu}$, the Reynolds number based on the shear velocity u_τ at the top wall and the channel half-height $h = (H - \alpha)/2$. Figure 3-18 shows the variation of Re_τ as a function of time. The mean friction velocity at the top wall is $u_\tau = 0.070U_b$, which compares favourably to the values obtained by Maas & Schumann (1996), $u_\tau = 0.070U_b$, and Cherukat *et al.* (1998), $u_\tau = 0.0705 - 0.0716U_b$. Once the flow has reached a

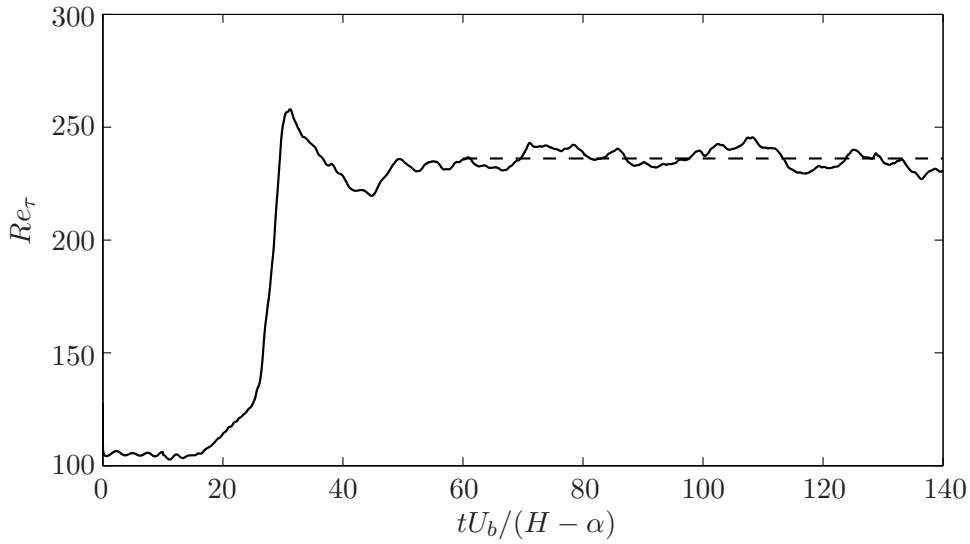


Figure 3-18: Temporal variation of the Reynolds number based on friction velocity, Re_τ.

statistically-stationary state, averaging is performed in time and in the spanwise direction in order to obtain the mean properties. The flow near the separation and reattachment points is characterized by large-scale structures and low frequency unsteadiness. The large characteristic time scales of these structures and the unsteady, complex flapping motion cause very slow statistical convergence in the separated and reattachment zones. Therefore, averaging needs to be carried out over many convective time scales in order to obtain converged statistics. Statistics are collected over a time period $tU_b/(H-\alpha) = 90$.

Figure 3-19 is a side view showing contours of the instantaneous spanwise vorticity at a plane in the middle of the span. The thin accelerating boundary layer which develops downstream of the separation region and the separated shear layer breaking off from the wall at the crest can be observed. The vortical structures that are present near the wavy wall can be seen in figure 3-20. They are strong quasi-streamwise vortices which develop downstream of the reattachment point (De Angelis *et al.*, 1997).

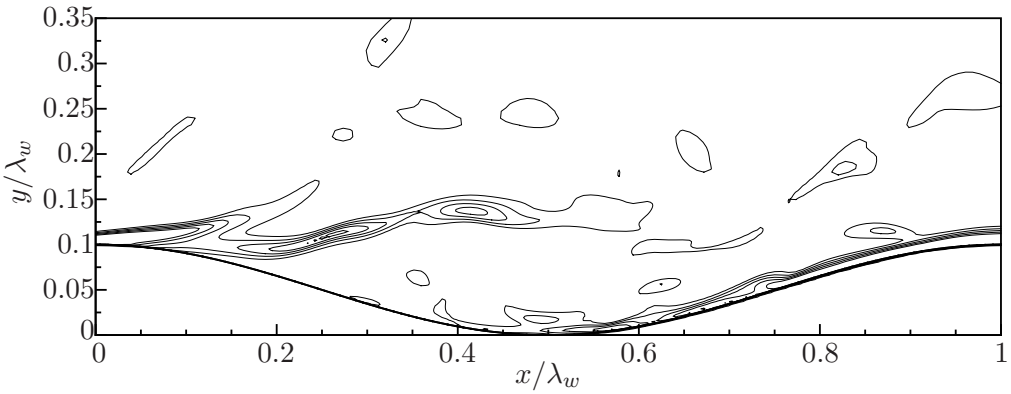


Figure 3-19: Instantaneous spanwise vorticity contours from -40.0 to -8.0 with increments of 8.0.

Contours of the mean streamwise and wall-normal velocities normalized by the bulk velocity at the inlet U_{in} are plotted in figure 3-21. Comparison with the literature (Cherukat *et al.*, 1998; Balaras, 2004) shows that the general dynamics of the flow are well predicted.

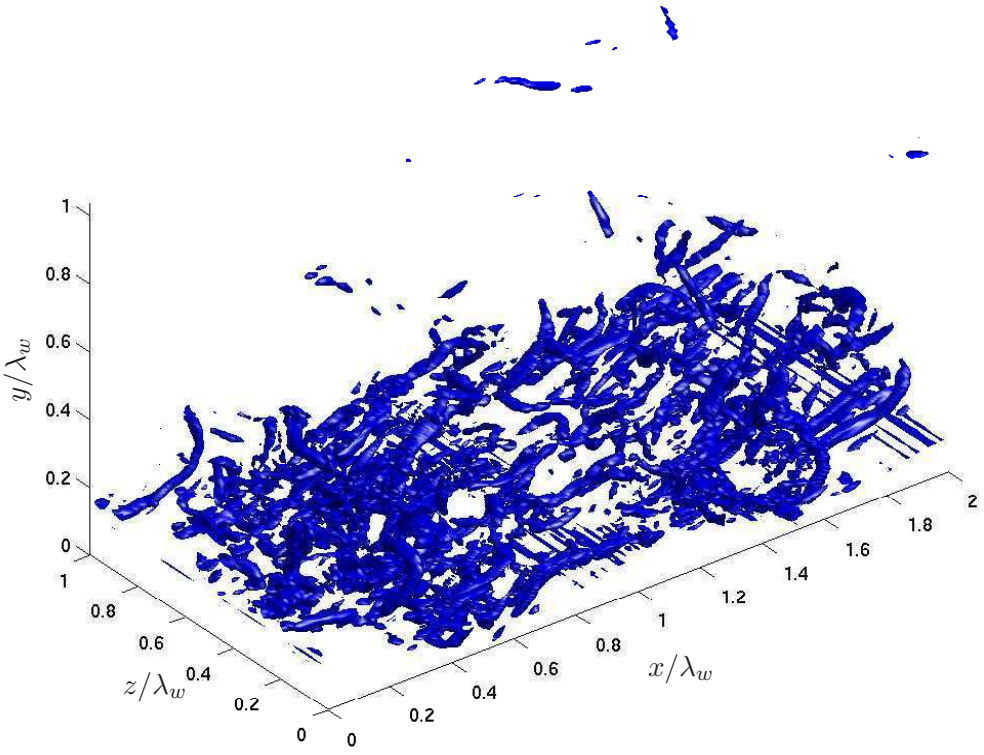


Figure 3-20: Vortical structures over wavy wall, visualized using an isosurface of $\lambda_2 = -75$.

The flow separates downstream of the crest, forming a recirculation region. After reattachment, downstream of the trough, the flow accelerates as it is deflected upwards by the wavy wall. The thin accelerating boundary layer can be seen in the contours of u velocity.

The location of the separation and reattachment points are shown in table 3.4 alongside values reported in the literature. Good agreement with previous studies is observed. Contours of the Reynolds shear stress $-\rho\overline{u'v'}$ normalized by ρU_{in}^2 are shown in figure 3-22. High shear stress, associated with the separated shear layer, develops downstream of the crest. The maximum value is found roughly above the trough and a region of negative Reynolds stresses occurs near the surface between $x/\lambda_w = 0.55$ and $x/\lambda_w = 1.0$, which is consistent with the results reported in the literature (Hudson *et al.*, 1996; Cherukat *et al.*, 1998; Balaras, 2004).

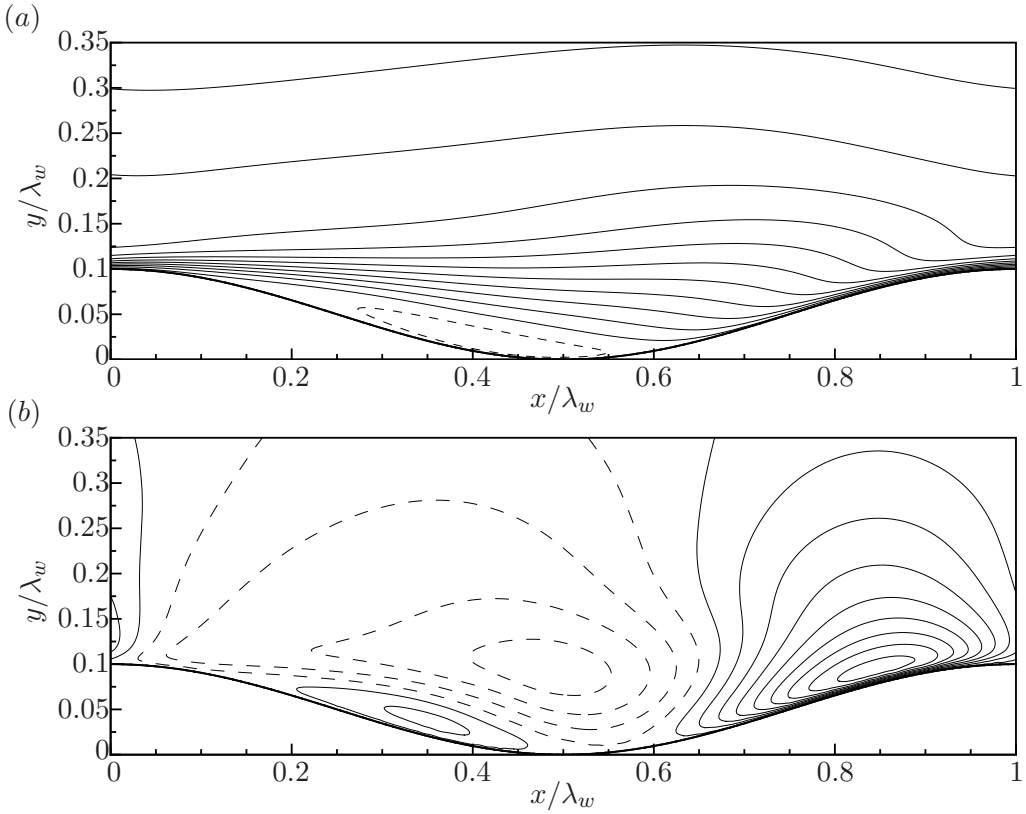


Figure 3-21: Contours of mean velocities normalized by U_{in}. (a) Streamwise velocity; (b) wall-normal velocity.

Table 3.4: Comparison of experimental and numerical studies for flow over a wavy wall.

	separation point (x/λ_w)	reattachment point (x/λ_w)
Hudson (1993)	0.22	0.58
Maas & Schumann (1996)	0.14	0.60
Cherukat *et al.* (1998)	0.14	0.59
Balaras (2004)	0.145	0.61
Present method	**0.135**	**0.61**

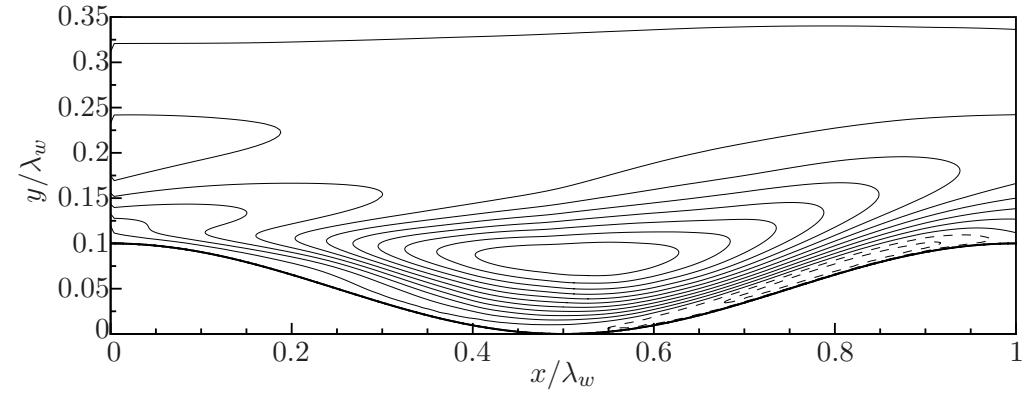


Figure 3-22: Contours of Reynolds shear stress normalized by ρU_{in}^2.

The mean streamwise velocity at different streamwise locations along the channel, normalized by the bulk velocity U_b, are shown in figure 3-23. The profiles are plotted alongside the DNS results of Maas & Schumann (1996) and of Cherukat *et al.* (1998), and very good agreement can be observed. Profiles of the mean wall-normal velocities are shown in figure 3-24. Some discrepancy is seen at $x/\lambda_w = 0.5$ and $x/\lambda_w = 0.7$, which are located in the separation region and downstream of the reattachment point, respectively. This can be attributed to the large variation of the flow in the separation and reattachment zones at any given time which requires averaging over a long time period in order to obtain converged statistics. Cherukat *et al.* (1998) averaged their data over a period $tU_b/(H-\alpha) = 5$ which did not prove to be sufficient for statistical convergence in our study. The wall-normal velocity at the trough is particularly sensitive as the location of the peak velocity, which lies in the separated shear layer, fluctuates in time and is characterized by a very large time scale. The turbulence intensities at the crest and trough plotted in figure 3-25 are in very good agreement with those of Cherukat *et al.* (1998).

Turbulent flow over a wavy wall exhibits complex features which are challenging to predict accurately. Four regions can be distinguished over each wave: an outer region, a separated shear layer, a recirculation zone and a thin accelerating boundary layer downstream of reattachment. In addition, the locations of the separation and reattachment points are not fixed but fluctuate significantly with time. The large time scales associated with this unsteady motion pose a further challenge. The current results, which show all the important features in the flow, demonstrate good agreement of statistical quantities with body-conforming grid simulations from the literature, and thus the accuracy of the herein developed IB method for complex turbulent flows.

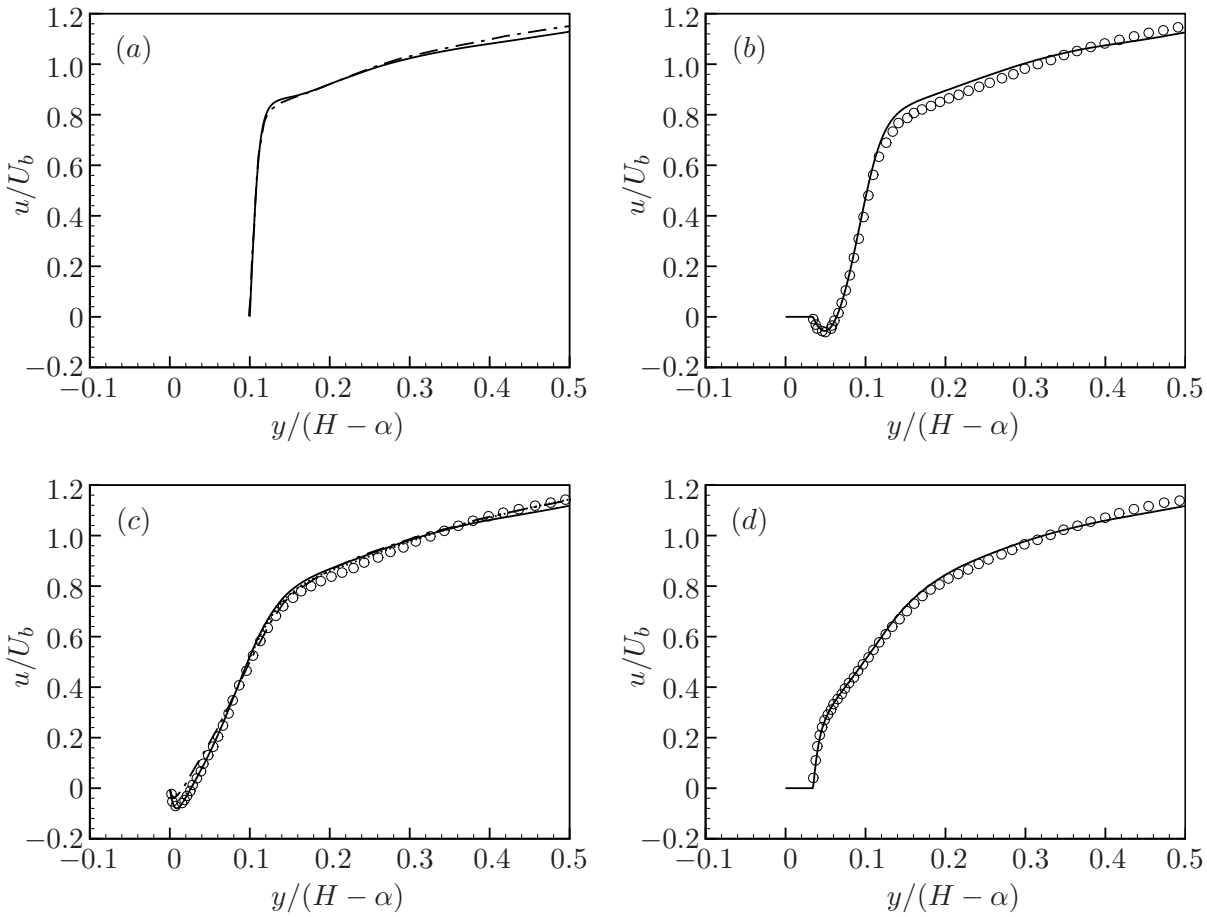


Figure 3-23: Mean streamwise velocity profiles at different streamwise locations. —, current method; - - -, Cherukat *et al.* (1998); ∘, Maas & Schumann (1996). (*a*) $x/\lambda_w = 0.0$; (*b*) $x/\lambda_w = 0.3$; (*c*) $x/\lambda_w = 0.5$; (*d*) $x/\lambda_w = 0.7$.

3.5 Flow in a square duct with strong curvature

Flow in a square duct with a 90° bend is simulated to validate the immersed boundary method on curvilinear coordinates. It also serves as a test case for internal flows and bears resemblance to the more complex simulation of flow in the extrathoracic airways that we wish to conduct; both flows being influenced by centrifugal forces due to the presence of strong curvature. Therefore, we expect the general characteristics of the flows to be similar, both generating a large secondary flow and exhibiting movement of fluid away from the inner wall of the bend and towards the outer wall.

The top and bottom walls of the duct are modelled as immersed boundaries whilst the

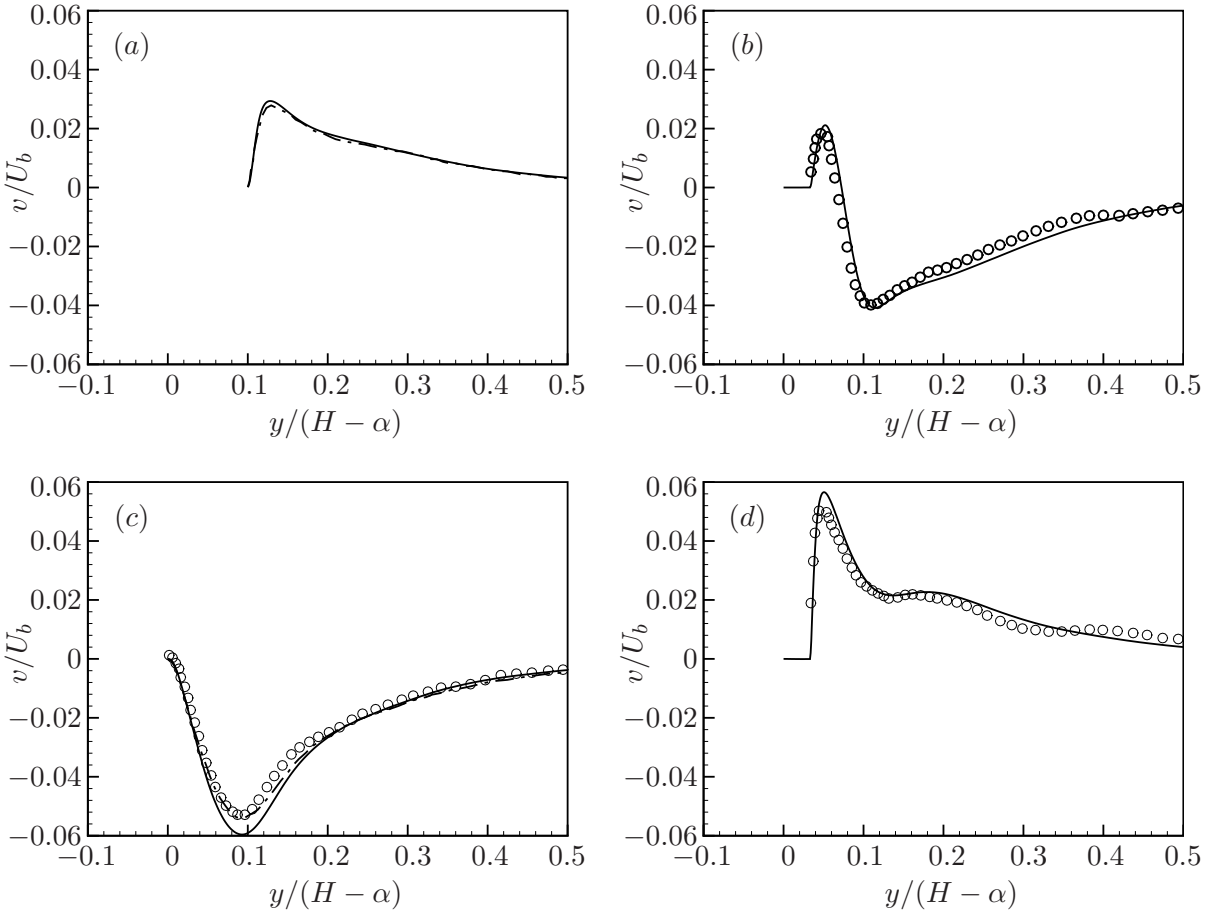


Figure 3-24: Mean wall-normal velocity profiles at different streamwise locations. —, current method; - - -, Cherukat *et al.* (1998); ∘, Maas & Schumann (1996). (*a*) $x/\lambda_w = 0.0$; (*b*) $x/\lambda_w = 0.3$; (*c*) $x/\lambda_w = 0.5$; (*d*) $x/\lambda_w = 0.7$.

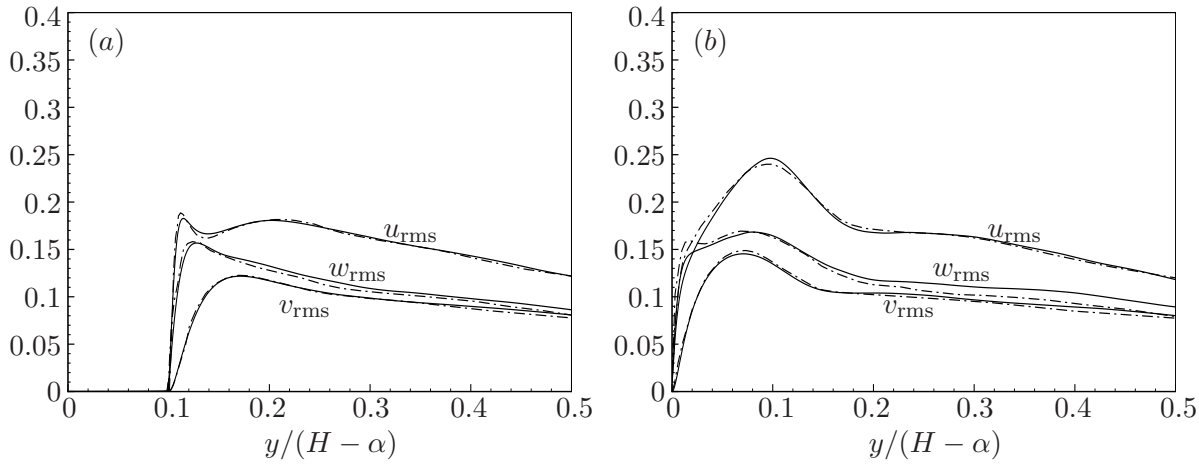


Figure 3-25: Turbulence intensities. —, current method; - - -, Cherukat *et al.* (1998). (*a*) $x/\lambda_w = 0.0$ (crest); (*b*) $x/\lambda_w = 0.5$ (trough).

spanwise walls lie on the domain boundaries, and hence coincide with the grid points. A $512 \times 192 \times 128$ non-uniform curvilinear grid is employed, with stretching in the cross-flow η direction to minimize the number of un-used grid points outside the duct and stretching in the streamwise ξ direction to provide a higher resolution inside the bend. The geometry and the grid used are shown in figure 3-26. The simulation is run at $Re_d = 790$, based on the hydraulic diameter and bulk velocity, for comparison with experimental and numerical data available in the literature (Humphrey *et al.*, 1977; Rosenfeld *et al.*, 1991; Rogers & Kwak, 1991). In addition, the simulation is also carried out on a boundary-fitted grid with the same resolution for direct comparison with the immersed-boundary case. The fully-developed laminar profile of flow in a straight square duct given by equation 3.6 is specified at the inlet and convective outflow conditions are applied at the exit.

$$\begin{aligned} u(y,z) &= \frac{48}{\alpha\pi^3}\beta(y,z) \\ \alpha &= 1 - \frac{192d}{\pi^5}\sum_{i=1,3,5,\ldots}^{\infty}\frac{tanh(\frac{\pi i}{2d})}{i^5} \\ \beta(y,z) &= \sum_{i=1,3,5,\ldots}^{\infty}(-1)^{\frac{i-1}{2}}\left[1 - \frac{cosh(2z\frac{\pi i}{2d})}{cosh(\frac{\pi i}{2d})}\right]\frac{cos(2y\frac{\pi i}{2d})}{i^3} \end{aligned} \tag{3.6}$$

Flow in ducts with strong curvature develops significant secondary flow and re-distribution of the streamwise velocity due to centrifugal forces. Figure 3-27 shows contours of the streamwise velocity and cross-flow velocity vectors at three streamwise locations inside the bend. At $\theta = 30^\circ$ the high velocity fluid has shifted from the centre of the duct towards the outer wall. This trend intensifies further along the bend and is accompanied by a move towards the side walls induced by the strong secondary velocities. This causes the fluid to swirl, bringing some of the high velocity fluid near the inner wall.

This behaviour can also be observed in figure 3-28 which shows the streamwise velocity

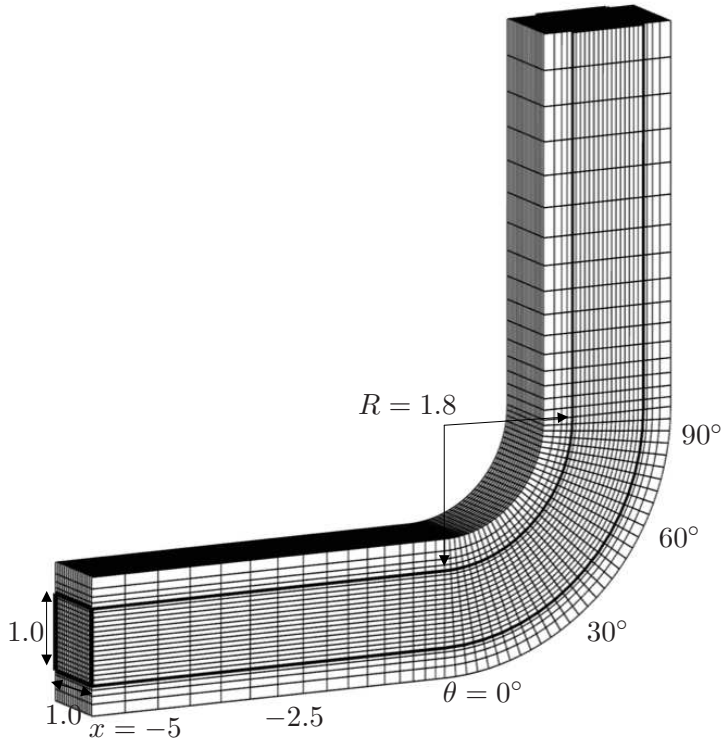


Figure 3-26: The geometry and the grid for the square duct with a 90° bend.

profiles at different cross-flow planes along the bend at $z = 0.5$, which is the xy symmetry plane, and at $z = 0.25$ which is half-way between the xy wall and the symmetry plane. The velocity has been normalized by the bulk velocity of the flow. It can be seen that there is a very good agreement between numerical results, and in particular a very good match of the immersed boundary results with the data of Rogers & Kwak (1991), obtained using a body-fitted grid. Some discrepancy between numerical and experimental results exists near the inner wall in the downstream locations. The maxima in velocity near the inner wall observed in the profiles are generated by the swirling motion of the fluid. Rogers & Kwak (1991) attributed the discrepancy in results to the high sensitivity of the swirling mechanism to Reynolds number and turbulent dissipation, claiming that a small deviation from the Reynolds number or a small amount of turbulence present in the flow would be sufficient to account for these differences.

These results show the complexity of the flow, and the agreement of the data so far with boundary-fitted results provides confidence that the immersed boundary method is capturing the flow characteristics accurately. The behaviour close to the wall also needs to be examined in order to ensure that the interpolation applied near the immersed boundary maintains the correct pressure and velocities. For this, the coefficient of friction C_f, and the pressure coefficient C_p are computed along the inner and outer walls of the bend (see figure 3-29). The only results available in the literature are those from the numerical simulation carried out by Humphrey *et al.* (1977). However, due to computational limitations, the grid employed in that work was not sufficiently refined to fully resolve the flow. Therefore a boundary-fitted grid simulation is performed at the same resolution as the IB case, for direct comparison of the results. The immersed boundary results are in very good agreement with the boundary-fitted predictions thus demonstrating the accuracy of the immersed boundary method near the walls where the forcing is applied.

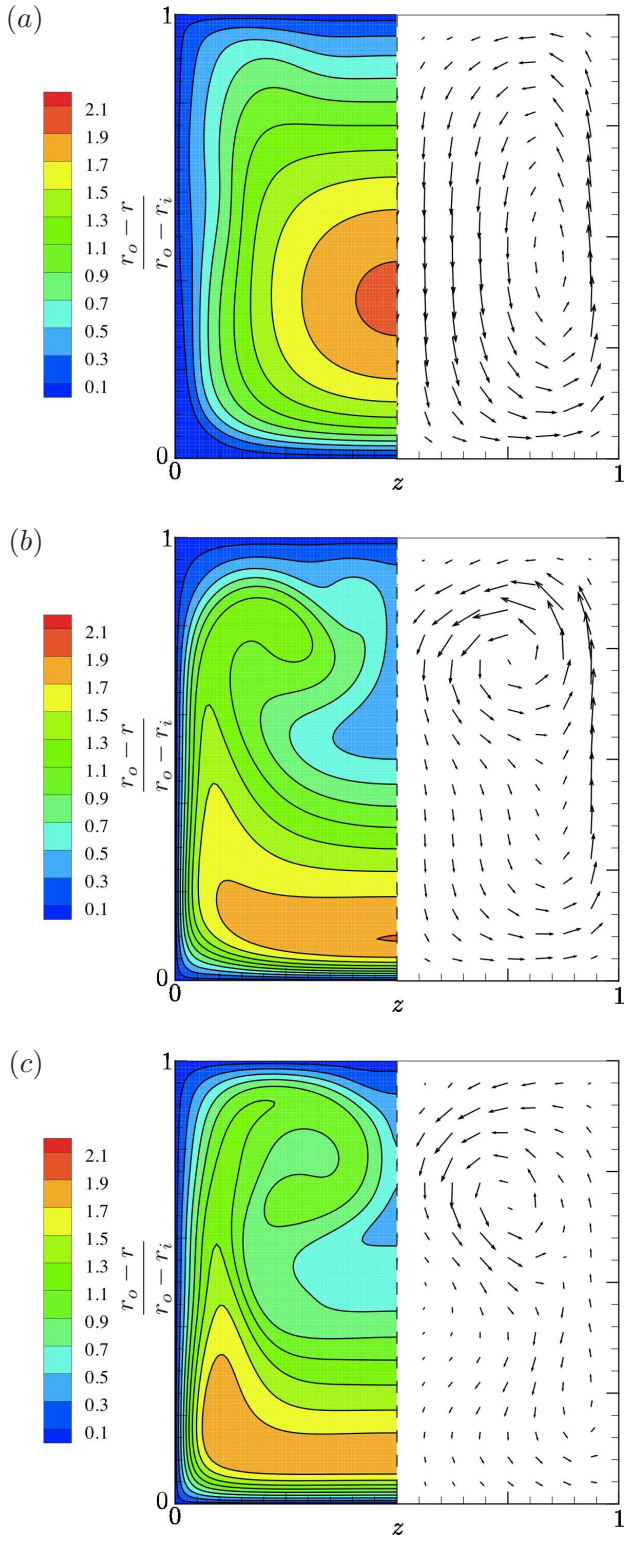
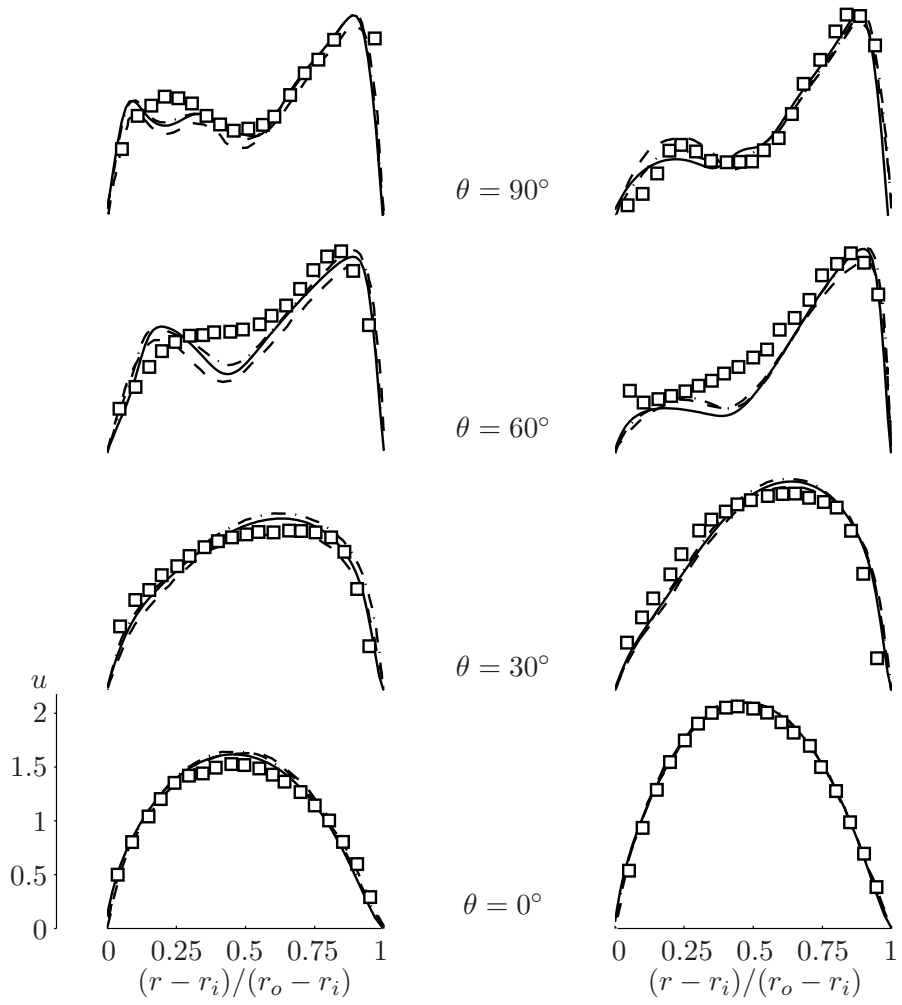


Figure 3-27: Streamwise velocity contours and secondary velocity vectors at three different cross-flow planes inside the bend. (*a*) $\theta = 30°$, (*b*) $\theta = 60°$ and (*c*) $\theta = 90°$.



(a) (b)

Figure 3-28: Streamwise velocity profiles at different crossflow planes along (a) $z = 0.25$ and (b) $z = 0.5$. —, current method; - - - Rosenfeld *et al.* (1991); - · - · Rogers & Kwak (1991); □ Humphrey *et al.* (1977).

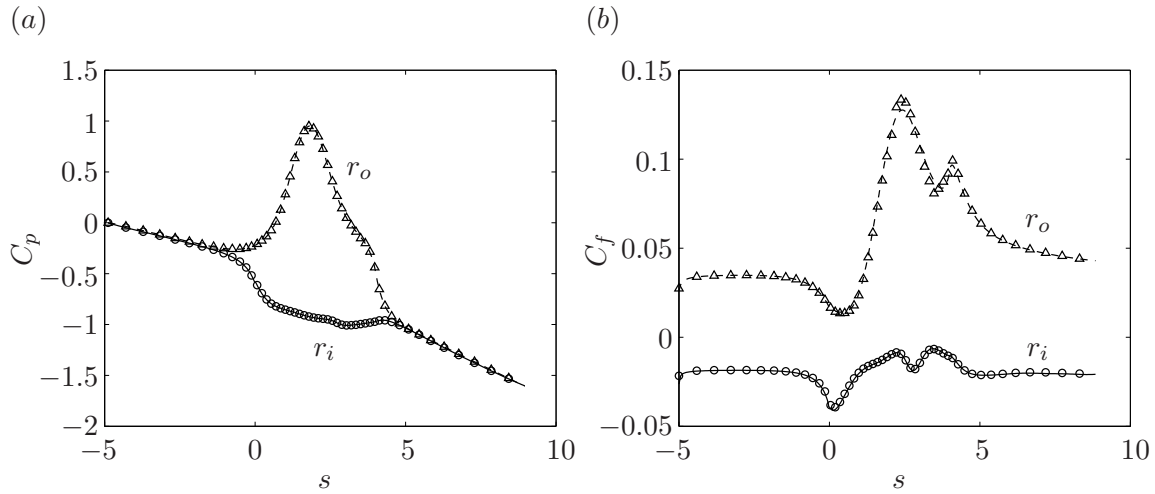


Figure 3-29: (a) Pressure coefficient and (b) skin friction along the centreline of the inner and outer walls of the bend. —, - - -, boundary-fitted; ×, + , immersed boundary.

Chapter 4

Flow and particle deposition in the extrathoracic airways

This chapter presents the flow fields and deposition efficiencies in a set of four realistic mouth and throat geometries obtained from MRI scans. The effect of geometric variation on the flow and on the particle deposition is examined. First, a description of the geometries used in this study is given. Then the computational grids and the boundary conditions used in the direct numerical simulations are described. The flow fields in each geometry are then presented. Contours of the velocity magnitude and the turbulent kinetic energy as well as streamlines in all four models are shown and are discussed in the context of particle deposition. The total and regional deposition fractions for the different-sized particles injected into the flow are then listed for the various geometries and the deposition efficiencies are compared to *in vitro* data. The scatter observed when the data is plotted against the Stokes number is reduced using an empirical Reynolds number correction. The physical significance of this empirical correction is explained by inspection of the particle relaxation time.

4.1 Geometries of the extrathoracic airways

A set of four physiologically realistic mouth and throat geometries were used in this study. They are a subset of the geometries used by Grgic *et al.* (2004*b*) for *in vitro* measurements of particle deposition. The anatomically accurate models were obtained using magnetic resonance imaging (MRI). The methodology is explained in detail in McRobbie *et al.* (2003). The MRI scans were converted to 3D volume files from which STL models were generated. These STL files were later used to manufacture the casts used in the *in vitro* studies. The geometries can be divided into four sub-regions (see figure 4-1):

A. The mouth region from the back of the teeth to the soft palate.

B. The nasopharynx region incorporating the nasal airways to the tip of the epiglottis.

C. The larynx, from the tip of the epiglottis to just below the vocal cords.

D. The trachea to a point two vertebrae below the vocal cords.

The geometries studied here will be named S1a, S1b, S2 and S4, keeping with the notation used by Grgic *et al.* (2004*b*). They are shown in figure 4-2. Cases S1a and S1b represent the same subject and correspond to different configurations: In S1a, the tongue is pulled back creating a large mouth opening and reducing the size of the nasopharynx whereas in S1b, the tongue is in the forward position touching the back of the teeth, creating a much smaller oral cavity and a wider nasopharynx. Models S2 and S4 belong to different individuals, both with large oral cavities. In S2, the mouth narrows at the back and the pharynx is wider. S4 has a wider mouth and a narrow pharynx with a bending angle close to 90°. The choice of geometries allows us to investigate the effect of both intrasubject and intersubject geometric variation on the flow and deposition patterns.

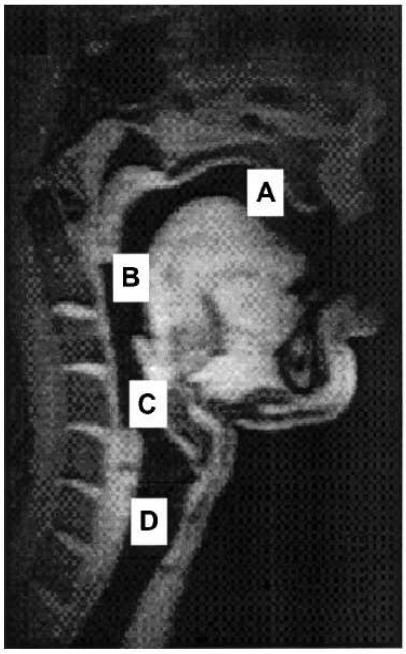


Figure 4-1: Sub-regions of the mouth-throat shown on the sagittal plane (McRobbie *et al.*, 2003).

Before they could be used, the STL models of the mouth and throat geometries required editing. The downstream region near the outflow was extended vertically (see § 4.3.2 for discussion), and an inlet pipe of the same dimension as the one used in the *in vitro* study was added at the entrance to the oral cavity. The modified geometries are shown in figure 4-3.

The main dimensions of the models are listed in table 4.1. In order to calculate the sagittal length, the geometries were split along the central sagittal plane. Because the geometries are not symmetrical, the mid-plane was chosen such that the two halves of the geometry contained approximately half the volume of the model each. Once cut, the path line along the centre of the geometry was measured on that plane, in order to determine the length. Assuming a circular mean cross-sectional area, an equivalent mean diameter was derived for each model,

$$D_{mean} = 2\sqrt{\frac{V}{\pi L}}. \tag{4.1}$$

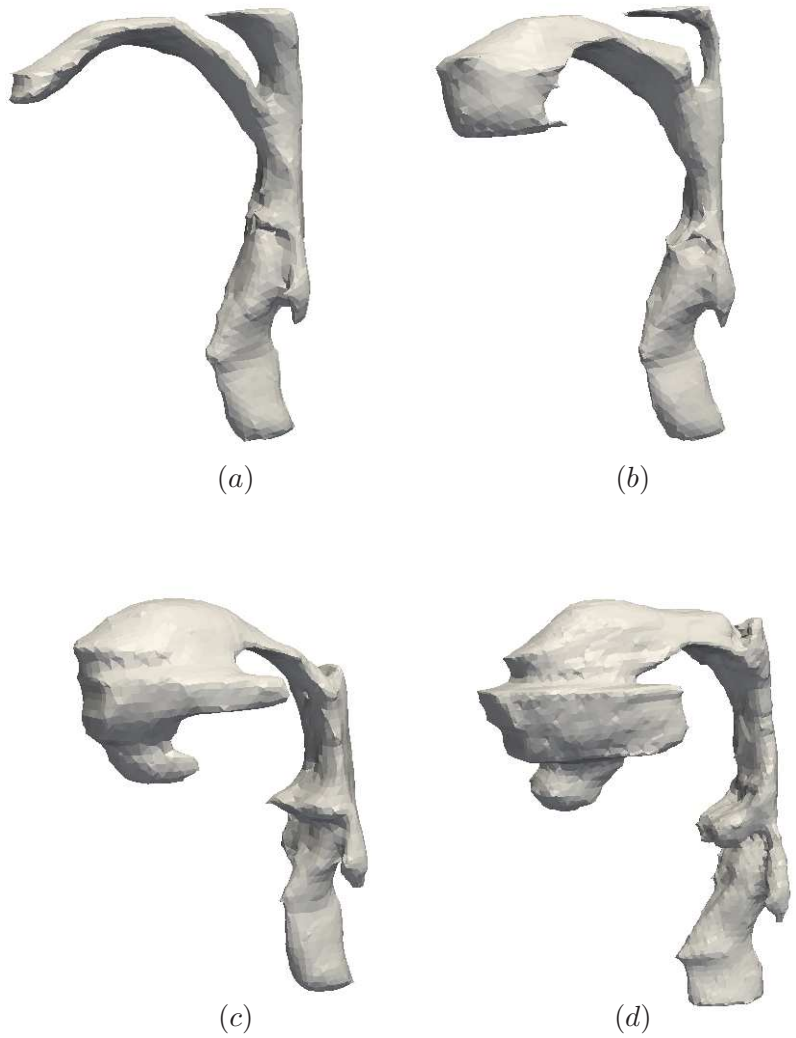


Figure 4-2: Extrathoracic airway geometries: (a) S1b, (b) S1a, (c) S2, (d) S4.

For all but S1b, D_{inlet} refers to the diameter of the circular tube at the entrance to the mouth, which is the same diameter as the tube used in the *in vitro* studies. Inserting an inlet tube in geometry S1b, however, would require a much smaller diameter than the one specified in Grgic *et al.* (2004*b*) and would therefore lead to a much higher inlet Reynolds

Table 4.1: Major dimensions of the models used.

Model	S1a	S1b	S2	S4
D_{inlet} (cm)	1.30	1.27	2.30	2.30
$Volume$ (cm^3)	51.56	33.80	99.30	82.60
$Length$ (cm)	19.1	18.5	18.6	19.1
D_{mean} (cm)	1.85	1.50	2.37	2.37

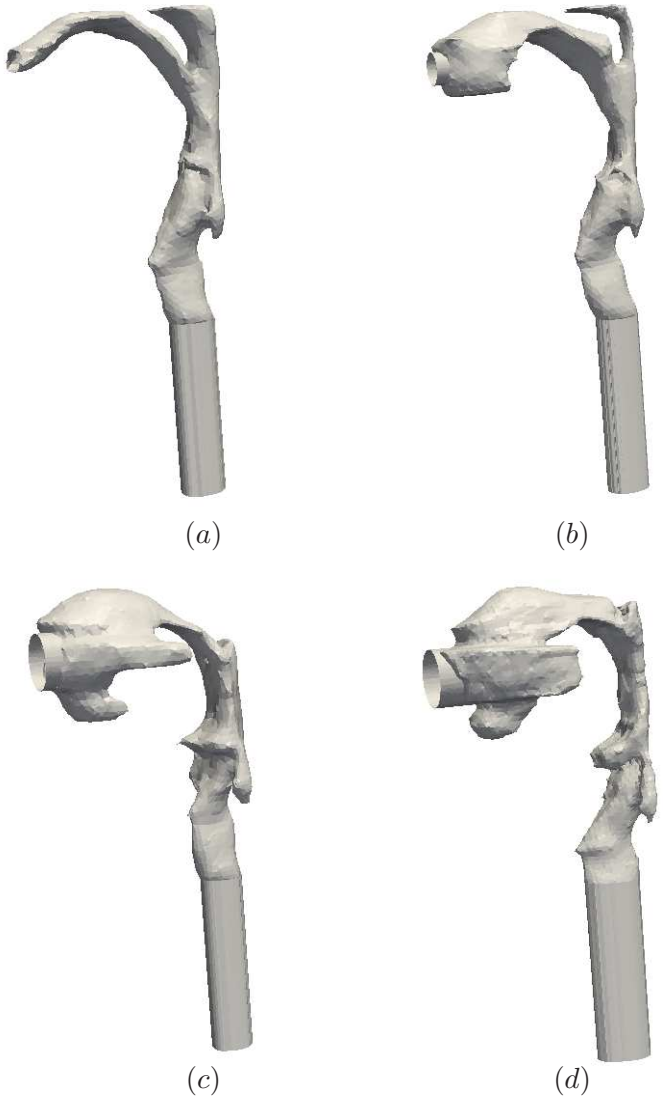


Figure 4-3: Modified geometries used in the DNS: (a) S1b, (b) S1a, (c) S2, (d) S4.

number for the same mass flow rate. Since the cross-sectional area of the mouth inlet is roughly that of a circular pipe of the same diameter as the inlet tube used in the *in vitro* measurements, the inflow for that particular geometry is applied over the entire mouth inlet in order to keep the inflow conditions as similar as possible to the experiments. Therefore, for model S1b, D_{inlet} refers to the equivalent diameter of the mouth inlet.

4.2 Computational grids

In order to accurately resolve the flow, a high grid resolution is required inside the geometries. Due to the shape of the extrathoracic airways, the use of Cartesian grids leads to many wasted grid points outside the flow domain. Even when grid stretching is applied, it is difficult to cluster the points efficiently inside the geometry. For turbulent flow, which is the case at the flow rates considered herein, the resolution requirements become prohibitively expensive. A more efficient alternative therefore is to use a curvilinear grid that roughly follows the shape of the geometry. This greatly reduces the number of points outside the geometry, allowing a much better resolution with a smaller grid than would be required in the Cartesian case. An added advantage of this grid is that the grid lines are approximately aligned with streamlines, which is favourable from a numerical accuracy point of view as this tends to reduce numerical diffusion.

The accuracy of the solution depends as much on the grid as on the discretization scheme used to solve the flow equations. It is therefore important to achieve the best grid quality possible. In addition to the alignment of the grid lines with the flow, the other three main desirable properties of a grid are orthogonality, smoothness and uniformity of spacing. A high grid skewness can cause unphysical solutions as it leads to larger errors from increased truncation errors from the cross-derivative terms and increased temporal discretization errors from the explicit treatment of these terms. The smoothness, which is a measure of the continuity of a grid line and its first derivative, and the length ratio affect the accuracy of the finite-difference approximations. Departure of these two properties from unity has an adverse effect on accuracy (Perić, 1985).

The grids are created using elliptic grid generation. First a central domain whose boundaries roughly follow the direction of the flow is generated in the region where the

highest grid resolution is required. Then it is extended to create two outer domains on either side, where the grid is stretched in the wall normal direction using a hyperbolic tangent function, in order to minimize the number of points outside the geometry. In the streamwise direction, the elliptic solver distributes the points such that the grid is orthogonal at the boundaries and as smooth and orthogonal as possible in the interior of the domain. The grid spacing and the angle on either side of the shared boundaries are kept constant in order to provide a smooth grid between domains.

The grid for one of the geometries is shown in figure 4-4. The grid spacing is $\Delta\xi = 0.01-0.08$, $\Delta\eta = 0.002 - 0.008$, $\Delta z = 0.0094$. The maximum length ratios are $\Delta\xi_i/\Delta\xi_{i-1} = 1.2$ and $\Delta\eta_j/\Delta\eta_{j-1} = 1.1$ and the minimum skewness equiangle is 0.83, which is outside the geometry.

4.3 Boundary conditions

Free-slip conditions are applied at the top, bottom, front and back boundaries of the global domain in order to avoid any boundary layers growing which might affect the solution inside the geometry. The properties of the free-slip boundary conditions are (1) no wall-normal flow and (2) no shear stress. Therefore the velocity field must be tangent to the global boundaries of the computational domain,

$$\boldsymbol{u} \cdot \boldsymbol{n} = 0. \tag{4.2}$$

The free-stress boundary conditions are enforced on the fluxes, which is accurate as long as the grid is orthogonal to the global domain boundaries. No-slip conditions are applied at the immersed boundary.

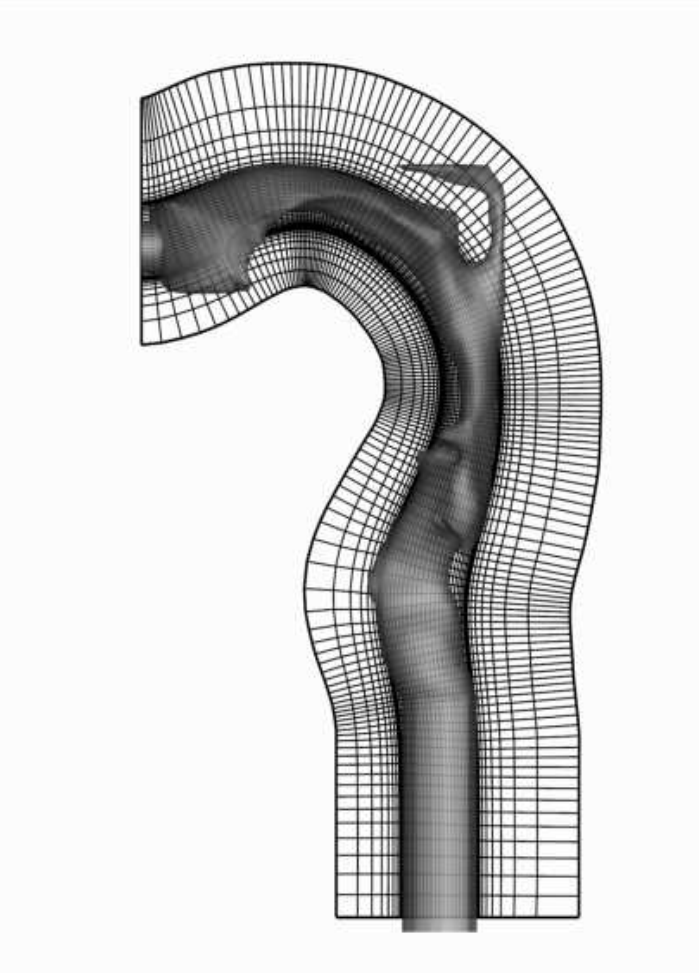


Figure 4-4: Grid used for model S1a, showing the geometry and the three domains of the grid. Every fourth grid line in ξ and eighth grid line in η has been plotted.

4.3.1 Inflow condition

At the inlet boundary, a number of different inflow conditions can be applied in order to reproduce experimental conditions. In the case of laminar flow through the inlet pipe (geometries S2 and S4), a parabolic velocity profile is prescribed. For S1b, a uniform flow is applied over the entire mouth inlet. In the case of S1a where the flow in the inlet tube is turbulent, accurate turbulent inflow conditions are required. For this, a separate direct numerical simulation of flow in a pipe is carried out at the same Reynolds number as that at the inlet to the S1a geometry, $Re_d = 3222$. This corresponds to $Re_\tau = 117$, based on the friction velocity and the radius of the pipe. The pipe simulation is performed in cylindrical coordinates (z, r, θ), using a streamwise periodic solver. The length of the pipe is $L_z = 5d$, which is sufficiently long to include the largest-structures in the flow (Eggels *et al.*, 1994). A $256 \times 128 \times 64$ grid is employed, with uniform spacing in the streamwise and circumferential directions, $\Delta z^+ = 4.55$, $(r\Delta\theta)^+ = 5.72$, and stretching in the radial direction in order to provide adequate resolution near the walls, $\Delta r^+ = 0.09 - 4.96$. Similar grid resolutions have previously been applied in the literature (Kim *et al.*, 1987; Eggels *et al.*, 1994).

Starting from an initial laminar flow field, fully-developed turbulence is generated after 10 flow-through times, $tU_b/d = 50$. An instantaneous flow field is then stored in order to use as inflow turbulence for the mouth-throat simulation. For this, the velocity field needs to be scaled first, so that the mean is the desired inlet bulk velocity. The Cartesian velocities are then computed from the cylindrical velocity components by:

$$\begin{aligned} u &= v_z \\ v &= v_r \sin\theta + v_\theta \cos\theta \\ w &= v_r \cos\theta - v_\theta \sin\theta \end{aligned} \tag{4.3}$$

Finally, the velocities are interpolated onto the grid at the inlet plane of the geometry, and the mean profile is subtracted in order to extract the fluctuations. These fluctuations are added to the inlet velocity profile if inflow turbulence is desired in the mouth-throat simulation. The frozen turbulent field is read in as a function of time, sweeping through the streamwise planes throughout the simulation. This can be done by invoking Taylor's hypothesis (Taylor, 1938) which allows convective spatial fluctuations to be interpreted as temporal fluctuations.

The velocity profile for turbulent flow through the inlet pipe is obtained by computing the mean flow profile from the pipe simulation. This mean is defined as the average of the instantaneous flow field in the streamwise and circumferential directions. As with the fluctuations, this profile is then interpolated onto the inlet plane of the grid for the mouth-throat simulations. The mean velocity and turbulence intensities are shown in figure 4-5.

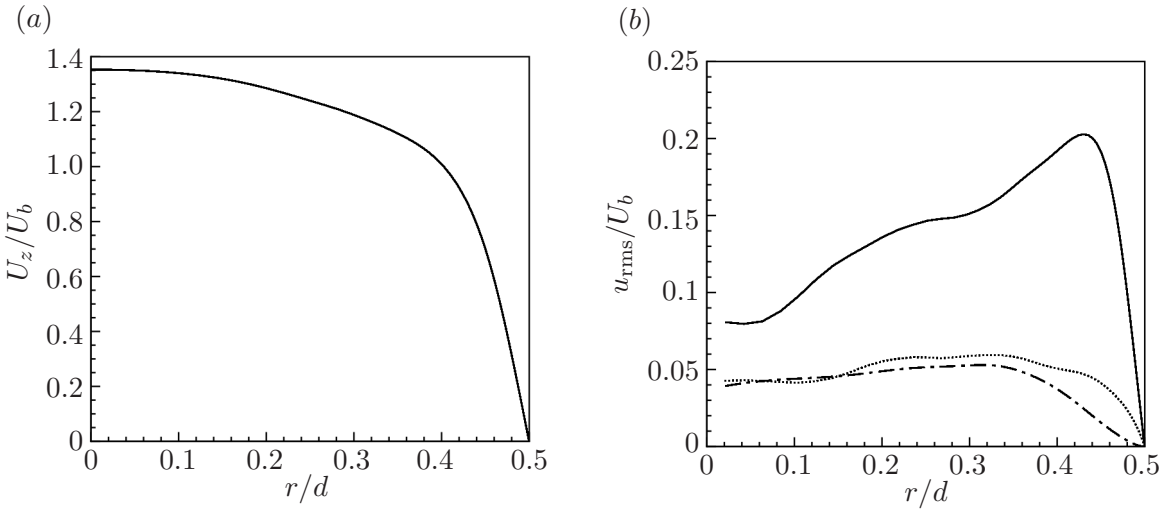


Figure 4-5: (*a*) Mean streamwise velocity U_z normalized by the bulk velocity U_b. (*b*) Turbulence intensities normalized by the bulk velocity: —, u_{rms}; - - -, v_{rms}; · · · ·, w_{rms}.

4.3.2 Outflow condition

At the outlet, a convective boundary condition is applied. This is given by

$$\frac{\partial \boldsymbol{u}}{\partial t} = -c\frac{\partial \boldsymbol{u}}{\partial n}; \qquad c < 0 \tag{4.4}$$

where c is the convective velocity and n is the direction normal to the outlet. The reason for extending the outlet of the mouth-throat geometries is two-fold. Firstly, the extended domain ensures that any inaccuracies in estimating the outflow conditions are not propagated upstream into the region of interest. Secondly, the extension ensures that the outflow plane is downstream of any separation zone. As a result, the flow everywhere is directed out of the domain and perpendicular to the boundary in order to minimize errors. Applying outflow conditions at a plane where there is recirculation (i.e. a region of reverse flow) can cause numerical instabilities, as was observed in initial simulations without the outflow extension.

4.4 Flow fields

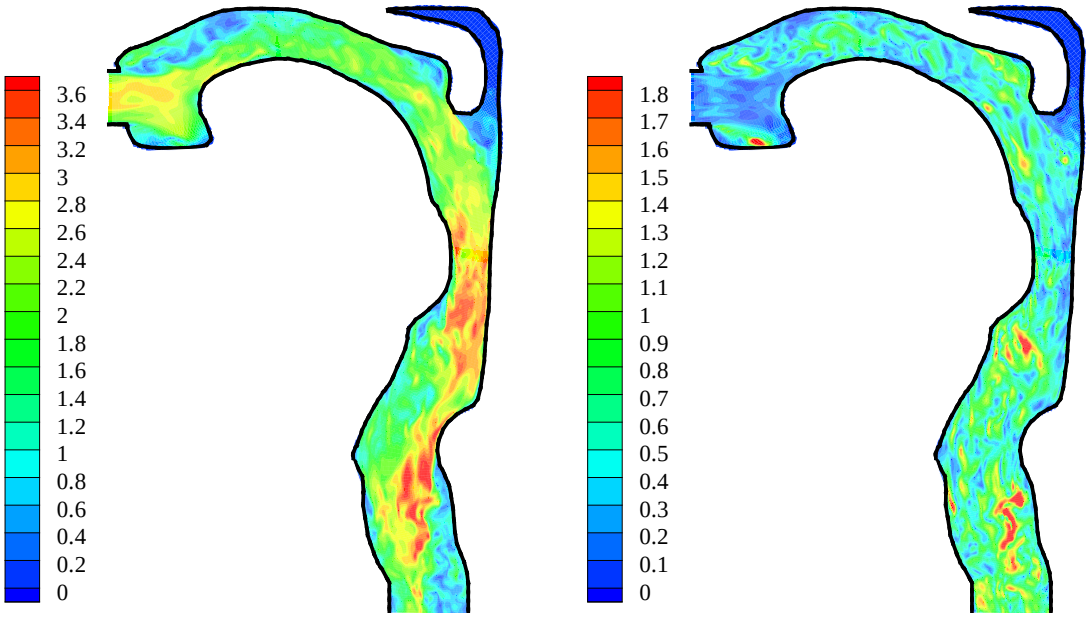
Direct numerical simulations in the four geometries were carried out at the same Reynolds number as the *in vitro* tests performed by Grgic *et al.* (2004*b*) at a flow rate $Q = 30L/min$. The Reynolds number is based on the mean velocity U_{mean} and the equivalent mean diameter D_{mean} of the geometry. The mean velocity is determined from the volume flow rate and the mean cross-sectional area according to,

$$U_{mean} = \frac{QL}{V}. \tag{4.5}$$

The main flow parameters in the different models are summarized in table 4.2 below. The simulations are started from an initial velocity field tangential to the surface of the geometries. Results for the first 10 time units are discarded in order to allow the flow to fully develop, after which statistics are collected over approximately 20 mean convective time scales.

Table 4.2: Flow parameters in the mouth and throat geometries.

Model	S1a	S1b	S2	S4
U_{inlet} (m/s)	3.77	3.92	1.20	1.20
U_{mean} (m/s)	1.88	2.74	1.13	1.13
Re_{inlet}	3222	3292	1815	1815
Re_{mean}	2262	2744	1761	1761



(a) (b)

Figure 4-6: Contours of (a) instantaneous velocity magnitude $|\boldsymbol{u}|/U_{mean}$, and (b) fluctuation magnitude $|\boldsymbol{u}^{'}|/U_{mean}$ in geometry S1a.

A snapshot of the instantaneous velocity magnitude, $|\boldsymbol{u}| = \sqrt{u^2+v^2+w^2}$, and the magnitude of fluctuations, $|\boldsymbol{u}^{'}| = \sqrt{(u-\bar{u})^2+(v-\bar{v})^2+(w-\bar{w})^2}$, in one of the geometries are shown in figure 4-6. The fields illustrate the turbulent nature of the flow. The mean velocity is responsible for the convective transport of particles, whereas the fluctuations

are responsible for particle dispersion. Understanding the deposition of particles in the airways therefore requires inspection of both the mean and the fluctuating components of the velocity. The effects of intrasubject and intersubject variation are studied below by comparison of the mean flow patterns and the mean turbulent kinetic energy across geometries.

4.4.1 Intrasubject variation (geometries S1b and S1a)

Comparison between geometries S1b and S1a shows how intrasubject variation can account for significant differences in the flow field. Figures 4-7*a* and 4-8*a* show contours of the mean velocity magnitude, $|\bar{\boldsymbol{u}}| = \sqrt{\bar{u}^2 + \bar{v}^2 + \bar{w}^2}$, in the central sagittal plane and at various cross-sections in models S1b and S1a respectively. The velocities have been normalized by the mean velocity in each geometry. Although the values of $|\bar{\boldsymbol{u}}|/U_{mean}$ are higher in model S1a, absolute values of velocity are higher in S1b ($U_{max} = 8.22ms^{-1}$ in S1b versus $U_{max} = 6.77ms^{-1}$ in S1a). Streamlines in the two-dimensional planes for geometries S1b and S1a are plotted in figures 4-7*b* and 4-8*b* respectively.

In the mouth, the velocity profiles are highly skewed towards the inner wall due to the airway curvature (A1-A2). In S1b, the flow accelerates at the back of the mouth due to the restriction in cross-sectional area, developing a pharyngeal jet which impinges onto the posterior wall (B1-B2). This jet is best observed in figure 4-11*a*. Due to the bend in the airway, the flow shifts towards the outer wall, separating from the inner wall and leading to a recirculation region (C1-C2). The maximum velocity then decreases as the larynx expands in the spanwise direction, and flow moves into the lateral expansions (D1-D2). A small recirculation region at the posterior side of the exit to the trachea can be observed under the 'sharp step' in the larynx (F1-F2).

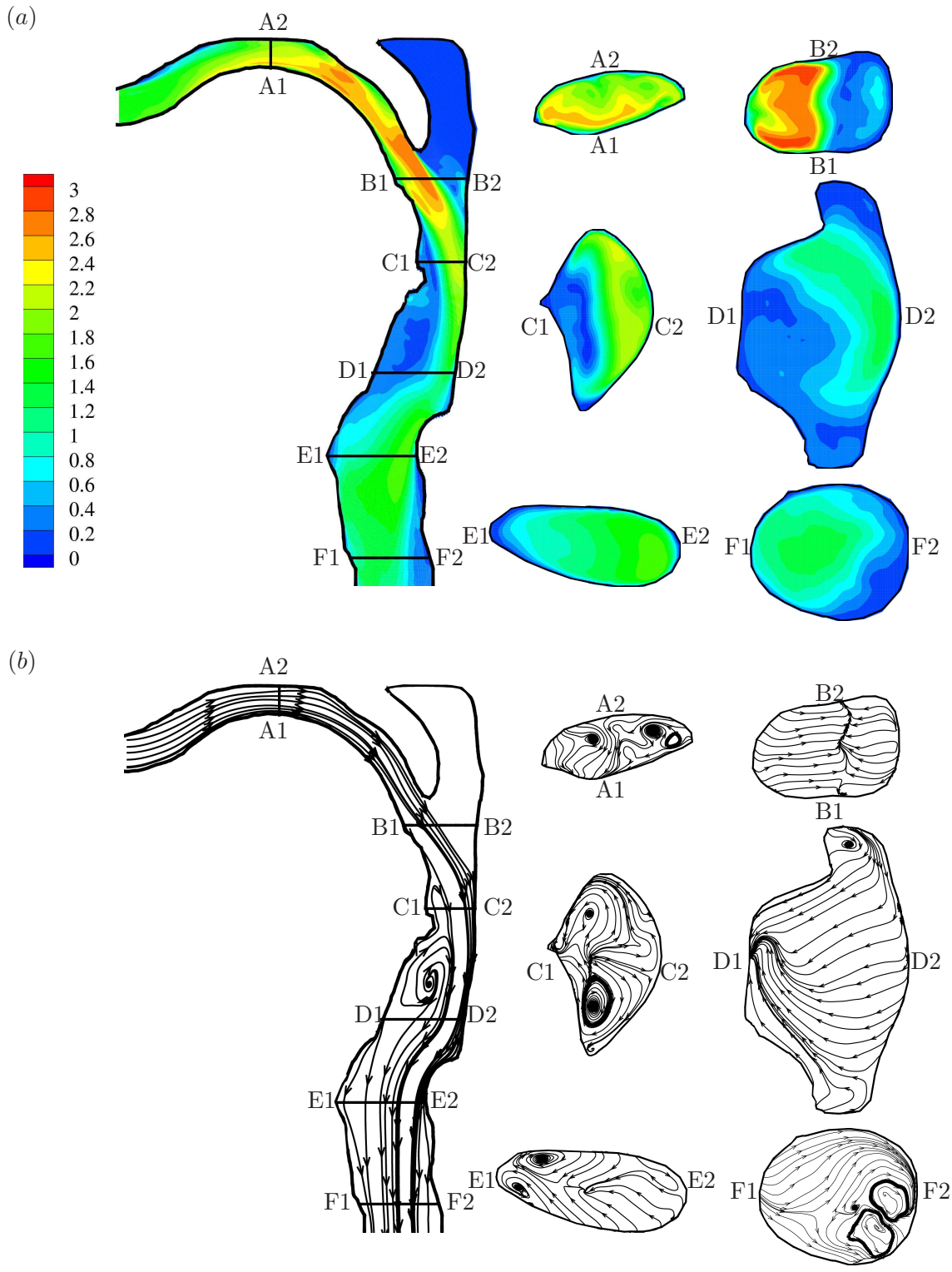


Figure 4-7: (*a*) Contours of mean velocity magnitude $|\bar{\boldsymbol{u}}|/U_{mean}$, and (*b*) 2D streamlines in the central sagittal plane and at various cross-sections of geometry S1b.

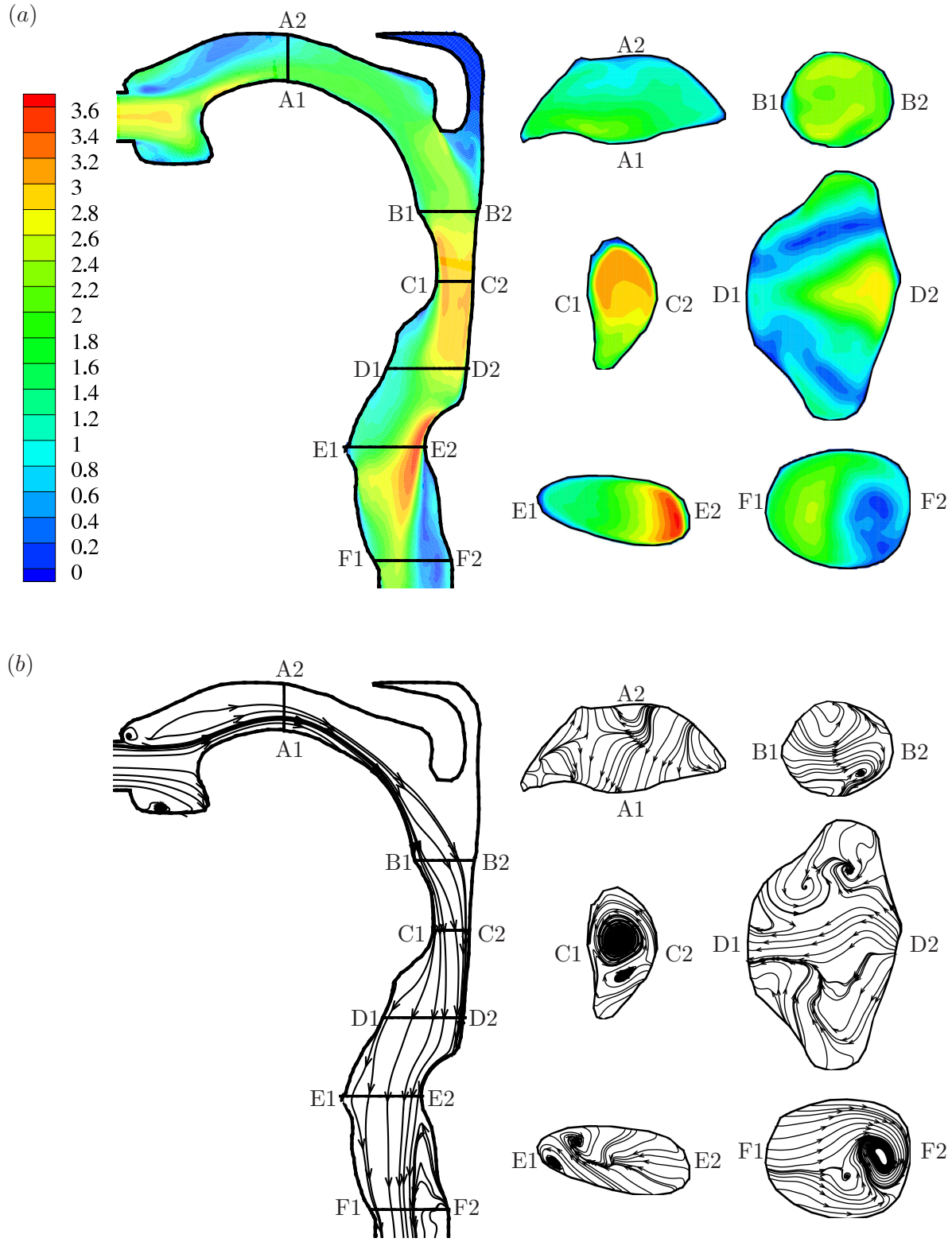


Figure 4-8: (*a*) Contours of mean velocity magnitude $|\bar{\boldsymbol{u}}|/U_{mean}$, and (*b*) 2D streamlines in the central sagittal plane and at various cross-sections of geometry S1a.

Due to the wider oral cavity in model S1a, there is no pharyngeal jet (B1-B2). As a result, the velocity in the pharynx is lower and the flow does not separate from the inner wall (C1-C2). Instead, the flow accelerates further downstream resulting in higher velocities in the larynx (E1-E2), due to the narrower nasopharynx than in S1b. This in turn leads to a larger separation region near the outer wall of the trachea (F1-F2).

Contours of the turbulent kinetic energy per unit mass, $k = \frac{1}{2}\left(\overline{u'^2} + \overline{v'^2} + \overline{w'^2}\right)$, in S1b and S1a are shown in figures 4-9 and 4-10 respectively. The plots show that the flow transitions further upstream and the turbulence intensity is higher in model S1a, even though the Reynolds number is lower. This is due to the inflow condition and the geometry of the airways. The flow in the mouth in S1b is similar to channel flow, whereas in S1a a jet from the inlet pipe impinges against the tongue. Separation occurs at the upper wall due to the wide oral cavity, and under the jet, where the flow resembles that over a backward-facing step. Higher levels of turbulent kinetic energy can be observed near the regions of separation, as adverse pressure gradients lead to an increase in k. The maximum kinetic energy in S1b occurs in the upper pharynx near the jet, and in S1a, in the larynx. High values of k can also be observed downstream of the vocal cords (see the sagittal plane in figure 4-10). These are locations where separated shear layers exist. Generally, turbulence is strongest where mean shear is largest.

Due to the complexity of the geometries, the flow is asymmetric. The maximum velocity and maximum turbulent kinetic energy are not located in the central sagittal plane (see figures 4-11 and 4-12).

We would expect total aerosol deposition to be slightly higher in S1b due to the higher velocities, in particular in the pharynx where the particles are likely to deposit on the back wall due to impaction. The slightly higher turbulence intensities in S1a, however, might

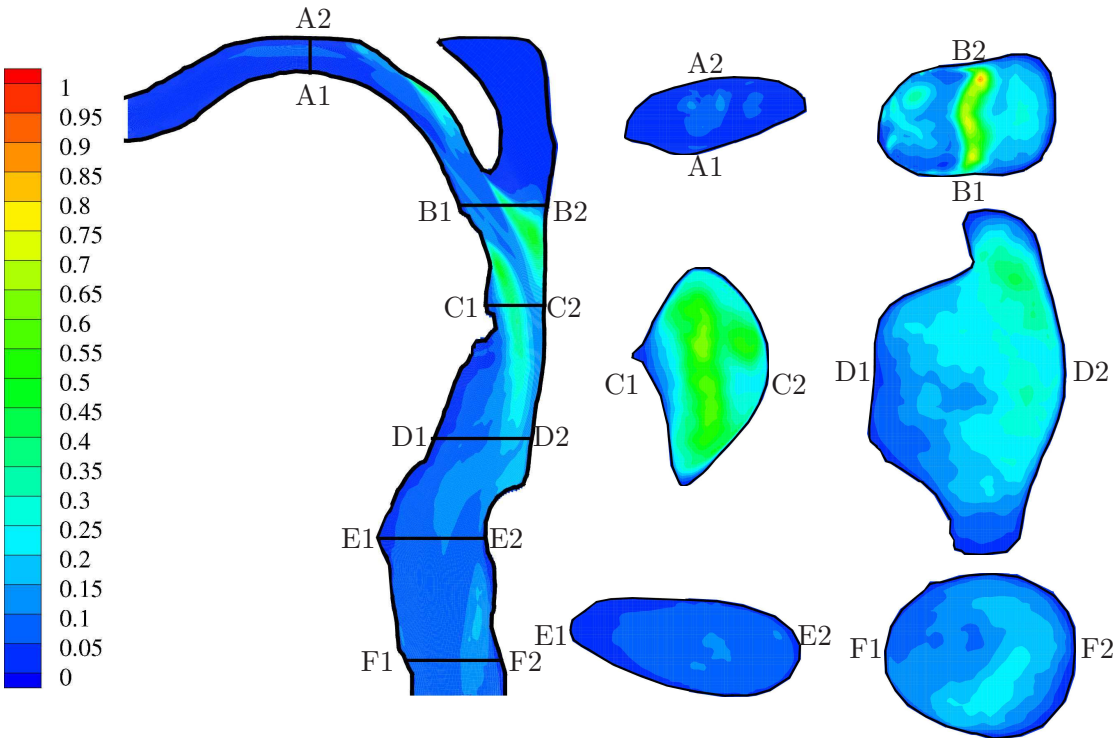


Figure 4-9: Contours of mean turbulent kinetic energy k/U^2_{mean} in the central sagittal plane and at various cross-sections of geometry S1b.

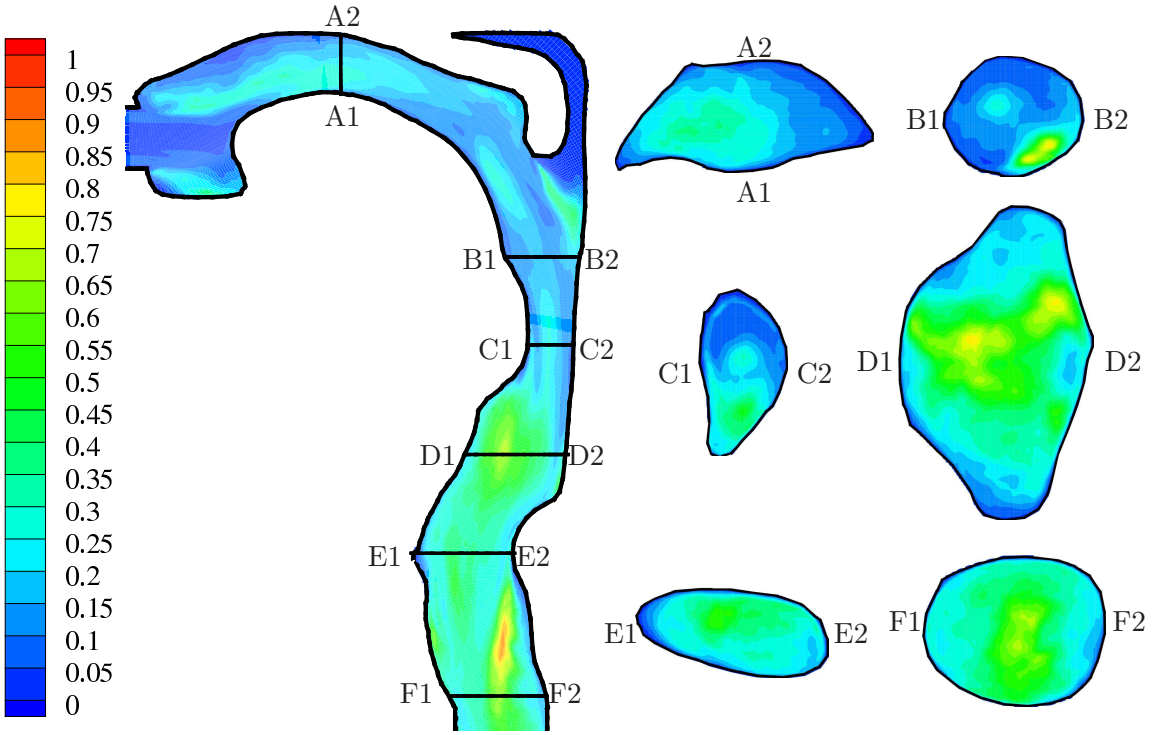
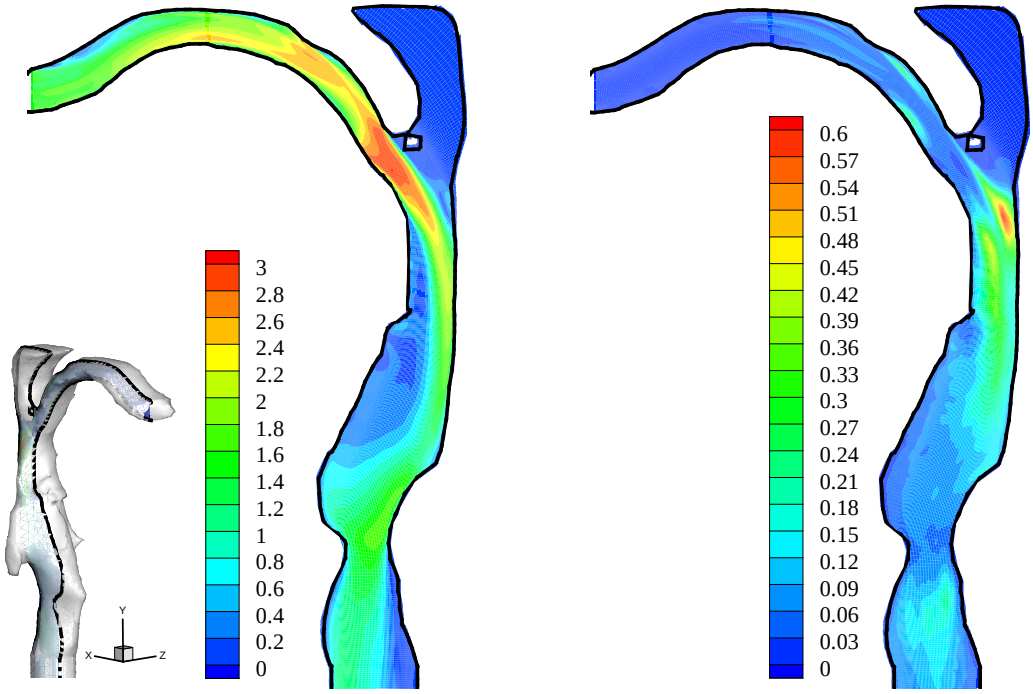
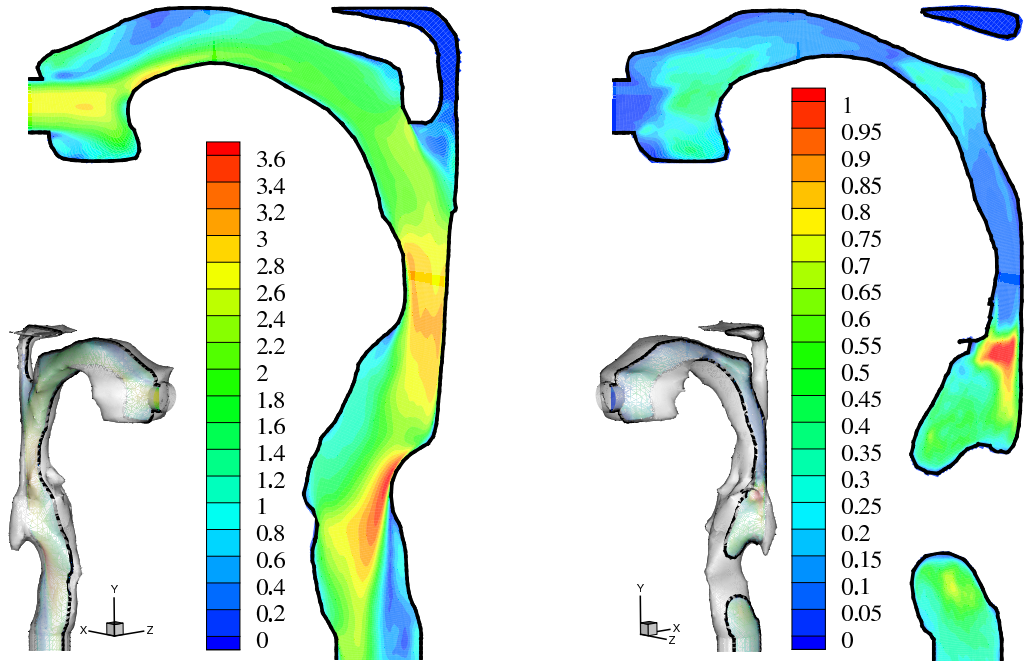


Figure 4-10: Contours of mean turbulent kinetic energy k/U^2_{mean} in the central sagittal plane and at various cross-sections of geometry S1a.



(*a*) (*b*)

Figure 4-11: Sagittal plane of maximum velocity in geometry S1b. Contours of (*a*) velocity magnitude and (*b*) turbulent kinetic energy.



(*a*) (*b*)

Figure 4-12: Sagittal planes of maximum velocity and maximum turbulent kinetic energy in geometry S1a. Contours of (*a*) velocity magnitude and (*b*) turbulent kinetic energy.

counterbalance this difference for the smaller particles, as diffusion will be stronger. Higher deposition for the larger particles in S1a can be expected in the mouth due to the position of the tongue blocking the flow which enters from the inlet pipe, and above the vocal cords in the larynx, due to the high velocity and sudden change in flow direction.

Heenan *et al.* (2004) conducted PIV measurements of the flow in the same geometries. They presented results for a volume flow rate $Q = 90L/min$. A larger inlet pipe was used in that study and therefore the Reynolds numbers and the reference velocities against which the data were normalized differ. However, their results can be used for qualitative comparison of the main flow features, which show good agreement with our data.

4.4.2 Intersubject variation (geometries S2 and S4)

Geometries S2 and S4 are considerably different to S1a and S1b. This results in significant differences in the flow fields, which can be observed in the velocity contours shown in figures 4-13*a* and 4-14*a*, and in the streamlines plotted in figures 4-13*b* and 4-14*b*. The velocities reach much higher levels when normalized by the reference speed, as the variation in the cross-sectional area is much larger. However, absolute values of velocity are lower as the geometries on average are wider. In S2, the velocities in the mouth are low due to the wide oral cavity, with recirculation at the top and bottom walls near the inlet. Strong secondary flow exists, as the fluid coming in from the pipe moves radially outwards to fill the wide area (A1-A2). The fluid then accelerates at the back of the mouth and upper pharynx due to the large reduction in cross-sectional area (B1-B2). An obstruction in the centre of the airway causes the flow to split into two diverging jets (C1-C2), shifting the flow towards the side walls (D1-D2). Four distinct counter-rotating vortices can be observed at this location: two main cells at the centre, and two smaller cells near the side walls. The

main cells resemble Dean vortices known to appear in curved ducts as a result of centrifugal instability. Smaller secondary cells have also been observed in curved pipe flow studies (Daskopoulos & Lenhoff, 1989). Further downstream, the secondary flow weakens and the velocity drops due to an increase in cross-sectional area (E1-E2). A small recirculation region develops near the anterior wall due to the sharp expansion. The flow in the trachea is similar to S1a, with the fluid accelerating again as it passes the sharp bend (G1-G2) and a small separation region developing near the posterior wall (H1-H2).

Similar to model S2, the velocity in the mouth of geometry S4 is low and strong secondary flow exists, due to the large oral cavity (A1-A2). The back of the mouth is wider than in S2, so velocities there are lower (B1-B2). Instead, the flow accelerates further downstream, after the sharp 90° bend into the pharynx (C1-C2). The velocity remains roughly constant throughout the pharynx as the cross-sectional area does not change appreciably. The small expansion near the anterior wall is sudden so the flow remains unaffected and attached to the posterior wall (D1-D2). A slight drop in the velocities is observed in the larynx, where the cross-sectional area is larger (E1-E2), before an increase in the trachea as the airway narrows and bends (F1-F2). The trachea is shorter and narrower than in the other geometries, therefore velocities are still high at the exit (G1-G2).

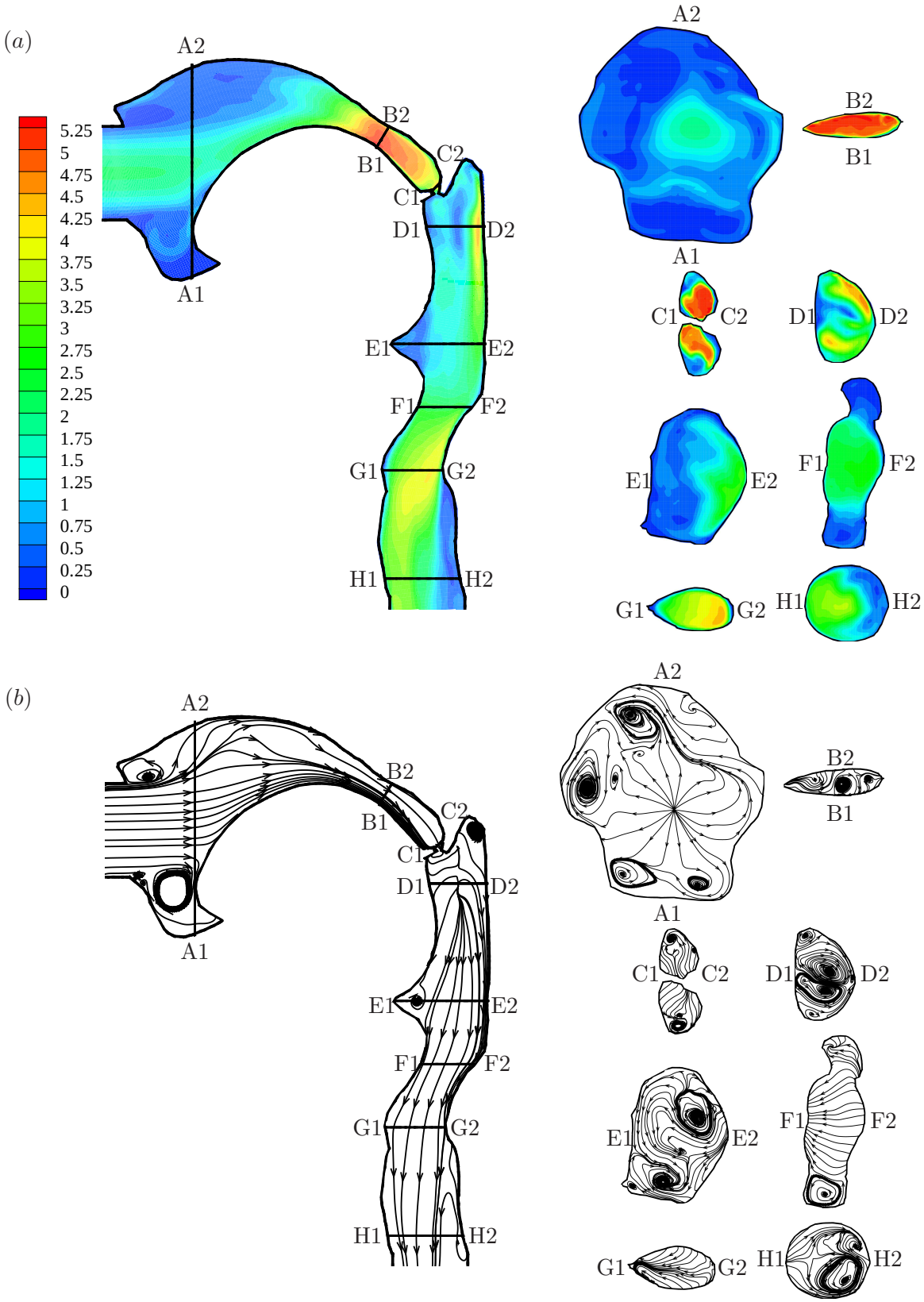


Figure 4-13: (*a*) Contours of mean velocity magnitude $|\bar{\boldsymbol{u}}|/U_{mean}$, and (*b*) 2D streamlines in the central sagittal plane and at various cross-sections of geometry S2.

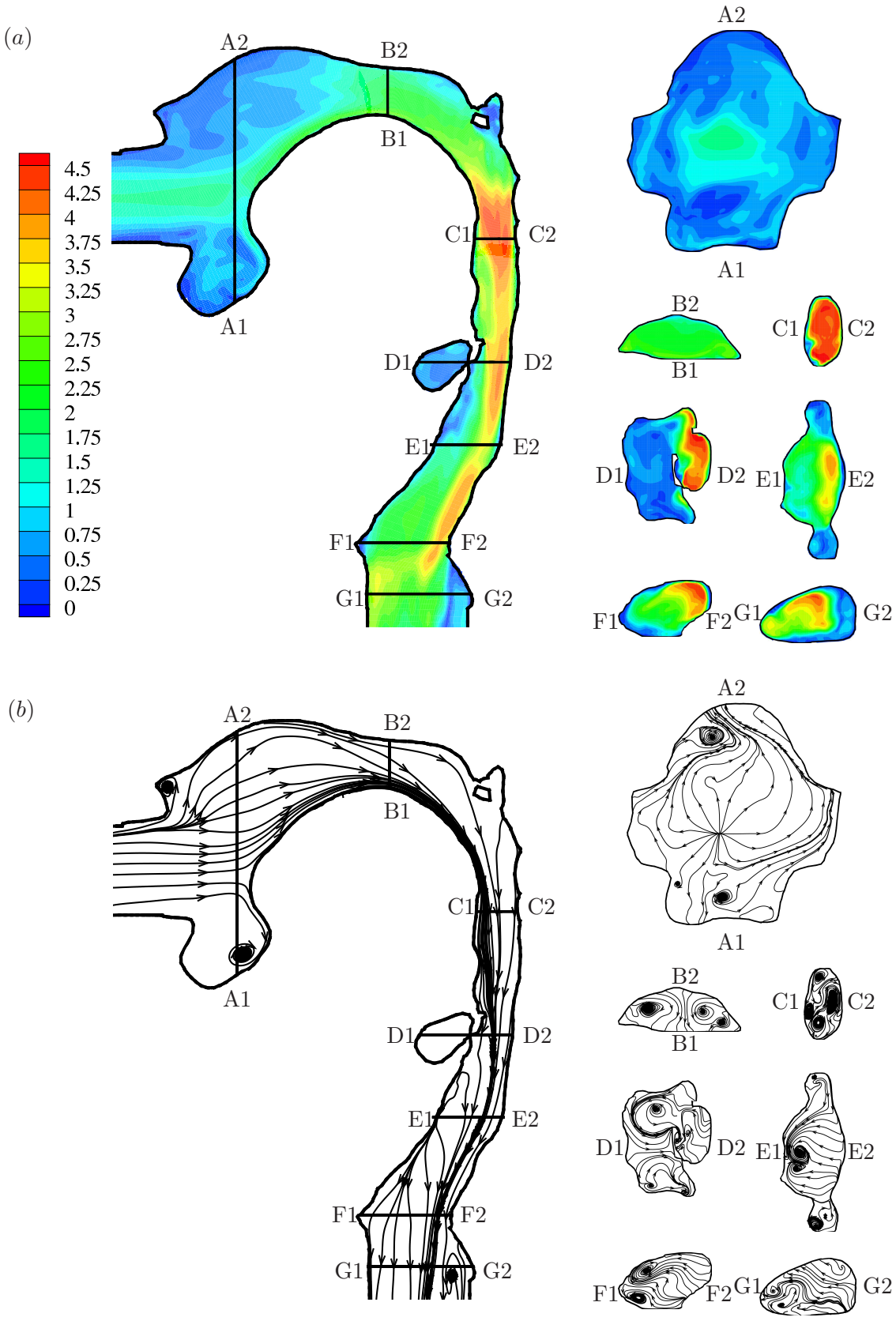


Figure 4-14: (*a*) Contours of mean velocity magnitude $|\bar{\boldsymbol{u}}|/U_{mean}$, and (*b*) 2D streamlines in the central sagittal plane and at various cross-sections of geometry S4.

Although the inflow is laminar, the flow in both geometries transitions to turbulence at the back of the mouth, as can be seen in figures 4-15 and 4-16. The contours of turbulent kinetic energy in S2 show much higher levels of turbulence intensity compared to all other geometries. The location of maximum k occurs close to the core of one of the main vortices, in the upper pharynx. This is due to the strong gradients in tangential velocity inside the vortex. In S4, most of the turbulent kinetic energy is produced in the pharynx and larynx due to the separated shear layers. The maximum value of k occurs in the upper pharynx, between the separation region and the pharyngeal jet, where shear is highest.

The plots of maximum velocity and maximum turbulent kinetic energy in figures 4-17 and 4-18 show that the flow in both geometries is highly asymmetric. One of the jets that develops in S2 after the flow passes by the obstruction at the back of the mouth is clearly visible in figure 4-17a. In figure 4-18a, a long vertical stream can be observed in the pharynx, which is then forced to turn as the geometry curves in at the height of the vocal cords, creating a separated shear layer. The flow is slightly skewed towards the outer wall due to the bend upstream.

Based on the flow fields, similar deposition efficiencies can be expected in S2 and S4. Fewer particles are likely to deposit in comparison with S1a and S1b, due to the lower velocities. Both geometries are expected to have low deposition in the mouth due to the large oral cavity. Slightly higher deposition by impaction is expected in the pharynx of S2, especially for the larger particles, due to the two jets that develop at the back of the mouth.

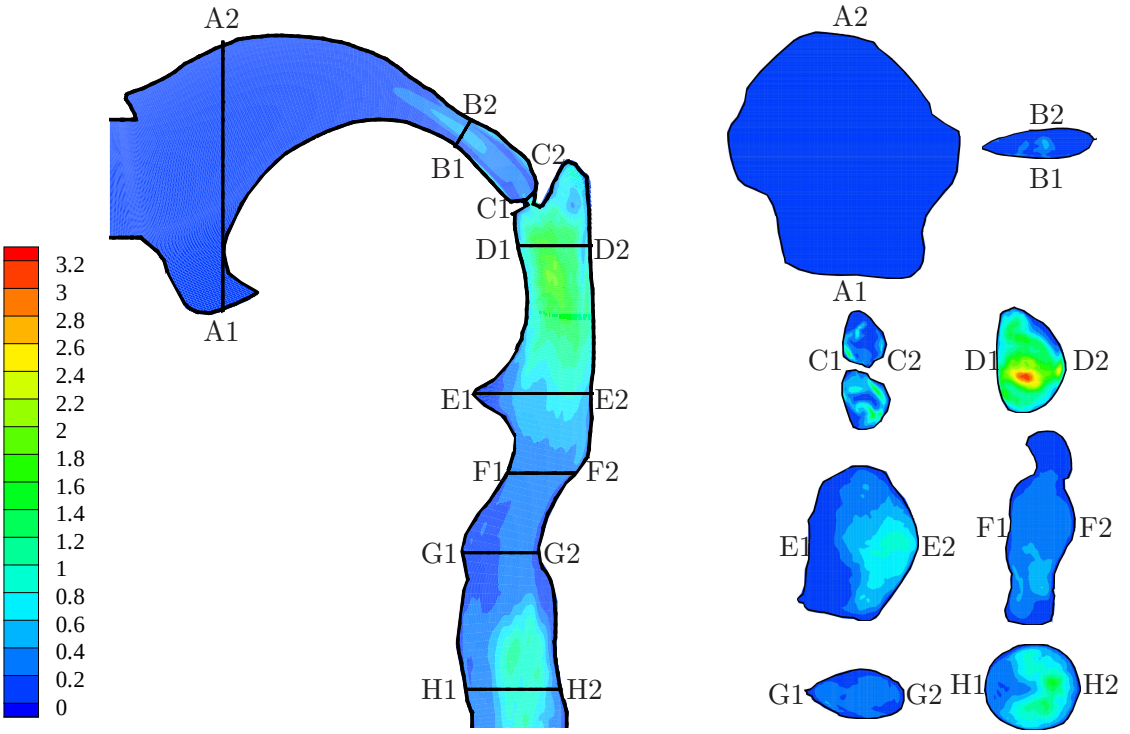


Figure 4-15: Contours of mean turbulent kinetic energy k/U^2_{mean} in the central sagittal plane and at various cross-sections of geometry S2.

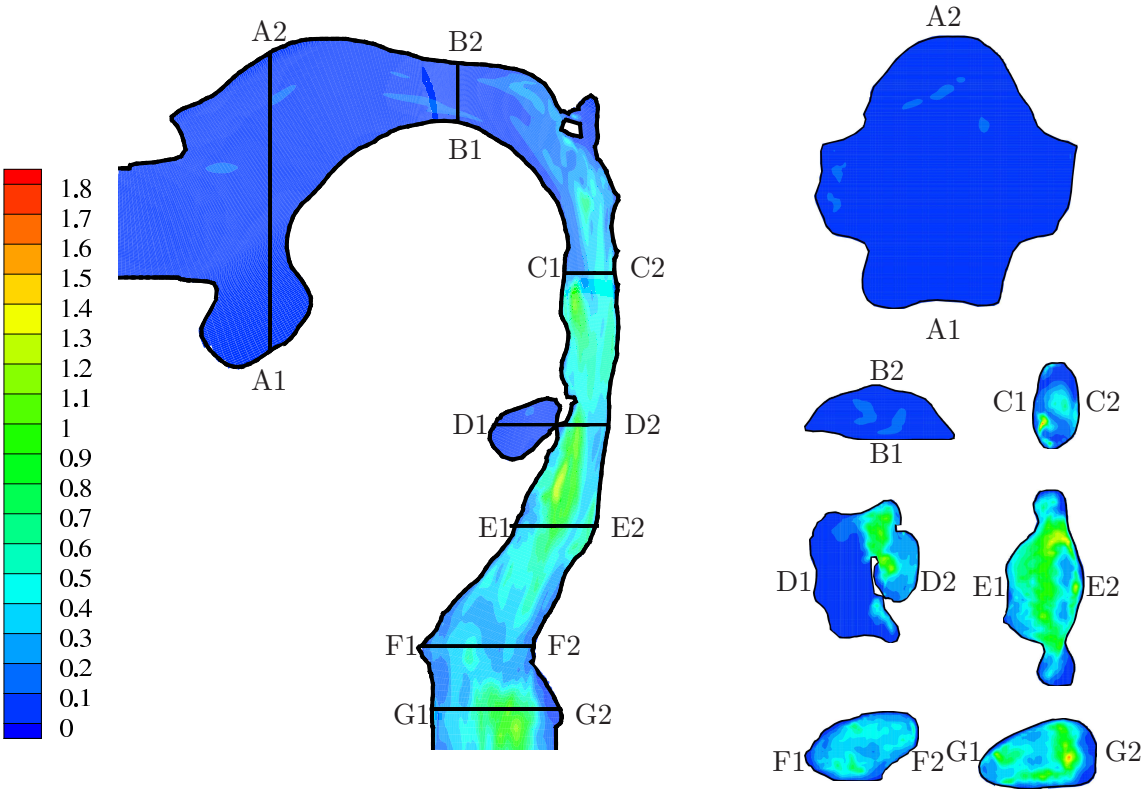
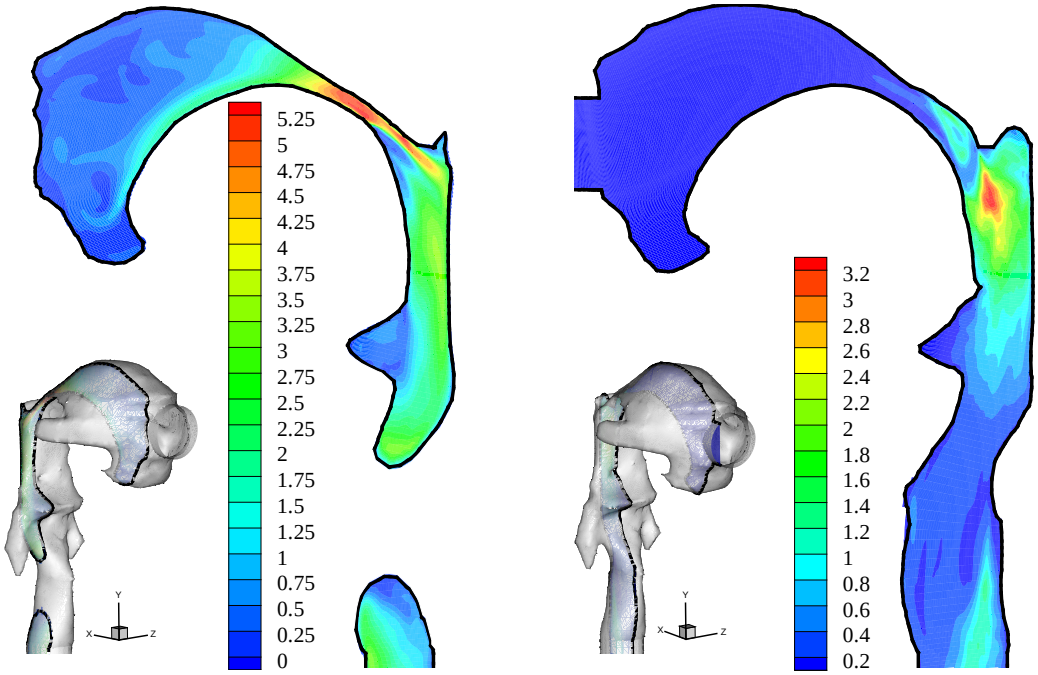
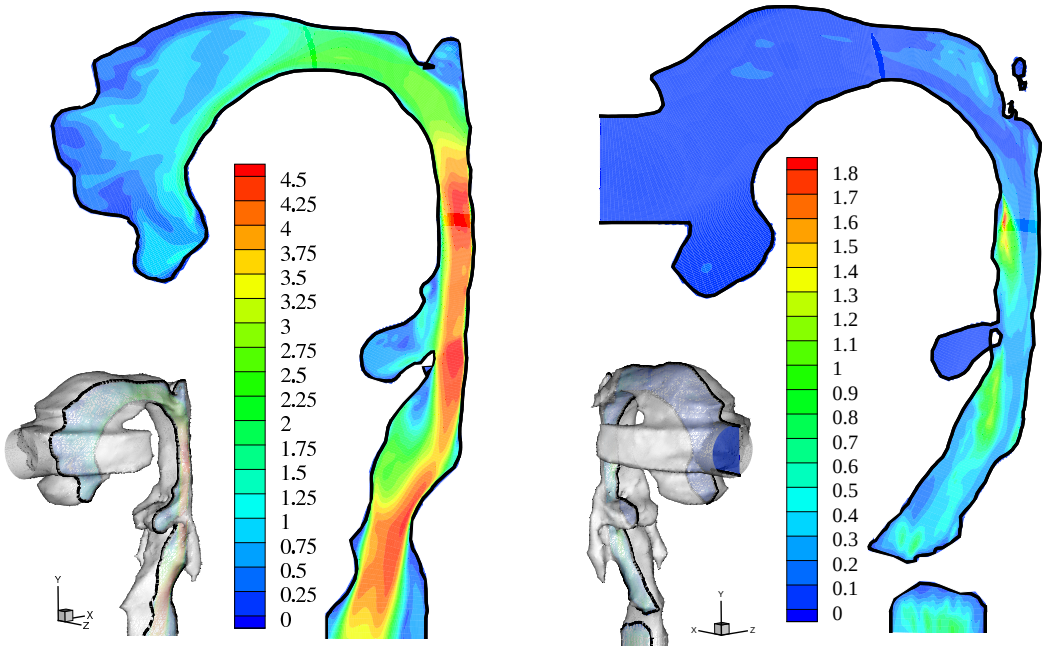


Figure 4-16: Contours of mean turbulent kinetic energy k/U^2_{mean} in the central sagittal plane and at various cross-sections of geometry S4.



(*a*) (*b*)

Figure 4-17: Sagittal planes of maximum velocity and maximum turbulent kinetic energy in geometry S2. Contours of (*a*) velocity magnitude and (*b*) turbulent kinetic energy.



(*a*) (*b*)

Figure 4-18: Sagittal planes of maximum velocity and maximum turbulent kinetic energy in geometry S4. Contours of (*a*) velocity magnitude and (*b*) turbulent kinetic energy.

4.5 Particle deposition

Particles of five different sizes, $d_p = (3, 5, 6.5, 8, 10)\mu m$, were distributed uniformly at the entrance of the inlet pipe and tracked dynamically in physical space using the Taylor expansion interpolation. Massless particles were also tracked to provide a control test. The Stokes numbers in the four geometries are summarized in table 4.3. The particles were released at regular intervals for the results to be independent of the release time. The time instant for release was chosen based on the characteristic time scale of the flow, τ_f, given by,

$$\tau_f = \frac{D_{mean}}{U_{mean}}. \tag{4.6}$$

Particles were released into the flow at $t_{release} \sim 0.5\tau_f$, during a period $tU_{mean}/D_{mean} \sim 10$ and then allowed to convect until they had all either deposited or exited the domain. The initial velocity of the particles was set to the mean fluid velocity at their release location. Approximately 100,000 particles in total were tracked for each size.

In order to accurately predict particle trajectories, the time step Δt used in advancing the particle equations must be smaller than the particle relaxation time, τ_p. The time step is set to

$$\Delta t \sim \frac{\tau_{p_{min}}}{5}, \tag{4.7}$$

where $\tau_{p_{min}}$ is the relaxation time of the smallest particle. This condition also ensures that the CFL constraint is satisfied and hence that particles do not travel more than one grid cell per time step.

Deposition is assumed once a particle comes into contact with the wall of the geometry. Reflection and re-suspension are not included as the existence of a mucus layer on the inner walls of the airways ensures that particles colliding with the surface deposit. Collision with

the wall is assumed when a particle trajectory crosses the wall. The location of deposition is computed from the intersection of the particle trajectory with the triangulated surface. A ray is traced from the particle's previous position, inside the fluid domain, to its current position on the other side of the wall. The point at which the ray intersects the surface gives the deposition location. Once a particle has deposited, its deposition location is stored and the particle is removed from the flow.

Table 4.3: Particle Stokes numbers in the mouth and throat geometries.

Model	Stk				
	$d_p = 3.0\mu m$	$d_p = 5.0\mu m$	$d_p = 6.5\mu m$	$d_p = 8.0\mu m$	$d_p = 10.0\mu m$
S1a	0.0025	0.0070	0.0119	0.0180	0.0281
S1b	0.0045	0.0125	0.0212	0.0320	0.0501
S2	0.0012	0.0033	0.0056	0.0085	0.0133
S4	0.0012	0.0033	0.0056	0.0085	0.0133

Based on the Stokes numbers in the different geometries, we expect higher deposition in models S1a and S1b. The aerodynamic particle sizes fall in the sedimentation/impaction regime, so most deposition is likely to occur via impaction. In particular, in the pharynx and larynx after the bend in the airways, since the high curvature makes it difficult for particles to follow the flow. In S1b, deposition is also likely to be high in front of the tongue as the incoming jet impacts with it. Regional and total depositions in each geometry are given in tables 4.4 through 4.6. The results for S1b are not included as the inflow condition differs significantly from the other geometries and from the *in vitro* study, and therefore this case cannot be used for a meaningful comparison. Deposition patterns in the different geometries, for three particle sizes, are shown in figures 4-19 to 4-21.

The results show that geometric variation has a large effect on particle deposition. The amount deposited, as well as the region of maximum deposition, vary across geometries. Even in the case of geometries S2 and S4, in which the Stokes numbers and the Reynolds numbers are the same, the regional and total depositions differ. This is because these

Table 4.4: Deposition in the different regions of the S1a geometry, given as a percentage of aerosol entering the mouth.

Particle size (μm)	Regions				
	Mouth (%)	Pharynx (%)	Larynx (%)	Trachea (%)	Total (%)
massless	15.02	1.84	6.59	1.50	24.94
3.0	17.09	2.40	8.73	2.08	30.31
5.0	25.01	3.91	13.42	3.16	45.49
6.5	36.05	5.53	16.73	3.33	61.64
8.0	51.11	7.00	16.66	3.05	77.81
10.0	70.57	7.18	11.77	1.96	91.48

Table 4.5: Deposition in the different regions of the S2 geometry, given as a percentage of aerosol entering the mouth.

Particle size (μm)	Regions				
	Mouth (%)	Pharynx (%)	Larynx (%)	Trachea (%)	Total (%)
massless	6.87	3.19	4.03	1.30	15.39
3.0	7.40	4.39	4.35	1.54	17.67
5.0	9.02	7.33	4.95	1.84	23.13
6.5	11.59	11.70	5.71	2.22	31.22
8.0	15.01	18.13	6.04	2.56	41.73
10.0	22.36	28.46	5.50	2.29	58.60

Table 4.6: Deposition in the different regions of the S4 geometry, given as a percentage of aerosol entering the mouth.

Particle size (μm)	Regions				
	Mouth (%)	Pharynx (%)	Larynx (%)	Trachea (%)	Total (%)
massless	8.30	7.07	4.07	1.50	20.94
3.0	7.84	7.88	4.66	1.71	22.10
5.0	8.24	10.70	7.03	2.10	28.07
6.5	9.13	14.36	8.99	2.20	34.69
8.0	11.06	19.89	10.70	2.19	43.84
10.0	15.34	27.75	11.81	2.10	57.00

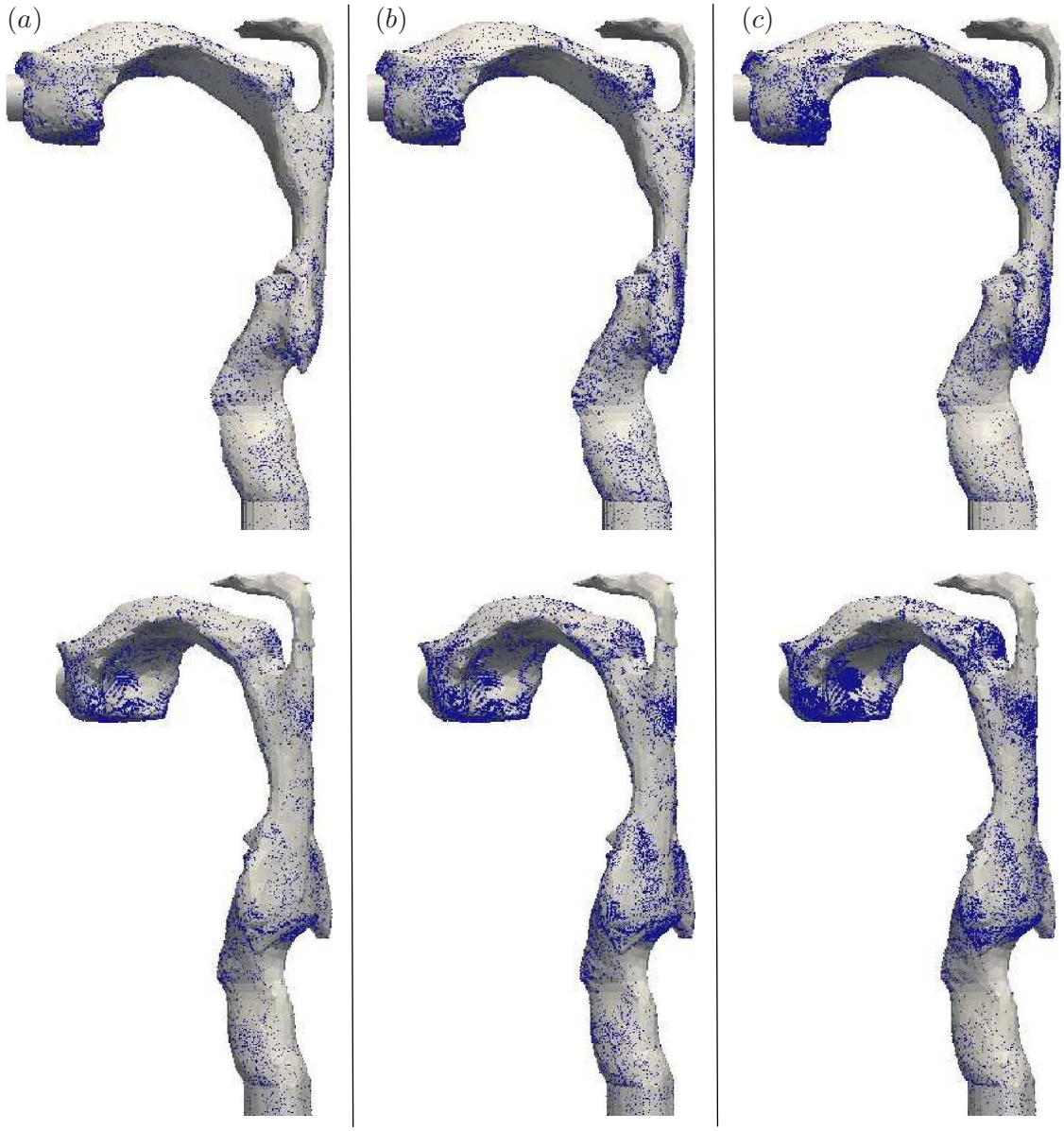


Figure 4-19: Deposition patterns on geometry S1a. Two views for (a) $d_p = 3.0\mu m$, (b) $d_p = 6.5\mu m$ and (c) $d_p = 10.0\mu m$.

parameters are based on the mean characteristic length of the geometries, but the diameters of the geometries deviate considerably from the mean in many sections of the airways. Comparison between the flow fields and the deposition efficiencies shows that particles tend to deposit where velocities are high and where the flow experiences sudden changes in direction.

In geometry S1a, the major regions of deposition are in front of the tongue, due to

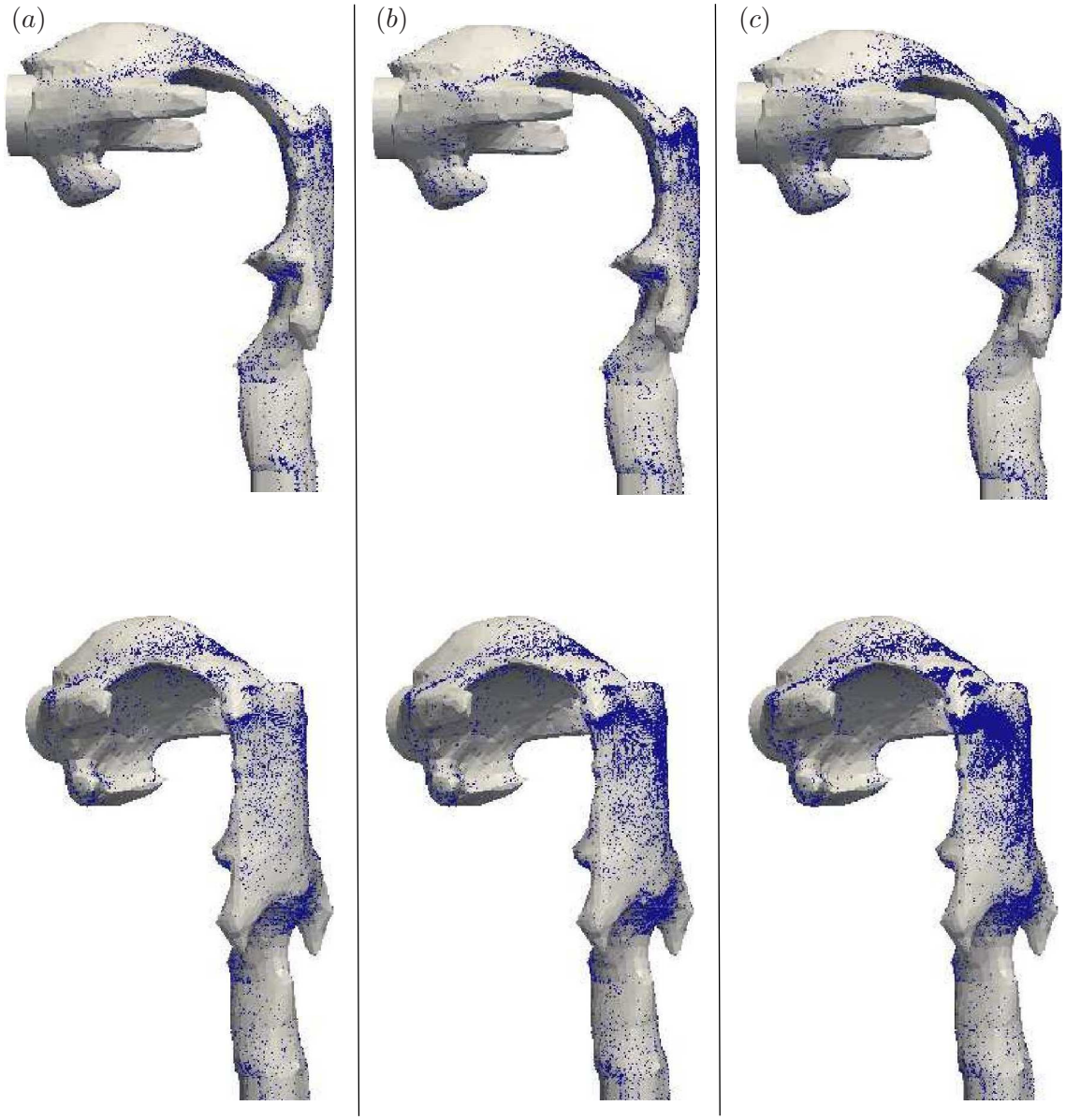


Figure 4-20: Deposition patterns on geometry S2. Two views for (*a*) $d_p = 3.0\mu m$, (*b*) $d_p = 6.5\mu m$ and (*c*) $d_p = 10.0\mu m$.

impaction of the incoming fluid, and the side walls of the mouth, due to the sideways movement of the fluid as it impinges on the tongue. Another deposition hot spot is the sharp step in the larynx. For larger particles, the posterior wall of the pharynx is also a major region of deposition, due to impaction of the particles as they deviate from the streamlines when the airway bends.

In the case of geometry S2, the patterns show major deposition at the back of the mouth

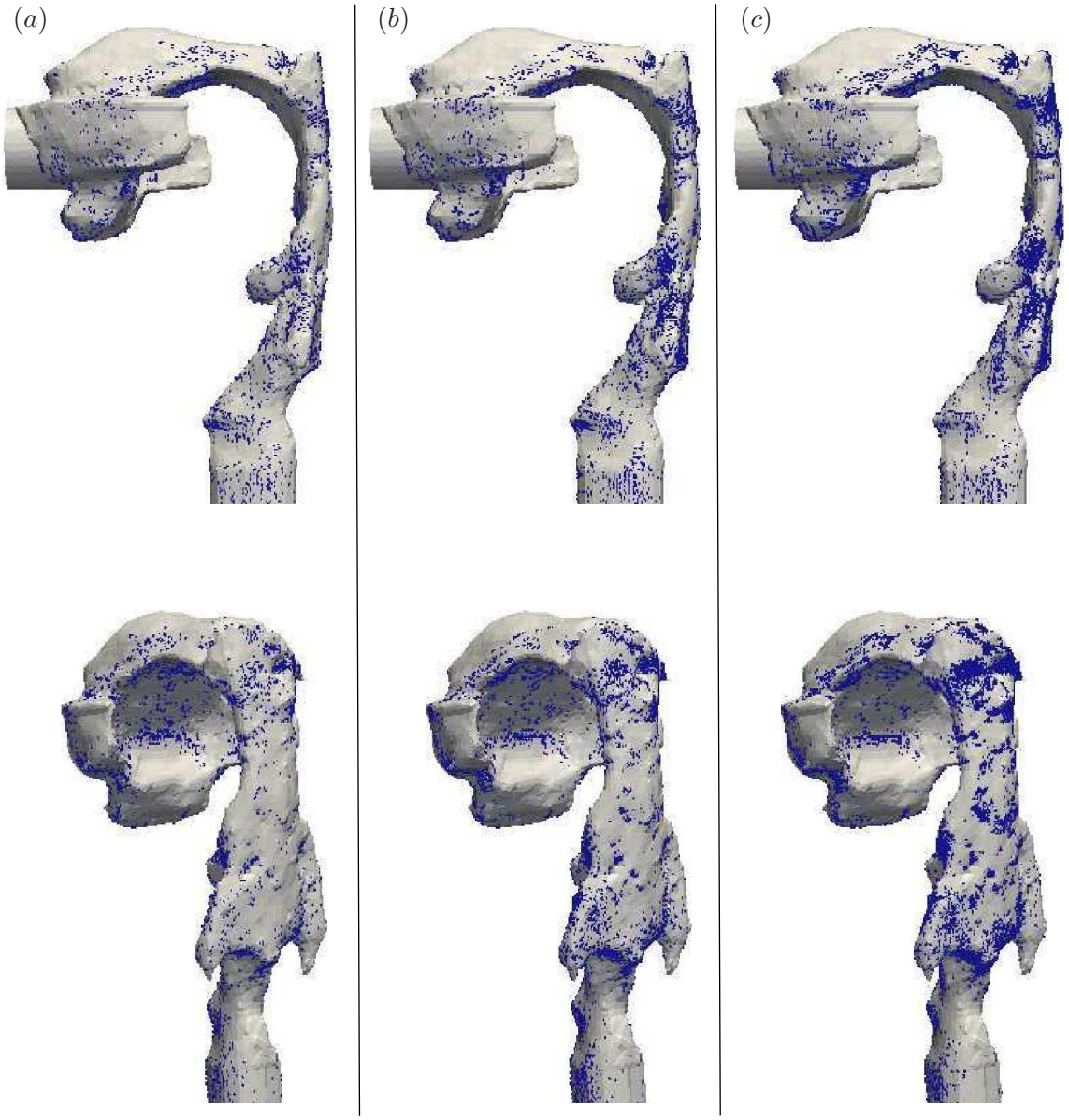


Figure 4-21: Deposition patterns on geometry S4. Two views for (*a*) $d_p = 3.0\mu m$, (*b*) $d_p = 6.5\mu m$ and (*c*) $d_p = 10.0\mu m$.

and the upper pharynx. The large reduction in cross-sectional area causes deposition at the back of the mouth, and the two diverging jets caused by the obstruction in the upper pharynx (see figure 4-13) cause deposition on the posterior wall. The patterns show two hot spots on either side, corresponding to the two jets impinging on the wall. Their location is consistent with the two velocity maxima observed in cross-section D1-D2 in figure 4-13*a*. The step in the larynx is also a deposition hot spot for all three particle sizes.

Deposition in geometry S4 occurs mainly in the pharynx and larynx. Some weak deposition is observed in the mouth, mainly along the side walls, due to the incoming flow moving radially outwards (see cross-section A1-A2 in figure 4-14*b*). The smaller particles are randomly distributed, and do not show any clear deposition hot spots. For the larger particles, the common hot spots can be observed, the posterior wall of the pharynx and the step in the larynx, where deposition occurs via impaction. The deposition patterns are consistent with those observed in the *in vitro* tests of Grgic *et al.* (2004*b*).

The effect of inflow turbulence was studied in geometry S1b. Comparison between two simulations, with and without inflow turbulence, did not show a significant difference in total deposition. Only a slight increase in deposition was observed with inflow turbulence due to higher oral deposition. In all other regions the effect was negligible as the flow transitions into turbulence at the back of the mouth even in absence of inflow perturbations.

No deposition should be observed in the case of the massless particles as they should follow the streamlines. However the recorded deposition in all three geometries is very high. Inspection of the regional deposition fractions and the deposition patterns of the massless particles in the different geometries shows that the highest deposition in all three geometries occurs in the mouth: in S1a, in front of the tongue; in S2, around the obstruction at the back of the mouth and along the upper wall of the oral cavity where it narrows; in S4, along the inner wall of the mouth. There is also high deposition under the sharp bend in the larynx in all geometries, and in S4 under the small expansion in the pharynx. The error on average is 20%. This error was not present in the tests carried out in the curved pipe which were presented in Chapter 2 (see table 2.1). The following possible sources of error were considered:

1. The turbulent field might not be sufficiently resolved, especially near the wall. However, tests were performed using a laminar flow in model S1b and the deposition of massless particles was still high.

2. the P-space algorithm might be introducing errors in the particle trajectories as the Cartesian velocities need to be interpolated from the fluxes at every time step. Errors could be accumulating and causing significant deviation from the true particle trajectories. However, tests in model S1b using the C-space algorithm yielded similar results.

3. The highly irregular geometries might lead to unwanted deposition of particles travelling close to the walls, as the triangles on the surface are oriented very unevenly. A simulation could be carried out on an idealized, smooth geometry in order to verify whether this is the case.

4. The complex nature of the flow in the throat (e.g. impinging jet against a wall) means particles are directed straight towards the walls making it very hard to avoid deposition, especially with an immersed boundary method which involves interpolation. A simple test of a jet impinging onto a flat plate could be carried out using an immersed boundary as well as a body-fitted grid in order to verify whether the issue is associated with the interpolation at the wall. It yet remains to be determined whether the accuracy can be improved or whether this is an inherent limitation of the method. It could also point to the reason why previous numerical models failed to predict deposition correctly. A definitive assessment of the source of errors in those models and their dependence on particle tracking versus turbulence modelling is, however, lacking.

The total deposition versus Stokes number is shown in figure 4-22 below, for the

different-sized particles in the three geometries. The results from the *in vitro* tests have been plotted alongside for comparison (Grgic *et al.*, 2004*b*). The deposition fraction of massless particles has been taken as the reference error and subtracted from all other deposition fractions. Good agreement can be observed between the numerical and experimental results which suggests that if the issue in the particle tracking can be corrected, very good predictions can be achieved.

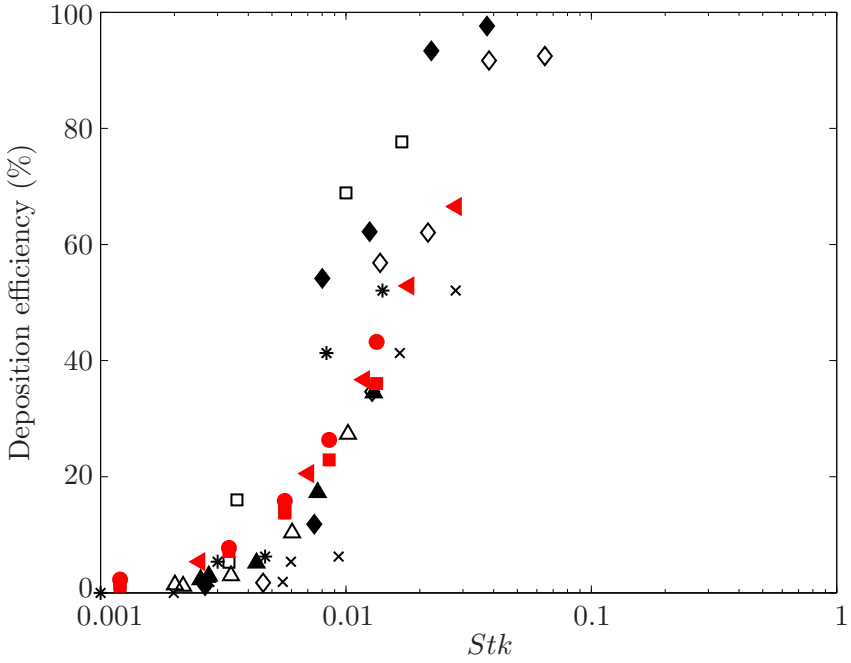


Figure 4-22: Deposition efficiency versus Stokes number based on the mean equivalent diameter D_{mean} and the mean velocity U_{mean}. Current method: ◀, S1a; ●, S2; ■, S4. *In vitro* studies in various geometries: ♦, ◊, ∗, ×, □, ▲, △.

Deposition experiments carried out in an idealized geometry showed a dependence of the deposition on Reynolds number, due to changes in the flow field (Grgic *et al.*, 2004*a*). An empirical Reynolds number correction $Re^{0.37}$ that collapsed the data more closely onto a single curve was proposed. The *in silico* and *in vitro* deposition efficiencies against $StkRe^{0.37}$ are shown in figure 4-23, along with the least squares fit curve. Better collapse of the data can be observed. The good agreement of the numerical results with the curve of best fit

demonstrates the capability of the current method to accurately predict particle deposition in the extrathoracic airways.

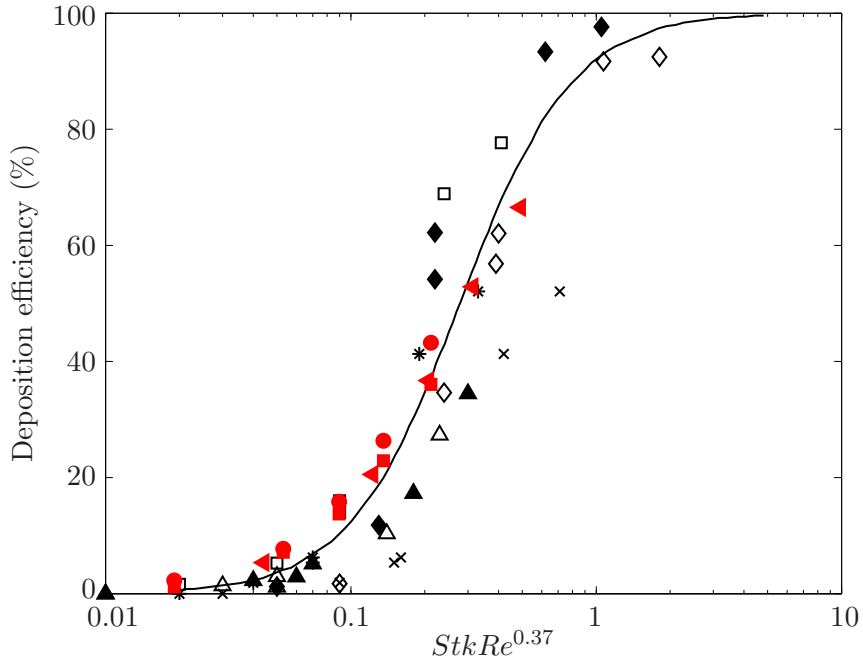


Figure 4-23: Deposition efficiency versus Stokes number with Reynolds number correction. Current method: ◀, S1a; ●, S2; ■, S4. *In vitro* studies in various geometries: ♦; ◊; ∗; ×; □; ▲; △; —, least squares curve fit function $\eta = 100 - 100/(11.5(StkRe^{0.37})^{1.912} + 1)$, where η is deposition efficiency.

The geometric variation is responsible for the data scatter in two ways:

1. The different shape of the airways leads to different flow patterns and hence different "hot-spots" in which the particles deposit.

2. For a given volume flow rate, the Reynolds number is different in various geometries. This changes the mean velocity profiles and the turbulence intensities which in turn affects particle trajectories and their deposition.

Therefore the scatter observed in figure 4-22 is partly caused by an incorrect choice of parameter against which to plot deposition; as the Stokes number does not take into account the change in deposition due to Reynolds number.

It was briefly discussed in the introduction that Grgic *et al.* (2004*b*) observed this dependence on Reynolds number in their *in vitro* experiments. Keeping the Stokes number fixed in a given geometry, the deposition fraction in the extrathoracic airways was different at different flow rates. The empirical correlation they proposed, $StkRe^{0.37}$, showed better collapse of the data onto a single curve. However, the physical significance of this Reynolds number correction $Re^{0.37}$ was not explained and is addressed herein.

The Reynolds number dependence is due to at least two contributing factors: (1) the difference in the mean flow characteristics and, (2) the difference in turbulence intensity. Whereas the effect of the mean flow field is already taken into account in the Stokes number, the level of turbulence intensities is not, which could be a reason for the observed scatter. The mean flow field only accounts for impaction as a deposition mechanism, and does not include the turbulence dispersion experienced by the particles due to velocity fluctuations.

For canonical turbulent flows, such as channel and pipe flow, particle deposition is well documented in the literature (Liu & Agarwal, 1974; Kallio & Reeks, 1989; McLaughlin, 1989; Wang & Squires, 1996; Young & Leeming, 1997) and is generally plotted against the dimensionless particle relaxation time, τ_p^+, given by

$$\tau_p^+ = \frac{\tau_p u_\tau^2}{\nu}. \tag{4.8}$$

This is the particle relaxation time non-dimensionalized by the friction velocity, u_τ. A summary of experimental data in fully developed turbulent pipe flow for the rate of particle deposition on the wall as a function of particle size is shown in figure 4-24. The dimensionless deposition velocity, V_{dep_+}, is given by

$$V_{dep_+} = \frac{J_w}{\rho_{pm} u_\tau}, \tag{4.9}$$

where J_w is the mass flux of particles to the wall per unit area and ρ_{pm} is the mean particle density in the pipe.

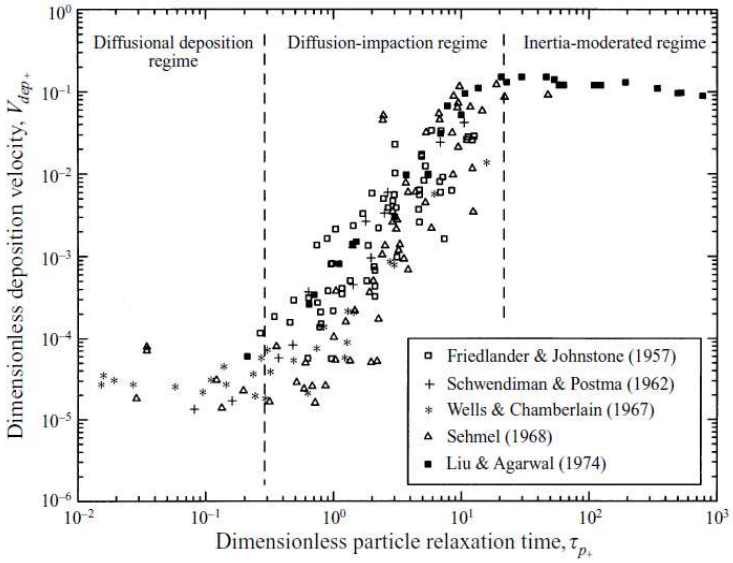


Figure 4-24: Particle deposition from fully developed turbulent pipe flow: a summary of experimental data (Young & Leeming, 1997).

The deposition curves are divided into three regimes: the turbulent diffusion regime, the diffusion-impaction regime and the particle inertia moderated regime. In the turbulent diffusion regime, deposition monotonically decreases with increasing τ_p^+ as the smaller the particle the larger the effect of the velocity fluctuations on its trajectory. In the diffusion-impaction regime, a large increase in the deposition with particle size is observed due to a mechanism known as turbophoresis. Turbophoresis is caused by the decay of turbulence intensity near the wall. Particles acquire a drift velocity in the direction of decreasing turbulence intensity, causing them to move towards the walls. This move is opposed by the mean viscous drag of the fluid. Therefore, drift velocity increases with particle size, as the inertia of the particle to overcome the drag increases. In the inertia moderated regime, the particles are so large that they no longer respond to turbulent fluctuations and so turbophoresis decreases. These particles deposit on the walls by impaction, as they deviate

from the streamlines due to their high momentum.

It is difficult to determine u_τ in the extrathoracic airways, partly because it is inhomogeneous due to the complexity of the geometry and partly because of the transitional nature of the flow. Using the friction velocity in the inlet tube as an estimate for the friction velocity in the mouth and throat, the non-dimensional relaxation times of the aerosol particles in the various mouth-throat geometries fall between the diffusional and diffusional-impaction regimes. Therefore, we would expect better collapse of the data if deposition were plotted against a parameter that takes into account both impaction and turbulent diffusion. Plotting against τ_p^+ takes both these deposition mechanisms into account. We can rewrite equation 4.8 as

$$\tau_p^+ = Stk \frac{L}{U} \frac{u_\tau^2}{\nu}, \tag{4.10}$$

where Stk is the Stokes number, $\frac{L}{U}$ is the mean fluid time scale and $\frac{u_\tau^2}{\nu}$ is the viscous time scale. Since fluctuations scale roughly with the friction velocity u_τ, the viscous time scale can be seen as representing the fluctuation time scale and equation 4.10 can be expressed as

$$\tau_p^+ = \frac{\tau_p}{\tau_{f_{mean}}} \frac{\tau_{f_{mean}}}{\tau_{f_{fluct}}}. \tag{4.11}$$

For fully-developed turbulent pipe flow, a relation between the friction velocity and the mean velocity can be obtained through the expression for the friction factor,

$$f = \frac{4\tau_w}{\frac{1}{2}\rho U^2} = 8\left(\frac{u_\tau}{U}\right)^2. \tag{4.12}$$

Blasius (1913) derived a fit for the experimental data, given by

$$f = \frac{0.3164}{Re^{0.25}}, \tag{4.13}$$

from which an expression for the friction velocity can be obtained

$$u_\tau^2 = \frac{0.3164U^2}{8Re^{0.25}}. \tag{4.14}$$

Substituting into equation 4.10 yields

$$\tau_p^+ = \frac{0.3164}{8} StkRe^{0.75}. \tag{4.15}$$

Equation 4.15 gives the nondimensional relaxation time in terms of Stokes and Reynolds numbers, showing the dependence of deposition on these two parameters. Unfortunately, this is only valid for fully-developed, smooth, turbulent pipe flow. A similar expression for the mouth and throat cannot be derived analytically as there is no such simple relation for u_τ. The empirical correlation of Grgic *et al.* (2004*b*), $StkRe^{0.37}$, suggests that the ratio of friction velocity to mean velocity decays faster in the mouth and throat, $\left(\frac{u_\tau}{U}\right)^2 \propto Re^{-0.63}$, than it does in a pipe $\left(\frac{u_\tau}{U}\right)^2 \propto Re^{-0.25}$. Since u_τ in the mouth-throat cannot easily be determined, τ_p^+ for the particles is computed based on the friction velocity at the inlet pipe. The deposition fractions in the four models plotted against τ_p^+ along with the *in vitro* data are shown in figure 4-25.

The results presented herein demonstrate that the flow in the extrathoracic airways is complex due to their geometry, which varies significantly across subjects. For a given flow rate, this geometric variation leads to different Reynolds numbers, which results in different flows and hence deposition patterns. Variation is observed even within the same subject, where the position of the tongue can create significant geometric differences resulting in qualitatively different flow features. For example, the impinging pharyngeal jet present in geometry S1b does not exist in S1a, where the tongue is pulled back. This variation is even

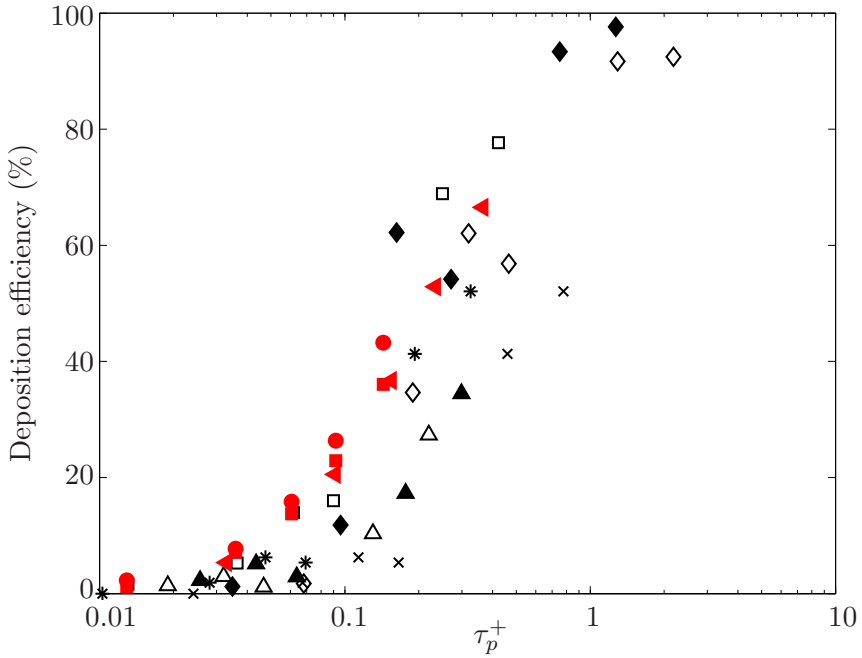


Figure 4-25: Deposition efficiency versus nondimensional particle relaxation time. Current method: ◀, S1a; ●, S2; ■, S4. *In vitro* studies in various geometries: ♦, ◇, ∗, ×, □, ▲, △.

more pronounced across subjects, as is observed by comparison of geometries S2 and S4 with S1a and S1b. Differences in the mean flow (impinging jets, separated shear layers, vortical patterns) as well as in the velocity fluctuations can be observed, both of which have an effect on particle trajectories, and hence their deposition. Even at the same Reynolds number and flow rate, as is the case in geometries S2 and S4, flow features differ significantly due to the difference in geometries. This is because the Reynolds number is based on a mean length scale whereas the diameters of the geometries deviate considerably from the mean in many sections of the airways. Therefore, knowledge of the particle Stokes numbers and the Reynolds number in the airways allows for a general prediction of deposition efficiency using the best fit curve. However, large scatter in the data still exists. This can be observed in figure 4-23 where, for a given value of $StkRe^{0.37}$, DNS results in different geometries vary by as much as 10% and *in vitro* results by as much as 30-40%. Therefore, in cases where

accurate predictions are desired in order to minimize extrathoracic deposition for optimal delivery to the lungs (e.g. for patients with severe COPD or asthma), subject-specific assessment of deposition is necessary. Numerical simulations can provide an effective and cost-efficient prediction relative to *in vitro* testing.

Chapter 5

Conclusions

5.1 Summary and key results

The main objective of this work was to develop a numerical model for the simulation of flow and particle deposition in the extrathoracic airways. This is of particular interest to the pharmaceutical industry in order to assess and optimize the delivery of therapeutic aerosols to the lungs. Numerical models offer a non-invasive and cost-effective alternative to *in vivo* and *in vitro* tests. However, a complete model of deposition in the extrathoracic airways was lacking from the literature. The limitations of the models to date can be attributed mainly to the use of idealized geometries and to an inaccurate representation of the turbulent flow field. These shortcomings have been addressed by carrying out direct numerical simulations in order to resolve all the scales in the flow and by using patient-specific geometries obtained from MRI scans. The two main aspects of this work have been the development of an immersed boundary method so as to model the realistic geometries efficiently, and the implementation of a particle tracking algorithm in order to determine deposition.

5.1.1 Immersed boundary method

The main advantage of immersed boundary methods is the fact that structured grids can be used for any arbitrary geometry, which greatly simplifies the task of grid generation. In addition, structured grids lend themselves to more efficient solvers. Therefore, using an IB method eliminates the need of constructing a new mesh for every new throat geometry and circumvents the high computational costs incurred by unstructured grid solvers. A direct forcing method has been applied due to its enhanced stability in comparison with other immersed boundary methods.

The accuracy and stability of direct forcing methods used in conjunction with the fractional step algorithm depend on the computation of the forcing term. Explicit forcing methods introduce an error near the immersed boundary which can cause the scheme to become unstable at high Reynolds numbers since the viscous stability constraint becomes much more restrictive than the CFL condition. Error analysis of the explicit forcing methods showed the errors introduced when an inconsistent scheme is used for the computation of the forcing term. A stable second-order accurate scheme was proposed, which consists of an iterative approach that removes the errors at the boundary and enhances stability. It was shown that the condition for convergence is always satisfied (except for $Re \rightarrow 0$) since the CFL constraint on the time step is much more restrictive. The scheme converges rapidly, ensuring that the immersed boundary conditions are being enforced accurately.

In addition, it was shown that the accuracy of IB methods depends on the form of the fractional step algorithm. Immersed boundary conditions applied on the Δp-form of the fractional step method are second-order accurate, whereas the p-form is only first-order accurate in time.

Finally, the proposed method was applied in generalized curvilinear systems. Most

immersed boundary methods to date have only been applied to Cartesian grids but some simulations are better suited to curvilinear grids. In the case of the mouth and throat geometries, a curvilinear grid is advantageous as it minimizes the number of unused cells outside the fluid domain. This results in improved computational efficiency. In addition, it also has a more natural alignment with the flow in the airways.

5.1.2 Particle tracking

Aerosols used in inhaled drug delivery are dilute dispersed two-phase flows which fall into the one-way coupling regime. The forces acting on the aerosol particles are drag and gravity; all other forces are negligible. A Lagrangian approach was employed to track the particles through the flow field. Two algorithms were developed, one in physical space and one in computational space. The C-space algorithm has the advantage that point location is more efficient to perform. In addition, it does not require interpolation of the fluxes in order to compute the Cartesian velocities, which can lead to errors in the particle trajectories. Therefore, it is more attractive when the flow equations are solved in terms of contravariant components. A limited number of interpolation schemes exists for use on curvilinear grids. The standard linear interpolation cannot be applied as the grid is not orthogonal in P-space and the velocities are discontinuous in C-space. Taylor expansion and inverse distance weighting schemes have been tested. It was concluded that the most accurate scheme in P-space is the Taylor expansion, whilst the inverse-distance weighting performs better in C-space.

5.1.3 Flow and particle deposition in the extrathoracic airways

The flow and particle deposition in four realistic mouth and throat geometries was studied in order to determine the effect of geometric variation and inflow turbulence on deposition

efficiency. The results showed that geometric variation has a large effect on both the mean flow characteristics and the levels of turbulence intensity. Due to their complex geometry, flow in the extrathoracic airways transitions to turbulence even if the inflow is laminar. Highly asymmetric velocity profiles, complex secondary flow and regions of separation were observed in all geometries.

Intersubject variation was shown to have a larger effect than intrasubject variation on particle deposition. Inflow turbulence leads to a slight increase in oral deposition but does not significantly affect total deposition. Both the total deposition and the main region of deposition vary across geometries. The maximum deposition tends to occur where velocities are largest and there are sudden changes in the flow direction, as also observed in the *in vitro* studies. This confirms that impaction is the main deposition mechanism in the extrathoracic airways.

The scatter in deposition efficiency when plotted against Stokes number can be attributed to the fact that Stk only accounts for the mean flow characteristics. However, turbulence intensity also has an effect on the particles. Using the dimensionless particle relaxation time τ_p, which takes into account both impaction and turbulent diffusion, the physical significance of the Reynolds number correction proposed in the literature was explained.

5.2 Future work

The capabilities developed in this project will be used to extend the work to the lower airways of the respiratory system. Modelling airways of patients with chronic obstructive pulmonary disease (COPD) and asthma is of particular interest since the airway morphology and behaviour of the lung differ to that of healthy subjects. Patients with asthma experience

a narrowing of the airways caused by airway inflammation and smooth muscle contraction. In addition, the chronic inflammatory process can also lead to airway remodelling, which results in permanent structural changes to the airways. In COPD, which consists of chronic bronchitis and/or emphysema, there is also a reduction in the elastic recoil of the lung due to the destruction of alveolar walls. This leads to closure of small airways, in particular during expiration.

Simulation of the flow and the particle deposition in the lungs of patients with COPD and asthma requires two main extensions to the current capabilities:

1. Extension of the immersed boundary method to moving boundaries in order to simulate airway collapse on expiration.

2. Extension of the flow solver to multiblock configurations in order to efficiently mesh the complex tracheobronchial tree.

These extensions are discussed in more detail below.

5.2.1 Immersed boundary method for moving boundaries

Extension of the immersed boundary scheme to moving boundaries can be implemented with relative ease. Unlike the approach for a stationary boundary, where the IB points and mirror points can be determined once as a pre-processing step' for a moving boundary this procedure is repeated at every time step. If the velocity of the boundary is known, the new boundary location is determined by moving each triangle on the surface by its velocity,

$$\frac{\boldsymbol{X}^{n+1} - \boldsymbol{X}^{n}}{\Delta t} = \boldsymbol{V}^{n+1}. \tag{5.1}$$

At every time step the new boundary location is computed, the IB points are determined and the forcing is added to the intermediate flux equations.

The main issues encountered with moving boundaries are: (1) stability, (2) "freshly-cleared cells" and (3) constructing a dynamic model of the geometry.

Kim & Choi (2006) experienced stability issues with an immersed boundary method for moving bodies developed in a non-inertial reference frame. Stability was enhanced by introducing the momentum forcing and mass source terms in the entire solid. Kang & Hassan (2011) stated that for moving boundary problems, the direct-forcing IB method could cause spurious oscillations due to the discontinuous changes of the interpolation points and the freshly-cleared cells. The implicit IB method developed, which enhances stability, should alleviate the problem in the case of moving boundaries also. In addition, restricting the boundary movement to less than one grid cell per time step ensures the CFL condition is being satisfied. Finally, the problem of freshly-cleared cells, which will be discussed below, should be properly addressed.

When an immersed boundary is moving, there are two possible scenarios: (1) it moves further into the fluid, or (2) it withdraws from the fluid domain. In the first scenario, there are two possible changes in the points near the boundary, since its movement is limited by the CFL condition to one grid cell per time step: (a) fluid to IB point and (b) IB point to solid. These changes do not pose any problems. In the second case where the boundary withdraws from the fluid however, the possible changes are: (a) solid to IB point and (b) IB point to fluid. The issue arises with IB points becoming fluid points; the so-called "freshly-cleared" cells. These are cells in the fluid which were in the solid at the previous time step. The issue with these cells is in the evaluation of the terms in the momentum equation, as the flow variables at these points do not have a valid time-history; the unphysical values

at previous time steps could cause large errors at the boundary and eventually lead to instability. Various solutions are possible:

1. Merge freshly-cleared cells with adjacent fluid cells (Udaykumar *et al.*, 1999). However, this approach suffers from the same problems as the cut-cell method for stationary boundaries discussed in section 2.2.

2. Have IB points lie in the fluid rather than in the solid so that IB points have physical values of velocity (Yang & Balaras, 2006). However, they will not have physical values of the derivatives, as these involve points from the solid. Therefore these points will still require special treatment.

3. Treat freshly-cleared cells as IB points (add forcing in momentum equations) and set their velocity by interpolation between a mirror point and the immersed boundary (Mittal *et al.*, 2008).

Applying approach 3 is the simplest and most robust solution for the current IB method. The velocities at the freshly-cleared cells need to be computed first, before determining the value at the IB points as the interpolation stencil for the IB points is likely to include freshly-cleared cells.

Finally, one added difficulty in this particular case is the construction of a dynamic model of the respiratory airways during inspiration. Only two geometries of the lung are provided, one at functional residual capacity (FRC) and another at total lung capacity (TLC), corresponding to the beginning and end of inspiration. In addition, there is no one-to-one mapping of the two triangulated surface meshes generated from the MRI scans. A registration method is required in order to determine the transformation between the two surfaces. A detailed review of the various image registration methods can be found in Zitova

& Flusser (2003). In this case, we want to determine the deformation transformation of the lungs from TLC to FRC. A non-rigid registration should be applied in order to capture the non-uniform expansion of the lung. A number of approaches for this specific purpose have been proposed in the literature (Li *et al.*, 2008; Yin *et al.*, 2009*a*,*b*, 2011).

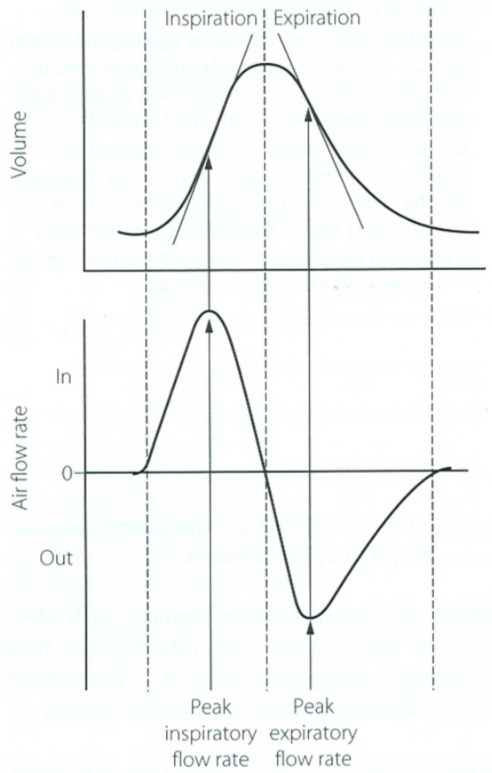


Figure 5-1: Relationship between volume and flow rate in the breathing cycle (Lumb, 2005).

Once an accurate transformation map has been obtained, the time-varying geometry can be derived using a suitable interpolation technique. An assumption has to be made as to the movement of the airways between TLC and FRC. The simplest approach is to assume linear movement and apply a constant velocity. This approach can only be used for simulation of half the breathing cycle, as it would otherwise lead to a step discontinuity in the velocity between inspiration and expiration. A more realistic assumption would be to model the motion sinusoidally, which approximates the flow during the breathing cycle (see

figure 5-1). If the inspiratory flow was monitored when the MRI scans were taken, then that data could be used for an even more accurate representation of the lung expansion. The displacement of the geometry at any given time, $\boldsymbol{d}_s = \boldsymbol{x}_s - \boldsymbol{x}_{FRC}$, can be determined from

$$\boldsymbol{d}_s(\boldsymbol{x}) = f_s(t)\boldsymbol{d}(\boldsymbol{x}) \tag{5.2}$$

where $\boldsymbol{d}(\boldsymbol{x}) = \boldsymbol{x}_{TLC} - \boldsymbol{x}_{FRC}$ is the displacement of a triangle centre between FRC and TLC and $f_s(t)$ is the displacement interpolation function, $0 < f_s(t) < 1$. An example of the lung geometry at different time points during inspiration is shown in figure 5-2.

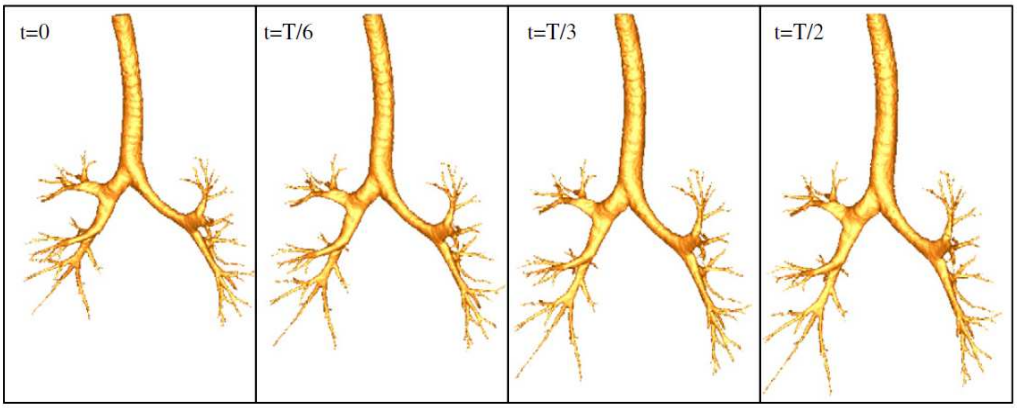


Figure 5-2: Airway geometries at four different time points from the dynamic airway geometrical model created with a registration method. From left to right: $t = 0$; $t = T/6$; $t = T/3$ and $t = T/2$, where T is the period (Yin *et al.*, 2011).

Another issue that requires consideration, which does not apply to the immersed boundary but to the flow solver, is the determination of the outflow conditions. Specifying equal outflows at all outlets of the model (either by applying uniform velocity, uniform pressure or uniform flow distribution) neglects the variation due to the geometry and the differences in lung compliance due to disease, which cause uneven regional distribution of flow in the lung. Yin *et al.* (2010) proposed a registration-based method for determining regional ventilation and applying subject-specific boundary conditions at the ending airway segments.

5.2.2 Multiblock solver

Meshing of the tracheobronchial tree using a single grid would be inefficient and would not provide the adequate resolution inside the numerous branches. A more practical approach would be to mesh the geometry using various patched or overlapping structured grids. Since the grid lines do not need to be continuous across the grid interfaces, this allows for much better local grid refinement. However it introduces some complexity, as grid interfaces

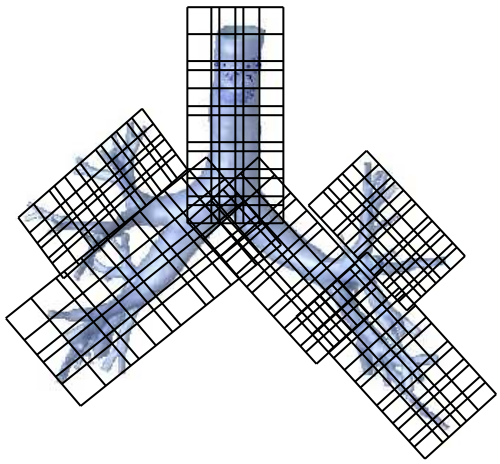


Figure 5-3: Schematic of the multiblock immersed boundary approach for the tracheobronchial tree.

now exist in the flow domain, which require boundary conditions in order to solve the flow equations. These boundary conditions need to be obtained from the adjacent block so a communication method to transfer data between blocks is necessary. Since grid lines are not continuous across block interfaces, interpolation is also required. Overlapping grids allow a better control of the grid, but increase the complexity of the communication between blocks. Care must be taken in order to ensure mass is conserved across block boundaries, as this is not guaranteed unless a conservative interpolation scheme is employed.

Zang & Street (1995) developed a multiblock solver for overlapping curvilinear grids, based on the semi-implicit finite volume method of Zang *et al.* (1994). A similar approach to theirs can be applied to our existing solver. In the fractional-step method, two types of

inter-grid boundary conditions are required. One is for the predictor step, and the other for the Poisson equation. In our case, no boundary conditions are required on the intermediate velocity for the predictor step (see Perot (1993) for an analysis of the fractional step method formulated as a block LU decomposition).

For the Poisson equation, inter-grid boundary conditions are traditionally applied on $\hat{\boldsymbol{u}}$ or $\hat{\boldsymbol{U}}$, by interpolation from the adjacent block, in order to compute the source terms on the right-hand side of the equation, and some type of pressure condition (either Dirichlet or Neumann) is applied for the pressure gradient on the left-hand side. Boundary conditions on pressure are usually not required on a single block domain, as the Navier-Stokes equations are well-posed if the velocity is prescribed on the boundary (Gresho & Sani, 1987). However, due to the nature of the Neumann boundary condition, the solution from the Poisson equation is unique only up to an additive constant (i.e: if ϕ is a solution, then $\phi + C$ is also a solution that satisfies the same boundary conditions). Therefore in a multiblock system where the equations are solved separately within each subdomain, each block generates a pressure field which is independent from those created in neighbouring blocks. The pressure fields must be coupled in order to avoid inconsistency of the solution, which is the reason that boundary conditions for pressure are required. Perng & Street (1991) discussed the choices of pressure boundary conditions and suggested that either pressure value or normal pressure gradient could be used as a boundary condition. However both Zang & Street (1995) and Thakur *et al.* (1998) observed that the use of the pressure value condition produced inconsistent solutions. Zang & Street (1995) proposed an alternative approach which does not require boundary conditions on the pressure. They suggested enforcing the boundary conditions for the Poisson equation on the volume flux $\boldsymbol{U}^n$, after projection rather than on the intermediate field. The projection step (equation 2.21c) for the points on the

inter-grid boundary becomes

$$\boldsymbol{U}^{n,k} = \left(\hat{\boldsymbol{U}}\right)_I - (\boldsymbol{S}^{\xi}, \boldsymbol{S}^{\eta}, \boldsymbol{S}^{\zeta})^T \cdot \Delta t \left(G\phi^{n,k-1}\right)_I, \tag{5.3}$$

where the subscript I denotes that the value is interpolated from the adjacent block and the superscript k denotes the k^{th} block-to-block pressure iteration.

Conservation of mass is a very important requirement in the numerical solution of incompressible flows. In the same way the outflow condition is enforced to satisfy global mass conservation in the domain, conservation of mass in each block should also be maintained. The difficulty in a multiblock composition, however, is in constructing a conservative interpolation scheme for the inter-grid boundaries in a generalized curvilinear co-ordinate system. Zang & Street (1995) used a third-order biquadratic Lagrange interpolation which is non-conservative and employed the mass imbalance correction (MIC) scheme of Meakin (1986) in order to guarantee mass conservation. The MIC scheme consists of removing the amount of mass residual on a given block, generated by the non-conservative interpolation at the inter-grid boundaries. The correction is made to the volume flux after it is computed from equation 5.3 by applying the following formula,

$$\bar{U}_m^{n,k} = U_m^{n,k} - \frac{\epsilon_\nu |U_m^{n,k}|}{F} \frac{\boldsymbol{n} \cdot \boldsymbol{e_m}}{|\boldsymbol{n} \cdot \boldsymbol{e_m}|}, \tag{5.4}$$

where ϵ_ν is the mass imbalance and F is the sum of the absolute value of the volume fluxes over the inter-grid boundaries. They are given by

$$\epsilon_\nu = \sum_I \left(U_m^{n,k} \frac{\boldsymbol{n} \cdot \boldsymbol{e_m}}{|\boldsymbol{n} \cdot \boldsymbol{e_m}|} \right) \tag{5.5}$$

$$F = \sum_{I} |U_m^{n,k}| \tag{5.6}$$

where $\sum_{I}$ is the sum over all the inter-grid boundaries in a given block, $\boldsymbol{e_m}$ is the covariant base vector and $\boldsymbol{n}$ is the outward normal unit vector of the inter-grid boundary. Finally, the sequence of operations and the transfer of data between blocks in the multigrid method should be discussed. Although the sequence of operations is straightforward in a single domain, different strategies can be adopted when solving the equations on multiple domains:

1. Solve the velocity and pressure fields independently on each block, followed by an update of the information at any grid interfaces. Sweep through blocks until convergence is achieved on all blocks.

2. Solve the velocity field globally on all blocks, by iterating from block to block until convergence is achieved. Then, solve globally for pressure using block-to-block iteration again.

3. Solve the velocity field independently on each block and then solve the pressure field globally by sweeping through the blocks.

Scheme 3, originally introduced by Perng & Street (1991), is the least computationally expensive, while still possessing good global consistency and accuracy.

When using a multigrid method to accelerate the convergence of the Poisson equation there are two approaches that can be followed. According to the terminology given by Hinatsu & Ferziger (1991) these are: the complete composite multigrid method (CCMG), in which data is transferred between blocks at all multigrid levels, and the incomplete multigrid method (ICMG), in which data is only transferred at the finest grid level. Based on the performance of both methods, and considering overall efficiency and robustness, Zang & Street (1995) favoured the ICMG method. It was shown by Meakin & Street

(1988) that the more frequently the iteration is switched between blocks, the faster the global convergence rate. Therefore Zang & Street (1995) performed only one multigrid cycle on each grid before switching to the next one. Global convergence of the Poisson equation was obtained when the following were satisfied:

$$\epsilon_p < \epsilon_p^c \tag{5.7}$$

$$d\phi < d\phi^c \tag{5.8}$$

where ϵ_p is the averaged residual of the Poisson equation, $d\phi$ is the averaged difference in the pressure on inter-grid boundaries and ϵ_p^c and $d\phi^c$ are the corresponding threshold values.

The multiblock scheme can be summarized as follows:

Algorithm 4 multiblock scheme

for all blocks **do**
  `solve intermediate flux equation to obtain intermediate flux field`
end for
$k = 0$
while $(\epsilon_p > \epsilon_p^c)$ **or** $(d\phi > d\phi^c)$ **do**
  for current block **do**
    `interpolate` $U^{n,k}$ `at inter-grid boundaries from adjacent blocks`
    `correct` $U^{n,k}$ `to ensure mass-conservation`
    `perform one multigrid cycle`
  end for
  `go to next block`
  $k = k + 1$
end while
`Project` $\hat{U}$ `to` U^n
`Compute` ϕ^n

Bibliography

Achenbach, E. 1974 Vortex shedding from spheres. *Journal of Fluid Mechanics* **62**, 209–221.

Balaras, E. 2004 Modeling complex boundaries using an external force field on fixed Cartesian grids in large-eddy simulations. *Computers & Fluids* **33**, 375–404.

Berthelsen, P. A. & Faltinsen, O. M. 2008 A local directional ghost cell approach for incompressible viscous flow problems with irregular boundaries. *Journal of Computational Physics* **227**, 4354–4397.

Beyer, R. P. & Leveque, R. J. 1992 Analysis of a one-dimensional model for the immersed boundary method. *SIAM Journal on Numerical Analysis* **29** (2), 332–364.

Bisgaard, H., O'Callaghan, C. & Smaldone, G. C. 2007 *Drug Delivery to the Lung*. Informa Healthcare.

Blasius, H. 1913 Das aehnlichkeitsgesetz bei reibungsvorgangen in flssigkeiten. *Forschungsheft* **131**, 1–41.

Braza, M., Chassaing, P. & Minh, H. H. 1986 Numerical study and physical analysis of the pressure and velocity fields in the near wake of a circular cylinder. *Journal of Fluid Mechanics* **165**, 79–130.

Calhoun, D. 2002 A Cartesian grid method for solving the two-dimensional streamfunction-vorticity equations in irregular regions. *Journal of Computational Physics* **176**, 231–275.

Chan, T. L. & Lippmann, M. 1980 Experimental measurements and empirical modelling of the regional deposition of inhaled particles in humans. *American Industrial Hygiene Association Journal* **41** (6), 399–409.

Cheng, Y., Fu, C., Yazzie, D. & Zhou, Y. 2001 Respiratory deposition patterns of salbutamol pMDI with CFC and HFA-134a formulations in a human airway replica. *Journal of Aerosol Medicine* **14** (2), 255–266.

Cheng, Y. S. & Wang, C. S. 1975 Inertial deposition of particles in a bend. *Aerosol Science* **6**, 139–145.

Cheng, Y. S. & Wang, C. S. 1981 Motion of particles in bends of circular pipes. *Atmospheric Environment* **15**, 301–306.

Cheng, Y. S., Zhou, Y. & Chen, B. T. 1999 Particle deposition in a cast of human oral airways. *Aerosol Science and Technology* **31**, 286–300.

Cherukat, P., Na, Y., Hanratty, T. J. & B., M. J. 1998 Direct numerical simulation of a fully developed turbulent flow over a wavy wall. *Theoretical and Computational Fluid Dynamics* **11**, 109–134.

Clift, R. & Gauvin, W. 1970 *Proceedings of Chemeca 70* **1**, 14–28.

Cormen, T. H. 2001 *Introduction to algorithms*. MIT Press.

Coutanceau, M. & Bouard, R. 1977 Experimental determination of the main features of the viscous flow in the wake of a circular cylinder in uniform translation. Part 1. Steady flow. *Journal of Fluid Mechanics* **79**, 231–256.

Daskopoulos, P. & Lenhoff, A. M. 1989 Flow in curved ducts: bifurcation structure for stationary ducts. *Journal of Fluid Mechanics* **203**, 125–148.

De Angelis, V., Lombardi, P. & Banerjee, S. 1997 Direct numerical simulation of turbulent flow over a wavy wall. *Physics of Fluids* **9** (8), 2429–2442.

Debhi, A. 2011 Prediction of extrathoracic aerosol deposition using RANS-random walk and LES approaches. *Aerosol Science and Technology* **45**, 555–569.

DeHaan, W. & Finlay, W. 2004 Predicting extrathoracic deposition from dry powder inhalers. *Journal of Aerosol Science* **35**, 309–331.

Dekker, E. 1961 Transition between laminar and turbulent flow in human trachea. *Journal of Applied Physiology* **16** (6), 1060–1064.

Dennis, S. C. R. & Chang, G. 1970 Numerical solutions for steady flow past a circular cylinder at Reynolds number up to 100. *Journal of Fluid Mechanics* **42**, 471–489.

Domenichini, F. 2008 On the consistency of the direct forcing method in the fractional step solution of the Navier-Stokes equations. *Journal of Computational Physics* **227**, 6372–6384.

Eggels, J. G., Unger, F., Weiss, M. H., Westerweel, J., Adrian, R. J., Friedrich, R. & Nieuwstadt, F. T. M. 1994 Fully developed turbulent pipe flow: a comparison between direct numerical simulation and experiment. *Journal of Fluid Mechanics* **268**, 175–209.

Elghobashi, S. 1994 On predicting particle-laden turbulent flows. *Applied Scientific Research* **52**, 309–329.

Elghobashi, S. & Truesdell, G. C. 1992 Direct simulation of particle dispersion in a decaying isotropic turbulence. *Journal of Fluid Mechanics* **242**, 655–700.

Emmett, P. C. & Aitken, R. J. 1982 Measurements of the total and regional deposition of inhaled particles in the human respiratory tract. *Journal of Aerosol Science* **13** (6), 549–563.

Fadlun, E. A., Verzicco, R., Orlandi, P. & Mohd-Yusof, J. 2000 Combined immersed-boundary finite-difference methods for three-dimensional complex flow simulations. *Journal of Computational Physics* **161**, 35–60.

Finlay, W., Stapleton, K. & Yokota, J. 1996 On the use of computational fluid dynamics for simulating flow and particle deposition in the human respiratory tract. *Journal of Aerosol Science* **9** (3), 329–341.

Foord, N., Black, A. & Walsh, M. 1978 Regional deposition of 2.5-7.5 μm diameter inhaled particles in healthy male non-smokers. *Journal of Aerosol Science* **9**, 343–357.

Fornberg, B. 1980 A numerical study of steady viscous flow past a circular cylinder. *Journal of Fluid Mechanics* **98**, 819–855.

Ge, L. & Sotiropoulos, F. 2007 A numerical method for solving the 3D unsteady incompressible Navier-Stokes equations in curvilinear domains with complex immersed boundaries. *Journal of Computational Physics* **225**, 1782–1809.

Ghias, R., Mittal, R. & Dong, H. 2007 Sharp interface immersed boundary method for compressible viscous flows. *Journal of Computational Physics* **225**, 528–553.

Gilmanov, A. & Sotiropoulos, F. 2005 A hybrid Cartesian/immersed boundary method for simulating flows with 3D, geometrically complex, moving bodies. *Journal of Computational Physics* **207**, 457–492.

Goldstein, D., Handler, R. & Sirovich, L. 1993 Modeling a no-slip flow boundary with an external force field. *Journal of Computational Physics* **105**, 354–366.

Gosman, A. D. & Ioannides, E. 1983 Aspects of computer simulation of liquid fuelled combustors. *Journal of Energy* **7**, 482–490.

Gresho, P. & Sani, R. 1987 On pressure boundary conditions for the incompressible Navier-Stokes equations. *International Journal for Numerical Methods in Fluids* **7**, 1111–1145.

Grgic, B., Finlay, W., Burnell, P. & Heenan, A. 2004*a* In vitro intersubject and intrasubject deposition measurements in realistic mouth-throat geometries. *Journal of Aerosol Science* **35**, 1025–1040.

Grgic, B., Finlay, W. & Heenan, A. 2004*b* Regional aerosol deposition and flow measurements in an idealized mouth and throat. *Journal of Aerosol Science* **35**, 21–32.

Guy, R. & Hartenstine, D. 2010 On the accuracy of direct forcing immersed boundary methods with projection methods. *Journal of Computational Physics* **229**, 2479–2496.

Heenan, A., Finlay, W., Grgic, B., Pollard, A. & Burnell, P. 2004 An investigation of the relationship between the flow field and regional deposition in realistic extra-thoracic airways. *Journal of Aerosol Science* **35**, 1013–1023.

Hinatsu, M. & Ferziger, J. 1991 Numerical computation of unsteady incompressible flow in complex geometry using a composite multigrid technique. *International Journal of Numerical Methods for Fluids* **13**, 971–997.

Hudson, J. D. 1993 The effect of a wavy boundary on turbulent flow. PhD thesis, University of Illinois.

Hudson, J. D., Dykhno, L. & Hanratty, T. J. 1996 Turbulence production in flow over a wavy wall. *Experiments in Fluids* **20**, 257–265.

Humphrey, J. A. C., Taylor, A. M. K. & Whitelaw, J. H. 1977 Laminar flow in a square duct of strong curvature. *Journal of Fluid Mechanics* **83**, 509–527.

Iaccarino, G. & Verzicco, R. 2003 Immersed boundary technique for turbulent flow simulations. *Applied Mechanics Review* **56** (3), 331–347.

Ikeno, T. & Kajishima, T. 2007 Finite-difference immersed boundary method consistent with wall conditions for incompressible turbulent flow simulations. *Journal of Computational Physics* **226**, 1485–1508.

Jayaraju, S. T., Brouns, M., Verbanck, S. & Lacor, C. 2007 Fluid flow and particle deposition analysis in a realistic extrathoracic airway model using unstructured grids. *Journal of Aerosol Science* **38**, 494–508.

Jeong, J. & Hussain, F. 1995 On the identification of a vortex. *Journal of Fluid Mechanics* **285**, 69–94.

Johnson, T. A. 1996 Numerical and experimental investigation of flow past a sphere up to a Reynolds number of 300. PhD thesis, University of Iowa.

Johnson, T. A. & Patel, V. C. 1999 Flow past a sphere up to a Reynolds number of 300. *Journal of Fluid Mechanics* **378**, 19–70.

Kalitzin, G. & Iaccarino, G. 2003 Toward immersed boundary simulation of high Reynolds number flows. *Center for Turbulence Research Annual Research Briefs* .

Kallio, G. A. & Reeks, M. W. 1989 A numerical simulation of particle deposition in turbulent boundary layers. *International Journal of Multiphase Flow* **15** (3), 433–446.

Kang, S. K. & Hassan, Y. A. 2011 A comparative study of direct-forcing immersed boundary-lattice Boltzmann methods for stationary complex boundaries. *International Journal for Numerical Methods in Fluids* **66**, 1132–1158.

Kim, D. & Choi, H. 2006 Immersed boundary method for flow around an arbitrarily moving body. *Journal of Computational Physics* **212**, 662–680.

Kim, J., Kim, D. & Choi, H. 2001 An immersed-boundary finite-volume method for simulations of flows in complex geometries. *Journal of Computational Physics* **171**, 132–150.

Kim, J. & Moin, P. 1985 Application of a fractional-step method to incompressible Navier-Stokes equations. *Journal of Computational Physics* **59**, 308–323.

Kim, J., Moin, P. & Moser, R. 1987 Turbulence statistics in fully developed channel flow at low reynolds number. *Journal of Fluid Mechanics* **177**, 133–166.

Kirkpatrick, M., Armfield, S. & Kent, J. 2003 A representation of curved boundaries for the solution of the Navier-Stokes equations on a staggered three-dimensional Cartesian grid. *Journal of Computational Physics* **184**, 1–36.

Kleinstreuer, C., Zhang, Z. & Donohue, J. F. 2008 Targeted drug-aerosol delivery in the human respiratory system. *Annual Review of Biomedical Engineering* **10**, 195–220.

Kontomaris, K. & Hanratty, T. J. 1992 An algorithm for tracking fluid particles in a spectral simulation of turbulent channel flow. *Journal of Computational Physics* **103**, 231–242.

Lai, M. & Peskin, C. 2000 An immersed boundary method with formal second-order accuracy and reduced numerical viscosity. *Journal of Computational Physics* **160**, 705–719.

Leach, C. 1998 Improved delivery of inhaled steroid to large and small airways. *Repiratory Medicine* **92**, 3–8.

Leveque, R. & Li, Z. 1994 The immersed interface method for elliptic equations with discontinuous coefficients and singular sources. *SIAM Journal on Numerical Analysis* **31**, 1019–1044.

Li, B., Christensen, G. E., Hoffman, E. A., McLennan, G. & Reinhardt, J. M. 2008 Pulmonary CT image registration and warping for tracking tissue deformation during the respiratory cycle through 3D consistent image registration. *Medical Physics* **35** (12), 5575–5583.

Lin, T. C., Breysee, P. N., Laube, B. L. & Swift, D. L. 2001 Mouthpiece diameter affects deposition efficiency in cast models of the human oral airways. *Journal of Aerosol Medicine* **14** (3), 335–341.

Linnik, M. N. & Fasel, H. F. 2005 A high-order immersed interface method for simulating unsteady incompressible flows on irregular domains. *Journal of Computational Physics* **204**, 157–192.

Lipworth, B. 1996 Pharmacokinetics of inhaled drugs. *British Journal of Clinical Pharmacology* **42**, 697–705.

Liu, B. Y. H. & Agarwal, J. K. 1974 Experimental observation of aerosol deposition in turbulent flow. *Journal of Aerosol Science* **5**, 145–155.

Liu, C., Zheng, X. & Sung, C. H. 1998 Preconditioned multigrid methods for unsteady incompressible flows. *Journal of Computational Physics* **139**, 35–57.

Lumb, A. B. 2005 *Nunn's Applied Respiratory Physiology*, 6th edn. Elsevier Limited.

Lumley, J. 1978 Two-phase and non-Newtonian flows. *Topics of Physics* **12**, 290–324.

Maas, C. & Schumann, U. 1996 Direct numerical simulation of separated turbulent flow over a wavy boundary. *Flow simulation with high performance computers. Notes on numerical fluid mechanics* **52**, 227–241.

Majumdar, S., Iaccarino, G. & Durbin, P. 2001 RANS solvers with adaptive structured boundary non-conforming grids. *Center for Turbulence Research Annual Research Briefs* pp. 353–366.

Marchioli, C., Armenio, V. & Soldati, A. 2007 Simple and accurate scheme for fluid velocity interpolation for Eulerian-Lagrangian computation of dispersed flows in 3D curvilinear grids. *Computers & Fluids* **36**, 1187–1198.

Marella, S., Krishnan, S. & Udaykumar, H. S. 2005 Sharp interface Cartesian grid method I: An easily implemented technique for 3D moving boundary computations. *Journal of Computational Physics* **210**, 1–31.

Mark, A. & van Wachem, B. G. 2008 Derivation and validation of a novel implicit second-order accurate immersed boundary method. *Journal of Computational Physics* **227**, 6660–6680.

Matida, E., Finlay, W., Lange, C. & Grgic, B. 2004 Improved numerical simulation of aerosol deposition in an idealized mouth-throat. *Journal of Aerosol Science* **35**, 1–19.

Matthys, H. & Kohler, D. 1985 Pulmonary deposition of aerosols by different mechanical devices. *Respiration* **48**, 269–276.

Mavriplis, D. J. 1997 Unstructured grid techniques. *Annual Reviews of Fluid Mechanics* **29**, 473–514.

Maxey, M. R. & Riley, J. J. 1983 Equation of motion for a small rigid sphere in a nonuniform flow. *Physics of Fluids* **26**, 883–889.

McLaughlin, J. B. 1989 Aerosol particle deposition in numerically simulated channel flow. *Physics of Fluids A* **1**, 1211–1224.

McLaughlin, J. B. 1994 Numerical computation of particles-turbulence interaction. *International Journal of Multiphase Flow* **20**, 211–232.

McRobbie, D. W., Pritchard, S. & Quest, R. A. 2003 Studies of the human oropharyngeal airspaces using magnetic resonance imaging. I. Validation of a three-dimensional MRI method for producing *ex vivo* virtual and physical casts of the oropharyngeal airways during inspiration. *Journal of Aerosol Medicine* **16** (4), 401–415.

Meakin, R. L. 1986 Application of boundary conforming coordinate and domain decomposition principles to environmental flows. PhD thesis, Department of Civil Engineering, Stanford University.

Meakin, R. L. & Street, R. L. 1988 Simulation of environmental flow problems in geometrically complex domains, part 2: A domain-splitting method. *Computational Methods in Applied Mechanics and Engineering* **68**, 311–331.

Mittal, R., Dong, H., Bozkurttas, M., Najjar, F. M., Vargas, A. & von Loebbecke, A. 2008 A versatile sharp interface immersed boundary method for incompressible flows with complex boundaries. *Journal of Computational Physics* **227**, 4825–4852.

Mittal, R. & Iaccarino, G. 2005 Immersed boundary methods. *Annual Review of Fluid Mechanics* **37**, 239–261.

Mohd-Yusof, J. 1997 Combined immersed-boundary/B-spline methods for simulations of flow in complex geometries. *Center for Turbulent Research Annual Research Briefs* pp. 317–327.

Ounis, H., Ahmadi, G. & McLaughlin, J. B. 1991 Brownian diffusion of submicrometer particles in the viscous sublayer. *Journal of Colloid and Interface Science* **143** (1), 266–277.

Pan, D. & Shen, T. T. 2009 Computation of incompressible flows with immersed bodies by a simple ghost cell method. *International Journal for Numerical Methods in Fluids* **60**, 1378–1401.

Patton, J. S. & Byron, R. 2007 Inhaling medicines: delivering drugs to the body through the lungs. *Nature Reviews* **6**, 67–74.

Perić, M. 1985 A finite volume method for the prediction of three-dimensional fluid flow in complex ducts. PhD thesis, Imperial College London.

Perng, C. Y. & Street, R. L. 1991 A coupled multigrid-domain-splitting technique for simulating incompressible flows in geometrically complex domains. *International Journal of Numerical Methods for Fluids* **13**, 269–286.

Perot, J. B. 1993 An analysis of the fractional step method. *Journal of Computational Physics* **108**, 51–58.

Peskin, C. S. 1972 Flow patterns around heart valves: A numerical method. *Journal of Computational Physics* **10** (2), 252–271.

Pope, S. D. 2000 *Turbulent flows*. Cambridge University Press.

Rajani, B., Kaqndasamy, A. & Majumdar, S. 2009 Numerical simulation of laminar flow past a circular cylinder. *Applied Mathematical Modelling* **33**, 1228–1247.

Rogers, S. E. & Kwak, D. 1991 Steady and unsteady solutions of the incompressible Navier-Stokes equations. *AIAA Journal* **29** (4), 603–610.

Roman, F., Napoli, E., Milici, B. & Armenio, V. 2009 An improved immersed boundary method for curvilinear grids. *Computers & Fluids* **38**, 1510–1527.

Rosenfeld, M., Kwak, D. & Vinokur, M. 1991 A fractional step solution method for the unsteady incompressible Navier-Stokes equation in generalized coordinate systems. *Journal of Computational Physics* **94**, 102–137.

Russel, D. & Wang, Z. J. 2003 A Cartesian grid method for modeling multiple moving objects in 2D incompressible viscous flow. *Journal of Computational Physics* **191**, 177–205.

Ruzer, L. S. & Harley, N. H. 2004 *Aerosols Handbook: Measurement, Dosimetry, and Health Effects*. CRC Press.

Saiki, E. & Biringen, S. 1996 Numerical simulation of a cylinder in uniform flow: application of a virtual boundary method. *Journal of Computational Physics* **123**, 450–465.

Schafer, F. & Breuer, M. 2002 Comparison of c-space and p-space particle tracing schemes on high-performance computers: accuracy and performance. *International Journal for Numerical Methods in Fluids* **39**, 277–299.

Sen, S., Mittal, S. & Biswas, G. 2009 Steady separated flow past a circular cylinder at low Reynolds numbers. *Journal of Fluid Mechanics* **620**, 89–119.

Sommerfeld, P. I. M. 2000 Theoretical and experimental modelling of particulate flows. *Tech. Rep.*. von Karman Institute for Fluid Dynamics.

Stahlhofen, W., Gebhart, J. & Heyder, J. 1980 Experimental determination of the regional deposition of aerosol particles in the human respiratory tract. *American Industrial Hygiene Association Journal* **41**, 385–398.

Stahlhofen, W., Gebhart, J. & Heyder, J. 1981 Biological variability of regional deposition of aerosol particles in the human respiratory tract. *American Industrial Hygiene Association Journal* **42**, 348–352.

Stahlhofen, W., Rudolf, G. & James, A. 1989 Intercomparison of experimental regional aerosol deposition data. *Journal of Aerosol Medicine* **2** (3), 285–308.

Stapleton, K. W., Guentsch, E., Hoskinon, M. K. & Finlay, W. H. 2000 On the suitability of $k - \epsilon$ turbulence modeling for aerosol deposition in the mouth and throat: A comparison with experiment. *Journal of Aerosol Science* **31** (6), 739–749.

Svartengren, K., Lindestad, P. A., Svartengren, M., Bylin, G., Philipson, K. & Camner, P. 1994 Deposition of inhaled particles in the mouth and throat of asthmatic subjects. *European Respiratory Journal* **7**, 1467–1473.

Taira, K. & Colonius, T. 2007 The immersed boundary method: A projection approach. *Journal of Computational Physics* **225**, 2118–2137.

Taneda, S. 1956 Experimental investigation of the wakes behind cylinders and plates at low Reynolds numbers. *Journal of the Physical Society of Japan* **11**, 302–307.

Taylor, G. I. 1938 The spectrum of turbulence. *Proceedings of the Royal Society of London. Series A, Mathematical and Physical Sciences* **164** (919), 476–490.

Thakur, S., Shyy, W., Udaykumar, H. S. & Hill, L. 1998 Multiblock interface treatments in a pressure-based flow solver. *Numerical Heat Transfer, Part B: Fundamentals* **33**, 367–396.

Tritton, D. J. 1959 Experiments on the flow past a circular cylinder at low Reynolds numbers. *Journal of Fluid Mechanics* **6**, 547–567.

Tseng, Y.-H. & Ferziger, J. H. 2003 A ghost-cell immersed boundary method for flow in complex geometry. *Journal of Computational Physics* **192**, 593–623.

Udaykumar, H. S., Mittal, R., Rampunggoon, P. & Khanna, A. 2001 A sharp interface Cartesian grid method for simulating flows with complex moving boundaries. *Journal of Computational Physics* **174**, 345–380.

Udaykumar, H. S., Mittal, R. & Shyy, W. 1999 Computation of solid-liquid phase fronts in the sharp interface limit on fixed grids. *Journal of Computational Physics* **153**, 535–574.

Verzicco, R., Mohd-Yusof, J., Orlandi, P. & Haworth, D. 1998 LES in complex geometries using boundary body forces. In *Center for Turbulence Research (Proceedings of the Summer Program)*.

Walsh, M., Black, A. & Foord, N. 1977 Apparatus for the administration by inhalation of radioactive particles to human subjects for studies of deposition and clearance. *Journal of Aerosol Science* **8**, 83–90.

Wang, Q. & Squires, K. D. 1996 Large eddy simulation of particle deposition in a vertical turbulent channel flow. *International Journal of Multiphase Flow* **22** (4), 667–683.

Williamson, C. H. K. 1989 Oblique and parallel modes of vortex shedding in the wake of a circular cylinder at low Reynolds numbers. *Journal of Fluid Mechanics* **206**, 579–627.

Williamson, C. H. K. & Roshko, A. 1990 Measurement of base pressure in the wake of a cylinder at low Reynolds numbers. *Z. Flugwiss. Weltraumforsch* **14**, 38.

Yang, J. & Balaras, E. 2006 An embedded-boundary formulation for large-eddy simulation of turbulent flows interacting with moving boundaries. *Journal of Computational Physics* **215**, 12–40.

Ye, T., Mittal, R., Udaykumar, H. S. & Shyy, W. 1999 An accurate Cartesian grid method for viscous incompressible flows with complex immersed boundaries. *Journal of Computational Physics* **156**, 209–240.

YEUNG, P. K. & POPE, S. B. 1988 An algorithm for tracking fluid particles in numerical simulations of homogeneous turbulence. *Journal of Computational Physics* **79**, 373–416.

YIN, Y., CHOI, J., HOFFMAN, E. A., TAWHAI, M. H. & LIN, C. 2010 Simulation of pulmonary air flow with a subject-specific boundary condition. *Journal of Biomechanics* **43**, 2159–2163.

YIN, Y., HOFFMAN, E. A. & LIN, C. 2009*a* Local tissue-weight-based nonrigid registration of lung images with application to regional ventilation. *SPIE Medical Imaging 09* **7262**, 72620C.

YIN, Y., HOFFMAN, E. A. & LIN, C. 2009*b* Mass preserving nonrigid registration of CT lung images using cubic B-spline. *Medical Physics* **36**, 4213–4222.

YIN, Y., HOFFMAN, E. A. & LIN, C. 2011 A cubic B-spline-based hybrid registration of lung CT images for a dynamic airway geometric model with large deformation. *Physics in Medicine and Biology* **56**, 203–218.

YOUNG, J. & LEEMING, A. 1997 A theory of particle deposition in turbulent pipe flow. *Journal of Fluid Mechanics* **340**, 129–159.

ZANG, Y. & STREET, R. L. 1995 A composite multigrid method for calculating unsteady incompressible flows in geometrically complex domains. *International Journal for Numerical Methods in Fluids* **20**, 341–361.

ZANG, Y., STREET, R. L. & KOSEFF, R. 1994 A non-staggered grid, fractional step method for time-dependent incompressible Navier-Stokes equations in curvilinear coordinates. *Journal of Computational Physics* **114**, 18–33.

Zhang, H., Fey, Y. & Noack, B. R. 1995 On the transition of the cylinder wake. *Physics of Fluids* **7**, 779–794.

Zhang, Z., Kleinstreuer, C. & Kim, C. S. 2002 Micro-particle transport and deposition in a human airway model. *Journal of Aerosol Science* **33**, 1635–1652.

Zitova, B. & Flusser, J. 2003 Image registration methods: a survey. *Image and Vision Computing* **21**, 977–1000.